Space Velocity Correlation In Orthogonal Time-of-Flight Mass Spectrometry

Dimitris Papanastasiou

Manchester Metropolitan University

November 2005

Acknowledgments

My thankfulness to my supervisor Dr Adam McMahon for his stimulating ideas and support throughout these years.

I feel indebted to Dr Martin McGuire and Dr Chris Poile for supporting the project and allowing me to diverge according to my willingness.

My gratitude to my father Yiannis for his elegant solutions in Chapter 2 and unlimited support.

My love to Malvina and Kaite for keeping the spirit higher than the usual.

To Akis, Tolis, Jonathan and Despina for their true friendship.

Declaration

No part of this work has been included or submitted for any other academic award. No material has been previously published except where due acknowledgment is made in the text.

Dimitris Papanastasiou

Abstract

The idea of space-velocity correlation in continuous ion beams is proposed and tested in a prototype orthogonal Time-of-Flight Mass Spectrometer (TOF MS). Analytical solutions to the time focusing properties of ions are presented based on linear phase space distributions at the start of the TOF experiment. The analysis is extended to non-linear distributions and their associated finite arrival time spreads. The prototype is equipped with a thermal/surface ionization source and an electron impact source, providing an excellent opportunity to investigate variations in the experimental variables required for enhancing resolving power. Theory and experiment merge in an effort to describe the behaviour of ions in the source and through the optical system, in terms of their time focusing properties in the mass analyzer.

Resolving powers exceeding 2000 with time spreads of the order of 1-3 ns across the atomic mass range are reported for small linear oTOF configurations. Optimum virtual sources for reflecting geometries are investigated by varying the dimensions of the mass spectrometer. The "open" orthogonal gate design is proposed as an alternative to the prevailing two-stage acceleration configuration. A low energy electron impact source is described and a triple filament thermal/surface ionization source for surface studies is constructed. The effect of a fast detection system on the overall performance of the prototype is demonstrated.

Exact solutions to the space focusing properties employing static and/or time dependent uniform electric fields are developed using the "ion pair" model. A focal region with variable temporal and spatial characteristics is identified along the field-free path of the ions by considering finite initial spatial distributions. The errors associated with the truncated *Taylor* series are highlighted. Focusing is not an instantaneous property in TOF MS. The analysis is extended to ions desorbing from surfaces and the theory of delayed extraction is reformulated. The focusing action of the TOF analyzer relies on the inherent ability of the system to provide ions with an initial distribution in electric potential energies. Space focusing theory and the delayed extraction technique were fundamental to the development of space-velocity correlation focusing in orthogonal geometries.

Further studies include the experimental determination of the work function of filaments based on their electron emission properties, measurements of the kinetic energy distribution of the emitted electrons, thermionic emission kinetics, SEM and XPS analysis of the filament surfaces and a literature survey of thermal/surface ionization and electron impact ion sources.

Acronyms

AP	Appearance Potential
ATOF	Aerosol Time-of-Flight
CHA	Concentric Hemispherical Analyzer
CID	Collision Induced Dissociation
DE	Delayed Extraction
EDS	Energy Dispersive Spectrometry
EI	Electron Impact/Electron Ionization
ESI	Electrospray Ionization
FAB	Fast Atom Bombardment
FT ICR	Fourier Transform Ion Cyclotron Resonance
FWHM	Full-width Half-maximum
FWTM	Full-width Tenth-Maximum
GC	Gas Chromatography
IM	Ion Mobility
IP	Ionization Potential
IT	Ion Trap
LAMMA	Laser Microprobe Mass Analysis
LD	Laser Desorption
MALDI	Matrix Assisted Laser Desorption Ionization
MCP	Micro-channel Plate
MS	Mass Spectrometry
oTOF	Orthogonal Time-of-Flight
PD	Plasma Desorption
PSD	Post Source Decay
QIT	Quadrupole Ion Trap
RF	Radio Frequency
RTOF	Reflectron Time-of-Flight
SEM	Scanning Electron Microscopy
SI	Surface Ionization
SID	Surface Induced Dissociation
SIMS	Secondary Ion Mass Spectrometry
TDC	Time-Digital Converter
TI	Thermal Ionization
XPS	X-Ray Photoelectron Spectroscopy

List of Symbols

Greek Symbols

α	degree of ionization in thermal/surface ionization.
α_{ϕ}	temperature coefficient of the apparent work function of a metal.
δ	denotes a finite spread of measurable variables, *e.g.* δs is the spatial spread of the ions prior to acceleration, δt is the arrival time spread of an isomass-to-charge ion packet.
ε	duty cycle of the orthogonal gate.
$\mathcal{E}_s$	electric field strength in the first field of a two stage acceleration system.
$\mathcal{E}_d$	electric field strength in the second field of a two stage acceleration system.
θ	flight angle of the ions in the field-free region of an orthogonal time-of-flight mass spectrometer.
κ_s	ratio of the average initial ion kinetic energy T_i to the energy stored in the first electric field U_s.
κ_d	ratio of the average initial ion kinetic energy T_i to the energy stored in the second electric field U_d.
λ	electric field ratio in a two stage acceleration system.
μ	ratio of the field-free region length D over the acceleration distance s_i in the first electric field.
ν	ratio of the second electric field d over the acceleration distance s_i in the first electric field.
ρ	length ratio of the two electric fields, s/d.
τ	time delay introduced between ionization and acceleration so that space-velocity correlated distributions are developed.
ξ	voltage ratio in a two stage acceleration system, V_s/V_d.
ω	cyclotron frequency.

English Symbols

a	constant acceleration in a static electric field.
a_s	constant acceleration in the first electric field s of a two stage acceleration system.
a_d	constant acceleration in the second electric field d of a two stage acceleration system.
B	magnetic field intensity.
d	length of the second electric field in a two stage system.
D	length of the field-free region; also used to define the length of the focal distance.
$e\phi$	apparent work function of a metal (equivalent to eV_w, where e is the electron charge).
$e\phi_o$	work function of a metal at absolute zero.
E_b	binding energy of a photoelectron.
E_e	kinetic energy of a photoelectron.
f	frequency of the extraction pulse in the orthogonal gate.
h	represents the difference in acceleration distance between the reference ion situated at s_o and any of the ions accelerating over a distance s_i or s_j.
j	thermoelectric current density emerging from a hot metal surface.
j_o	saturation thermoelectric current density emerging from a hot metal.
K_v	equilibrium coefficient between atoms, ions and electrons in a metallic enclosure containing a vapour.
l_i	ratio of the correlated velocity of the ith ion, u_{ci}, to that at the end of the first electric field u_{si}.
l_j	ratio of the correlated velocity of the jth ion, u_{cj}, to that at the end of the first electric field u_{sj}.
m	mass of an ion, expressed as amu for atomic species.
m_i	ratio of the correlated velocity of the ith ion, u_{ci}, to that in the field-free region u_{di}.

m_j	ratio of the correlated velocity of the jth ion, u_{cj}, to that in the field-free region u_{dj}.
n_i	effective flight path for the ith ion.
n_j	effective flight path for the jth ion.
p	ratio of the correlated initial ion velocities u_{ci} and u_{cj}.
q	total charge of an ion, defined as the product of the number of charges z and the elementary charge e.
$\tilde{r}$	ratio of reflected electrons to the total number of electrons arriving at the surface boundary of a metal.
s	length of the second electric field in a two stage system.
s_o	acceleration distance of the reference ion, situated at the centre of a finite initial spatial spread.
s_i	acceleration distance within the first electric field s for the ith ion.
s_j	acceleration distance within the first electric field s for the jth ion.
s_1	maximum acceleration distance of an ion within the first electric field s.
s_2	minimum acceleration distance of an ion within the first electric field s.
t_{di}	acceleration time of the ith ion in the second electric field d.
t_{d1}	flight time in the second electric field d for an ion accelerating over s_1 in the first field s.
t_{d1}	flight time in the second electric field d for an ion accelerating over s_2 in the first field s.
t_{Di}	flight time of the ith ion in the field-free region D.
t_{D1}	flight time in the field-free region for an ion with the maximum drifting velocity u_{d1}.
t_{D2}	flight time in the field-free region for an ion with the minimum drifting velocity u_{d2}.
$t_{i,j}$	flight time where the ith and jth ions meet in the field-free region.
t_{si}	acceleration time of the ith ion in the first electric field s.
t_{sj}	acceleration time of the jth ion in the first electric field s.
t_{s1}	maximum flight time in the first field for an ion accelerating over a distance s_1.

t_{s2}	minimum flight time in the first field for an ion accelerating over a distance s_2.
T	absolute temperature.
T_i	initial kinetic energy of an ion with mass m and initial velocity u_i.
u_{ci}	correlated velocity of the i th ion.
u_{cj}	correlated velocity of the j th ion.
u_{di}	ion velocity at the end of the second electric field of length d.
u_{d1}	maximum drifting velocity for the ion accelerating over the greatest distance s_1.
u_{d2}	minimum drifting velocity for the ion accelerating over the shortest distance s_2.
u_i	initial velocity of the i th ion within the first electric field of length s.
u_{si}	ion velocity at the end of the first electric field of length s.
u_{s1}	maximum velocity at the end of the first electric field for the ion accelerating over the greatest distance s_1.
u_{s2}	minimum velocity at the end of the first electric field for the ion accelerating over the shortest distance s_2.
U	initial potential energy of an ion in an electric field.
U_d	energy stored in the second electric field, representing the loss in the potential energy or the gain in the kinetic energy of an ion traversing the field.
U_e	total potential energy of an electron leaving a conductor/metal surface.
U_f	image potential of an electron leaving a conductor/metal surface due the surface charge.
U_o	reduction in the work function due to the presence of an external electric field (*Schottky* effect).
U_s	energy stored in the first electric field, representing the loss in the potential energy or the gain in the kinetic energy of an ion traversing the field.
U_ε	potential energy of an electron leaving a conductor/metal surface due to the presence of an external electric field $\mathcal{E}$.
v_a	number of neutrals desorbing from a hot filament.
v_e	number of electrons emitted from a hot filament.

v_p	number of positive ions emitted from a hot filament.
V	contact potential difference between a clean metal surface and a surface covered with a sample.
V_d	voltage applied across the first electric field d.
V_i	ionization potential of gas phase species.
V_s	voltage applied across the first electric field s.
V_w	work function (or electron affinity) of a metal.
x_i	initial position of the ith ion within the first electric field s.
x_j	initial position of the jth ion within the first electric field s.
$x_{i,j}$	overall distance where the ith and jth ions meet in the field-free region at time $t_{i,j}$.

Contents

CHAPTER 2 *Unification of Energy and Space Focusing*

CHAPTER 3 *Focusing in Laser Desorption*

CHAPTER 4 *A New TOF Theory*

CHAPTER 5 *Experimental*

CHAPTER 6 *Theory & Experiment*

CHAPTER 7 *Further Studies & Conclusions*

Chapter 1

An Introduction to TOF MS

1.1 Mass Spectrometry

1.1.1 Introduction

The direct demonstration of the existence of isotopes, the determination of appearance potentials for gaseous ions generated by electron impact, the highly precise measurements of atomic masses and nuclear packing fractions to test Einstein's $E = mc^2$, are the first scientific breakthroughs accomplished by mass spectrometry. As studies of the elements were under way, the idea of extending the utility of the "mass spectrograph" to the analysis of chemical compounds was proposed. In recent years, novel ionization techniques have extended the application of mass spectrometry to the exciting field of biology. Modern investigations involve the characterization of macromolecular structures from synthetic polymer studies, protein analysis, to the DNA quest. Mass spectrometry has long played a very significant role in quantitative gas measurements, fast analysis of trace pollutants and drugs, material and process monitoring in the petroleum, chemical and pharmaceutical industries. Mass spectrometers are involved in exotic applications such as geochronology, archaeological investigations, astronomical studies, spectroscopy and nuclear physics. Today, modern mass spectrometry has evolved into a powerful versatile analytical tool. The unique art of hybrid and tandem instrumentation has its origins in the earlier innovative investigations of electrical discharges in gases.

1.1.2 Historical Overview

By the end of the nineteenth century, most chemists considered atoms to be the ultimate constituents of matter. Concurrently, experiments with electrical discharges in a variety of rarefied gases and the observed complex structures clearly indicated that atoms incorporated charged particles. It was during the 19th century that their indivisible structure began to break down in the face of new discoveries in physics. The roots of these experiments can be traced back to Michael Faraday and his wonders in electrochemistry as early as 1834. Faraday introduced terms such as the ion, anion and cation. The term ion originates from the greek *ἰόν*, neutral present participle of *ἰέναι*, to go, or "the wanderer". So, anion, *ἀνιόν*, and cation, *κατιόν*, mean "going up" and "going down", respectively, and anode, *ἄνοδος*, and cathode, *κάθοδος*, mean "a going up" and "a going down", respectively, from *ὁδός*, "way".

A contemporary of Faraday, William Grove carried out a series of experiments on electrical discharges through gases (Grove, 1852). It was inferred that both negatively and positively charged species are formed when an electrical discharge proceeds through a tube containing a mixture of rarefied hydrogen and oxygen. The observation indicated that the electrodes in a gas are polarized as the electrodes in a liquid are. The deflection of gases in electrical discharges by both magnetic and electrostatic means was reported by Gassiot in 1858 and Plucker was credited with the discovery of the “cathode rays”. It was Eugen Goldstein some decades later who gave the name *Kathodenstrahlen* or cathode rays and who is also credited with the discovery of the *Kanalstrahlen* or “canal rays” (Goldstein, 1876; Goldstein, 1886). Goldstein also demonstrated that canal rays are unaffected by weak magnetic fields.

From the magnitude of deflection of negatively charged rays, J.J. Thomson discovered that all gases produced the same negatively charged particles and determined their m/z ratio (Thomson, 1897). The value of $5x10^{-12}\ Kg\ C^{-1}$, the mass of the electron, was confirmed one year later by Wilhelm Wien and his apparatus known as the Wien filter, which utilized crossed electric and magnetic fields (Wien, 1898), and subsequently by Millikan in 1908 (Millikan, 1908; Millikan 1910). The deflection of canal rays by the presence of strong superimposed parallel electric and magnetic fields was demonstrated by Wien in 1898. The experiments revealed that particles with different m/z ratios generated parabolic curves. Experiments at lower pressures performed by J. J. Thomson in 1905 clearly indicated that for a ray of ions with a single m/z value the deflection generated a sharp parabola. The position of the ions on each of the parabolas determined their energy. In 1907 Thomson recorded positive ion parabolas from discharges of H_2 and He and extended his experiments to hydrocarbon molecules. The description of the mass spectrograph in which the photographic plates used for ion detection had been replaced by a narrow slit and an electrometer was presented in 1911 (Thomson, 1911). The first m/z was obtained by measuring electric current as the strength of the magnetic field was varied. A direct method for demonstrating the existence of isotopes and a device for estimating their relative abundances was thus invented by Thomson.

A satisfactory explanation for the appearance of the extra line in the mass spectrum of neon remained elusive until Francis Aston extended the newly developed concept of radioactive isotopes, developed by Frederick Soddy, to the stable elements of the periodic table. Aston's new design of the mass spectrograph, shown in Figure 1.1, incorporated two slits to collimate the ion beam from the discharge tube and utilized the electric and magnetic fields in tandem rather than being superimposed as in Wien's and Thomson's designs. An analogy can be drawn between Aston's design and achromatic prisms[1] (Beynon, 1960). For an isomass-to-charge ion beam, the dispersion produced by the electrostatic field leads to a velocity spectrum. This dispersion is cancelled by the focusing action of the magnetic field. With this improvement ions of the same m/z ratio were focused on a line on the photographic plate and the relative abundance of the ions was indicated by the line's optical density. The resolution of this instrument was ~130, one order of magnitude greater than Thomson's design and clearly indicated the existence of the three isotopes of Neon. The year 1919 was the end of Dalton's long standing atomic theory (Aston 1919; Aston 1920; Aston 1923). By the year 1935 the spectra all of the known elements had been recorded and only rare isotopes remained to be discovered by the more sensitive next generation instruments.

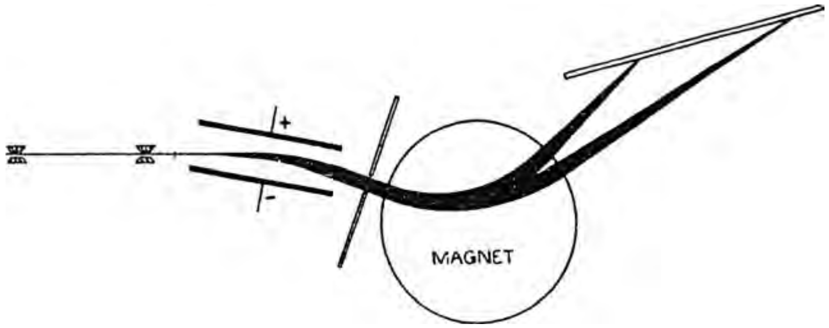

SOURCE: Beynon, 1960

Figure 1.1 Schematic diagram of Aston's first velocity focusing mass spectrograph. A discharge tube generates ions with energies ~1000 eV. Ions are accelerated from 20 kV to 50 kV and collimated through slits. The electric and magnetic fields are arranged geometrically so that the dispersion in the first field is cancelled by the second.

---

[1] Prisms are used to deviate rays, disperse white light into visible spectrum or erect an inverted image; they cannot focus. A lens is a curved material used for the refraction of light and can bring rays of a beam into a principal focus. Aberration is a defect in an image formed by a lens. Chromatic aberrations are coloured fringes in an image formed by a lens as a result of the different extend to which light of different colours is refracted. An achromatic lens corrects for chromatic aberrations by using a combination of two lenses such that their dispersion neutralize each other although their refraction do not.

The two “diachronic” ion sources, thermal/surface ionization (TI/SI) and the electron impact ionization (EI), were both introduced into mass spectrometry by Dempster (Dempster, 1918; Dempster, 1921). The former is know established as an exceptional tool for isotope ratio analysis when high precision and utmost sensitivity are required (Smith, 2000), while the latter became the classical ionization method in mass spectrometry (Barnard, 1953). Dempster also invented an ion source where a high-frequency spark was discharged between two electrodes made of the sample material to be analyzed. The concept evolved into the spark source used for the analysis of solid metals. At about the same time, Dempster modified Classen’s electron analyzer (Classen, 1908) for the analysis of positive ions. His design is considered as the first mass spectrometer, which achieved any kind of focusing (Dempster, 1918). Whereas Aston used his deflecting fields as prisms, Dempster used the magnetic field as a lens for separating and focusing ions. A schematic of the first direction focusing mass spectrometer is shown in Figure 1.2.

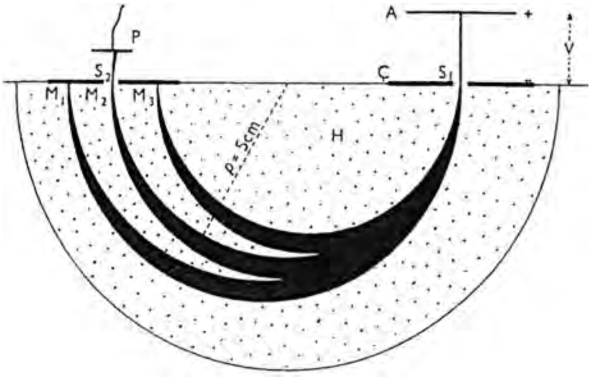

SOURCE: Barnard, 1953

Figure 1.2 Schematic diagram of Dempster’s direction focusing mass spectrometer. The distinction drawn between this first mass spectrometer and the mass spectrograph is the detection system and the ability of the former to deliver more accurate abundance measurements by collecting electric current.

The description of a 180° analyzer with an EI source, in which the transverse electron and ion beams are controlled separately, was presented by Bleakney (Bleakney, 1929; Bleakney, 1930). The first electron impact source is, in fact, usually called the *Bleakney* source and became a standard in mass spectrometry research (Inghram & Hayden, 1954). Refinements of this novel design have been made by a plethora of experimentalists over the years (Tate & Smith, 1934; Nier, 1937; Nier, 1938; Nier, 1940*a*).

In 1939 Nier was motivated to isolate the uranium isotopes spectrometrically in an effort to determine which isotope underwent fission. Nier used his EI 180° magnetic sector mass spectrometer to isolate the uranium isotopes and published his results one year later (Nier, 1940*b*). Purified quantities of ^{235}U became available and the enormous energy released when nuclei split following neutron bombardment was finally confirmed. The development of the first atomic bomb was under way.

Continuing his research in mass spectrometry, Nier described an instrument for precise isotope ratio measurements, which became the model for EI sources, known as the “orthdodox” model (Nier *et al*, 1947). The EI source became an increasingly valuable tool for many years later as structural analysis of complex molecules, such as hydrocarbons and biological compounds, moved into the forefront of research in mass spectrometry.

First-order double focusing analyzers incorporated an electrostatic sector for velocity/energy focusing followed by a magnetic sector for directional focusing. Nearly all of the existing mass spectrometrically determined packing fraction values have been obtained using this system (Beynon, 1960). At the early stages of mass spectrometry development these configurations were used to compensate for the large kinetic energy spread of the ions generated in the high frequency spark ion source, an ion source that gave ionization efficiency independent of atomic number.

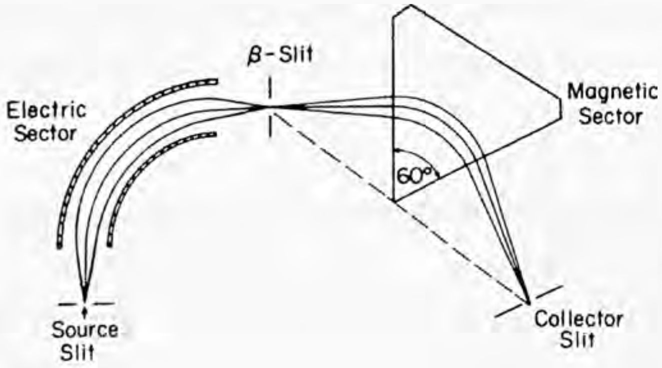

SOURCE: Cooks *et al*, 1973

Figure 1.3 Arrangement of the electric and magnetic fields for a double-focusing mass spectrometer of the Nier-Johnson type geometry.

Much of the improvement in mass spectrometers for precision mass analysis is attributed to Alfred Nier. His contributions greatly enhanced resolving power and sensitivity to a level of performance exceeding those of the most advanced mass spectrographs. The Nier-Johnson second-order double focusing mass spectrometer introduced in 1953 achieved high sensitivity and resolution thus significantly improved the mass accuracy of the analytical technique (Johnson & Nier, 1953). A schematic of the instrument is shown in Figure 1.3. *Kratos Analytical Instruments* in Manchester commercialized such an instrument in the early 1960's.

High mass resolution and high mass accuracy static double focusing instruments dominated the field well into the 1990's. In an effort to avoid the use of the magnet and reduce the size and cost of the instrument, several types of dynamic mass analyzers were slowly developed along side the high performance static mass spectrometers. In the mid 1950's, quadrupole devices and time-of-flight mass spectrometers were introduced. The former proved ideal for gas chromatography and the latter became known for its elegant simplicity. An explosive development is now being experienced both in instrumentation design as well as in novel ionization methods and applications.

1.1.3 Instrumentation Classes

Mass spectrometers constitute a large, very diverse and widely employed class or family of instruments. A mass spectrometer is an analytical instrument in which neutral molecules are converted into gaseous ions, directed and separated into their components by a mass analyzer. The ions are arranged into a mass spectrum according to their mass-to-charge ratios and their relative abundances.

The heart of a mass spectrometer is its analyzer, a region of high vacuum where ions are made to move under some kind of carefully controlled static or dynamic/oscillating electromagnetic fields. Ions of different mass, charge and velocity are separated, collected and accurately determined. Different types and arrangements of analyzers, the new concepts in ion production introduced at the front end of the mass spectrometer and the continuous development in ion source interfaces have resulted in a remarkably extensive range of instrumentation. The mass spectrometer islands are shown in Figure 1.4. Each of the islands has its own features and limitations. Four major types of mass analyzers are recognized, these are sector instruments, quadrupoles and ion traps, ion cyclotron resonance and time-of-flight mass spectrometers. New applications have fathered new designs of instruments and instrumental improvements have in their turn extended the range of application of the technique. The expansion of scope and diversity is mainly attributed to hybrid and tandem instrumentation, the so-called modern mass spectrometry.

Sector instruments were the first mass spectrometers implemented, following the novel work of J. J. Thomson and his predecessors. Sector instruments make no use of time-dependent variables to separate an ion beam and this particular class of instruments is defined as static mass spectrometry. A mass spectrum is recorded by scanning the magnetic field. Although the focusing action of magnets for slightly divergent beams of monoenergetic ions had already been appreciated, at least experimentally, it was not until 1933 that a theoretical treatment was established (Barber, 1933; Stephens & Hughes, 1934; Stephens, 1934). In 1934 the general analysis of double focusing systems incorporating magnetic and electrostatic fields in tandem (with sharp boundaries) that provided simultaneous directional and velocity focusing respectively was published by Herzog (Herzog, 1934; Mattauch & Herzog, 1934). First-order aberrations were eliminated and the analysis was extended to second-order focusing by Johnson and Nier (Johnson & Nier, 1953). This type of mass analyzer has dominated the high performance mass spectrometry field well into the 1990's. A detailed review of the focusing action of sector instruments can be found in several textbooks (Barnard, 1953; Inghram & Hayden, 1954; Beynon, 1960; Duckworth, 1960).

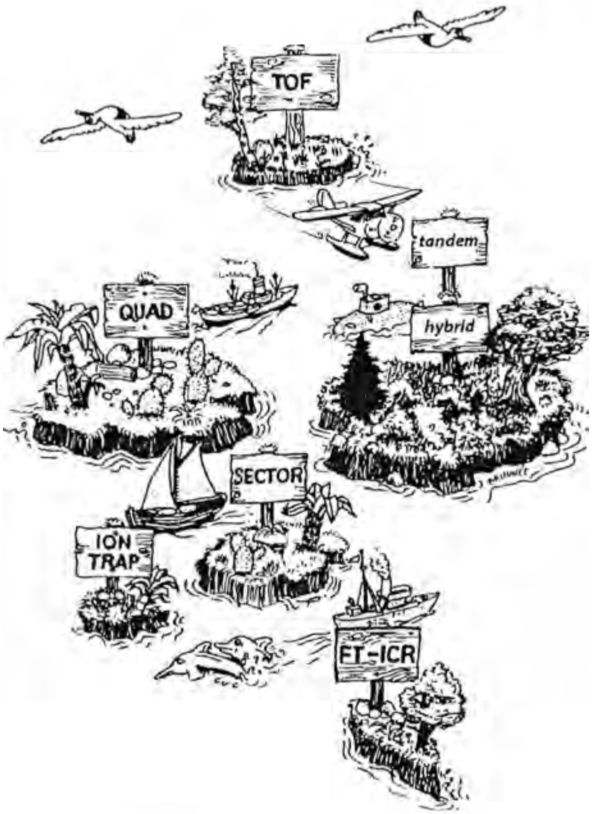

SOURCE: Brunee, 1987

Figure 1.4 The mass spectrometer islands.

A number of limitations in static mass spectrometry initiated the design of dynamic systems. Major drawbacks of static systems are the relatively low upper mass limit for biomolecular analysis and the prohibitive cost of heavier magnets, miniaturization, fast identification and high throughput analysis. The development of dynamic mass spectrometry evolved slowly, primarily due to the well established theoretical basis of static systems. However, the range of instrumentation and applications nowadays is remarkable. Technical advances, mainly in electron optics and fast electronics, had a significant contribution to the explosive development of dynamic systems.

In dynamic mass spectrometry the time dependence of one or more variables is fundamental to mass analysis. Attempts to arrange the dynamic systems according to the principles by which the time dispersion of the ion motion is implemented have been made (Blauth, 1966). These are divided into (a) energy balance mass spectrometers, (b) path stability spectrometers and (c) time-of-flight systems.

In energy balance mass spectrometry ions fulfil certain “resonance conditions” and energy can be continuously supplied to or withdrawn from them during their motion in suitable RF fields. The resonant ions achieve the maximum energy exchange with the RF field and a mass spectrum is recorded by varying the mass dependent resonance conditions. The theoretical principles of operation of the Fourier Transform Ion Cyclotron Resonance Mass Spectrometer (FT ICR MS) dates back to the description of the cyclotron as a device for accelerating charged particles to high energies in 1932 (Lawrence & Livingston, 1932). The existence of the ^3He isotope was demonstrated with the cyclotron operated as an energy balance mass spectrometer (Alvarez & Cornog, 1939*a*; Alvarez & Cornog, 1939*b*). The development of the *omegatron* device was reported several years later and was used as a precision mass spectrometer (Hipple *et al*, 1949; Sommer *et al*, 1951). In the *omegatron* device ions are immersed in an extended homogeneous RF field and a static magnetic field and they follow a continuous *Archimedes* spiral trajectory. A schematic of the device is shown in Figure 1.5. The development of FT ICR MS (Marshall & Schweikhard, 1992) and its principles of operation are based on these

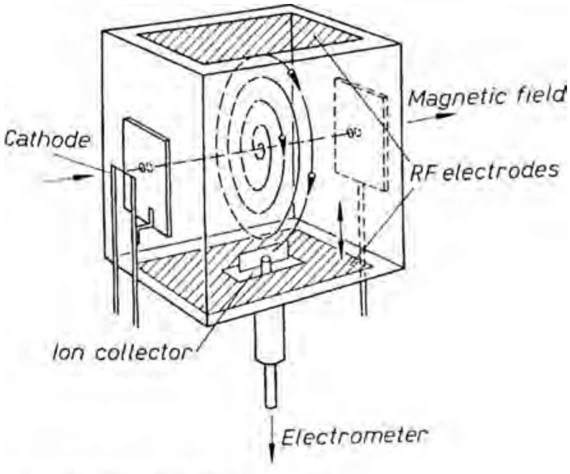

SOURCE: Reich & Noller, 1957

Figure 1.5 A simplified omegatron device.

original devices as well as the technique of detecting ion power resonant absorption (Wobschall, 1965; Baldeschwieler, 1968; Llewellyn, 1969). FT ICR MS holds the world record in mass resolution and mass accuracy and it is unlikely to be challenged by any other mass analysis technique. The origin and principles that comprise the working library of the FT ICR mass spectrometer have been recently reviewed (Marshall *et al*, 1998; Marshall, 2000).

In path stability mass spectrometers the ion motion is described either as stable or unstable. Under suitable combination of electromagnetic fields only a certain mass range is stable or unstable. A direct mass analysis is then possible and there are several methods for detecting either stable or unstable ions. Three categories are distinguished (Blauth, 1966), these are velocity-stability, phase-stability and m/z-stability spectrometers. The non magnetic quadrupole mass spectrometer and the quadrupole ion trap (QIT), disclosed in 1953 by Paul and Steinwedel (Paul & Steinwedel, 1953; Paul & Steinwedel, 1956) fall into the latter category. The origin of the use of alternating quadrupole fields lay in advances in the design of high energy accelerators. The original work by Christophilos, an electric engineer in Athens who is credited with the invention of the strong focusing technique using alternating gradient quadrupole magnetic fields in 1950, was overlooked at the time (Blauth, 1966). Two years later the focusing method was published with a great impact on particle accelerator design (Courant *et al*, 1952). The technique is an example of dynamic stabilization, and the mathematical treatment leads to the Mathieu differential equations with their typical stable and unstable solutions (McLachlan, 1947). The 3D quadrupole ion trap is only one of a family of quadrupole devices and at the early stages of its development, rotationally symmetric

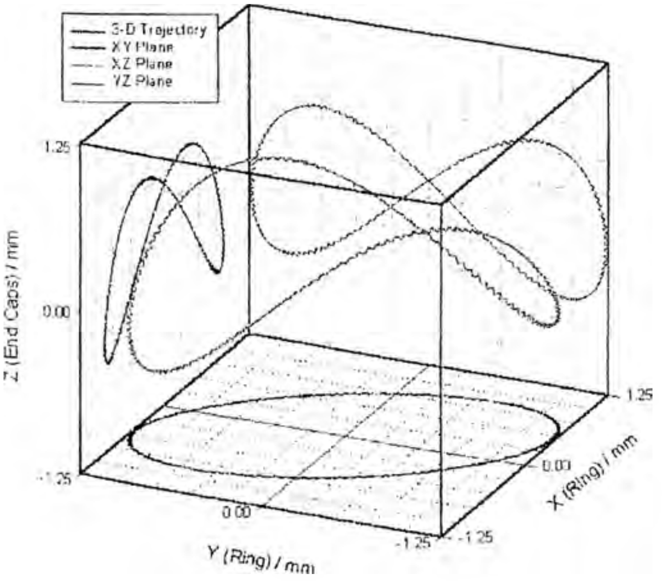

SOURCE: Forbes *et al*, 1999

Figure 1.6 Two- and three-dimensional representation of an ion's trajectory in a quadrupole ion trap. The macromotion (*Lissajous* figure) and micromotion (minute oscillations) are clearly visible.

hyperboloid geometries had survived in only a few laboratories as objects of curiosity. The confined trajectory of an ion in a 3D ion trap is shown in Figure 1.6. The confinement of charged particles made possible the investigation of some of the most fundamental properties of matter-radiation interaction. The application of the quadrupole fields to tandem and hybrid mass spectrometry and the structural analysis of molecules as well as miniaturization have been enormous. The immense impact of these studies was acknowledged in 1989 by the award of the Nobel Prize in Physics to Wolgang Paul[2] for the 2D and 3D quadrupole devices and to Hans Dehmelt[3] for his contributions to the development of the Penning trap, the magnetic ion trap introduced by Penning in 1936. The 2D quadrupole mass filter and the 3D quadrupole ion trap have been treated in a few excellent monographs (Dawson, 1976; March *et al*, 1989; March & Todd, 1995, March & Todd, 2005). The orbitrap (Makarov, 2000) and the digital ion trap (Ding *et al*, 2002) are the latest developments in the field of path stability spectrometry.

1.2 Time-of-Flight Mass Spectrometry

1.2.1 Introduction

The simplest form for time-of-flight mass analysis was proposed by Stephens *in 1946* (Stephens, 1946). The concept was based on the selection of ion packets from a low voltage ion source and their ejection into a field-free region. Since all ions acquire the same kinetic energy as they traverse the electric field, ions of different m/z ratios fly with different velocities and arrive at the detector at the end of an evacuated tube at different times. Stephens had foreseen ~60 years ago significant advantages over other types of instruments that have established TOF MS as an indispensable mass analyzer today, including high throughput sensitive mass spectrometry by the elimination of narrow slits, fast response for rapid analysis and promising portable use. In conjunction with the unlimited mass range and the panoramic view of the mass spectrum for single ionization events, TOF MS is now the dominating technique for high mass high throughput fast analysis of molecules.

---

[2] nobelprize.org/physics/laureates/1989/paul-lecture.pdf
[3] nobelprize.org/physics/laureates/1989/dehmelt-lecture.pdf

The TOF mass spectrometer visualized by Stephens did not incorporate a magnet, which greatly simplified the construction of such an instrument. In addition the problem of obtaining spectra in very short time intervals was partially solved since TOF MS could operate in the μs scale with the aid of an oscillograph. Although this system far superseded the time response of magnetic & radio-frequency TOF systems that were already put in practise by the late 1940's, and clearly had several advantages over other types of mass analyzers, it was submerged by scanning techniques for a long time. The delayed establishment of the non-magnetic TOF analyzer is due to the slow development of fast electronics. The implementation of the technique was definitely not as simple as the original concept presented 60 years ago. Milestones in TOF MS are discussed in the following historical overview and a separate treatment of the early innovative TOF systems developed along lines with the linear/reflecting mode is presented.

1.2.2 A Brief History of Time-of-Flight

The landmark paper presented by Wiley & McLaren and the development of the two-stage acceleration ion source (Wiley & McLaren, 1955), led to the commercialization of the first TOF mass spectrometer with an EI source, the *Bendix* TOF instrument (Wiley, 1956). A reasonable resolution of a few hundred could be attained in those early days but the fascinating advantage was its very high recording speed of 10,000 spectra per second. For many years, this feature proved essential for the application of the TOF technique to the study of fast reactions. The first gas chromatographer (GC) coupled to the TOF analyzer was reported a few years later (Gohlke, 1959; Ebert 1961; McFadden *et al*, 1963; Oyly-Watkins *et al*, 1970). It is surprising that there was no subsequent development of the GC TOF MS technique. The quadrupole device was utilized instead and became the dominant non-magnetic analyzer coupled to GC. Even more surprising is the existence of very few GC TOF research instruments today. Since the early days of the *Bendix* instrument, TOF systems have slowly developed into a versatile mass analysis technique, mainly for biomolecular analysis. Tandem and hybrid TOF technology and biological mass spectrometry have merged into an extremely powerful analytical tool. A survey of major applications and instrumentation development of the TOF analyzer as well as key experiments on mass measurements of macromolecules is presented.

The 1960's

During the *1960's*, all TOF spectrometers were based on simple variations of the two-stage *Bendix* original design and were applied to the study of fast reactions and kinetics. The pulsed nature of lasers proved ideal for timing ionization events and techniques such as the rapid vaporization and analysis of coals, isotope ratio measurements and pyrolysis were developed (Conzemius & Capellen, 1980). The use of the *Bendix* system as a pulmonary and residual gas analyzer, its application to the study of ion/diatomic molecule reactions, studies at high temperatures with the *Knudsen* cell, investigations with negative ions as well as the most recent developments of the *Bendix* TOF analyzer were reported by Damoth (Damoth, 1964*a*; Damoth 1964*b*). The first laser microprobe TOF MS was presented in 1966 (Knox & Vastola, 1966). In 1968 Muller coupled the TOF analyzer to the atom-probe ion microscope to identify the chemical nature of the individually imaged atoms (Muller *et al*, 1968). TOF MS was in its infancy and several reviews on these early investigations were published (Joy, 1969; Price & Williams, 1970; Price, 1971).

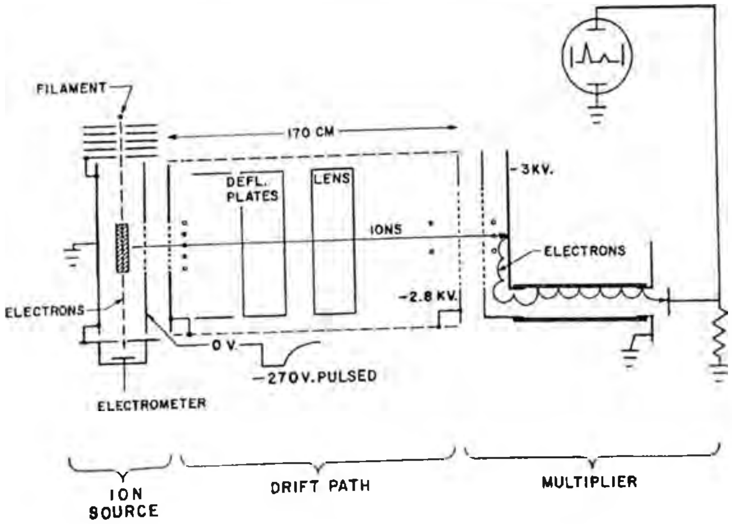

SOURCE: Damoth, 1964*b*

Figure 1.7 Schematic diagram of the *Bendix* TOF MS

In 1968 Malcolm Dole presented results from his first efforts to measure the molecular weights of oligomers of synthetic polymers with the electrospray ionization (ESI) source (Dole *et al*, 1968). Early attempts to weigh the heavy molecules with the *Bendix* mass spectrometer were unsuccessful (Dole *et al*, 1971; Gieniec *et al*, 1984). By the end of the 60's, all the common methods of ionization involved an energetic gas phase encounter of a neutral molecule with an electron, photon or ion. The vaporization of heavy molecules without excessive fragmentation and decomposition was a long cherished but elusive goal at the time[4]. An exception in these early steps of biomolecular analysis is the field desorption ionization technique in which non-volatile species adsorbed on the surface of thin metallic wires, surrounded by an intense electric field, could migrate by surface diffusion to the tip and desorb as intact ions (Beckey & Schuelte, 1960; Beckey, 1977).

The 1970's

The early 1970's were marked by the construction of the two stage reflectron device (Karataev *et al*, 1972; Mamyrin *et al*, 1973) based on Alikhanov's single stage energy focusing system (Alikhanov, 1957). The energy focusing properties of the reflectron improved the resolution of the linear TOF configuration by an order of magnitude and have had a major impact on the development of modern TOF MS. Poschenrieder presented his theoretical analysis of magnetic and electric sectors in tandem with linear TOF segments (Poschenrieder, 1971; Poschenrieder, 1972*b*). The analysis described for the first time the stigmatic focusing properties of such systems and predicted their future application to surface science and imaging techniques.

The origin of biomolecular TOF mass spectrometry has its roots in nuclear physics and time-of-flight measurements of short-lived nuclides. Surprising results that ^{252}Cf fission fragments could produce heavy ions from labile and involatile biomolecules were the first experimental evidence of a nearly impossible achievement that spread enthusiasm. The advantage of exploring the high-mass end with a TOF system was evident when Ron MacFarlane reported his first results. The technique became known as plasma desorption (PD) (MacFarlane *et al*, 1974; MacFarlane & Torgesson, 1976; MacFarlane, 1983*a*; MacFarlane, 1983*b*). PD TOF MS, the first instrument intended specifically for the analysis of biological macromolecules, was commercialized by Bio-Ion Nordic AB (Sweden) in 1984.

The principles of desorption/ionization are based on the "rapid heating" or "sudden energy sudden", originally presented by Beuhler (Beuhler *et al*, 1974). On the grounds of rate theory for unimolecular decomposition, it was argued that sufficiently

---

[4] nobelprize.org/chemistry/laureates/2002/fenn-lecture.pdf

rapid heating could vaporize complex molecules before they had time to decompose. Advanced techniques based on this principle were developed including pyrolysis mass spectrometry (Meuzelaar *et al*, 1973), static secondary ion mass spectrometry (static SIMS) (Benninghoven *et al*, 1976; Benninghoven & Sichtermann, 1978) and laser desorption mass spectrometry (Unsoeld *et al*, 1976). The laser microprobe mass analysis (LAMMA) technique was further developed (Hillenkamp *et al*, 1975*a*; Hillenkamp *et al*, 1975*b*) and commercialized by *Leybold-Hereaus* in 1978 (Germany). Several other methods were devised in an effort to bring heavier intact molecules into the gas phase (Giessmann & Rollgen, 1976; Rollgen *et al*, 1977; Ohashi *et al*, 1978; Hunt, 1977; Hansen & Munson, 1978; Cotter & Fenselau, 1979). All the above techniques produced intact ions from many complex species however the yields were very low and there was always an upper mass limit. The late 70's are reviewed in the last of the *Dynamic Mass Spectrometry* series volumes (Price & Todd, 1981).

The 1980's

The 1980's is the renaissance period for TOF MS. This is largely attributed to the development of the matrix-assisted laser desorption/ionization (MALDI) method for the structural analysis of biomolecules. Concurrently, the re-invention of the orthogonal configuration technique and the ability to record time-of-flight spectra from continuous ion sources revolutionizes TOF MS. Challenging biomedical applications emerge, supported by hybrid systems, demanding enhanced resolving power, exploring the unlimited mass range and stretching the detection limits of this remarkable mass analyzer. Secondary ion mass spectrometry (SIMS) studies have also had a significant contribution to the establishment of TOF MS as a mainstream technique.

Pioneering studies on the pulsed SIMS TOF technique for analyzing organic compounds were carried out by Benninghoven (Benninghoven, 1983; Niehuis *et al*, 1987) and Standing (Standing *et al*, 1988). TOF SIMS instruments with one and two stage reflectrons were developed (Chait & Standing, 1981; Niehuis *et al*, 1986). A schematic of a SIMS TOF instrument is shown in Figure 1.8. Incorporation of reflectron devices as a means of enhancing resolution stimulated the investigation of ions during their flight and metastable decay studies were presented (Chait & Standing, 1981; Chait & Field, 1981). It was then realized that the metastable properties of excited species provided a method for the determination of the structure of parent ions without using a tandem spectrometer (Della Negra & LeBeyec, 1985; Della Negra & LeBeyec, 1986). Advances in TOF instrumentation were very important at the time. The Wiley & McLaren principles of pulsed extraction were first demonstrated in a fast atom bombardment (FAB) TOF system and the enhanced ion yield of heavy molecular weight species was reported (Tabet & Cotter, 1984; Cotter, 1984). The different operating modes of TOF instruments coupled to PD, LD, FAB and SIMS ion sources and a comparison of the relative ion yields have been discussed (Cotter *et al,* 1986).

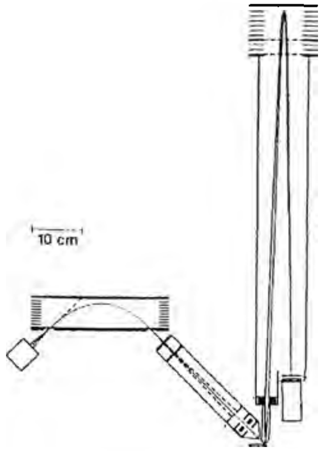

SOURCE: Niehuis *et al*, 1986

Figure 1.8 Schematic of a SIMS TOF instrument.

A very important contribution to the TOF family is the re-invention of the orthogonal configuration in the late 80's, which made possible the interfacing of continuous ion sources with the TOF analyzer. Orthogonal Time-of-Flight (oTOF) MS was re-invented independently by two groups (Dawson & Guilhaus, 1989; Dodonov *et al*, 1991). A schematic of the orthogonal TOF is shown in Figure 1.9.

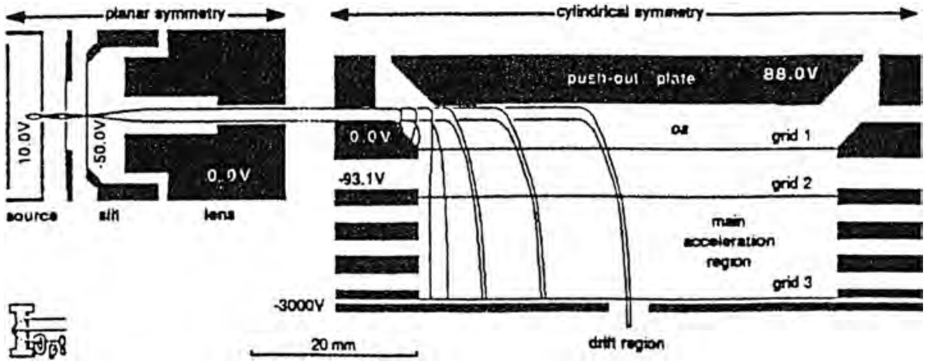

SOURCE: Dawson & Guilhaus, 1989

Figure 1.9 Selected ion trajectories from an EI source, through a collimation lens and into the oTOF.

In tandem TOF MS, instruments were developed for the study of collision induced dissociation (CID) and surface induced dissociation (SID) products. A novel design with a quadrupole filter for precursor ion selection, a collision cell and an "on axis"

TOF analyzer for recording the daughter ions was reported in 1984 (Glish & Goeringer, 1984; Glish *et al*, 1987). TOF/TOF systems were also designed and constructed for studying polyatomic ion/surface collisions (Schey *et al*, 1987).

Laser evaporation and subsequent multiphoton or resonance ionization for elemental trace analysis of solids was performed with TOF analyzers (Becker & Gillen, 1984; Williams *et al*, 1984; Fasset *et al*, 1985). Laser ionization TOF MS with reflectron technology is reviewed by Boesl (Boesl *et al*, 1992). The developing interest of using laser desorption for the analysis of polymers has also been discussed (Wilkins *et al*, 1985). Based on the rapid heating principles, the idea of matrix assisted desorption of labile organic compounds became quite popular at the time. The role of glycerol as an ionization promoter (Barber *et al*, 1981*b*; Hsu *et al*, 1983) was demonstrated in a FAB source, also known as high flux liquid SIMS (Barber *et al*, 1981*a*; Surman & Vickerman, 1981). Nitrocellulose was used in PD (Johnson *et al*, 1986) and the beneficial matrix action in LD was also discussed (Zakket *et al*, 1981; Wright *et al*, 1985).

Desorption/ionization of thermally labile biomolecules in the high mass range was finally accomplished by Tanaka's group and later by Karas and Hillenkamp towards the end of the 1980's. In both techniques lasers was used to irradiate a mixture of the analyte and an absorbing medium to convert light to thermal energy. The development of the soft laser ionization technique using a mixture of ultra fine metal powder and glycerin (Tanaka *et al*, 1988) and the MALDI method using a polymer matrix to assist ionization (Karas & Hillenkamp, 1988) were acknowledged as scientific breakthroughs achieved by the mass spectrometry community. Both experiments were performed by TOF systems. Koichi Tanaka shared the chemistry nobel prize in 2002 with John Fenn for the development of ESI (Yamashita & Fenn, 1984) and Kurt Wutrich for the determination of the three-dimensional structure of macromolecules in solution using nuclear magnetic resonance spectroscopy.

In the 1980's TOF MS departed into space for the first time. The small reflection instrument designed for the analysis of particulates from *Halley's* Comet is shown in the next Figure 1.10 (Kissel, 1986).

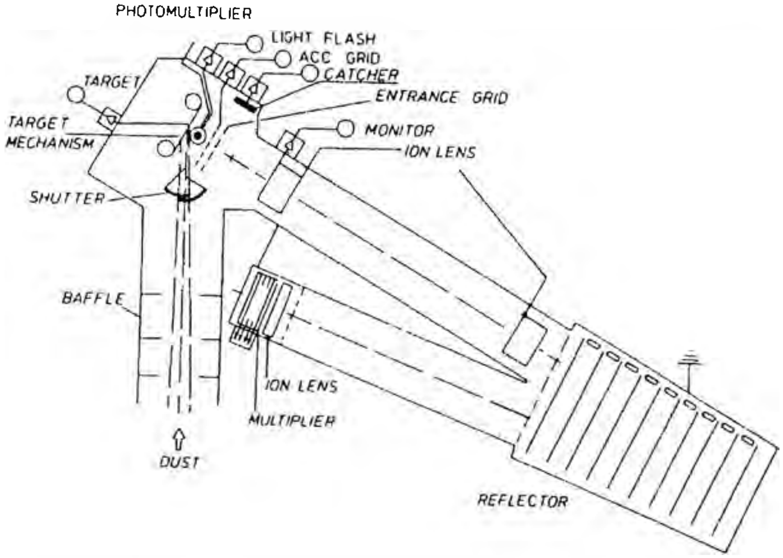

SOURCE: Kissel, 1986

Figure 1.10 Schematic diagram of the TOF instrument for particulate analysis in space.

The 1990's and Current State

The 1990's is the period of establishment of TOF MS at the forefront of MS research. An explosion in the field is experienced and several TOF instruments become available in the market. The TOF analyzer is no longer considered a low resolution spectrometer. Tandem and hybrid TOF machines are developed.

The MALDI technique became the driving force for new instrument design. Fundamental studies on the ionization mechanism are carried out. Significant advances are the rediscovery of the delayed extraction (DE) technique (Colby *et al*, 1994; Brown & Lennon, 1995) and the incorporation of high performance reflectron devices (Cotter, 1997). The combination of focusing techniques defeated the major disadvantage of the TOF analyzer, its low resolution. DE is an extension of time-lag focusing for gas phase ionization (Wiley & McLaren, 1955) to the desorption of ions from surfaces and is developed in Chapter 3. Reflectrons are also discussed separately in Chapter 1, Section 1.4. Special techniques using a gate for selecting the parent ion and studying post-source decay products were developed (Kaufman *et al*, 1993; Spengler, 1997; Chaurand *et al*, 1999). A comprehensive account of TOF instrumentation and applications in the field of biology is given by Cotter (Cotter, 1997).

Tandem Reflectron Time-of-Flight (RTOF) MS has become an invaluable tool in biomolecular analysis. The first analyzer selects a particular mass while the second provides structural information following the dissociation of the target species. Ion activation is achieved either by collision induced dissociation (CID), surface induced dissociation (SID) or photodissociation. Post-source decay (PSD) methods are an imperfect approach in MALDI TOF MS in which activation occurs during ionization by increasing the laser power (Cotter, 1997). Focusing of the daughter ions can be achieved by a non-linear reflectron only if fragmentation occurs in the field-free region (Cordero *et al*, 1995, Fabris *et al*, 1995). Special TOF/TOF systems incorporating a gate before the CID cell were developed and reacceleration techniques for enhancing the resolution of the fragment ions have been reported (Jardine *et al*, 1992). SID (Schey *et al*, 1989) and photodissociation (Boesl *et al*, 1992) methods for obtaining structural information have been performed with TOF/RTOF systems. RTOF/RTOF geometries have been constructed in order to utilize the focusing properties of the analyzer at the gating point and narrow the mass selection window (Cornish & Cotter, 1994; Beussman et al, 1995). MALDI TOF/TOF MS is an active field of research (Cordero *et al*, 1996; Medzihradszky *et al*, 2000; Suckau et al, 2003). A schematic of a TOF/TOF MS configuration incorporating a gate, a collision cell and a re-acceleration region is shown in Figure 1.11.

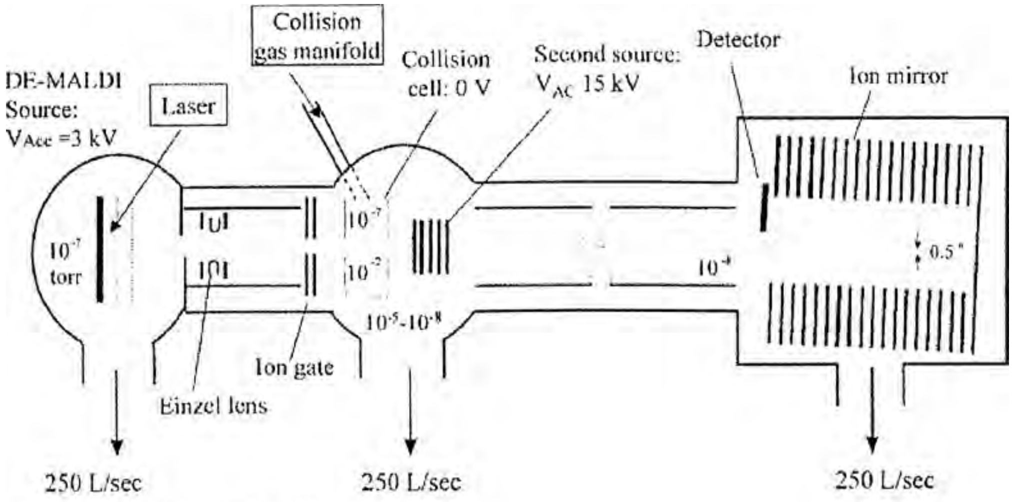

SOURCE: Medzihradszky *et al*, 2000

Figure 1.11 Schematic of a TOF/TOF configuration

ESI is established as a complementary method to MALDI for the analysis of biomolecules (Cole, 1997). In contrast to the pulsed mode in MALDI ion production, ESI ions form a continuous multiply charged beam. Continuous ion production facilitates the use of quadrupole instruments, which are however scanning devices. The formation of non-covalent complexes formed in ESI usually exceeds the upper mass limit of the quadrupole hence a TOF mass analyzer is a more appropriate choice. The transformation of the continuous ion beam to the pulsed mode was achieved with high efficiency by coupling the ESI source with the oTOF MS (Dodonof *et al*, 1987; Dodonof *et al*, 1991; Dodonof *et al*, 1994). Collisional cooling of the ions, introduced initially for quadrupole mass spectrometers (Douglas & French, 1992; Xu *et al*, 1993), was a very practical interface between the source and the orthogonal region of the TOF system. The quadrupole device, operating in the rf mode only at 0.01-1 *torr*, reduced the high energy spread of the ions in the source and provided suitable initial conditions for the orthogonal acceleration experiment. Improved resolution, reduced discrimination and enhanced transmission are few of the advantages of this configuration. It has been demonstrated theoretically that the ions at the exit of the rf-guide posses nearly thermal energies (Krutchinsky *et al*, 1998*a*). Collisional cooling devices have also proved successful for coupling the pulsed MALDI source to the oTOF analyzer (Krutchinsky et al, 1998*b*; Harvey *et al*, 2000).

The counterpart of MALDI TOF instruments, the orthogonal configuration, evolved rapidly and had a profound influence on the design of hybrid instruments. The coaxial quadrupole TOF reported by Glish suffered from poor resolution, mainly because the initial conditions of the ions prior to TOF analysis were characterized by wide spatial and energy spreads (Glish & Goeringer, 1984; Glish *et al*, 1987). Orthogonal acceleration again provided a remedy to the problem by choosing a separate direction for mass analysis where the initial set of conditions is more clearly defined. Two remarkably successful designs have been

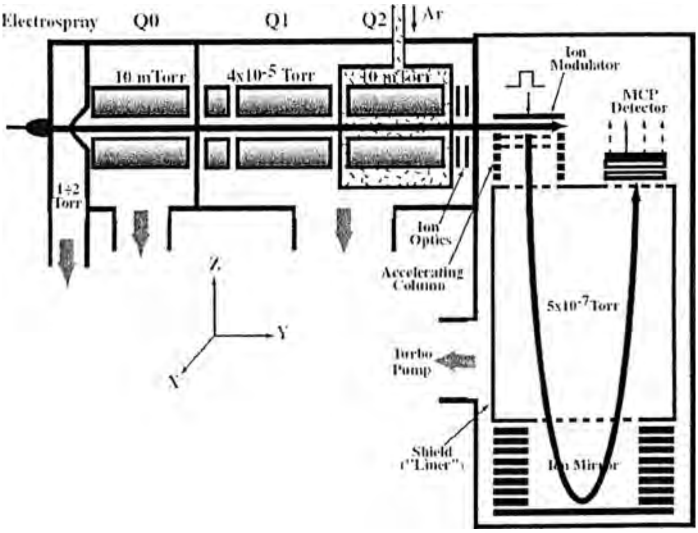

SOURCE: Chernushevich, 2001

Figure 1.12 Schematic diagram of the QqTOF coupled to an ESI source.

reported and are available in the market today, the first with a collision cell in a rf hexapole (Morris *et al*, 1996) and the second with a collision cell in a rf quadrupole (Shevchenko *et al*, 1997). The hybrid instrument is known as the QqTOF and has been recently reviewed (Chernushevich *et al*, 2001). A schematic of the instrument is shown in Figure 1.12. Orthogonal TOF systems have been coupled to electron impact (EI) (Chen *et al*, 1999; Berkout *et al*, 2001), and inductively coupled plasma (ICP) ion sources (Myers *et al*, 1994; Myers *et al*, 1995*a*; Myers *et al*, 1995*b*; Guilhaus, 2000*a*). Several review papers on oTOF MS can be found in the literature (Chernushevich *et al*, 1999; Guilhaus *et al*, 2000).

Ion trap TOF MS is a fascinating hybrid instrument with unique features. The advantages of merging the MS^n capabilities of the IT device with high resolution and high mass accuracy TOF spectra are enormous. However, the development of such a system has not been proven to be a straight forward process and fundamental limitations still remain unresolved. These include rapid rf start up and switch off for trapping and ejecting respectively, fragmentation of hot molecules immersed in the rf field, reduction of the mean free path when static background pressures are used and relatively low resolution as the initial spatial and kinetic energy spreads of the ions before extraction are difficult to control.

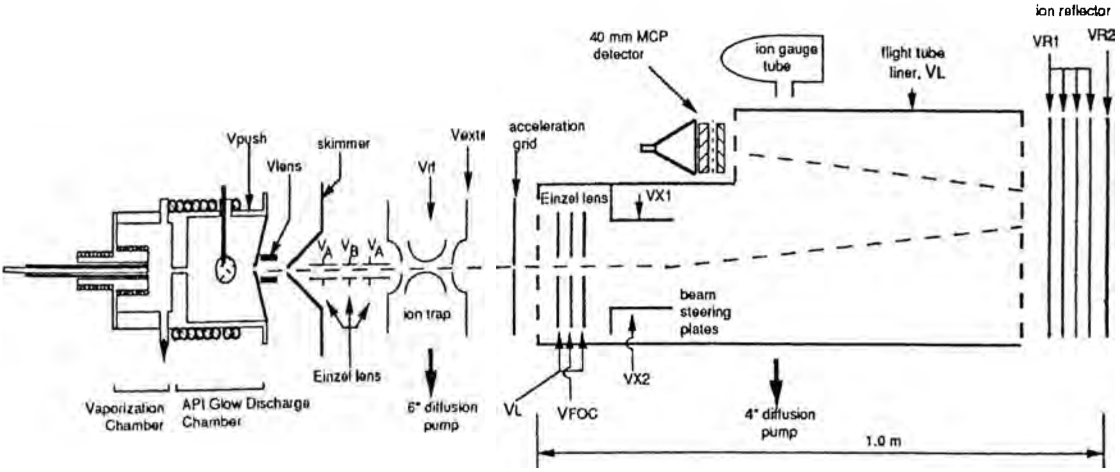

SOURCE: Chen & Lubman, 1992

Figure 1.13 Ion trap reflectron TOF MS with axial injection.

The first IT TOF MS was reported in 1992 as a method for converting a continuous ion beam from an atmospheric glow discharge ion source to the pulsed mode for TOF analysis (Chien & Lubman, 1992; Chien *et al*, 1993). A few advantages of the IT

TOF MS reported are the reduction of the energy and spatial spread of the ions at the centre of the trap in the presence of a buffer gas prior to TOF analysis, possible enhanced sensitivity based upon storage and integration of the ion signal prior to ejection and fast spectra acquisition without having the need to scan. A time spread of the order of $\sim 8\,ns$ at $m/z = 2100$ was reported for this first design and a schematic diagram of the instrument is shown in Figure 1.13.

Time-resolved fragmentation spectra and reflectron tuning techniques for studying the kinetic energy release of fragmentation reactions were demonstrated in a similar design with a resolving power of <1000 (Aicher *et al*, 1995). Simulations of external ion ejection, cooling and extraction processes have been presented (He & Lubman, 1997) and first results from a MALDI IT RTOF MS were reported (He *et al*, 1997). An ESI IT TOF MS has been recently developed (Hashimoto *et al*, 2005). Linear ion traps coupled to orthogonal TOF geometries have also been constructed (Collings et al, 2001; Michaud et al, 2005). There is only one MALDI IT RTOF mass spectrometer available in the market[5].

Ion mobility (IM) measurements in a drift tube based on the time-of-flight principles were presented in 1970 (Young *et al*, 1970). The combination of ESI sources with IM and orthogonal TOF mass analysis is a relatively new technique developed for the separation and determination of various biochemical compounds (Hoaglund *et al*, 1997; Hoaglund *et al*, 1998; Guevremont *et al*, 1997). Ion traps and collision-induced dissociation (CID) cells have also been implemented in IM oTOF MS (Henderson *et al*, 1999; Screbalus *et al*, 1999; Hoaglund *et al*, 2000). A method of determining cross sections of peptides using ESI IM oTOF MS has been reported (Valentine *et al*, 1999). MALDI IM oTOF mass spectrometers have been recently constructed (Gillig *et al*, 2000) to simultaneously acquire peptide mass map and peptide sequence information (Stone *et al*, 2001).

The MALDI TOF imaging technique was initially demonstrated in a laser microprobe mass analysis spectrometer (LAMMA) for the analysis of low mass range ions (Huber *et al*, 1994). The image analysis was extended to peptides and proteins in tissues exceeding 25 kDa (Caprioli *et al*, 1997). TOF imaging is still at an early stage nonetheless the potential of such an analytical tool is enormous for the investigation of cellular processes in both health and disease. The field has been recently

---

[5] www.shimadzu-biotech.net/pages/products/1/aximaqit.php

reviewed (Chaurand *et al*, 2002). The techniques and applications for the characterization of biomaterial surfaces (Belu *et al*, 2003) and the progress in cellular analysis using the TOF SIMS technique (Lockyer & Vickerman, 2004) have also been recently reported.

Aerosol Time-of-Flight Mass Spectrometry (ATOF MS) is a unique analytical technique for the determination of the chemical composition of individual aerosol particles (Wood & Prather, 1998). Real time analysis of particulate matter has diminished concerns over losses and reactions between sampling and analysis with traditional methods of collection and measurement of size and chemical composition. Transportable ATOF instruments incorporating reflectrons have been developed, which overcome the single polarity limitation (Gard *et al*, 1997). A schematic of the ATOF configuration is shown in Figure 1.14. Aerosol mass spectrometry has been recently reviewed (Suess & Prather, 1999). Latest developments include the on-line analysis of organic compounds in fine and ultra-fine particles by photoionization aerosol oTOF MS (Oktem *et al*, 2004) and MALDI ATOF MS for the analysis of bioaerosols (van Wuijckhuijse et al, 2005).

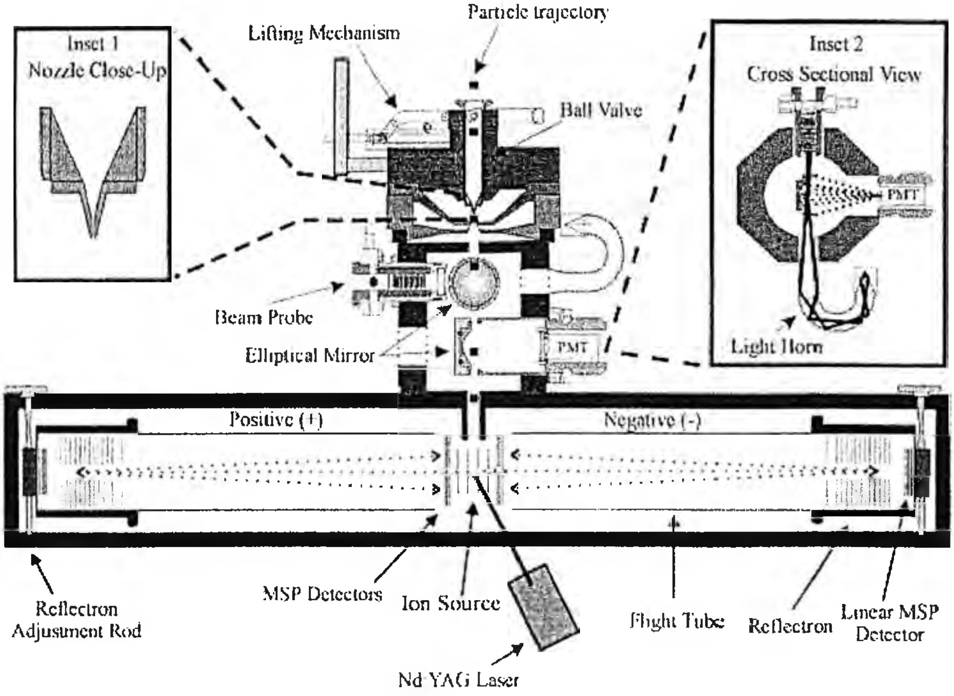

SOURCE: Gard *et al*, 1997

Figure 1.14 Schematic of a transportable bipolar ATOF MS

Advances in space research and instrumentation have also been an important driving force for the development of TOF systems. The scope of the in-situ *Rosina RTOF Sensor*, a special instrument designed for the Rosseta comet rendezvous mission, is to measure chemical elemental and isotopic composition of neutral as well as ionized volatiles in the atmosphere of comet 46/P Wirtanen (Mildner *et al*, 2001). The first results of the *TOF-E* telescope installed onboard of the Nozomi spacecraft were recently reported (Ihara *et al*, 2002). The field of miniature TOF MS for in-situ composition studies, for future landed planetary missions was published in 2003 (Brinckerhoff *et al*, 2003). Pportable and miniature mass spectrometry in the US space program has been discussed (Palmer & Limero, 2001).

Advances in focal plane detectors and digital timing electronics play an ongoing contribution in the establishment of TOF MS as a high resolution mass analysis technique. The development of microchanel plates (MCP), fast preamplifiers, time-to-digital converters (TDC) and transient recorders with *pico*-second resolution have significantly reduced detector pulse width and jitter. High performance TOF mass spectrometers can record arrival time spreads of the order of $\geq 1\ ns$. The temporal interaction of the detection system with the arriving ions at the surface of the detector is by no means trivial. Continuous developments in fast electronics and electron optics have supported the TOF experiment (Selby et al, 2002) and the next challenge to be met is the efficient detection of ions exceeding 1 MDa. It is likely that electron optics in ion detectors will present fundamental limits to the pulse width delivered and that in each case the conflicting requirements of narrow pulse width, high gain and dynamic range will be balanced to meet the needs of the instrumentation (Coles & Guilhaus, 1994).

Several review papers have been published during the last 15 years focusing on the different areas of application and the diverse TOF instrumentation with historical aspects and personal perspectives (Cotter, 1992; Guilhaus, 1995; Guilhaus *et al*, 1997; Standing, 2000; Hillenkamp & Karas, 2000; Mamyrin, 2001).

TOF principles have been extended to the field of spectroscopy mainly for kinetic energy distribution measurements of electrons and ions. A few examples are the use of first-order reflectron lenses in an optical tomographic atom probe (Bemont *et al*, 2002), the construction of variable angle reflectron TOF mass analyzers for studying synchrotron radiation photochemistry of polyatomic molecules (Hiraya *et al*, 1999), the study of chemical reactions of core-excited large molecules with linear and reflectron TOF MS (Ibuki *et al*, 2001), and the use of simple imaging energy filters based on electron time-of-flight principles in photoemission electron microscopy (PEEM) (Oelsner *et al*, 2004). The most recent applications of TOF MS in the field of nuclear physics extend from the accurate measurements of mass and angular distribution of fission fragments in heavy ion induced fission reactions (Ghosh *et al*, 2005) to the search for deeply bound kaonic nuclear states by measuring proton and neutron energy spectra (Suzuki *et al*, 2005).

TOF MS and TOF related techniques constitute an enormously dynamic field of research at the present. A comprehensive literature review of the latest years of academic and industrial instrumentation development and applications is a rather frightening thought. Instead, the TOF instrumentation field is discussed and the historical development of linear and reflecting geometries is reviewed in the following sections.

1.2.3 The Early TOF Instrumentation

A plethora of TOF mass spectrometers based on the time separation principle has been proposed and developed over the past ~65 years. The use of electric, magnetic and RF fields and their combination has resulted in a very diverse and complicated TOF instrumentation. The early TOF designs that differ from linear and reflecting as well as orthogonal configurations are outlined. Latest developments of those first designs that survived since the early days including a few new concepts are also considered.

Chronotron

The first theoretical treatment of circular periodic magnetic time-of-flight mass spectrometer appeared in 1948, known as the *chronotron* (Goudsmit, 1948). The mass analysis principle of the *chronotron* makes use of the rotational period of an isomass-to-charge ion packet, which is independent of the velocity and the direction. One complete cycle of an ion's trajectory in a homogeneous magnetic field is shown in Figure 1.15.

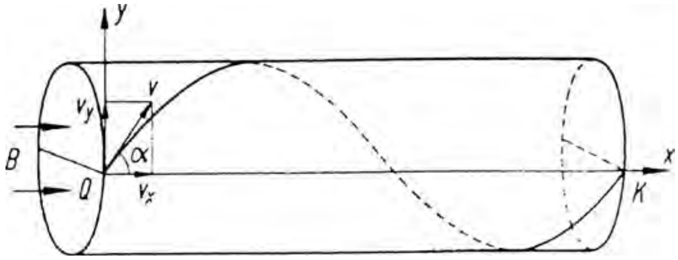

SOURCE: Blauth, 1966

Figure 1.15 Ion path in a homogeneous magnetic field.

Let the magnetic field be in the direction of the x axis. The velocity vector u of the ion motion has an angle a with the field lines (the axis of the solenoid). The velocity perpendicular to the magnetic field is then $u_y = u \sin a$. This velocity component produces a circular motion due to the Lorentz force experienced by the particle, $mu_y^2 / r = qBu_y$ hence the radius of the motion is:

$$r = \frac{m}{z} \frac{u \sin a}{eB} \tag{1.2.1}$$

Where m/z is the mass-to-charge ratio of the charged particles, e the elementary charge and B is the magnetic field strength. For one complete cycle $u_y = 2\pi r / T$ and the period of the rotation is expressed as:

$$T = \frac{m}{z} \frac{2\pi}{eB} \tag{1.2.2}$$

which is independent of both the ion's velocity u and it's direction a. The angular frequency of the motion is $\omega = eB/(m/z)$. The displacement of the charged particle in the direction of field lines during the period time is $l = u_x T$, that is:

$$l = \frac{2\pi}{eB} \frac{m}{z} u \cos a \tag{1.2.3}$$

The solenoid is thus a magnetic lens whose focal length depends on the momentum of the ions and the direction of the velocity vector among other things. The solenoid lens exhibits spherical aberration *i.e.*, ions starting from a point source fail to converge to a single focal point. Thus a point source at Q is imaged along the focal line on the x-axis. It is interesting to note that the time-of-flight of an ion with $m/z = 200$ in a magnetic field of $10^{-2}\ T$ according to Eq. (1.2.2) is $1305.2\ \mu s$ and that of $m/z = 201$ is $1309.0\ \mu s$, $\sim 3.8\ \mu s$ greater. The focal length for a 500 eV ion energy and an angle of 45° is $\sim 20.2\ m$ for $m/z = 200$. Both length and flight time can be reduced by an order of magnitude if the magnetic field is increased to $10^{-1}\ T$.

Successful measurements with the *chronotron* were reported a few years later (Hays *et al*, 1951). In this original device ions were formed by electron impact and they were accelerated by a voltage pulse of $\sim 600\ V$ and $500\ ns$ long so that they all received the same momentum. Detection was achieved by the use of a magnetic electron multiplier (Smith, 1951*a*). Results on the resolving power and the mass accuracy of the *chronotron* mass spectrometer were reported a few years later (Hays, 1954).

Mass Synchrometer

The *mass synchrometer*, developed by Smith in 1951 (Smith, 1951*b*; Smith, 1951*c*) differs from the *chronotron* in that the ions move in a plane perpendicular to the magnetic field. In the original design, $1\ keV$ ions describe circular orbits with an angular frequency, independent of the energy, $\omega = (q/m)B$. The period of revolution is similarly given by Eq. (1.2.2). With reference to Figure 1.16, a group of ions of limited mass range passes through slits S$_2$, S$_3$, S$_4$, where S$_2$, S$_4$ are earthed. A retarding field is introduced by the pulsed nature of slit S$_3$ and momentum is removed forcing the ions to smaller orbits. The first pulse reduces the orbit radius and after a time nT, a second pulse is applied to direct ions onto the detector. The time nT is deduced from the time separation between

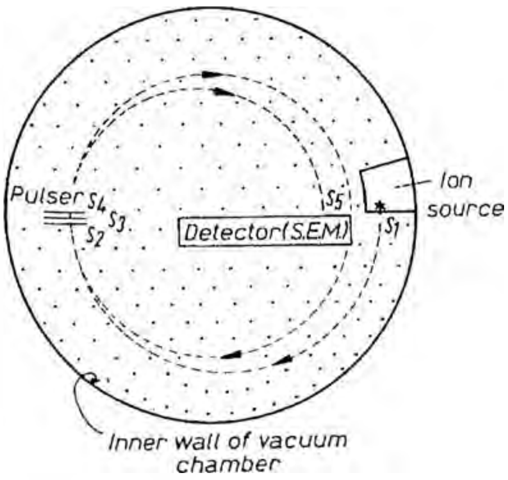

SOURCE: Blauth, 1966

Figure 1.16 The *mass synchrometer*.

the voltage pulses and the ion masses are determined by Eq. (1.2.2). The final form of the instrument appeared in 1956 (Smith & Damm, 1956). Although the system achieved the highest resolution and mass accuracy than that achieved with the best double focusing systems, it suffered from low duty cycle (Beynon, 1960). The *mass synchrometer* is further discussed by Blauth (Blauth, 1966).

Trochoid Mass Spectrometer

A few methods for attaining perfect double focus are known, which have been investigated by the construction of appropriate instruments. The *trochoidal-path* mass spectrometer is such an instrument in which the ion beam is introduced into crossed homogeneous magnetic and electric fields. The *trochoidal* mass spectrometer produces mass dispersion therefore is a scanning instrument. The description of the static focusing trochoidal path spectrometer appeared in 1936 (Hipple & Bleakney, 1936; Hipple & Bleakney, 1938). A schematic of the mass spectrometer is shown in Figure 1.17.

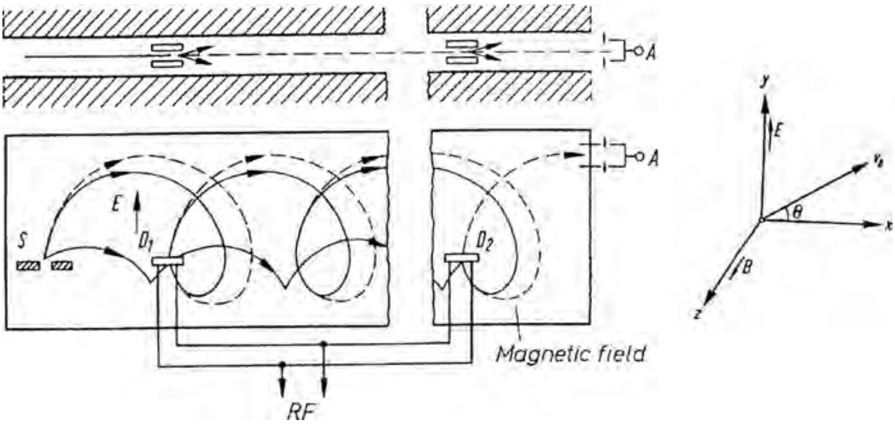

SOURCE: Blauth, 1966

Figure 1.17 Trochoid time-of-flight mass spectrometer.

The trochoidal path is generated by the locus of a point on the radius of a circle, as the circle rolls on a fixed straight line. Ions emerging from the slit S with an angle $(90-\theta)$ relative to the electric field lines experience the crossed field. The equations of motion are (Blauth, 1966):

$$\begin{aligned} m\ddot{y} &= q\mathcal{E} - qB\dot{x} \\ m\ddot{x} &= qB\dot{y} \end{aligned} \tag{1.2.4}$$

In the z direction there is no force acting on the particle and the z velocity component is uniquely determined by the energy of the ion beam. The period of the trochoidal motion is equal to the period of the rotation of the circle and the angular frequency is that of the cyclotron, $\omega = (q/m)B$. The midpoint of the rolling circle moves with velocity $u_x = \mathcal{E}/B$, the radius of the circle is $a = m\mathcal{E}/qB^2$ and the trochoid repeats its self after a distance:

$$d = 2\pi a = 2\pi \frac{m\mathcal{E}}{qB^2} \tag{1.2.5}$$

The focal point for an isomass-to-charge ion packet is therefore independent of the initial velocity and angular divergence and exact double focusing conditions are satisfied. The focused ions are directed through two rf condensers and only ions that pass through at zero transits can reach the collector unperturbed. The time-of-flight between the condensers must then be equal to a whole number multiple of half the rf period T_{rf}, $nT = gT_{rf}/2$ where n is the number of trochoid periods, T the period of ion motion and g an integer, from which the mass of the ions can be determined. A resolving power of 12000 was reported in 1952 (Hipple & Sommer, 1952). A commercial instrument became available in 1957 (Robinson & Hall, 1957). The cycloidal-type focusing mass spectrometers have been briefly discussed (Beynon, 1960; Blauth, 1966). Linear and circular cycloid TOF analyzers are available in the market[6].

Spiratron

The *spiratron*, a unique circular periodic non-magnetic time-of-flight mass spectrometer, was presented by Bakker in 1969 (Bakker, 1969). Two concentric cylinders were used for the assembly of a radial electrostatic field analyzer in which ions describe helical paths. Radial electric sector fields with cylindrical symmetry are also known as electrostatic cylindrical condensers. The radial electrostatic field of the

---

[6] www.monitorinstruments.com

cylindrical condenser had already been used as a high resolution energy filter for electrons.

The advantage of the *spiratron* as a time-of-flight mass analyzer is that a very long field-free ion path can be folded within a small vacuum chamber. The schematic of the *spiratron* is shown in Figure 1.18. Ions are produced in the gas phase by electron impact. Deflection plates are used for the production of ion bunches, a method introduced into TOF MS to provide the "pulsed event" necessary for timing the charged particles (Cameron & Eggers, 1948). Ion packets are injected with a small angular divergence into the mass analyzer. The direction of injection is tangential, with a small component in the axial direction.

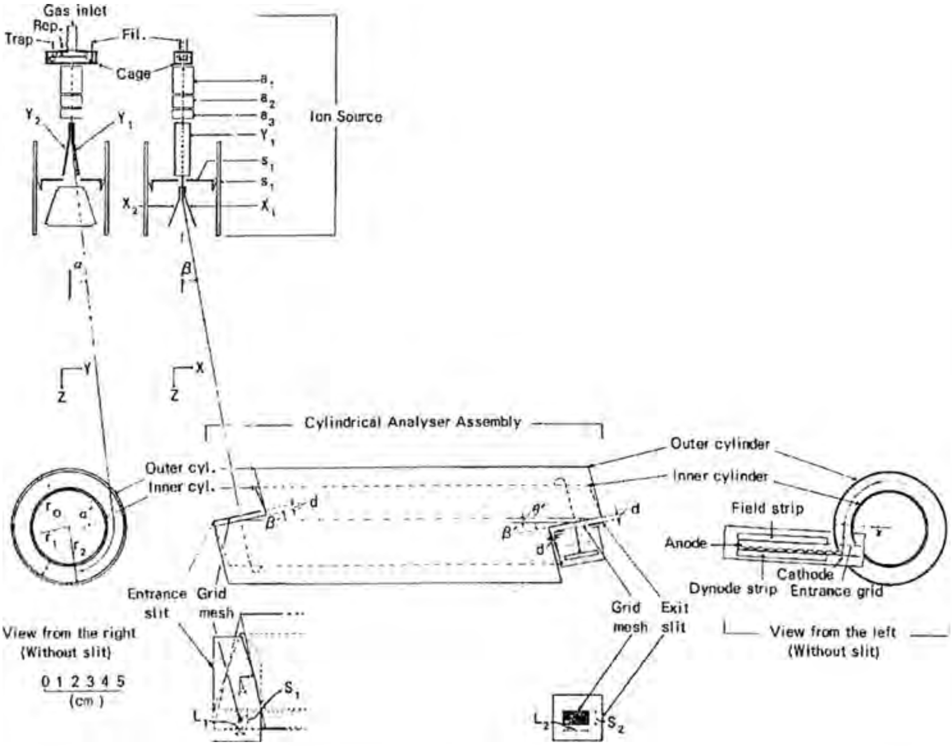

SOURCE: Bakker, 1969

Figure 1.18 Basic components of the *spiratron*.

The electric field between the two concentric cylindrical electrodes is (Cosslett, 1950):

$$\mathcal{E} = -\frac{V}{r\ln(r_2/r_1)} \qquad (1.2.6)$$

Where r_1 and r_2 are the radius of the concentric radial electrodes with $r_1 < r_2$ and V, voltage difference between them. The special case of the equilibrium orbit of constant radius $r = r_o$, or circular orbit, is defined by the relationship $mu_o^2 / r_o = qV / r_o \ln(r_2 / r_1)$, where u_o is the velocity component normal to the field lines. The expression relating the kinetic energy T_o of the charged particle with the voltage across the condenser is:

$$T_o = \frac{qV}{2\ln(r_2 / r_1)} \tag{1.2.7}$$

Much of the theoretical analysis developed for the *spiratron* is based on the directional focusing properties of radial electric sector fields, similar to those exhibited by magnetic sectors instruments. In 1929 a theoretical analysis of the electric sector field demonstrated the ability of such a system to correct for the angular spread of the ions after they had turned through $127^o\ 17'$ $(\pi / \sqrt{2})$ degrees (Hughes & Rojansky, 1929). Experimental results further supported the claim (Hughes & McMillen, 1929), which was proven to be a general property of the radial electrostatic field.

The analysis is based on the deviation of ion trajectories from the equilibrium orbit as a function of initial angular and velocity spreads. A numerical analysis of ion trajectories in the *spiratron* are shown in Figure 1.19. The vertical axis represents the deviation of an ion's trajectory from the equilibrium orbit r_o in terms of the ratio r / r_o. It follows that the equilibrium orbit, trajectory (c) in Figure 1.19, lies on the horizontal axis. The ordinate represents the angle of the radius vector as the ions spiral through the mass analyzer. Trajectories (a) and (e) show the refocusing property of the radial electric field at $\pi / \sqrt{2}$ for ions with an initial angular spread $a = \pm 5^o$, where a is the angle with which ions enter the trajectory. The cross-over point is shifted inwards by a measurable quantity S_e with respect to r_o (Henneberg, 1934; Bakker, 1969). Trajectories (b) and (d) show the effect of the initial velocity spread along the circular orbit and exhibit a maximum deviation at $\pi / \sqrt{2}$. Thus, the maximum energy resolution of the system is determined by the measurable quantity d_e (Hughes & Rojansky, 1929; Bakker, 1969). The perfect re-focusing of the system occurs at

$2\pi/\sqrt{2}$. To conclude, the trajectories cross the perfect orbit of radius r_o every $2\pi/\sqrt{2}$ and the general expression for perfect re-focusing is $n\pi/\sqrt{2}$ where $n = 0, 2, 4...$ The time-of-flight of the ions of mass m and velocity u_o, where $T_o = mu_o^2/2$ over the k-fold direction focusing angle is (Blauth, 1966):

$$t_a = \frac{k\pi}{2}\sqrt{\frac{m}{T_o}}, \quad k = 1,3,5... \tag{1.2.8}$$

Similarly, the time-of-flight over the n-fold direction focusing angle, $n\pi/\sqrt{2}$, where perfect re-focusing occurs is:

$$t_u = n\pi\sqrt{\frac{m}{T_o}}, \quad n = 0,2,4... \tag{1.2.9}$$

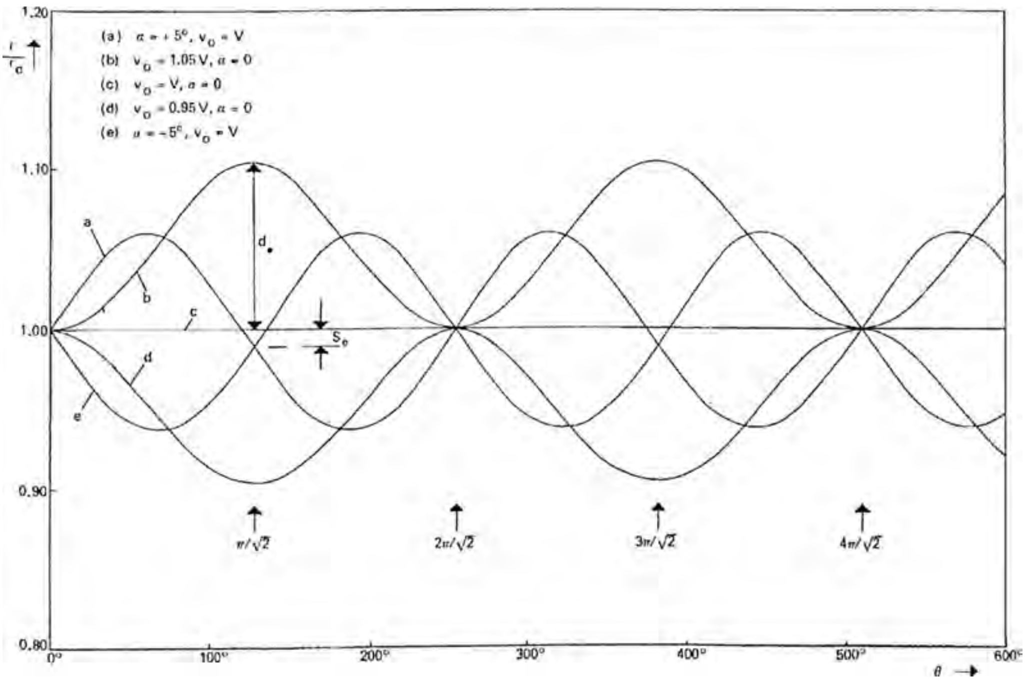

SOURCE: Bakker, 1969

Figure 1.19 Trajectories of particles in radial electrostatic fields. The vertical axis represents the deviation of an ion's trajectory relative to the equilibrium orbit in terms of the ratio r/r_o and the horizontal axis is the angle of the radius vector of the ions as they spiral through the analyzer.

An interesting feature of the *spiratron* was that the apparent drift path length of $140\ cm$ was folded in a $26\ cm$ long vacuum chamber. Ions were accelerated to a kinetic energy of $\sim 2\ keV$. The arrival time spread achieved by this configuration for the ^{131}Xe isotope was $\sim 20\ ns$ with a flight time of $25.25\ \mu s$ recorded by a $50\ MHz$ oscilloscope. The resolution is ~ 630, higher than that of the linear TOF systems at the time. Major contribution to the extended arrival time spread is attributed to the bunching method used for ion production-injection into the analyzer and the associated spread in ion energies. Ion bunching techniques for beam modulation in time-of-flight experiments and particle accelerators have been discussed and a general theoretical treatment of the problems involved has been reported (Fowler & Good, 1960).

Extending his theoretical analysis to the time-of-flight principles for mass separation, Bakker came to the odd result that the slow ions, ions that enter the trajectory with a velocity deficit, will overcome the faster ones as they spiral through the system and arrive at the detector first. He thus proposed a tandem configuration with a linear field-free region such that the spread in the arrival flight times in the linear segment will compensate for the time spread inside the *spiratron* (Bakker, 1971). Such a system was never constructed thus many aspects of the *spiratron* analyzer still remain unexplored.

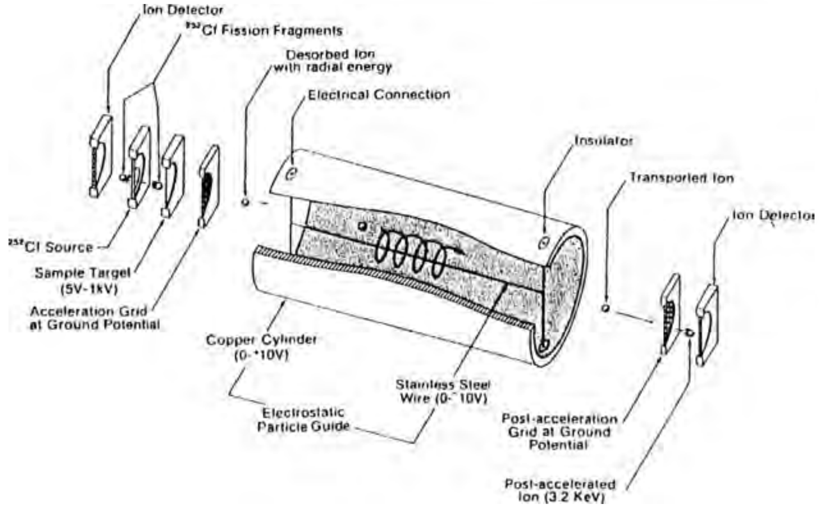

SOURCE: Geno & MacFarlane, 1986

Figure 1.20 Low energy TOF system with a plasma desorption ion source and the electrostatic wire guide.

The electrostatic particle guide was a method used for high resolution studies of thermal neutron reactions as a means for obtaining intense fluxes of fission fragments (Oakey & MacFarlane, 1967). The principle of the technique involved the capture of charged particles into a spiral orbit in an electrostatic field produced by two concentric cylinders. The same concept was applied two decades later for the construction of a low energy plasma desorption TOF system, the schematic of which is shown in Figure 1.20.

Phase Relation TOF Configurations

The *isotron*, the first time-of-flight mass spectrometers with phase relations, was developed in 1952 (Wilson, 1952). The principles of operation are those of a scanning non-magnetic mass spectrometer. Isotopes are separated using velocity modulation and subsequent phase focusing. Several modifications of the original device have been proposed (Blauth, 1966). In a similar design constructed by Glenn (Glenn, 1952) ions from the source are accelerated by a constant voltage and enter a second region where the acceleration is defined by a time-dependent sawtooth periodic voltage. During velocity modulation, ions of the same mass which start out last in a given period always acquire the highest velocity. The desired mass-to-charge ratio is focused at a definite position in the consecutive field-free region. The focal point is mass dependent and different masses can be brought into focus either by varying the constant acceleration voltage or the frequency of the sawtooth waveform. The focused ions are post-accelerated by a voltage pulse and detected by an electrometer. The described TOF configuration is very similar to the direct linear TOF MS systems without phase relations as far as the sensitivity is concerned. Variations of this design have been proposed (Ezoe & Hayashi, 1959) and the theory of phase focusing in TOF MS appeared a few years later (Dutt, 1961). A detailed account of TOF systems with phase relations is given by Blauth (Blauth, 1966). The early rf TOF systems are reviewed by Brunee (Brunee, 1964).

Miscellaneous TOF Instruments

The first Fourier transform TOF spectrometer was introduced in 1986 (Knorr *et al*, 1986; Knorr & Chatfield, 1993). A symmetric waveform was applied on two grids used to bind a linear flight tube at both ends. Source and detector where situated on opposite ends, outside the grids. For an isomass-to-charge ion packet with a narrow spread in drifting velocities, there is a certain frequency that allows them to pass the second grid and reach the detector. The mass spectrum is acquired by scanning the frequency and transforming the ion signal obtained in the time domain to the frequency domain. It must be noted that although this system is discussed as a TOF spectrometer, the method for obtaining a mass spectrum is based on the principles of energy balance analysis.

Another FT TOF system in which ions are forced to circulate around the central electrode of a tube-shaped capacitor was introduced by Oksman (Oksman, 1995). In this system the speed of the ions determines their angular frequency which is measured and converted to a mass spectrum. Again, the performance of such an instrument is heavily determined by the energy spread of isomass-to-charge ion packets. The background of the invention dates back to the use of cylindrical ionization chambers with a central electrode used for trapping and ejecting ions into a TOF analyzer (Talrose & Karachevtsev, 1966) and the *spiratron* (Bakker, 1971; Bakker *et al*, 1981).

The Hadamard Transform Time-of-Flight (HT TOF) mass spectrometer is a high duty cycle method for coupling continuous ion sources with the TOF analyzer (Brock *et al*, 1998; Zare *et al*, 2003; Trapp *et al*, 2004). In HT TOF MS a continuous beam is accelerated and modulated on and off the axis of detection by a binary, pseudorandom encoding sequence at MHz rates applied on a Bradbury-Nielson gate (Kimmel *et al*, 2001). As a result, thousands of ion packets interpenetrate each other as they traverse the field-free region and the detected signal corresponds to the time shifted spectra of the individual packets. The acquired data set is mathematically deconvoluted with the knowledge of the applied encoded sequence to recover the TOF spectrum.

A special instrument, known as the inhomogeneous oscillatory electric field TOF MS utilizing the quadrupole field for decoupling the ion's flight time from the initial spatial and velocity spreads was developed by Carrico (Carrico, 1977). Coincidence TOF MS (Harvey et al, 1970), cylindrical TOF systems with radial ion paths (Zabielski et al, 1970), and segmented TOF analyzers (Srivastava et al, 1995), they are all extensions of the TOF principles for mass analysis.

Sector TOF MS

Sector TOF MS combines linear drift spaces with sector fields. Sector TOF systems can correct for the initial energy spread of the ions and exhibit stigmatic focusing properties, which makes them favourable systems for imaging mass analysis.

Consider a homogeneous magnetic field with 180° deflection into which a packet of ions is ejected with a spread in their momentum. The radius of the motion $r = mu / qB$ is a function of the momentum and the distance traversed is $S = \pi r$. The time-of-flight is then $t = \pi m / qB$, independent of the ions velocity. It is evident that magnetic sector TOF systems can tolerate a wide velocity spread by forcing the more energetic ions to follow longer flights by just the right amount to compensate for the speed effect on the flight time.

Magnetic sector TOF systems impose fundamental restrictions on the design of the instrument. Since the radius is a function of the momentum, isomass-to-charge ion packets with a momentum spread will be laterally dispersed as they are deflected in the magnetic field. The effect is known as chromatic aberration. A large area detector would then be required to collect all the ions. The lateral dispersion between different m / z ratios is compensated by accelerating the ions to equal momentum. Magnets limit the choice of the source and detector (Wollnik, 1993). Since it is favourable to have the ion source and the detector away from the magnet, the combination of field-free drift regions and magnetic sector fields is more practical. Such geometries were first treated theoretically by Poschenrieder (Poschenrieder, 1971). In this novel theoretical analysis, ions were accelerated to equal momentum and velocity focusing conditions were derived for linear drift regions combined with magnetic fields. The time-of-flight in such systems is independent of the ion's velocity and several geometries with stigmatic focusing properties have been studied. The increased cost and complexity of the tandem system with multiple heavy magnets and the necessity of large amplitude

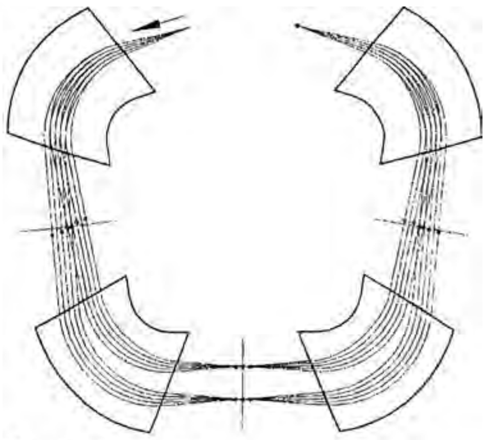

SOURCE: Wollnik, 1993

Figure 1.21 Schematic of the TOF MS with four identical magnets for the analysis of energetic ions.

voltage pulses with well defined shapes has limited the construction of such instruments. The theory of magnetic sector TOF analyzers has been a subject of several publications (Poschenrieder, 1972*a*; Wollnik, 1987*a*). The first TOF analyzer of this kind has been built for the mass determination of nuclear fragmentation products (Wollnik *et al*, 1987*b*). A schematic of this instrument is shown in Figure 1.21. The resolving power of such multi-sector instruments can be further increased by extending the flight path length. This is done efficiently by using the same physical path length in *energy-isochronous ring* TOF systems (Wollnik, 1993).

In electric sector systems the radius of ion motion is $r = mu^2 / q\mathcal{E}$ and the distance traversed by an ion with a velocity normal to the field lines after 90^o deflection is $S = \pi r / 2 = T\pi / q\mathcal{E}$, where $T = mu^2 / 2$. The time-of-flight is then $t = \pi mu / 2q\mathcal{E}$, which unlike in magnetic fields depends on the ion's velocity. It follows that the more energetic ions will describe a longer orbit as they traverse the electrostatic sector with extended flight times. This fundamental principle of the electric sector was patented by *Bendix* in a TOF system where a linear and an electric sector field were combined to mutually compensate for the time spread of the ions in each region separately (Moorman & Parmater, 1971). The following year, Poschenrieder extended his theoretical analysis of equal momentum acceleration and multiple focusing with magnetic sector TOF systems to equal energy acceleration and multiple focusing electric sector TOF systems (Poschenrieder, 1972*b*). Special geometries are discussed which provide stigmatic imaging. Further development of the multiple electric sector TOF systems has resulted in multiturn TOF designs (Toyoda *et al*, 2004). Ions are redirected through the four electric sectors 500 times. The resolving power is of the order of 350,000 at the low mass range, at least an order of magnitude higher than the resolution achieved by any other modern TOF system. However, transmission reduces with the number of turns. A major disadvantage is the narrow mass range that can be analyzed. A theoretical treatment of the "perfect" space-time focusing principles in multiturn TOF MS have been discussed (Ishihara *et al*, 2000). A schematic of a symmetric electric sector TOF is shown in Figure 1.22.

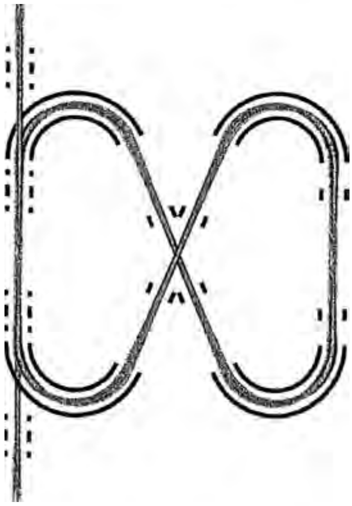

SOURCE: Toyoda et al, 2003

Figure 1.22 Ion trajectories in the symmetric multiturn TOF MS.

1.3 Linear TOF systems

TOF mass analysis constitutes a separate class of dynamic instruments. In most of the systems discussed so far an instrumental parameter is scanned in order to obtain a mass spectrum. Scanning instruments lack the most desirable feature of the TOF analyzer, the ability to collect the entire mass spectrum for single ionization/pulsed events. High resolution TOF systems, such as the multiturn sector configuration are limited to special cases where high resolving power over a very narrow mass range is required. One exception is the *spiratron* but its performance at the high mass end has not been demonstrated.

Based on its unique ability to collect the entire mass spectrum for single events, as well as sensitivity issues, the direct linear TOF configuration has emerged as the principal TOF design. The incorporation of the reflectron device and the re-discovery of the orthogonal gating technique have extended the utility of linear systems and established the TOF analyzer as a fundamental mass analysis technique in modern mass spectrometry. The linear TOF analyzer is reviewed with emphasis on its time-focusing properties.

1.3.1 The Concept and First Attempts

The first pulsed linear time-of-flight mass spectrometer was proposed by Stephens in 1946 (Stephens, 1946):

> *Advances in electronics seem to make practical a type of mass spectrometer in which microsecond pulses of ions are selected every millisecond from an ordinary low voltage ion source. In travelling down the tube, ions of different m/z have different velocities and consequently separate into groups spread out in space.*

Stephens described the principle of separation of the linear TOF configuration and soon the first model was constructed (Cameron & Eggers, 1948). A schematic diagram of the *ion velocitron* is shown in Figure 1.23. Ions formed via collisions with a pulsed electron beam in the presence of a static uniform electric field are ejected into a field-free region with their final velocities, $u = \sqrt{2eV(z/m)}$, where V is the voltage drop for the ions of mass m, e the elementary charge and z the number of charges. For two singly charged ion packets with $m_1 < m_2$ accelerated over the same distance, the drifting velocities are $u_1 > u_2$ and the difference in the transit times in the field-free region is proportional to the square root of the m/z values, $t_1 - t_2 = D/\sqrt{2eV}(\sqrt{m_1} - \sqrt{m_2})$. As the mass increases the arrival time gap between adjacent masses decreases. The first TOF MS achieved resolution of only a few units. A few characteristics of this original device are the use of a cathode ray oscillograph whose time base was triggered by the original pulse in the source, an effective ion energy of $\sim 480\ eV$, a $3\ m$ long flight tube, the absence of narrow slits and an electrostatic lens to correct for the lateral dispersion of the ions. No time-focusing principles were applied.

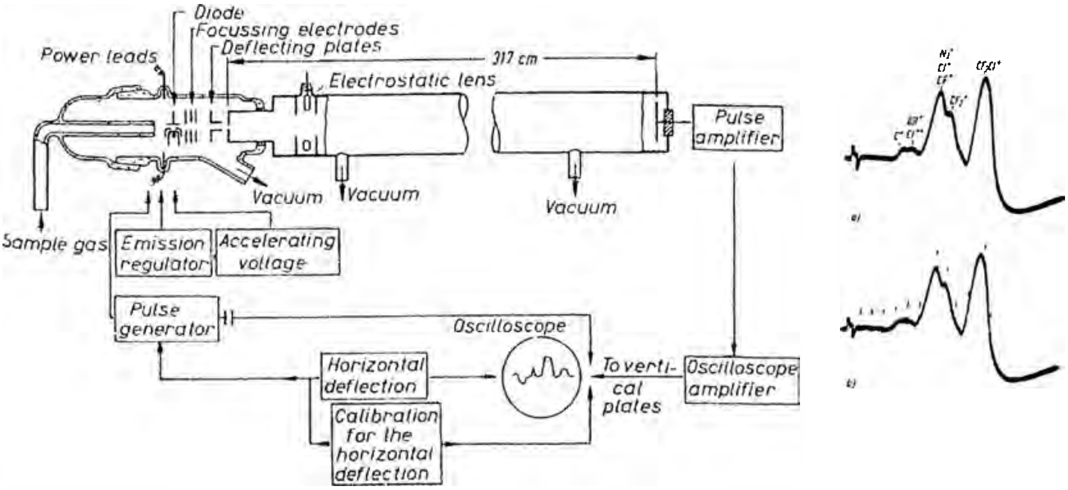

SOURCE: Blauth, 1966

Figure 1.23 The first TOF model presented in 1948, known as the i*on velocitron*. The mass spectrum of *freon-12* is also shown (a) and with 10 μs marker ticks (b).

Similar designs, with minor improvements in the resolving power by increasing the drifting energy of the ions, were reported during the next few years (Keller, 1949; Takekoshi, 1951; Ionov & Mamyrin, 1953). In these early configurations the ions were accelerated to equal kinetic energies. The first linear TOF system with uniform momentum acceleration was reported in 1953 (Wolff & Stephens, 1953) based on voltage pulse techniques for accelerating ions (Goudsmit, 1948; Hays *et al*, 1959). In 1955 key features in the operation of the EI ion source coupled to the linear TOF MS were introduced (Katzenstein & Friedland, 1955). The pulsed extraction method was for the first time presented during which ions are formed by a pulse of electrons in a field-free region and a pulsed electrode is used to extract them through a two-stage acceleration configuration. It was also demonstrated theoretically that equal momentum acceleration may potentially offer higher resolution than equal energy acceleration.

When ions are accelerated to equal energy the drifting velocity is $u=\sqrt{2eV(z/m)}$ and the flight time in the field-free region is proportional to the square root of the mass, $m=ct^2$ where c is the proportionality constant. The error in the mass measurement can be related to the error in the arrival time of the ions:

$$\delta m \approx \frac{dm}{dt}\delta t \tag{1.3.1}$$

It follows then that if $dm/dt=2ct$, the error is $\delta m \approx 2ct\delta t$ and diving by $m=ct^2$, resolution in a linear TOF system with equal energy acceleration can be approximated by:

$$R=\frac{m}{\delta m}=\frac{t}{2\delta t} \tag{1.3.2}$$

For acceleration to equal momentum the drifting velocity is $u=(z/m)e\mathcal{E}/t_a$ where $\mathcal{E}$ is the electric field and t_a the mass independent acceleration time. In this case the flight time is proportional to the mass of the ion $m=ct$, and $dm=cdt$. Eq. (1.3.1) becomes $\delta m=c\delta t$ and dividing with $m=at$ the expression for the resolution in a linear TOF system with equal momentum acceleration is:

$$R=\frac{m}{\delta m}=\frac{t}{\delta t} \tag{1.3.3}$$

twice that of the system with equal energy acceleration. It also follows that in the latter case mass and flight time have a linear relationship in contrast with the former situation in which the flight time differences between adjacent masses decrease as the mass number increases.

1.3.2 Time Focusing

The first theoretical treatment of the time focusing properties in TOF MS was developed by Wiley & McLaren in their landmark publication ~50 years ago (Wiley & McLaren, 1955). Their influential and original work is responsible for the widely adopted two-stage acceleration geometry. The theory of space focusing with uniform electric fields was presented and resolution limitations due to the energy spread of the ions were discussed. The principles for time focusing were later extended to reflecting systems (Alikhanov, 1957). Wiley & McLaren also formulated the post ionization time-delay technique introduced earlier that year by Katzenstein & Friedland (Katzenstein & Friedland, 1955). The technique was termed time-lag focusing and an ambiguous mass dependent focusing condition was derived. The analysis concluded that time-lag and space focusing are mutually exclusive. The time-lag introduces a correlation between position and initial ion velocity and a focusing condition does exist. The missing focusing formula, and its extension to the mass independent focusing properties in orthogonal TOF systems, is developed in this thesis in Chapter 4. A significant advantage of the time-delay technique was the decoupling of the temporal spread introduced by the finite ionization time from the final arrival time spread of the ions at the detector. The time-lag focusing concept was successfully extended to the MALDI ion source, known as delayed extraction (Lenon & Brown, 1994; Colby et al, 1994; Whittal & Liang, 1995; Brown & Lenon, 1995). The key theoretical advances of this method are based on the space velocity correlation concept (Colby & Reilly, 1996) with subsequent velocity focusing of the ions (Vestal & Juhasz, 1998).

Under space focusing conditions, the initial kinetic energy is neglected and focusing is achieved due to the spatial distribution of the ions. The difference in initial potential energies for two isomass-to-charge ions with a spatial separation is translated to a difference in their drifting velocities. Focusing is achieved since the faster ion is the last one ejected in the field-free region. The ideal situation of ions with no velocity has no practical implementation since in a real situation ions travel at least with thermal speeds. The space focusing requirements therefore no longer hold. Space focusing can only correct the flight times for two ions with a spatial separation and equal velocity vectors both in magnitude and direction. This is true for linear, $d^2x/dt^2 = a$, and non-linear, $d^2x/dt^2 = f(x)$, time-independent electric fields. The application of space focusing to axial (Boesl *et al*, 1992) and orthogonal geometries

(Cotter, 1997; Guilhaus *et al*, 2000) is unjustifiable and is both theoretically and experimentally demonstrated in this work.

The time-lag focusing method introduced to simultaneously correct for the initial spatial and kinetic energy distributions of the ions formed by electron impact, is unfortunately mass dependent and therefore not practical when a panoramic view of the mass spectrum is required. Furthermore, the Wiley & McLaren mathematical formulation does not provide a complete focusing condition, that is, an equation relating the dimensions and the applied voltages, as was demonstrated by the space focusing principle. The theoretical analysis of the time-lag lag technique is based on a series of approximations and is not considered as a complete solution[6].

Velocity focusing in linear systems has been a challenge since the early days of TOF MS. It has been demonstrated both theoretically (Stein, 1974) and experimentally (Opsal *et al*, 1985) that space and velocity focusing cannot be simultaneously satisfied with static electric fields in linear TOF systems. This is true however if there is no correlation between the starting positions and velocities of the ions. Although in the time-lag method a degree of correlation was assumed in the derivation of the focusing equation, the concept of correlated distributions was not described at the time. The delayed extraction technique proved that a focusing condition in linear TOF systems with pulsed uniform electric fields exists, which unfortunately was mass dependent.

Space-velocity correlation focusing requires an assumption for the initial phase space distribution of the ions to be made. Time focusing is therefore specific to the ionization technique employed and the overall geometry of the TOF analyzer. The focusing condition for two ions with a spatial spread and opposite velocity vectors, equivalent to the ion distribution at the end of the time-lag, was presented in 2004 (McMahon & Papanastasiou, 2004) based on the ion pair approach (Papanastasiou, 2001; McMahon & Papanastasiou, 2003). The mass independent focusing properties in linear TOF were demonstrated in an orthogonal geometry and the results were summarized in this years ASMS meeting in San Antonio (Papanastasiou & McMahon, 2005). Mass-independent space-velocity correlation focusing in orthogonal TOF MS is the core of this work.

---

[6] http://www.sisweb.com/referenc/applnote/app-46.htm

1.3.3 Existing Linear TOF Theory

The space focusing conditions are determined by a *Taylor* series expansion of the one dimensional time-of-flight equation. If $t(s_i)$ is the arrival time of an ion accelerating over a distance s_i taken at the centre of an infinitely narrow spatial distribution, the arrival time of an adjacent ion accelerating over a distance s_j is:

$$t(s_j) = t(s_i) + \left(\frac{\partial t}{\partial s_i}\right)(s_j - s_i) + \left(\frac{\partial^2 t}{\partial s_i^2}\right)\frac{(s_j - s_i)^2}{2} + \ldots \tag{1.3.4}$$

The time spread defined by the arrival time difference between the two ions is then:

$$\delta t = \left(\frac{\partial t}{\partial s_i}\right)(s_j - s_i) + \left(\frac{\partial^2 t}{\partial s_i^2}\right)\frac{(s_j - s_i)^2}{2} + \ldots \tag{1.3.5}$$

First-order focusing requires that the arrival time spread defined by Eq. (1.3.5) is independent of the first-order term, $\partial t / \partial s_i = 0$ (Wiley & McLaren, 1955). The remaining terms define the arrival time spread of the ions at the focal plane. The second-order term falls in the *pico*-second time frame, an elusive goal for the existing instrumentation in 1955 and in this early work only first-order focusing conditions were considered. Second-order focusing was accurately discussed by Conover and co-authors for their *tilted-plate* TOF MS, a primitive version of the orthogonal TOF (Conover *et al*, 1989) and by Seccombe & Reddish, which showed that the geometrical restrictions imposed under the 2nd-order focusing criteria are removed by the addition of a third consecutive electric field in the accelerating region (Seccombe & Reddish, 2001). Second-order focusing has been a favourite topic in the literature and several authors re-addressed the focusing requirements with extended equations without introducing any new ideas to the TOF theory (Eland, 1993; Chandezon et al, 1994; Piseri *et al*, 1996; Even & Dick, 2000*a*; Even & Dick, 2000*b*).

The maximum contribution of the initial velocity spread to the final resolution of system is determined by two ions with the same starting position and opposite velocity vectors (Wiley & McLaren, 1955). The minimum time spread at the detector is then defined by the turn-around time:

$$\delta t_c = \frac{2mu_i}{q\mathcal{E}} \tag{1.3.6}$$

The effect of the initial velocity can be reduced by either increasing the ratio of the ion's total energy to its initial energy or employing the time-lag focusing technique. Stein demonstrated theoretically that for the above case, $\partial t / \partial s_i$ and $\partial t / \partial u_i$, cannot be simultaneously set to zero with time-independent electric fields (Stein, 1974). Multiple acceleration regions and their ability to correct for the initial ion energy spread while operating in the space focusing mode were investigated (Sanzone, 1970). The two-stage acceleration geometry provided the theoretical limit for energy resolution.

In time-lag focusing (Wiley & McLaren, 1955), ions are allowed to re-arrange their positions within the field-free source according to their nascent velocities, thus obtain a spatial separation prior to the extraction pulse. A schematic of the re-arrangement of a single mass is shown in Figure 1.24. The amplitude of the extraction pulse has to satisfy the space focusing criteria while the length of the time delay should provide energy focusing. Unfortunately, the technique is mass dependent and only a narrow mass range can be brought into focus at the detector plane.

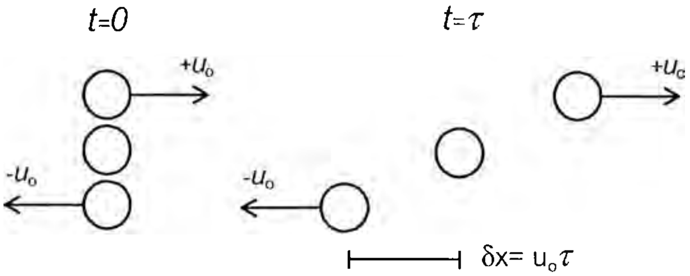

Figure 1.24 Position re-arrangements during the time-lag for three ions in the field-free ion source.

The focusing principle was developed as follows. During the lag period each ion moves a distance $\delta x = u_i\tau$, where τ is the time lag. The change in the flight time can then be expressed by the differential of the time-of-flight equation $t(s_i)$, $dt = (\partial t / \partial s_i)dx$ and the arrival time spread is approximated by:

$$\delta t_{dx} = \frac{\partial t}{\partial s_i} u_i \tau \tag{1.3.6}$$

assuming that the displacement during the time-lag is small, *i.e.*, $\delta x = dx$. The change in the flight time with no time lag for a small change in the initial ion velocity is $dt = (\partial t / \partial u_i)du$ and the arrival time spread is approximated by:

$$\delta t_{du} = \frac{\partial t}{\partial u_i} \delta u \tag{1.3.7}$$

Considering only the latter case with no lag, the flight time difference between the two ions is defined by their flight times in the electric field. The flight time for the ion with the forward initial velocity is reduced by an amount of $(-u_i / a)$ while for the upstream ion it is $(2u_i / a)$ where a is the acceleration. Therefore, the average change in the flight time due to the initial velocity spread is approximated with half the turn-around time, $(t = u_i / a)$ and $\partial t / \partial u_i = 1/a$. During this time interval, which represents the time until the upstream ion stops, the change in the velocity is, $\delta u = u_i$[7].

If the initial energy effect is to be eliminated, the change in the flight time introduced by the time lag and Eq. (1.3.6) must compensate for the flight time difference with no time-lag and Eq. (1.3.7). The proposed focusing condition is obtained by setting $\delta t_{dx} + \delta t_{du} = 0$. Using the relationship $a = q\mathcal{E} / m$ and solving for the time-lag:

$$\tau = -\frac{m}{q\mathcal{E}[\partial t / \partial s_i]} \tag{1.3.8}$$

---

[7] The derivation assumes that the partial derivatives $\partial t / \partial s_i$ and $\partial t / \partial u_i$ are assumed constant over the range of interest. This is a fundamental property of differentials where in general $\delta y \neq dy$. In this case, if $\delta x = dx$ and $\delta u = du$ are "small", then dt is a good approximation for δt.

The time-lag is mass dependent, proportional to $\sqrt{m}$ and independent of the initial ion velocity. The solution has a physical meaning only if $\partial t / \partial s_i < 0$, which violates the space focusing criteria. The mass dependence of the time-lag focusing technique has been studied by Erickson and co-workers (Erickson *et al*, 1990).

Several instrument modifications have been examined in an attempt to eliminate the mass dependency of the ion focus in TOF MS. Among these are beam deflection (Bakker, 1973), energy filtering with beam deflection (Pinkston et al, 1986), post source pulse focusing (Kinsel & Johnston, 1989; Kinsel *et al*, 1991), velocity compaction (Muga, 1987), impulse field focusing (Marable & Sanzone, 1974) and dynamic field focusing (Studier, 1963). These methods are rather difficult to implement and have not been widely applied.

Analytical expressions for ideal space focusing in TOF MS have been presented (Flory et al, 1996; Doroshenko, 2000), however the construction of such fields has not been realized. Miniature linear TOF MS with pulsed extraction (Prieto *et al*, 2002), incorporating higher-order fields for improved space focusing (Gardner & Holland, 1999) and dynamic field focusing (Gardner & Cotter, 2003) have been constructed.

The theory of space focusing in linear TOF MS and space-velocity correlation focusing in laser desorption, particularly MALDI TOF MS, is revised in the following Chapters 2 and 3 respectively. Exact analytical solutions are developed and contrasted with the existing theory. The theory of oTOF systems is considered in the last theoretical Chapter 4. The analysis delineates the difference between the mass dependency of the focusing condition as expressed by the time-lag technique and the mass independent focusing action in oTOF MS.

1.4 Reflectron TOF MS

The reflectron device has an almost equally long history as the linear geometry and is wrongly considered as an invention of the 1970's. The development of the reflectron has greatly facilitated the renaissance experienced in time-of-flight instrumentation over the last 20 years. This is mainly attributed to its ability to deliver high mass resolution without increasing the dimensions of the TOF analyzer. Reflectrons, also known as ion mirrors, utilize a focal point in the field-free region, which is then reproduced at the detector plane. In conventional designs the energy focusing properties are mass independent. Modern reflectrons have been used with mass-dependent virtual sources and can tolerate a broad energy range of product ions. Most of the accomplishments with modern TOF systems rely on high performance reflectron devices.

Accurate mass measurements for the determination of the binding energies of nucleons prompted the development of the first reflectron in 1957 (Alikhanov, 1957):

> *This mass spectrometer has the form of a drift tube which is bounded at both ends by retarding fields with a linear potential distribution. The entire instrument is placed in a weak longitudinal magnetic field. A bunch of ions from the pulsed source is injected into the tube with simultaneous switching-off the retarding field. Having entered the potential well the bunched ions move from one repeller to another but the gain in the time-of-flight by the faster ions with given m/z will be balanced by loss of velocity in the retarding field. Ions with identical m/z and different energies will be focused at a certain point in the drift tube.*

Alikhanov demonstrated the first-order energy focusing properties of a single-stage reflectron in a multipass coaxial TOF system. The focusing condition was developed by setting the first-order term with respect to the initial kinetic energy T_i to zero, $\partial t / \partial T_i = 0$. It was also shown that second-order focusing $\partial^2 t / \partial T_i^2 = 0$ is impossible with the single-stage system. The presence of the magnetic field intended to correct for the lateral dispersion of the ions as they travelled back and forth the flight tube.

The *reflektron* configuration, described in 1962, bears a certain similarity to Alikhanov's system (Melzner, 1962). Ions are generated at the top of a potential barrier and are ejected into a field-free region. At the end of the drift space they are reflected back by a pulsed potential barrier arranged so that ions having a transit period determined by a prescribed velocity remain stable in the system. The principles for mass analysis are those of velocity-stability spectrometers (Blauth, 1966). A schematic diagram of the *reflektron* is shown in Figure 1.25.

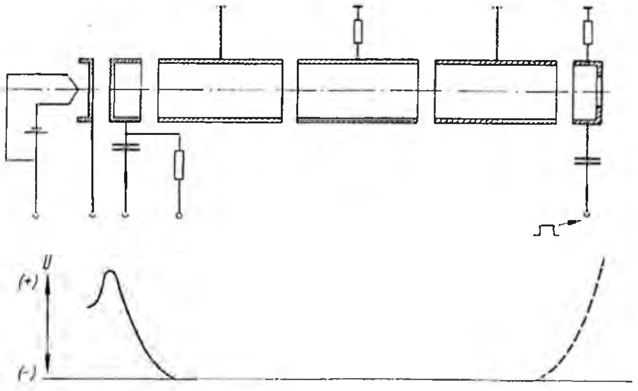

SOURCE: Blauth, 1966

Figure 1.25 Diagram of the *reflektron* and its potential distribution.

An advanced two-stage energy focusing system that became widely known as the reflectron was proposed in 1972 (Karataev *et al*, 1972). One year later an improvement in resolution of one order of magnitude compared with that achieved with linear systems was reported (Mamyrin *et al*, 1973). A schematic of the first two-stage reflectron is shown in Figure 1.26.

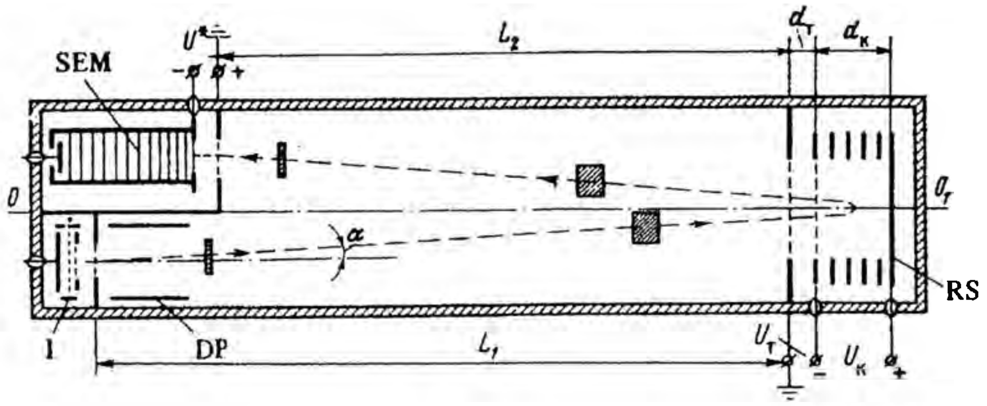

SOURCE: Mamyrin 1973

Figure 1.26 Two-stage reflectron coupled to a conventional linear EI source.

Based on Alikhanov's single stage first-order focusing device, a second retarding field was incorporated and second-order energy-time focusing was achieved. The principles of operation are as follows. Ions are ejected from the two-stage acceleration configuration with their final energies and a set of deflectors provides the necessary flight angle for the ions to hit the detector. Ions are space-time focused near the source. This focal point serves as a virtual source for the reflectron. The ion packets disperse and separate in space as they travel down the field-free region. The reversed fields decelerate them until they stop and reflect them back towards the detector. The faster ions of each individual ion packet arrive at the reflectron entrance first. They penetrate deeper and spend more time as they traverse the electric fields. The differences in the transit times through the reflectron compensate for the differences between the flight time in the acceleration and field-free region. With the proper selection of voltages and dimensions the virtual source can be reproduced at the detector plane. A resolution of ~ 2800 was demonstrated for $m/z = 453$.

A few approximations must be taken into consideration. The space-time focus of the ions near the source was assumed perfect with practically no contribution to the final time spread (Mamyrin et al, 1973). Although it was mentioned that the ion source can be operated in both the pulsed mode and/or the static mode it was not clear which mode of operation was chosen for maximum resolution. In the former case, if time-lag focusing was applied, the so-called space-time focus is mass dependent and only a narrow mass range can be brought into focus. In the latter case the temporal spread introduced by the pulsed ionization process would limit resolution and space focusing principles do not apply to define the position of the virtual source. In either case, the time width of the ion packet at the so-called space-time focal point is by no means trivial and can set a lower limit to the final time spread of the ions. The incompressibility of an ion packet in conservative fields has been discussed by Stein using Liouville's theorem and phase space dynamics (Stein, 1994). A representation of a transformation in phase space is shown in Figure 1.27. Any attempt to time focus ions by reducing the position volume can be achieved only by increasing the momentum space. Since ions in the source have both spatial and kinetic energy spreads the virtual source for a reflectron is not ideal.

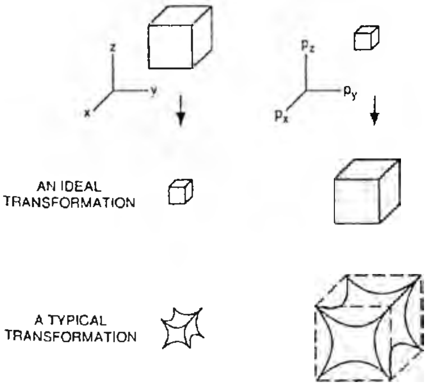

SOURCE: Stein, 1994

Figure 1.27 Incompressibility of particles in phase space.

The deflection of the ions near the source and the corresponding trajectory angle distorts the virtual focal point. The deficiency of the original design due to field imperfections around the deflectors was soon recognized and the linear mass reflectron was proposed. In coaxial designs the detector is situated behind the source (Mamyirn & Shmikk, 1979). The inherent angle of the ions in the orthogonal TOF configuration has proved very convenient for coupling the reflectron device.

The early reflectron designs were intended to correct the energy spread introduced by electron impact ionization process, surface desorption techniques and gas phase laser ionization. The method proposed for implementing time focusing with reflectrons in TOF MS involves the creation of a focal point, and its projection to the detector plane. In most of the early designs a virtual source assumed for enhancing the resolving power of the analyzer. Space focusing has been most commonly used for locating the virtual source in the field-free region of the mass analyzer, irrespective of the method of ion generation and the geometry of the TOF system. An exception is the delayed extraction technique, which can accurately localize such a virtual source.

In the conventional two-stage reflectron, grids are usually employed to separate adjacent electric fields and approximate the sharp boundaries imposed by the theoretical principles of time focusing with uniform fields. Single stage configurations have been equally successive and resolving powers of the order of $\sim 10,000$ with time spreads of the order of $\sim 2\ ns$ have been demonstrated in SIMS TOF MS (Tang *et al*, 1988). A theoretical analysis for first-order energy focusing for ions desorbing from a surface was also presented. A resolution of $35,000$ was reported one year later with a laser ionization reflectron TOF MS (Bergmann *et al*, 1989).

Grid-free designs were mainly developed as an approach to eliminate scattering of the ions and enhance transmission compared with the conventional two-stage configuration. Although the performance is much more sensitive to the lateral dispersion of the ions and can accommodate a narrower range of incoming trajectories, it offers distinctive advantages over traditional designs. Grid-free systems introduced extended regions with higher-order fields. The idea of implementing higher-order fields motivated the design of non-linear reflectrons and their extended energy focusing properties were soon reported.

A resolving power of $\sim 20,000$ has been demonstrated with a grid-free reflectron in EI storage TOF MS (Grix *et al*, 1988). The high resolution achieved is mainly attributed to the very long flight times, ($\sim 800\ \mu s$) and not the time spread ($\sim 22\ ns$) of the ions at $m/z = 870$. The transverse and longitudinal three-dimensional focusing properties of grid-free non-linear reflectrons were investigated by Wollnik and co-workers (Kutscher *et al*, 1991). Grid-free designs have been considered by many authors (Berger, 1983; Walter *et al*, 1986; Glashchenko & Semkin, 1987; Bergmann *et al*, 1990). Generally, the relative kinetic energy range of the ions accelerated from the sources employed by the end of the 1990's was small (<10%) and focusing was effective across the mass range.

Advanced reflectrons incorporating non-linear axial voltage gradients have been constructed by multi-stacked electrode arrangements. The concept is traced back on the original design presented by Carrico (Carrico, 1977). A schematic diagram of a time-of-flight analyzer having a plurality of ring-like electrodes is shown in Figure 1.28. The main problem in curved axial voltage gradients is the curvature of the fields in the radial direction which converts the reflectron into a divergent lens. Losses in sensitivity can be minimized by maximizing the ratio of the length to inner diameter.

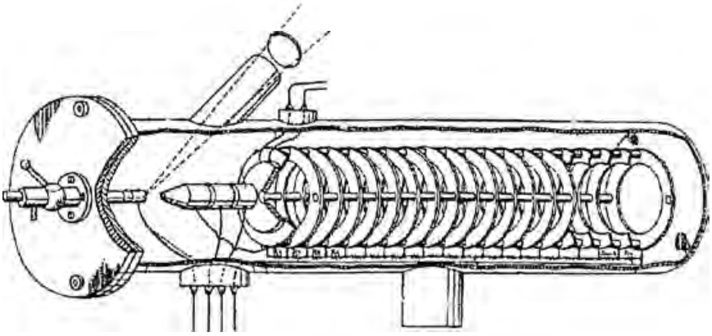

SOURCE: Yoshida, 1986

Figure 1.28 Multi-stacked electrode arrangement of a non-linear reflectron.

Special non-linear reflectrons based on the stacked electrode arrangement have been designed to compensate for the broad energy range of fragment ions produced in induced dissociation processes and metastable decay products formed by laser desorption. The curved-field reflectron was implemented in a RTOF/RTOF instrument to correct for the wide energy spread of the daughter ions (Cornish & Cotter, 1993). A coaxial version was presented for focusing metastable decay products (Cornish & Cotter, 1994) and later used with miniature designs providing higher order energy focusing (Cornish & Cotter, 1997; Brinckerhoff *et al*, 2003). Broad energy range focusing reflectrons for tandem TOF experiments have also been designed by Enke and co-workers (Vlasak *et al*, 1996). The quadratic reflectron, known as the *perfectron*, was introduced by Rockwood (Rockwood, 1986). The flight times of the ions in such a field are independent of their energy. The quadratic field ion mirror has been incorporated in several tandem TOF instruments (Makarov et al, 1995; Giannakopulos et al, 2002).

Analytical expressions of ideal one-dimensional mirror potentials yielding perfect energy focusing (Flory *et al*, 1996) and ideal velocity focusing (Doroshenko & Cotter, 1999) in reflectron TOF MS have been presented. Reflectrons are reviewed by Cotter (Cotter, 1997).

1.5 Orthogonal TOF MS

The concept of accelerating ions normal to the direction of propagation of an ion beam was presented in 1964 (O'Halloran *et al*, 1964). The apparatus was designed for the study of ions formed in argon and air plasmas at atmospheric pressures. The formation of a supersonic jet and the use of deflection plates to reduce the source-axis velocity component limited the resolving power of the prototype. The schematic of this early innovative system is shown in Figure 1.29. The design of the first orthogonal TOF MS was not published in the general literature and remained unknown until the late 1980's when the technique was re-invented independently by two groups in Australia (Dawson & Guilhaus, 1989) and Russia (Dodonov *et al*, 1991). Since its rediscovery, the orthogonal configuration has been established as a method well suited to interfacing the TOF analyzer to

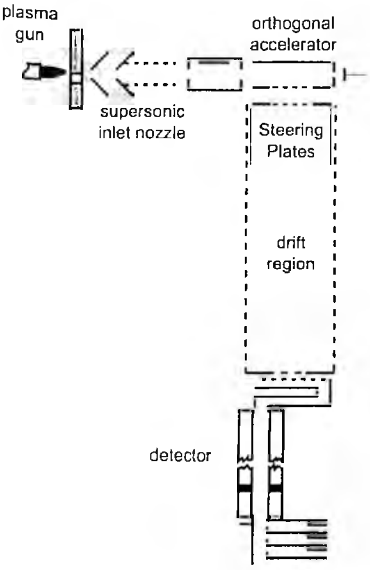

SOURCE: Guilhaus *et al*, 2000

Figure 1.29 The *Bendix* plasma source mass spectrometer.

continuous ions sources. Today, hybrid oTOF mass spectrometers are state of the art instruments. The versatility of modern TOF MS is much attributed to the re-invention of the orthogonal acceleration method. The orthogonal configuration has several distinctive advantages over other types of TOF analyzers and key features are discussed.

In oTOF the mass analysis axis is orthogonal to the direction of propagation of an ion beam. The velocity components normal to the source axis and their contribution to the final arrival time spread of the ions are usually assumed negligible. Space focusing conditions have therefore been widely applied as a method for tuning the system (Guilhaus, 1989; Bondarenko &MacFarlane, 1997; Cotter, 1997; Guilhaus *et al*, 2000*a*). It is interesting to note that the relative dimensions in two-stage orthogonal acceleration regions are chosen so, as to minimize the turn-around time effect. In conjunction with the space focusing mode, configurations where the first pulsed electric field is much shorter than the second static one have been built. For this particular mode of operation the applied voltage across the first field is maximized satisfying both the space focusing requirements and those of Eq. (1.3.6). A deviation from the general misconception that the spatial spread of the ions is the dominant factor limiting the resolving power in oTOF MS is the work by Laiko and Dodonov (Laiko & Dodonov, 1994). They introduced the idea of a linear dependence of the initial ion velocity on initial ion position and they derived focusing conditions for their reflecting geometry. The theoretical analysis presented is rather difficult to implement and the idea of space-velocity correlated ion beams in orthogonal TOF was not fully explored.

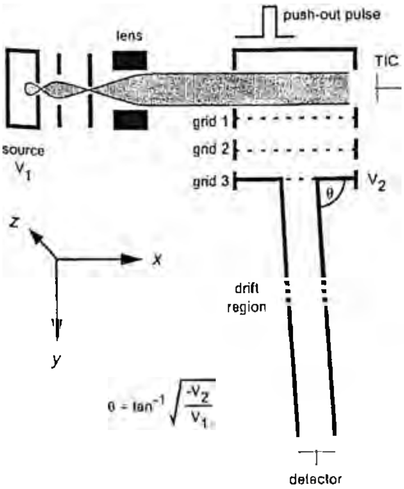

SOURCE: Guilhaus *et al* 2000*a*

Figure 1.30 Schematic of the orthogonal TOF configuration.

Vector decoupling is an essential feature in oTOF MS. The ions retain the velocity perpendicular to the TOF axis. As a result their drifting trajectories in the flight tube are inclined by an angle defined by the velocity components in the ion beam and TOF directions. If the ion source produces ions with constant kinetic energy-to-charge ratios, the flight angle is defined by (Dawson & Guilhaus, 1989):

$$\theta = \tan^{-1}\frac{u_{TOF}}{u_{BEAM}} = \tan^{-1}\sqrt{\frac{V_{TOF}}{V_{BEAM}}} \qquad (1.3.9)$$

The inclination is a very convenient characteristic when employing a reflectron, since the detector can be mounted beside the orthogonal system. It is demonstrated that any attempts to correct for this inclination by applying steering plates result in a reduction in both the resolving power and the sensitivity of the system (Dodonov *et al*, 1994; Guilhaus, 1994).

Early studies with orthogonal TOF systems identified the mass discrimination effects when sampling a supersonic beam. The use of deflection plates in the field-free region was proposed as solution to the problem (O'Halloran, 1964; Sin *et al*, 1991; Myers *et al*, 1994;). Monoenergetic ion beams are ideal for mass analysis in oTOF systems since the flight angle is mass independent and the ability to collect the entire mass spectrum from single pulsed events is preserved. The side drift of the heavier ions during their extended flight times is compensated by the lower velocity in the source axis. This is not the case however with supersonic ion beams were the common velocity generates a mass dependent energy spread and consequently a longitudinal spread at the detector. The situation has been demonstrated with an inductively coupled plasma (ICP) ion source and the mass discrimination effects are depicted in Figure 1.31. Since the side drift velocity is mass independent, the heavier the mass, the longer the flight time in the field-free region and the greater the displacement at the detector plane.

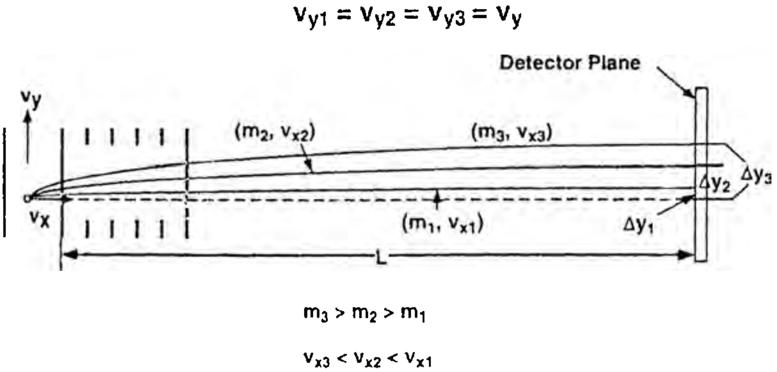

SOURCE: Myers *et al*, 1994

Figure 1.31 Ion trajectories of supersonic formed ions and their displacement on the detector plane according to their masses.

The early orthogonal TOF prototypes coupled to atmospheric ion sources, and especially the ESI source suffered from such mass discrimination effects. Sensitivity was also an important issue (Boyle & Whitehouse, 1992; Mirgorodskaya *et al*, 1994; Verentchikov *et al*, 1994). Ions were introduced directly from the ion source into the oTOF analyzer through an interface that merely provided collimation to define the beam shape. Differential pumping was used to transfer the ions from atmospheric pressure conditions in the source to the high vacuum side of the mass spectrometer. The significant divergence of the ion beam passing from the high to the low pressure region of the mass spectrometer imposed a trade-off between transmission and the narrow beam cross section required for high resolution experiments.

Collisional cooling, introduced for quadrupole mass spectrometry (Douglas & French, 1992; Xu *et al*, 1993), proved an ideal interface for reducing the energy of the ions to near-thermal values (Krutchinsky *et al*, 1998*a*). Ion trajectories in the collisional cooling ion guide are shown in Figure 1.32. Reduced mass discrimination and enhancement in both resolution and sensitivity were reported.

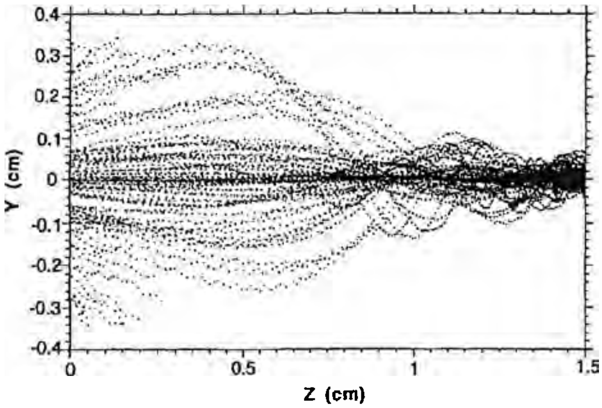

SOURCE: Krutchinsky *et al*, 1998*a*

Figure 1.32 Computer simulation of ion motion in the quadrupole ion guide. As the ions pass through the buffer gas energy is removed via collisions and they relax to near-thermal energies.

A TOF MS system can accept an input pulse of ions only after the previous packet is mass analyzed. As the initial input pulse of ions is dispersed in space travelling down the flight tube, the extraction pulse is relaxed and ions re-fill the first field-free stage of the orthogonal gate. The length of the time interval before the next pulse arrives is determined by the velocity of the slowest ion in the source axis. If d_1 is the displacement of the heavier mass $(m/z)_1$ the duty cycle can be defined as $\varepsilon = l/d_1$ where l is the effective length defined by the grid area and/or the dimensions of the apertures on the orthogonal electrodes. For a monoenergetic ion beam a lighter ion $(m/z)_2 < (m/z)_1$ drifts faster since velocity is inversely proportional to $(m/z)^{1/2}$. During the same "filling up" time interval it covers a longer distance $d_2 > d_1$ along the source axis. Since $l/d_1 > l/d_d$, there is a constant discrimination against the lighter mass a measure of which is the mass dependent duty cycle, $\varepsilon_1 > \varepsilon_2$. Nevertheless this discrimination is predictable and is preferable to the cut-off at high mass values found in quadrupole mass filters (Chernushevich *et al*, 1999).

The expression for the duty cycle in orthogonal TOF MS is defined by the pulse repetition frequency and residence time of any given ion (Boyle & Whitehouse, 1992):

$$\varepsilon = f \times t_r \tag{1.3.10}$$

where f is the frequency of the extraction pulse with an upper limit of approximately $10\ kHz$ $(T = 100\ \mu s)$ and t_r is the time required for an ion to travel the effective length of orthogonal geometry l. If the repetition frequency is defined by the slowest ion to fill the orthogonal region $f = u/d$ and the residence time is $t_r = l/u$, where u is the velocity in the source axis, the duty cycle reduces to l/d, as shown previously. Typical values for duty cycles in oTOF MS are usually well below 50%.

The influence of grids and grid geometry on ion trajectories has been a subject of several investigations especially related to orthogonal TOF systems. Girds are semitransparent conducting "planes" that are used to terminate an electric field at a controlled potential (Guilhaus *et al*, 2000). Typical designs consist of evenly spaced metal conductors running at right-angles to each other. As grids are used to divide regions into linear electric fields of controlled strength, there are always inhomogeneities generated by penetration of high field to low and vice versa.

Scattering of the ions passing through the grids introduces an energy spread which is transformed into a mass dependent arrival time spread at the detector. Early investigations demonstrated the significant contribution of wires transverse to the source axis (Laiko & Dodonov, 1994). Wires with a parallel direction have therefore been proposed. Rectangular wire patterns have also been constructed to facilitate the mounting to the supports (Selby *et al*, 2000). A schematic of the rectangular wire pattern is shown in Figure 1.33.

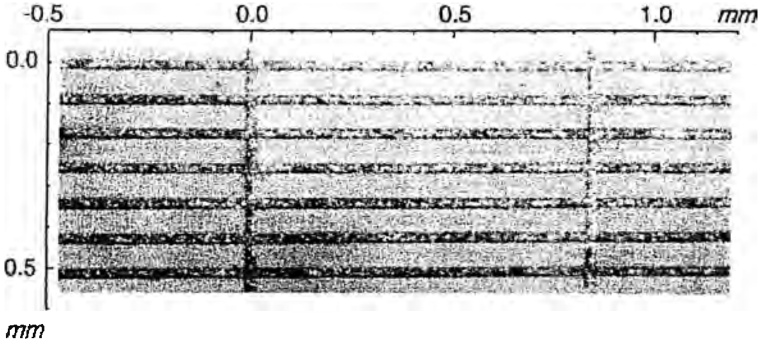

SOURCE: Selby *et al*, 2000

Figure 1.33 Small section of the grid material. In the optimum orientation the closed spaced wires run parallel to the continuous ion beam.

In orthogonal TOF scattering of the ions is important since the ion velocity in the source axis is preserved and ions approach the grids with an angle that deviates from the normal. This is particularly true for the early grids were ions haven't reached their final energies in the TOF direction and the angle is even smaller (Selby *et al*, 2001). The dispersion of the ions and the lens effect in terms of the angle of approach was recently discussed (Lewin et al, 2002). A method for reducing scattering by modifying the two-stage geometry according to the principles of space focusing was also presented (McMahon & Papanastasiou, 2003). Distortions in ion trajectories using a position sensitive detector were demonstrated in an oTOF system (Antoine *et al*, 2004).

Chapter 2

Unification of Energy and Space Focusing

2.1 Resolution in TOF MS

TOF mass spectrometers have been considered for many years as low resolution instruments. Advances in fast electronics, the delayed extraction technique and high performance reflectrons have furthered the development of TOF instruments and enhanced resolution and mass accuracy. Although high mass resolving powers of 1 part in 35,000 (Bergmann *et al*, 1989*b*) and 1 part in 55,000 (Piyadasa *et al*, 1999) have been reported, and more recently the extraordinary number of 1 part in 350,000 was demonstrated in the MULTUM II (Toyoda *et al*, 2004), they are by no means routine. Extra high resolution has been achieved for adjacent masses or single shot spectra and can by no means be extended across the entire mass range when spectra are accumulated over a finite number of ionization/pulsed events. The parameters that influence resolution are addressed in this chapter and the principles of space focusing are discussed with particular emphasis on a new analytical method for describing time focusing using ion pairs.

2.1.1 Time Focusing

Resolution in TOF is a measure of the time spread of isomass-to-charge ions at the detector. The spread in the arrival times of individual ion packets reflects, in addition to the initial conditions in the source, various other aspects of the technique and instrument design. Machining and mechanical precision, power supply stability, detection system response and higher-order fields in the vicinity of grids, lenses and slits, can all influence the resolving power of the spectrometer. An attempt is made to divide the parameters into those that have a direct effect on the resolving power of the instrument, hence can be reduced by focusing techniques, and those that cannot be corrected by tuning the instrument externally.

It must be emphasized that the traditional method of increasing the flight path in linear instruments as a method for enhancing the resolving power has not proven very successful. Longer flight paths result in extended arrival time spreads for the ions. Reduced arrival time spreads can be achieved by increasing the total energy of the system with respect to the initial energy of the ions. The effect on resolution is however counterbalanced by the shorter flight times.

The introduction of the reflectron device offered two distinct advantages. The first is longer flight times by folding the flight path without increasing the dimensions of the instrument. The second and most important is the utilization of a virtual source/focal plane near the source where the time spread of the ions is minimized. The virtual source can then be reproduced at the detector with an additional spread introduced during the remaining flight. The ability of the acceleration system to provide an optimum focal point determines the overall resolving power to a great extent. In tandem TOF MS, the ability to time focus at the mass selection gate, influences the performance of instrument and the quality of daughter spectra. The proficiency of the acceleration system in delivering time focused ion packets into the field-free region is therefore essential. A first-order approximation for independent variables can be used to estimate the time spread at the virtual source or detector plane (Chen *et al*, 1999):

$$\delta t \approx \sqrt{\delta t_{dx}^2 + \delta t_{du}^2 + \delta t_t^2 + \delta t_g^2 + \ldots + \delta t_j^2 + \delta t_e^2} \qquad (2.1.1)$$

The parameters δt_{dx}, δt_{du} and δt_t refer to the initial spatial, velocity and temporal spreads respectively and define the initial conditions of the ions during ionization. They are specific to the ionization technique employed as well as the orientation of the TOF analyzer. Along with δt_g, the contribution of the grids, they can be reduced by focusing techniques. The parameters δt_j and δt_e are inherent and specific to instrument design and are discussed further below.

The *temporal spread* δt_t is associated with the finite time of pulsed ionization events. The classic example is the finite time of ionization in the original Wiley & McLaren EI TOF system in which ions are formed in the gas phase by a pulsed electron beam. The ionization time interval defines the minimum arrival time spread at the detector and cannot be corrected with time-independent fields. The development of the time-lag technique for gas phase ionization (Wiley & McLaren, 1955) and that of delayed extraction in laser desorption TOF MS eliminated the problem by forming the ions in a field-free region. The pulsed extraction scheme then provides the starting event for timing the ions. Unfortunately, both techniques are mass dependent and only a narrow mass range can be brought into focus. More recently, the development of orthogonal configuration instruments with pulsed ion sources coupled to collision cells has been proposed as a remedy to this challenging problem, which however exhibit their own limitations.

The *energy spread*, also referred to in terms of *velocity spread*, is an innate property of the ionization process and can differ significantly between the various techniques of ion production. The associated arrival time distribution, δt_{du}, is considered the major limiting factor for breaking into *pico*-second arrival time spreads. For gas phase ionization the maximum contribution is defined by the turn-around time, illustrated in Figure 2.1. The turn-around time is reduced by higher extraction voltages at the expense however of shorter flight times. Longer flight paths and longer flight times have also been considered (Cotter, 1997). Turn-around time effects are equivalent to the temporal spread, since the ion decelerating and re-accelerating in the static electric field will be found at its original position with the same speed at the end of the time interval δt_t, identical to the finite time of ion formation from a pulsed event.

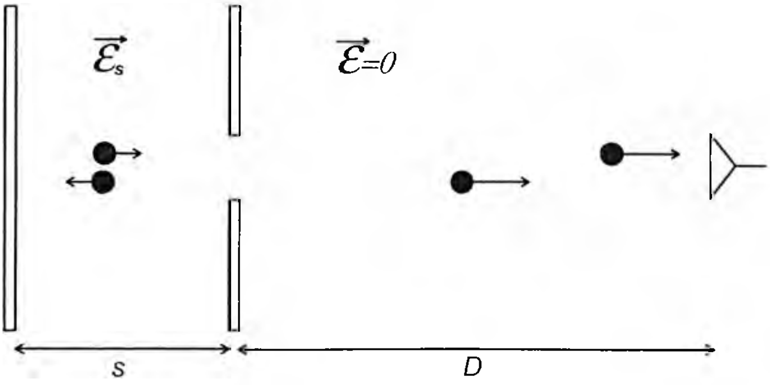

Figure 2.1 The turn-around time effect in a single stage TOF MS.

Correcting for the energy spread of the ions in the source has been a challenging task with no universal solution and special methods apply to specific ionization techniques. The most striking example is delayed extraction and the concept of space-velocity correlation developed for a supersonic jet of laser desorbed ions. The idea of space-velocity correlation in orthogonal systems developed in this work is an extension of the former idea to an isotropic energy spread, and provides the missing focusing condition from the original time-lag technique (Wiley & McLaren, 1955).

The spatial distribution of the ions and the associated arrival time spread, δt_{dx}, was primarily concerned with gas phase ionization techniques and the finite volume of ion formation. More recently, post ionization of surface desorbed neutrals, the thickness of sample layers on surfaces and delayed extraction, which disperses the ions in space prior to the extraction pulse, are all susceptible to the spatial spread of the ions. The theory of space focusing provides a method for correcting the spatial spread of the ions by neglecting their initial velocity or energy spreads. An ion pair and their focal point in a single stage system are illustrated in Figure 2.2. Space focusing is in practise energy focusing and demonstrates that time-focusing with time-independent fields is possible only if ions have obtained a distribution in their electric potential energies. Space focusing is not applicable in any real situation since the newly formed ions travel with at least their thermal energies. The inapplicability of space focusing in orthogonal TOF MS is explained theoretically and demonstrated experimentally in Chapters 4 and 6 respectively. It is rather more accurate to conceive a spatial spread associated with a particular velocity distribution. Space-velocity correlation techniques offer a unique advantage to simultaneously correct for both δt_{dx} and δt_{du} since the former can be expressed as a function of the latter and vice versa.

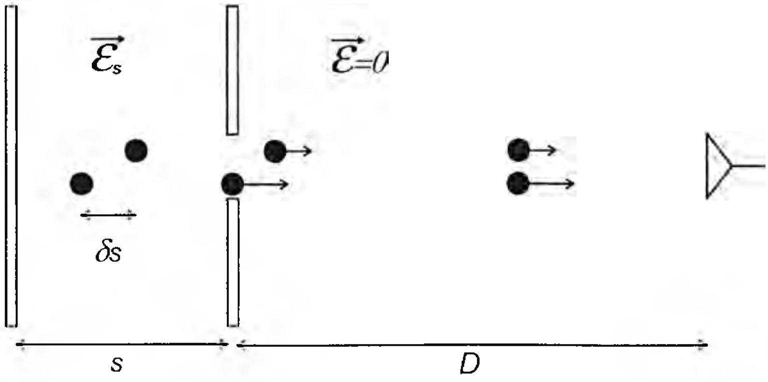

Figure 2.2 The spatial spread of the an ion pair and their focal point in a single stage TOF MS.

Exact solutions to the space focusing theory are developed based on a new analytical approach and compared with the existing theory. The analysis is extended to MALDI TOF and space-velocity correlation focusing for a *forward* velocity distribution in Chapter 3. The theory of space-velocity correlation for an isotropic distribution is developed in Chapter 4 and experimental results from the prototype orthogonal TOF MS are presented in Chapter 6.

The first theoretical analysis of field distortions in the vicinity of wire meshes and their contribution to the arrival time spread of the ions, δt_g, was developed for a reflecting system (Bergmann *et al*, 1989*a*). SIMION[1] was employed to simulate grids related to time-of-flight experiments (King *et al*, 1991). For a two stage linear system and a normal approach of the ions to the wire mesh separating the adjacent electric fields, the following conclusions were made. Deflection and time spread are mass dependent. The heavier masses experience the higher-order fields for longer times and thus spread further. The ion velocity has a similar effect. Slower ions experience stronger deflection. Scattering is strongly related to the position of the ions relative to adjacent wires. An important factor is the relative strength of successive electric fields. The greater the difference, the more the electric field punches through the grid, which maximizes scattering and time spread. Field penetration can be reduced by increasing the number of wires per area at the cost of transmission. The effects of grids and the associated time spreads have been treated with respect to orthogonal systems (Laiko & Dodonov, 1994, Guilhaus *et al*, 2000*a*; Selby *et al*, 2000; Selby *et al*, 2001; Lewin *et al*, 2002) and have no direct solution. A technique for maximizing the angle of approach to intermediate grids in orthogonal systems has been proposed (McMahon & Papanastasiou, 2002).

The parameters δt_e and δt_j are concerned with trajectory errors and detector pulse width respectively. Trajectory errors refer to the effect introduced by three-dimensional instrumental imperfections as opposed to the usual one-dimensional analysis of ion trajectories (Vestal & Juhasz, 1998). Detector pulse width and the associated jitter can set a lower limit in the resolving power in TOF MS. The finite width of single ion events measured by microchannel plate detectors is currently[2] in the *pico*-second scale ($\sim 500\ ps$).

2.2 *Taylor* Series and Error Propagation

A differential expression of the time-of-flight equation and the associated Taylor series is used to approximate the arrival time distribution of the ions. The focusing

---

[1] Dahl DA. and Delmore J.E., SIMION PC/PS2 v4.0, Idaho National Engineering Laboratory, Idaho Falls, ID 83415

[2] www.burle.com/cgi-bin/byteserver.pl/pdf/EP110.pdf

conditions are obtained by the successive coefficients of the expansion. The highest order referred in the truncated form of the equation defines the order of focusing, only if the theoretical requirements are satisfied by the experimental parameters involved. It must be emphasized that the method provides an approximate solution. Fundamental concepts of the expansion theory for a function of a single variable are discussed in the following paragraphs. The *Taylor* expansion for a function of two independent variables and the application of error propagation theory to the TOF experiment are presented in Appendix I.

The *Taylor* series with its associated truncation errors is a mathematical formulation that is widely used in numerical methods to express functions in an approximate fashion. The *Taylor* series assumes that any smooth function can be approximated as a polynomial. It can specify the value of a function at any point in terms of the function and its derivatives at a reference point. For a function of a single variable $f(x)$ the general form of the *Taylor* series is:

$$f(x+dx)=\sum_{n=0}^{\infty}\frac{(dx)^n}{n!}\left(\frac{\partial^n f}{\partial x^n}\right) \qquad (2.2.1)$$

Neglecting third and higher-order terms:

$$f(x+dx)=f(x)+\frac{\partial f}{\partial x}dx+\frac{\partial^2 f}{\partial x^2}\frac{(dx)^2}{2!} \qquad (2.2.2)$$

The error in determining $f(x+dx)$ is proportional to the step size dx and can be reduced by the addition of terms to the series. This fundamental approximation of calculus asserts that given the derivative of the function and an estimate of the error in the independent variable, the error in the value of the function $\delta f=f(x+dx)-f(x)$ is:

$$\delta f=\frac{\partial f}{\partial x}\delta x+\frac{\partial^2 f}{\partial x^2}\frac{(\delta x)^2}{2!} \qquad (2.2.3)$$

The application of the *Taylor* expansion in TOF MS is two-fold. It defines the focusing requirements by the successive coefficients and provides an approximation for the error by the remaining terms in the series. The coefficients designate a focusing constraint, which relates dimensions and electric fields for optimum resolution. The remaining terms give a numerical estimation of the arrival time spread of the ions.

2.3 Energy-Time Focusing

In contrast to the application of the *Taylor* series and the related approximations, in this work exact solution to the focusing properties in time-of-flight mass spectrometry (TOF MS) employing static and/or time dependent uniform electric fields are developed. Achromatic aberrations in linear TOF systems are for the first time evaluated analytically. The analysis incorporates finite distributions of ion starting positions and velocities, and shows their dependence on the focusing action of the apparatus. The model considers a distribution of n ions as a system of $n(n-1)/2$ ion pairs and computes their individual focal points along the mass analysis axis. Individual ion pair focal points are dispersed both in time and space. A focal region with variable temporal and spatial dimensions is identified along the field-free path of the ions. The dimensions of the focal region are a measure of the aberration introduced by the acceleration geometry and the initial conditions. The mass-independent non-ideal focusing action of the linear TOF analyzer is contrasted to the existing theory, where a single focal plane is computed and focusing is realized as an instantaneous property of the system. Focusing is a dynamic property in TOF MS and can be qualitatively and quantitatively examined by the spatial and temporal extent of the focal region. Preferred acceleration configurations are selected that minimize its dimensions. The analysis highlights the finite errors associated with truncated *Taylor* series solutions as applied to the space focusing conditions in TOF MS. The focusing action in TOF MS relies on the inherent ability of the system to provide ions with an initial distribution in electric potential energy. The space focusing conditions are derived in terms of initial electric potential energy, hence the concept of energy-time focusing.

2.3.1 Space Focusing

Figure 2.3 shows the three regions of a linear, Wiley-McLaren ToF-MS. The system is assumed to have one-dimensional symmetry, i.e. that the lens components are infinite parallel plates and that grids are infinitely thin transparent conductors that can generate sharp discontinuities between fields. The acceleration distance within the first electric field of length s is $s_i = s - x_i$. The length of the second electric field is given by d and D is the field-free ion path length. The initial ion velocity is given by u_i.

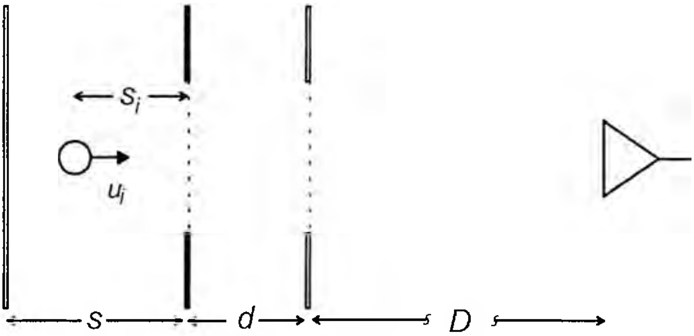

Figure 2.3 Geometry of a two stage TOF MS

The time-of-flight for an ion is the sum of the flight times in the two acceleration regions and the flight time in the field-free region. These are respectively:

$$t_{si} = \frac{\sqrt{u_i^2 + 2s_i a_s} - u_i}{a_s} \tag{2.3.1}$$

$$t_{di} = \frac{\sqrt{u_i^2 + 2s_i a_s + 2da_d} - \sqrt{u_i^2 + 2s_i a_s}}{a_d} \tag{2.3.2}$$

$$t_{Di} = \frac{D}{\sqrt{u_i^2 + 2s_i a_s + 2da_d}} \tag{2.3.3}$$

where a_s and a_d are the successive accelerations experienced by the ions in the electric fields.

Neglecting the initial velocity, $u_i = 0$, the overall time-of-flight expressed as a function of the acceleration distance s_i is:

$$t(s_i) = \sqrt{\frac{2s_i}{a_s}} + \frac{\sqrt{2s_i a_s + 2da_d} - \sqrt{2s_i a_s}}{a_d} + \frac{D}{\sqrt{2s_i a_s + 2da_d}} \tag{2.3.4}$$

First order space focusing conditions consider the first-order term in the *Taylor* series expansion of Eq. (2.3.4). The focusing constraint is derived by setting the rate of change in flight time with respect to initial position to zero, $\partial t / \partial s_i = 0$. The variable s_i is taken at the mean of the initial spatial spread, $s_i \pm ds$. The focusing condition applies only to infinitely small displacements in s_i. Ions in the vicinity of the average starting position exhibit identical arrival times and therefore do not contribute to the arrival time spread.

The focusing action of the system is qualitatively described by the rate of change in the flight times as the ions travel through the consecutive fields. In the first region the partial derivative is positive, $\partial t_s / \partial s_i > 0$. The longer the acceleration distances the later the ejection times into the second field. In the first electric field the faster ions are the last ones ejected. For the two consecutive regions (d, D) the partial derivatives are negative, $\partial t_d / \partial s_i < 0$ and $\partial t_D / \partial s_i < 0$, indicating that any additional fields allow the faster moving ions to catch-up with the slower ones and focusing can occur. The focusing constraint to be satisfied is:

$$D = 2(s_i \lambda + d)\left[1 + \frac{(1-\lambda)\sqrt{s_i \lambda + d}}{\lambda \sqrt{s_i \lambda}}\right] \tag{2.3.5}$$

Eq. (2.3.5) is an expression for the distance of the focal point as a function of the acceleration geometry and the applied voltages for a given mean starting position. If the system variables satisfy the above constraint, the TOF MS configuration is space focused to the first-order. The space focusing distance D is a function of the acceleration lengths s_i and d and the dimensionless ratio λ:

$$\lambda = \frac{\varepsilon_s}{\varepsilon_d} = \frac{d}{s}\frac{V_s}{V_d} \tag{2.3.6}$$

Variations on the applied voltages can therefore shift and project the focal point to the appropriate distance. The focusing condition reduces to the purely geometric relationship, $D = 2s_i$, for the single stage system.

The arrival time spread introduced by an ion situated at s_j, the maximum deviation from the mean s_i, can be approximated by a *Taylor* series. The time-of-flight equation is expanded about s_i:

$$t(s_j) = t(s_i) + \left(\frac{\partial t}{\partial s_i}\right)(s_j - s_i) + \left(\frac{\partial^2 t}{\partial s_i^2}\right)\frac{(s_j - s_i)^2}{2!} + \ldots \tag{2.3.7}$$

If $\partial t / \partial s_i = 0$, the time spread of the ions at the optimum distance is evaluated by the remaining terms:

$$\delta t = \sum_{n=2}^{\infty}\left(\frac{\partial^n t}{\partial s_i^n}\right)\frac{(s_j - s_i)^n}{n!} \tag{2.3.8}$$

where $\delta t = t(s_j) - t(s_i)$. When first-order focusing conditions are satisfied the arrival time distribution exhibits a minimum $\left(t(s_i) < t(s_j),\ \partial^2 t / \partial s_i^2 > 0\right)$, a maximum $\left(t(s_i) > t(s_j),\ \partial^2 t / \partial s_i^2 < 0\right)$ or a point of inflection with respect to s_i (see Figure 2.11b). The point of inflection requires also that $\partial^2 t / \partial s_i^2 = 0$ and the additional focusing requirement is:

$$D = \frac{2}{3}(s_i\lambda + d)\left[1 + \frac{(1-\lambda)(s_i\lambda + d)^{3/2}}{s_i^{3/2}\lambda^{5/2}}\right] \tag{2.3.9}$$

Second-order space focusing requires that both Eq. (2.3.5) and (2.3.9) are simultaneously satisfied and the remaining time spread can be approximated by Eq. (2.3.8) for $n = 3$. In practise, first-order space focusing conditions are applied to a fixed geometry and the focal plane is projected to the detector distance along the field-free region by adjusting λ. The value of λ is adjusted externally by voltage alterations. For a fixed acceleration geometry there is a unique distance along the field-free ion path where the system exhibits its second order focusing properties. At this distance the arrival time distribution exhibits a point of inflection. Two-stage acceleration geometries tuned to the second-order utilize this focal plane along the field-free region as the virtual source for incorporating a reflectron (Boesl *et al*, 1992). For such configurations the virtual focal plane is fixed. An additional acceleration field allows the position of the focal point to be varied with voltage (Seccombe & Reddish, 2001).

A three-dimensional representation of the solutions for second order space focusing conditions is shown in Figure 2.4. Any point on the surface satisfies both Eq. (2.3.5) and (2.3.9). Short s and long d acceleration distances minimize the contribution of the "turn-around time" to the final arrival time spread of the ions by increasing the ratio of the electric fields. That is, a stronger first electric field is required to project the ions to a particular distance and the value of λ approaches unity. Greater λ ratios reduce field penetration between the adjacent electric fields.

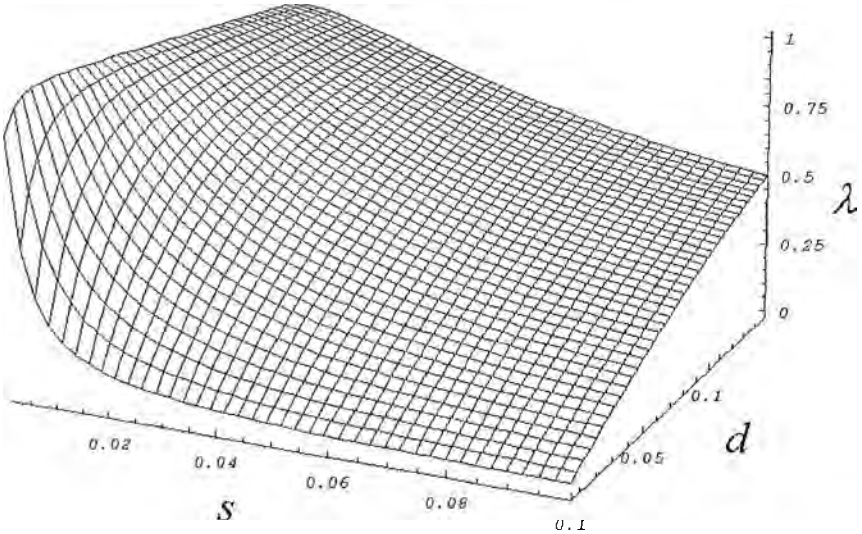

Figure 2.4 Second-order space focusing conditions in three dimensions. The acceleration lengths are given in *m*. The optimum field-free distance is obtained by substituting the surface coordinates to any of the focusing conditions (2.3.5) and/or (2.3.9).

An alternative expression for the space focusing properties in the TOF MS system introduces dimensionless variables (Seccombe & Reddish, 2001). By introducing the length ratios $\mu = D/s_i$ and $\nu = d/s_i$, Eq. (2.3.5) and (2.39) reduce to the dimensionless expressions:

$$\mu = 2(\lambda+\nu)\left[1+\frac{(1-\lambda)\sqrt{\lambda+\nu}}{\lambda^{3/2}}\right] \tag{2.3.10}$$

$$\mu = \frac{2}{3}(\lambda+\nu)\left[1+\frac{(1-\lambda)(\lambda+\nu)^{3/2}}{\lambda^{5/2}}\right] \tag{2.3.11}$$

Eq. (2.3.10) and (2.3.11) define the relative dimensions of the instrument and are useful for scaling down the TOF MS when miniature designs are considered. Relative dimensions designed according to second-order focusing constraints are defined by the surface intersection in Figure 2.5. The position of the focal plane for systems satisfying second-order conditions can be projected to longer field-free distances by increasing the ratio $\nu = d/s_i$.

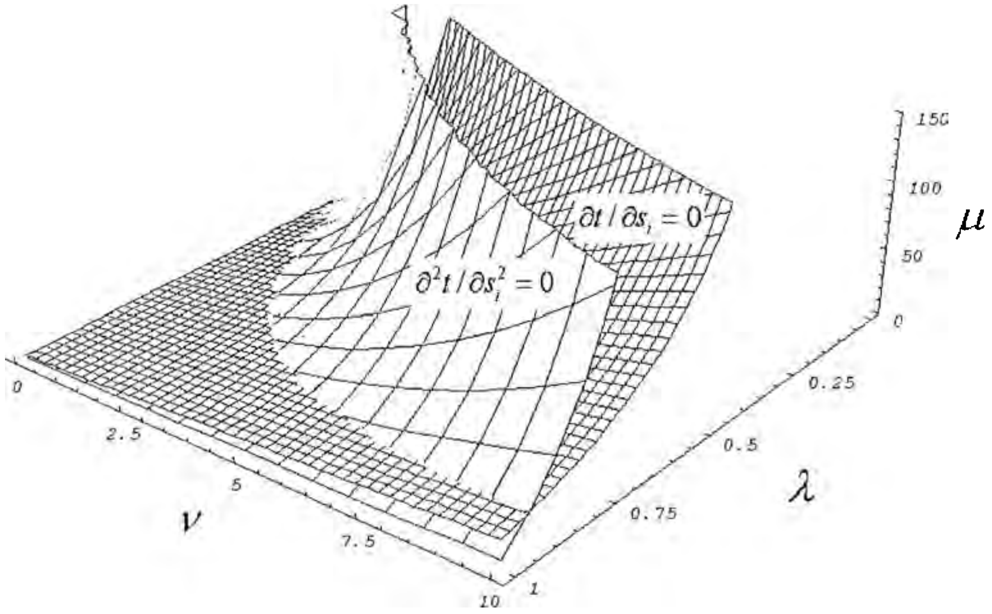

Figure 2.5 Three-dimensional representation of first and second order focusing constraints. The surfaces intersection defines all possible second order configurations in relative dimensions.

2.3.2 Potential Energy Focusing

At the end of the acceleration region the initial electric potential energy is converted into kinetic energy and the ions drift with a constant velocity towards the detector. The greater the potential energy of an ion in the first field, the longer the acceleration distance and the greater the starting velocity for the subsequent field-free motion. The ability of a system to space focus relies on the distribution in initial electric potential energies of the ions. This is true when initial ion velocities are also considered. The introduction of a time-lag provides the ions with a spatial, therefore potential energy distribution. It is the differences in the drifting kinetic energy of the ions, as a result for their loss in potential energy that brings isomass-to-charge ions into focus.

Space focusing conditions are obtained by minimizing the partial derivative of the time-of-flight equation with respect to a single starting position. The flight times can be equally expressed in potential/kinetic energy terms and the derivatives can be evaluated over the average initial potential energy. In a single stage system, the times spent in the acceleration and field-free region respectively are:

$$t_s = s_i\sqrt{2m}\frac{1}{\sqrt{U}} \qquad (2.3.12)$$

$$t_D = D\sqrt{2m}\frac{1}{2\sqrt{T}} \qquad (2.3.13)$$

where s_i and D are the acceleration and field-free distances traversed by a single m/z ion and U is a negative quantity expressing the positive work done by the field on the particle. Therefore, the gain in the kinetic energy for zero initial velocity is $T=-U$. For the first electric field, the rate of change in the acceleration time is evaluated over the initial potential energy while for any successive regions the evaluation is made over the total kinetic energy of the system. For the single stage configuration:

$$\frac{\partial t_s}{\partial U} = s_i\sqrt{2m}\frac{1}{2U^{3/2}} \qquad (2.3.14)$$

$$\frac{\partial t_D}{\partial T} = -D\sqrt{2m}\frac{1}{4T^{3/2}} \qquad (2.3.15)$$

For a given accelerating voltage across the first field, the greater the acceleration distance (electric potential energy), the longer the extraction time, and $\partial t_s / \partial U > 0$, since $\partial t_s / \partial s_i > 0$. The derivative for the field-free region is a negative quantity since the greater the kinetic energy of the particle the shorter the flight time. The focusing condition requires that $\partial t / \partial U + \partial t / \partial T = 0$ which results in the simple geometrical condition, $D = 2s_i$.

In the two-stage system, ions undergo a subsequent acceleration as they travel the second electric field. For zero initial ion velocity, the total kinetic energy in the field-free region is defined by the loss in the initial potential energy, the positive work done by the field on the ions. The flight times in the two regions are given in terms of the total potential energy U:

$$t_s = s_i \sqrt{2m} \frac{1}{\sqrt{U - U_d}} \tag{2.3.16}$$

$$t_d = d\sqrt{2m} \left[\frac{\sqrt{U}}{U_d} - \frac{\sqrt{U - U_d}}{U_d} \right] \tag{2.3.17}$$

$$t_D = D\sqrt{2m} \frac{1}{2\sqrt{U}} \tag{2.3.18}$$

where $U = U_s + U_d$, and s_i, d, D are the acceleration and field-free region distances. Evaluating the partial derivatives with respect to U and T:

$$\frac{\partial t_s}{\partial U} = s_i \sqrt{2m} \frac{1}{2U_s^{3/2}} \tag{2.3.19}$$

$$\frac{\partial t_d}{\partial T} = -d\sqrt{2m} \frac{1}{2U_d} \left[\frac{1}{\sqrt{U}} - \frac{1}{\sqrt{U_s}} \right] \tag{2.3.20}$$

$$\frac{\partial t_s}{\partial T} = -D\sqrt{2m} \frac{1}{4U^{3/2}} \tag{2.3.21}$$

Summing and solving for the field-free distance:

$$D = s_i \frac{4U^{3/2}}{2U_s^{3/2}} + d\frac{4U^{3/2}}{2U_d}\left[\frac{1}{\sqrt{U}} - \frac{1}{\sqrt{U_s}}\right] \tag{2.3.22}$$

The last expression reduces to the focusing condition (2.3.5) by replacing the potential energies according to $U = U_s + U_d = qs_i\mathcal{E}_s + qd\mathcal{E}_d$ and introducing the field ratio $\lambda = \mathcal{E}_s / \mathcal{E}_d$. Second-order energy focusing can be developed in a similar manner. Eq. (2.3.22) is a description of the time-focusing action of the linear TOF MS in terms of ion energies, hence the term energy-time focusing.

2.4 Ion-pair focusing

An alternative description of the time focusing properties in TOF MS is developed. Achromatic aberrations and the associated imperfect space focus are delineated by introducing the idea of ion pairs. An analytical expression is derived for the focal distance of two ions with a finite initial spatial separation. Their trajectories are represented in a time-distance plot and a unique focal point is defined at the intersection of these trajectories as shown in Figure 2.6. The analysis is extended to all ion pairs confined within the initial spatial spread giving rise to a focal aberration, or a focal region. The dispersion of focal points in distance and time, define the limits of the region. The spatial extent of focusing correlates with the arrival time distribution of the ions to a particular plane within this region. It is demonstrated that its width can be described by two ion pairs, situated at the front and the back extremes of the starting ion ensemble respectively. Their focal distances define the beginning and the end of focusing along the mass analysis axis. The mathematical approach goes on to prove that the optimum distance for the detector in cases where finite size distributions are considered is given by the extreme ion pair, the two ions that define the initial spatial spread. Exact solutions to the space focusing properties are provided and deviations from the existing approximate method (Wiley & McLaren, 1955) are discussed.

2.4.1 Single Stage System

With reference to Figure 2.6, a two-dimensional trajectory is constructed involving the ion displacement along the mass analysis axis and the time taken. For an isomass-to-charge ion pair with a finite initial spatial separation, δs, prior to acceleration a unique focal point is generated along the field-free region.

For an ion situated in the $\mathcal{E}_s$ electric field of length s, the acceleration is experienced over a distance $s_i = s - x_i$, where x_i is the starting position relative to the back plate. Neglecting the initial velocity u_i, the displacement x as a function of time t within the electric field is described by a parabola[3]:

$$x(t) = x_i + \frac{1}{2}a_s t^2 \qquad (2.4.1)$$

where a_s is the acceleration exerted on the ion, $a_s = \mathcal{E}_s q/m$. At the end of the electric field the time spent t_{si} and the acquired velocity, u_{si} are respectively:

$$t_{si} = \sqrt{\frac{2s_i}{a_s}} \qquad (2.4.2)$$

$$u_{si} = \sqrt{2s_i a_s} \qquad (2.4.3)$$

where s_i is the starting position relative to the grid separating the electric field from the field-free region. The time for an ion to traverse the field-free region of length D is:

$$t_{Di} = \frac{D}{\sqrt{2s_i a_s}} \qquad (2.4.4)$$

The distance-time plot, ion motion is described by the tangent to the parabola at the end of the electric field:

$$x(t) = s + u_{si}(t - t_{si}) \qquad (2.4.5)$$

---

[3] The equations of motion and the time integral are derived from first principles in Appendix II.

For two isomass-to-charge ions with a finite spatial separation $\delta s = s_i - s_j$ there will be two distinct parabolae yielding tangents of different slope. The crossing point of these tangents determines where the ions are brought into focus. The lower parabolic curve refers to the ion accelerating from x_i while the second ion starts at x_j. At the end of the acceleration region ions have acquired different kinetic energies as a result of the potential differences through which they fall. The ion initially placed at x_i falls through the greatest potential difference and is thus ejected into the field-free region with the highest velocity, $u_{si} > u_{sj}$. The ion at x_j is ejected sooner, but with smaller velocity as a consequence of its relative position to x_i and eventually is overtaken by the faster ion. The time at which these two ions meet defines a mass independent focal point, unique for these starting positions.

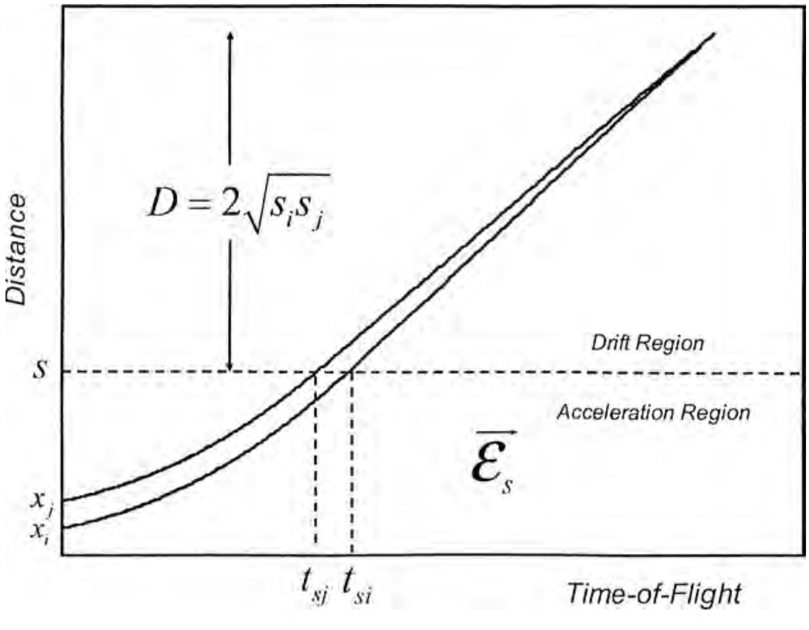

Figure 2.6 Time-distance trajectories in a single stage TOF MS. A unique mass independent focal point is introduced by an ion pair with a finite spatial separation.

The optimum distance for an isomass-to-charge ion pair is analytically determined by the simultaneous equation system for the two tangents:

$$\begin{cases} x(t) = s + u_{si}(t - t_{si}) \\ x(t) = s + u_{sj}(t - t_{sj}) \end{cases} \tag{2.4.6}$$

The coordinates of the focal plane are:

$$[t_{i,j}\ ,\ x_{i,j}] = [\sqrt{\frac{2}{a_s}}(\sqrt{s_i} + \sqrt{s_j})\ ,\ s + 2\sqrt{s_i s_j}] \tag{2.4.7}$$

where $t_{i,j}$ is arrival time and $x_{i,j}$ is the distance from the back plate. The time coordinate is mass dependent and the arrival time to the focal plane is proportional to the square root of the mass-to-charge ratio, $t \propto \sqrt{m/z}$. The focal plane for the two ions is mass independent and the focal distance measured from the start of the field-free region is:

$$D = 2\sqrt{s_i s_j} \tag{2.4.8}$$

Eq. (2.4.8) defines a unique focal plane for two ions and converges to the *W&M* focusing condition $D = 2s_i$ when $s_i = s_j$, i.e., when the finite initial spatial spread converges to a single starting position.

The analysis is extended to an ensemble of n ions giving rise to $n(n-1)/2$ ion pairs and therefore focal points. Figures 2.7 & 2.8 illustrate how these focal points are dispersed over a focal region for a rectangular spatial distribution of ions in the acceleration region. In TOF MS the optimum focal distance must be defined in terms of the time spread of the ions to that particular plane. The focal region is characterized by a spatial and temporal distribution of ion-pair focal points for which time and distance are correlated. This implies that for the same number of focal points, a spatially narrower focusing region will lead to narrower arrival time distribution at a particular plane. In order to minimize the spatial extent over which focusing occurs we must identify its extremes.

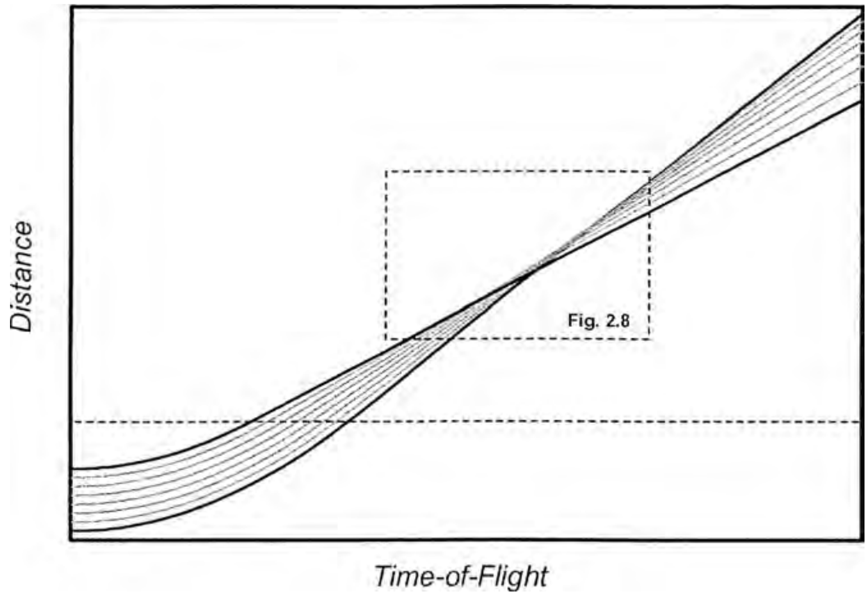

Figure 2.7 Trajectories in a time-distance diagram of a rectangular spatial distribution of an arbitrary number of ions.

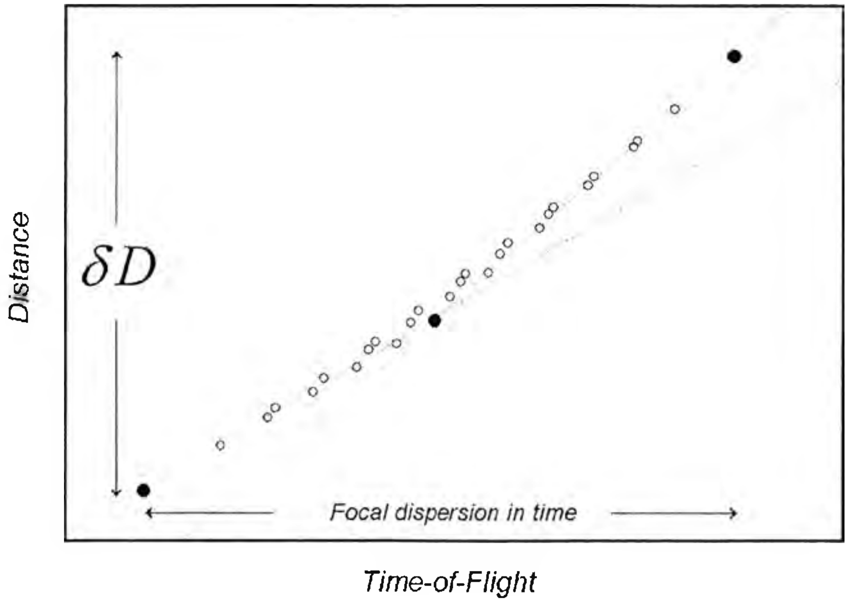

Figure 2.8 Focal points of a representative selection of ion pairs dispersed both in time and along the mass analysis axis.

2.4.2 Time Domain Analysis

An initial starting position x_i is confined within a finite spatial spread δs defined by the two extremes, $x_1 \le x_i \le x_2$. For the single stage system, the arrival time expressed as a function of the acceleration distance s_i is:

$$t(s_i) = \frac{2s_i + D}{\sqrt{2s_i a_s}} \tag{2.4.9}$$

The arrival time spread of an ion ensemble with a finite initial spatial distribution is given by $\delta t = t_{\max}(s_i) - t_{\min}(s_i)$. The maximum and/or minimum arrival time is a function of the acceleration distance s_i and is determined by the derivatives of the arrival time distribution. Partial differentiation with respect to s_i determines the rate of change of arrival times as a function of s_i, D and a_s, namely :

$$\frac{\partial t}{\partial s_i} = \frac{2s_i - D}{2s_i\sqrt{2s_i a_s}} \tag{2.4.10}$$

The condition $\partial t / \partial s_i = 0$ specifies a unique focal point along the field-free region for a particular acceleration length, $D = 2s_i$. The arrival time distribution exhibits a minimum for the s_i position. Since all possible starting positions are confined by the extremes of the ion ensemble $s_2 \le s_i \le s_1$, individual ion pair focal points lie within $2s_2 \le D \le 2s_1$. Within this focal region the arrival time expressed as a function of initial position exhibits a stationary point, in this case a minimum at $s_i = D/2$. The extremes of the focal region are therefore defined by the extremes of the initial ion distribution, thus $\delta D = 2(s_1 - s_2) = 2\delta s$. For a single stage system, the condition is a purely geometric one and the spatial dimensions of the focal region are solely determined by the initial ion spatial spread.

Having defined the spatial limits of the focal region it is necessary to consider the temporal spread of the ions for each plane within this region. The dimensions of the focal region are equally determined by considering two ion pairs, one at the front and one at the back extremes of the initial ion ensemble. As the focal plane moves to longer field-free distances the arrival time distribution to that particular distance folds yielding a unique stationary point for each detector position within the specified limits. Therefore, a subset of the ion pairs is focused isochronously. Focusing first occurs for the ions in the vicinity of the s_2 starting position at a distance $D_2 = \lim_{s_i \to s_2} D = 2s_2$ and ends at $D_1 = \lim_{s_i \to s_1} D = 2s_1$. The width of the focal region is then expressed as $\delta D = D_1 - D_2$.

Considering arrival time distributions at planes situated before the focal region, $D < 2s_2$, the rate of change in arrival times determined by Eq. (2.4.10) is positive, $\partial t / \partial s_i > 0$. Since $s_1 > s_2$, then $t(s_1) > t(s_2)$, and the arrival time spread is expressed by:

$$\delta t = t(s_1) - t(s_2) \qquad (2.4.11)$$

For $D > 2s_1$, the rate of change of the arrival times with respect to s_i is always negative, $\partial t / \partial s_i < 0$ and the time spread is expressed by:

$$\delta t = t(s_2) - t(s_1) \qquad (2.4.12)$$

The monotonic behaviour of the two arrival time distributions is shown in Figures 2.9a and 2.9d respectively. Within the focal region which is spatially located by $2s_2 \le D \le 2s_1$, the arrival time distribution exhibits a minimum at the s_i starting position, where $s_i = D/2$.

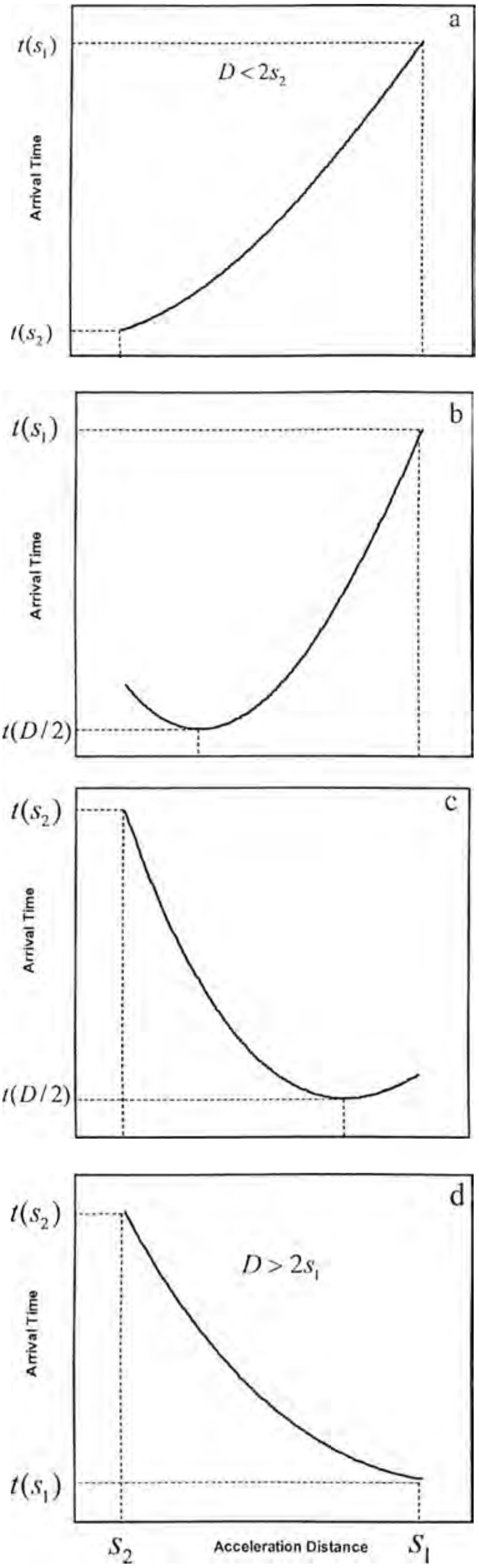

Figure 2.9 Figures 2.9a and 2.9d show the monotonic arrival time distributions corresponding to a finite initial spatial spread, before and after the focal region. In Figures 2.9b and 2.9c the arrival time distributions are obtained within the focal region where the extremum is a function of $s_i = D/2$. Moving from shorter towards longer flight paths the successive arrival time distributions are given in the following sequence, 2.9a to 2.9d.

As we enter the focal region at $2s_2$ moving towards longer flight distances focusing occurs first for ions initially in the vicinity of s_2. At these distances $t(s_1) > t(s_2) > t(D/2)$ where $t(D/2)$, the minimum arrival time, is a function of D as shown in Figure 2.9c. Since the minimum throughout the focal region is $t(D/2)$, the time spread is determined by the slowest arrival time at a particular plane, hence defined by the value of D. In this case $t(s_1) - t(s_2) > 0$ and the time spread is expressed as:

$$\delta t = t(s_1) - t(D/2) \tag{2.4.13}$$

As we move towards the end of the focal region focusing occurs for ions in the vicinity of s_1 and $t(s_2) > t(s_1) > t(D/2)$ as shown in Figure 2.9d. The time spread of the ions is:

$$\delta t = t(s_2) - t(D/2) \tag{2.4.14}$$

The last expression is valid for $2\sqrt{s_1 s_2} < D < 2s_1$ since $t(s_1) - t(s_2) < 0$. The arrival time spread exhibits a quasi-symmetric distribution when $t(s_1) = t(s_2)$. Eq's (2.4.11)-(2.4.14) give the overall time spread of the ions as a function D:

$$\delta t = \begin{cases} (2\sqrt{s_1 s_2} - D)\dfrac{\sqrt{s_1} - \sqrt{s_2}}{\sqrt{2 s_1 s_2 a_s}}, & D < 2s_2 \\ \dfrac{(\sqrt{D} - \sqrt{2s_1})^2}{\sqrt{2 s_1 a_s}}, & 2s_2 \le D \le \sqrt{2 s_1 s_2} \\ \dfrac{(\sqrt{D} - \sqrt{2s_2})^2}{\sqrt{2 s_2 a_s}}, & \sqrt{2 s_1 s_2} \le D \le 2s_2 \\ (D - 2\sqrt{s_1 s_2})\dfrac{\sqrt{s_1} - \sqrt{s_2}}{\sqrt{2 s_1 s_2 a_s}}, & 2s_1 < D \end{cases} \tag{2.4.15}$$

Eq. (2.4.15) is a continuous function of D and non-differentiable at $D = 2\sqrt{s_1 s_2}$, the distance where the arrival times of the extreme starting positions are equal,

$t(s_1)=t(s_2)$. At this distance the derivative of the time spread function is negative, $\partial\delta t/\partial D<0$ for $D<2\sqrt{s_1 s_2}$ and positive, $\partial\delta t/\partial D>0$ for $D>2\sqrt{s_1 s_2}$. The time spread for a particular m/z ratio is shown in Figure 2.10. Figure 2.11a illustrates the quasi-symmetrical arrival time distribution at the optimum distance defined by Eq. (2.4.15) and Figure 2.11b the asymmetrical distribution at the *W&M* optimum.

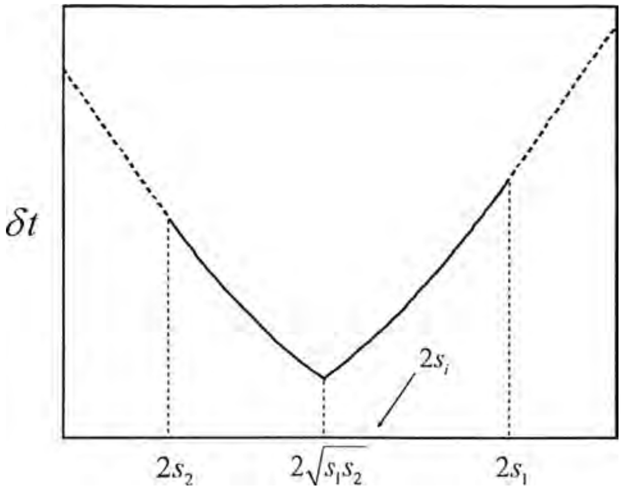

Figure 2.10 The arrival time spread of an isomass-to-charge ion ensemble falls through a minimum as we move from shorter to longer flight paths. The optimum distance is a function of the two extremes that spatially localize the initial spatial separation. The optimum position as determined by the *W&M* approximation is located to greater distances.

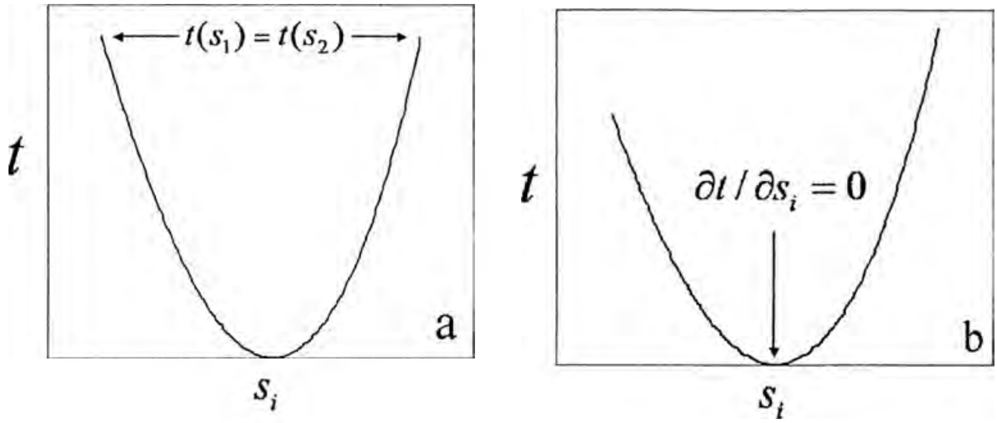

Figure 2.11 The arrival time distributions of an isomass-to-charge ion packet at the optimum (a) and the *W&M* distances (b) respectively.

The optimum distance $D = 2\sqrt{s_1 s_2}$ is a function of the size of the finite initial spatial distribution, $\delta s = x_2 - x_1 = s_1 - s_2$ and can be identified in time-distance plots using Eq. (2.4.8) when the extreme ion pair is considered, i.e. $s_i = s_1$ and $s_j = s_2$.

2.4.3 Two Stage System

The scale and nature of the error associated with the "single point" analysis of space focusing was demonstrated in Sections *2.4.1* and *2.4.2*. The same issues are relevant to a two stage acceleration system. Achromatic aberrations of space focusing conditions for a real spatial spread are discussed using the ion pair method.

In a two stage system, at the end of the first electric field, ions undergo subsequent acceleration. The distance travelled from the starting position x_i through the consecutive electric fields $\mathcal{E}_s$ and $\mathcal{E}_d$ are $s_i = s - x_i$ and d respectively. The ion then drifts with its final velocity through the field-free region. The ion position in the second electric field as a function of time is given by:

$$x(t) = s + u_{si}(t - t_{si}) + a_d (t - t_{si})^2 / 2 \qquad (2.4.16)$$

The time spent in the second electric field t_{di} and the subsequent velocity u_{di} with which the ion is ejected in the field-free region are respectively:

$$t_{di} = \frac{\sqrt{2 s_i a_s + 2 d a_d} - \sqrt{2 s_i a_s}}{a_d} \qquad (2.4.17)$$

$$u_{di} = \sqrt{2 s_i a_s + 2 d a_d} \qquad (2.4.18)$$

The velocity u_{di} at the end of the second electric field is retained throughout the field-free region. In a time-distance plot the field-free ion motion is represented by the tangent to the second parabolic curve and the ion displacement is expressed as a function of time:

$$x(t) = s + d + u_{di}(t - t_{si} - t_{di}) \qquad (2.4.19)$$

The ion-pair focal point and the corresponding time-distance coordinates are calculated from the "tangential" simultaneous equation system for the x_1 and x_2 starting positions respectively:

$$\begin{cases} x(t) = s + d + u_{d1}(t - t_{s1} - t_{d1}) \\ x(t) = s + d + u_{d2}(t - t_{s2} - t_{d2}) \end{cases} \tag{2.4.20}$$

where u_{d1}, t_{s1}, t_{d1} and u_{d2}, t_{s2}, t_{d2} are the drifting velocities and the times spent in each electric field for the s_1 and s_2 starting positions respectively. Solving for the independent variable t and equating:

$$D = \frac{u_{d1}u_{d2}}{u_{d1} - u_{d2}}(t_{s1} + t_{d1} - t_{s2} - t_{d2}) \tag{2.4.21}$$

Utilizing Eq. (2.4.2), (2.4.17), (2.4.18) and introducing λ, the analytical focal equation for any isomass-to-charge ion pair is:

$$D = 2\sqrt{s_1\lambda + d}\sqrt{s_2\lambda + d}\left[1 + \frac{(1-\lambda)\left(\sqrt{s_1\lambda + d} + \sqrt{s_2\lambda + d}\right)}{\lambda\left(\sqrt{s_1\lambda} + \sqrt{s_2\lambda}\right)}\right] \tag{2.4.22}$$

This is a mass independent expression for the focal distance and reduces to the Wiley & McLaren focusing constraint (2.3.5) when the finite initial spatial separation δs converges to a single starting position. Furthermore, as the size of the second electric field converges to that of the first $(\lambda = 1)$, the system becomes equivalent to the single stage case and the focusing condition reduces to that for the single stage configuration, $D = 2\sqrt{s_1 s_2}$.

For the single stage system, the optimum distance for finite size spatial distributions with zero initial velocity is determined by the two extreme starting positions, as shown by Eq. (2.4.15). Extending the analysis to the two stage configuration requires Eq. (2.3.5) to be solved for s_i, a rather unattainable task. However, Eq. (2.4.22) defines the optimum distance and can readily be validated numerically. The focal point of the extreme ion pair defines the optimum detector distance and can also be deduced by setting $t(s_1) = t(s_2)$.

The focusing condition (2.4.22) considers a finite spatial separation, symmetrically surrounding the s_i position, situated at the centre of the spatial spread. The deviation between Eq's. (2.4.5) and (2.4.22) is demonstrated by the following numerical example for a series of initial spatial separations, shown in Figure 2.12. Considerable deviations between the two "optimum" focal distances are observed for the lower values of λ and consequently for the greater values of D. The further the focal point is located from the acceleration region the greater the deviation between the two optima. A decrease in the initial spatial separation δs reduces the difference which becomes negligible when δs converges to single starting position. The deviation effectively vanishes when the system satisfies second-order focusing conditions.

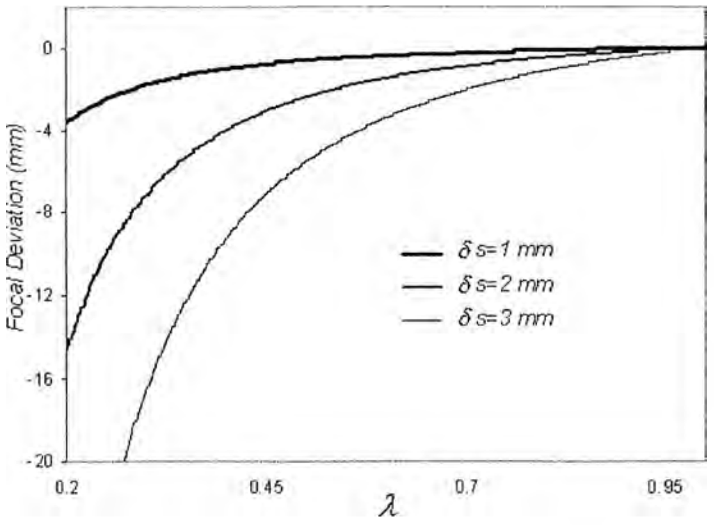

Figure 2.12 Deviation in the focal distance as calculated by equations (2.4.5) and (2.4.22) as a function of λ for a fixed acceleration configuration (s=10 mm, d=50 mm, s_o=5 mm). For the second order geometry λ=0.938 and the difference vanishes.

The ratio of the acceleration distances, s/d, is an important instrument parameter and has not been given the appropriate attention in the literature. Further comparison between the two theories shows that the deviation in the optimum operating conditions is enhanced for $s < d$. The case for which $s > d$ exhibits a less pronounced effect. In addition, for a fixed s/d ratio, the deviation is reduced as initial ion positions shift towards the back plate. A numerical example to quantify the discrepancy between the *W&M* solution and the ion-pair approach is given. The relative adjustment in the electric fields required to project the focal point to the detector situated at $D = 1\ m$ can exceed 100 V when the total energy of the system is 3 kV. The correction increases linearly with acceleration voltage.

2.4.4 Focal Distribution

The ion pair method identifies a focal region with well-defined limits along the mass analysis axis. Within the focal region, pairs of ions exhibit isochronous flight times but their individual focal points are dispersed in time. For the single stage system the dimensions of the focal region are determined either analytically, in terms of the time spread of the ions and Eq. (2.4.15), or by using two ion pairs, each pair at the front and back extremes of the spatial distribution respectively. The spatial extent over which focusing occurs is $\delta D = |D_1 - D_2|$, where $D_1 = \lim_{s_i \to s_1} D$ and $D_2 = \lim_{s_i \to s_2} D$. In the two-stage case, D is determined by Eq. (2.4.22). The optimum focal distance D and the associated width of the focal region (error bars) for a predefined acceleration geometry are shown as a function of λ in Figure 2.13. The focal width δD is a function of λ and shows a minimum at a particular field-free distance. This distance coincides with the second-order space focus as defined by the simultaneous Eq's (2.3.5) and (2.3.9). Figure 2.14 shows the "density" of the ion pair focal points as a function of distance for first and second-order geometries. The width of the focal region is considerably reduced when the system variables satisfy second-order focusing conditions. The focal aberration introduced by the finite initial spatial spread of the ions is reduced for systems tuned to the second-order.

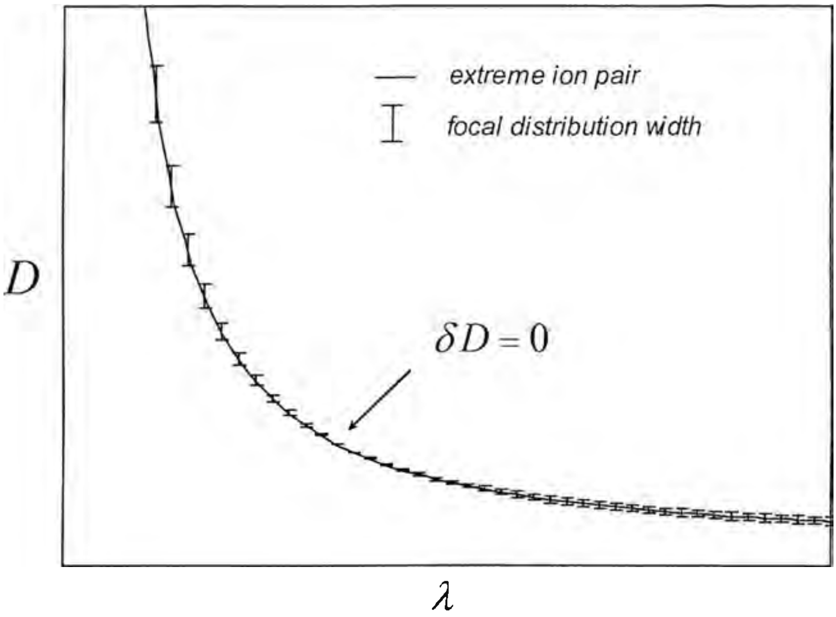

Figure 2.13 The optimum focus for a two stage system with a defined acceleration configuration as determined by the ion pair approach and equation (2.4.22). The focal distance and the focal width shown using error bars are both functions of λ.

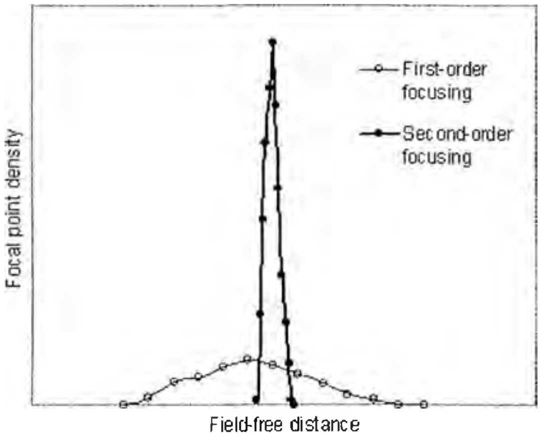

Figure 2.13 Structure of the focal regions for first and second-order focusing conditions. Under first-order conditions focusing occurs over a wide region. Ion pairs are brought into focus over a narrower region along the time-of-flight axis when second-order focusing is achieved.

Second-order focusing conditions impose geometrical restrictions on the dimensions of two-stage TOF spectrometers. Second-order focusing is realized when reflectrons are incorporated and a virtual source is required in order to enhance resolution.

Miniature linear mass spectrometers designed according to the principles of second-order focusing have not been implemented since the time-of-flight is generally considered too short. This is however a misconception and experimental results presented in this work demonstrate that resolution can be maintained, if not further enhanced, as the detector is displaced to shorter distances. The shorter flight times are compensated by the reduced time spread of the ions. The latter argument is supported by the principles of space focusing and variations in the dimensions of the focal region, qualitatively addressed in Figure 2.13.

The effect of the acceleration configuration on the size of the focal region, for first-order TOF systems, is illustrated in Figure 2.14. As the length of the first electric field increases relative to the second, while the total acceleration length and the focal distance are fixed, the width over which focusing occurs is reduced. For the $s > d$ configuration the focal region is compressed and the local density of ion-pair focal points at a particular plane increases. A preferred configuration for first-order space focusing is thereby identified, $s > d$. It should be noted that the $s > d$ configuration has the ability to project the second-order focal point to longer distances.

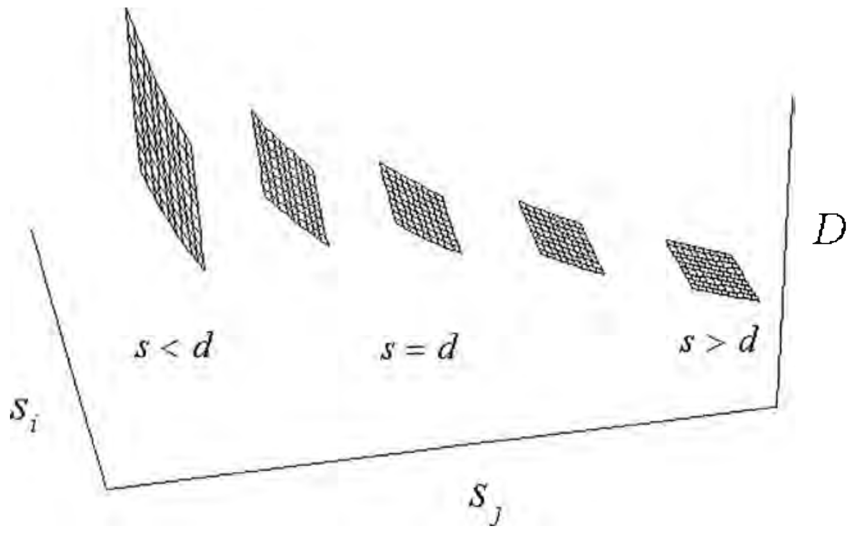

Figure 2.14 First-order focusing and the distribution of focal points for the series of two-stage acceleration geometries. The graph shows the higher degree of space focusing for the $s > d$ geometry. A measure of the degree of space focusing is the spread of the focal points in the direction of the vertical axis D.

2.5 Remarks and Discussion

Focusing in TOF MS relies on the ability of the system to provide ions with a distribution in initial electric potential energies. The fundamental focusing property of the TOF mass analyzer was theoretically demonstrated by Wiley & McLaren in 1955, for ions with zero initial velocity and was termed space focusing (Wiley & McLaren, 1955). The analysis is developed on the basis of a *Taylor* series expansion of the time-of-flight equation. The truncated series provides an approximate analytical solution for the arrival time distribution. The coefficients in the series are evaluated for a single starting position (the mean of the spatial distribution) and the focusing condition identifies a unique focal point along the mass analysis axis. The existing theory describes focusing as an ideal instantaneous property of the system.

Focusing is a result of the spatial distribution of the ions prior to their acceleration (when static or uniform/linear time-dependent fields are employed). The focusing conditions must therefore incorporate information of real size distributions. Our discussion on ion-pairs and their individual focal points demonstrated the existence of a finite region over which focusing occurs. The achromatic aberrations (mass independent focusing) introduced by finite size distributions are evaluated by the dimensions of the focal region. The error associated with the truncated *Taylor* series is discussed.

The validity of the space focusing concept is questionable when a real situation is considered. Space focusing is generally accepted to be applicable in cases where the spatial spread of the ions dominates over the initial velocity distribution. Historically, space focusing conditions provide a reference point for determining the "optimum" electric field ratio in predefined two-stage geometries, followed by trial and error to optimize the system experimentally and maximize resolution. The discrepancy between theory and experiment, among other things, is largely due to the absence of initial ion velocities and is demonstrated in Chapter 6.

Concluding, focusing in TOF MS is not instantaneous as implied by the existing theoretical analysis. Preferred acceleration geometries are identified that minimize the aberrations introduced by a finite initial spatial distribution of ions. General focusing conditions are provided through rigorous analytical solutions of the ion pair model.

Chapter 3

Focusing in Laser Desorption

3.1 Velocity Focusing

Mass resolution in Time-of-Flight Mass Spectrometry (TOF MS) is mainly determined by the set of initial conditions during ion formation. The orthogonal extraction technique has succeeded in decoupling the conditions in the source from the initial spatial and velocity spreads of the ions for the TOF experiment. Orthogonal systems however exhibit low duty cycles as well as mass discrimination effects. Direct linear systems do not suffer from these difficulties but exhibit poor velocity focusing properties. Their enhanced sensitivity is therefore counterbalanced by their low resolution.

The use of reflectrons has partially corrected for the kinetic energy spread of the ions in the source. Reflectron designs are specific to the ionization technique employed and the overall geometry of the instrument. In contrast with the simple case of space focusing, velocity or kinetic energy focusing requires a more detailed analysis, since an assumption for the initial ion distributions has to be made. Spatial and energy distributions are inherent to the mechanism of ion formation and can differ significantly between sources. In addition, reflectrons require the presence of a virtual source in the field-free region. The ability of a two-stage configuration to provide such a focal point is therefore essential to the operation and performance of the instrument.

To achieve space focusing, we have shown that spatially distributed ions, with zero initial ion velocity, are provided with a distribution in potential energies. The turn-around time, introduced for gas phase ionization methods and used as an upper limit for the maximum resolving power, cannot be corrected with static fields. Initial ion kinetic energies can be partially compensated by forming the ions in a relaxed electric field and allowing them to rearrange their positions with their nascent velocities during a predefined time interval. During this interval ions redistribute in space and obtain a correlation between starting positions and velocities prior to the application of the extraction pulse. The method was introduced in the early days of TOF MS (Katzenstein and Friedland, 1955) and formulated into the time-lag focusing technique (Wiley & McLaren, 1955). Delayed extraction is an extension of this method to laser desorbed ions. A correlation between starting positions and initial ion velocities results in mass-dependent focusing conditions. The concept of space-velocity correlation focusing in MALDI TOF MS was essential to the work presented in this thesis and a full account of the theory is presented. Ion pairs are then introduced and the analysis is extended to the space domain. Chromatic aberrations (mass dependent imperfect focusing) in MALDI TOF MS are investigated.

3.1.1 Single Stage Instrument with Delayed Extraction

In TOF mass spectrometers employing laser ionization at surfaces, the newly formed ions enter the gas phase with a common velocity distribution. Ideally, all ions start from the same equipotential plane. Under prompt acceleration conditions they fall through the same potential difference and no focusing is allowed since the faster ions are the first ones ejected into the field-free region. In the absence of an electric field, ions rearrange their positions according to their nascent velocities. At the end of the time delay, defined by the electric field pulse, the initial velocity spread of the ions is converted into a correlated distribution in electric potential and kinetic energies. The time-lag provides the initially slower ions with greater final kinetic energies and allows for focusing to occur. Figure 3.1 shows a single ion with initial velocity u_i and its position before and after the time delay in a single stage TOF system. Considering the mean velocity of a single ion along the mass analysis axis, at the end of the time delay τ the displacement is $\delta x = u_i \tau$. The starting position for the accelerating motion relative to the grid is $s_i = s - \tau u_i$.

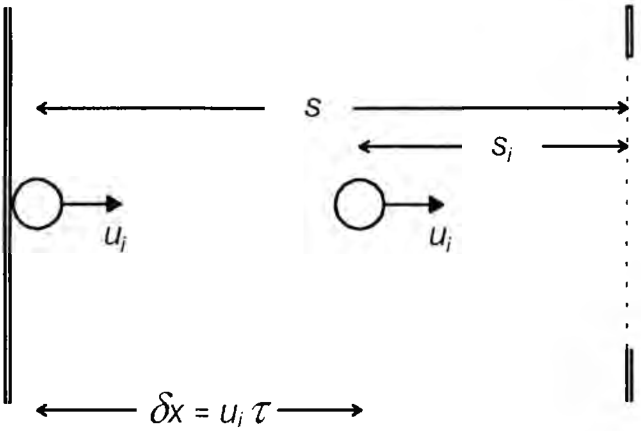

Figure 3.1 Initial conditions in a single stage acceleration system and the ion position before and after the time delay. The starting position for the subsequent acceleration motion is a function of the ion's initial position, initial velocity and the length of the time delay.

The application of the electric field pulse provides the starting signal for the time-of-flight experiment. The ion is ejected into the field-free region with its final velocity:

$$u_s = \sqrt{u_i^2 + 2s_i a_s} \tag{3.1.1}$$

For the single stage system the acceleration and field-free flight times are, respectively:

$$t_s = \frac{\sqrt{u_i^2 + 2s_i a_s} - u_i}{a_s} \tag{3.1.2}$$

$$t_D = \frac{D}{\sqrt{u_i^2 + 2s_i a_s}} \tag{3.1.3}$$

where $s_i = s - u_i \tau$ correlates the initial ion position s_i and nascent velocity u_i with the length of the time delay τ. In space-velocity correlation focusing, optimum conditions are identified by setting the first coefficient of the *Taylor* expansion to zero, $\partial t / \partial u_i = 0$ (Vestal & Juhasz, 1998), in accordance with the original method for space focusing ions (Wiley & McLaren, 1955). The existence of the mass dependent stationary point in the arrival time distribution of the ions with respect to initial ion velocity was first reported in a numerical analysis (Colby *et al*, 1994). An alternative approach is to eliminate the mean initial velocity term from Eq. (3.1.2) and (3.1.3) and evaluate the rate of change in arrival times with respect to the mean starting position s_i, at the end of the time delay:

$$\frac{\partial t_s}{\partial s_i} = \frac{(\tau a_s - u_i) + \sqrt{u_i^2 + 2s_i a_s}}{\tau a_s \sqrt{u_i^2 + 2s_i a_s}} \tag{3.1.4}$$

$$\frac{\partial t_D}{\partial s_i} = -\frac{D(\tau a_s - u_i)}{\tau \left(u_i^2 + 2s_i a_s\right)^{3/2}} \tag{3.1.5}$$

The longer the acceleration distance (for a given acceleration voltage), the greater the acceleration time and the kinetic energy in the field-free region, since

$\partial t_s / \partial s_i > 0$. The field-free path is a catch-up region for the ions, since $\partial t_D / \partial s_i < 0$. Setting the total partial derivative of the time-of-flight equation to zero, the first-order focusing constraint can be solved to give the optimum field-free distance as a function of instrumental parameters:

$$D = \frac{(u_i^2 + 2s_i a_s)(\tau a_s - u_i + \sqrt{u_i^2 + 2s_i a_s})}{a_s(\tau a_s - u_i)} \tag{3.1.6}$$

Introducing the "correlated velocity" $u_c = \tau a_s - u_i > 0$ and substituting for the ion's drifting velocity u_s, the first-order space-velocity correlated (svc) focusing condition is simplified:

$$D = \frac{u_s^2}{a_s}\left(1 + \frac{u_s}{u_c}\right) \tag{3.1.7}$$

In the derivation process it is assumed that a single average initial ion velocity is constant over the whole mass range. For the MALDI experiment this has been shown to be valid (Beavis & Chait, 1991). Figure 3.2 shows the mass dependent focusing properties of the system. A single m/z ratio is brought into focus at a distance defined by Eq. (3.1.7).

In contrast with the geometrical restrictions imposed by space focusing, the focal point in this case can be adjusted externally by either scanning the applied voltage or the time delay. For a constant accelerating voltage V_s, variations in the time delay can bring different m/z into focus at fixed distance. Relatively small fractional variations in the time delay can scan a broader mass range. For a fixed detector distance, voltage and time delay are coupled when a single m/z is considered.

It has been demonstrated that the optimum time delay is proportional to the square root of the ions mass, $\tau \propto \sqrt{m}$ (Colby & Reilly, 1996). Numerical simulations however show that the optimum time lag depends on the geometry of the system and that $\tau \propto m^n$, where $0.5 < n < 0.7$. Figure 3.3 shows the optimum time delay as a function of the m/z ratio for a fixed TOF geometry and two different applied voltages. The stronger the applied electric field the shortest the time delay required to project ions in focus to the appropriate distance. Increased accelerating voltages can significantly reduce the arrival time spread of the ions with an overall enhancement in resolution despite the shorter flight times (Whittal & Liang, 1995; Brown & Lennon, 1995).

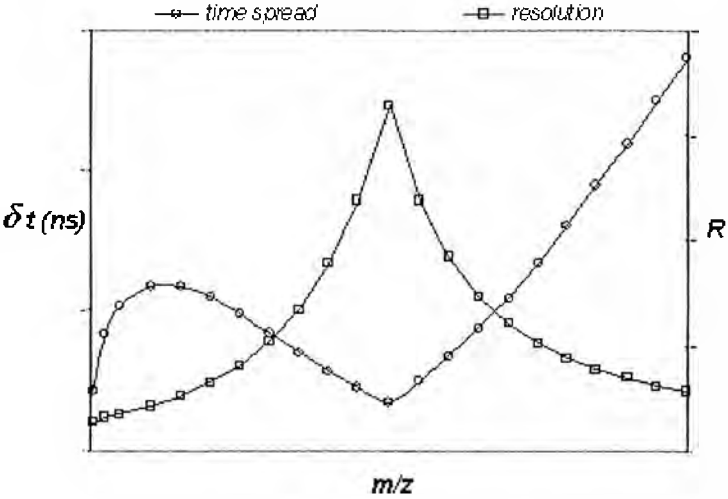

Figure 3.2 Arrival time spread and resolution as a function of mass-to-charge ratio. A single mass-to-charge ratio satisfies the first-order svc focusing condition.

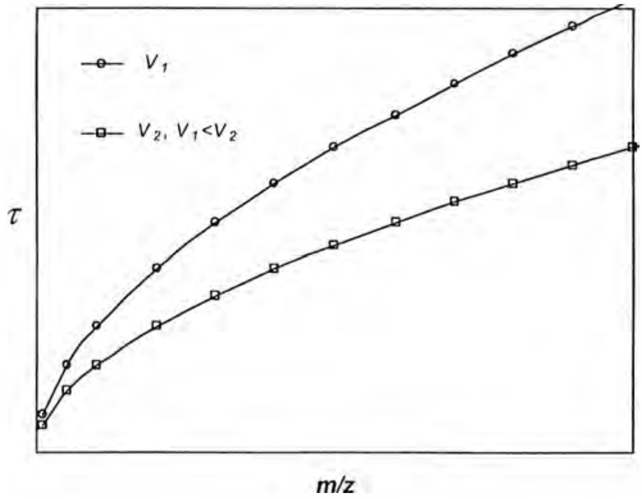

Figure 3.3 The optimum time delay that satisfies first-order svc focusing is approximately proportional to the square root of the mass-to-charge ratio.

A third-order approximation for the remaining time spread of the ions under first-order focusing is:

$$\delta t = \frac{(s_j - s_i)^2}{2}\frac{\partial^2 t}{\partial s_i^2} + \frac{(s_j - s_i)^3}{6}\frac{\partial^3 t}{\partial s_i^3} \tag{3.1.8}$$

The third-order terms gives precision down to a few *pico*-seconds. Extending the analysis to second-order focusing, the partial derivatives to be determined are:

$$\frac{\partial^2 t_s}{\partial s_i^2} = -\frac{\tau^2 a_s - 2s}{\tau^2 (u_i^2 + 2s_i a_s)^{3/2}} \tag{3.1.9}$$

$$\frac{\partial^2 t_D}{\partial s_i^2} = \frac{3D(\tau a_s - u_i)^2 - D(u_i^2 + 2s_i a_s)}{\tau^2 (u_i^2 + 2s_i a_s)^{5/2}} \tag{3.1.10}$$

The focusing condition is obtained by setting the total second-order partial derivative to zero:

$$D = \frac{(\tau^2 a_s - 2s)(u_i^2 + 2s_i a_s)}{3(\tau a_s - u_i)^2 - (u_i^2 + 2s_i a_s)} \tag{3.1.11}$$

Introducing the "correlated distance" $s_c = \tau^2 a_s - 2s$ the last expression is simplified:

$$D = \frac{s_c u_s^2}{3u_c^2 - u_s^2} \tag{3.1.12}$$

Second-order focusing is achieved when both focusing conditions (3.1.7) and (3.1.12) are satisfied. The system to be solved contains six independent variables in two equations. For an arbitrary set of instrumental dimensions and a given initial average ion velocity and m/z ratio, the remaining system variables (time delay and applied voltage) cannot be tuned to the second-order. Second-order, single stage MALDI TOF designs impose geometrical restrictions (Vestal & Juhasz, 1998). The focusing condition is m/z dependent and therefore the arrival time distribution will exhibit a point of inflection for a very narrow mass range.

3.1.2 Two Stage Instrument with Delayed Extraction

The addition of a second electric field introduces two more variables, the acceleration distance d and the voltage drop across the second field, V_d. In a time-lag experiment, the two stage configuration decouples the time delay from the total energy of the system *i.e.*, a range of time delays can be applied and first-order focusing can be satisfied by adjusting the electric field ratio, V_s / V_d while the total acceleration voltage is constant. This is in contrast with the single stage geometry where variations in the time delay require that the system provides the ions with different final energies to achieve first-order focusing at a fixed distance.

The velocities of the ions at the end of each acceleration region are given by, respectively:

$$u_s = \sqrt{u_i^2 + 2s_i a_s} \tag{3.1.13}$$

$$u_d = \sqrt{u_i^2 + 2s_i a_s + 2da_d} \tag{3.1.14}$$

where s_i is the post time-lag starting position for all ions, $s_i = s - \tau u_i$. The ion flight times in a two-stage system are respectively:

$$t_s = \frac{\sqrt{u_i^2 + 2s_i a_s} - u_i}{a_s} \tag{3.1.15}$$

$$t_d = \frac{\sqrt{u_i^2 + 2s_i a_s + 2da_d} - \sqrt{u_i^2 + 2s_i a_s}}{a_d} \tag{3.1.16}$$

$$t_D = \frac{D}{\sqrt{u_i^2 + 2s_i a_s + 2da_d}} \tag{3.1.17}$$

The derivatives are similarly evaluated with respect to the mean starting position, s_i:

$$\frac{\partial t_s}{\partial s_i} = \frac{u_c + u_s}{\tau a_s u_s} \tag{3.1.18}$$

$$\frac{\partial t_d}{\partial s_i} = -\frac{u_c (u_d - u_s)}{\tau a_d u_s u_d} \tag{3.1.19}$$

$$\frac{\partial t_D}{\partial s_i} = -\frac{D u_c}{\tau u_d^3} \tag{3.1.20}$$

Setting the total partial derivative of the time-of-flight to zero, $\partial t / \partial s_i = 0$, first-order focusing in two stage systems is expressed as:

$$D = \frac{u_d^3}{a_s}\left(\frac{1}{u_s} + \frac{1}{u_c}\right) - \frac{u_d^3}{a_d}\left(\frac{1}{u_s} - \frac{1}{u_d}\right) \tag{3.1.21}$$

The two stage system has the additional property that variations in the time delay can be compensated by variations in the voltage ratio, $\xi = V_s / V_d$, while the total acceleration voltage is constant. An optimum time delay can therefore be identified, for a particular m/z value. For this time delay, the arrival time spread of the ions is minimized as shown in Figure 3.4. The focused mass range is also enhanced. The optimum delay is shifted to greater values when greater m/z ratios are considered.

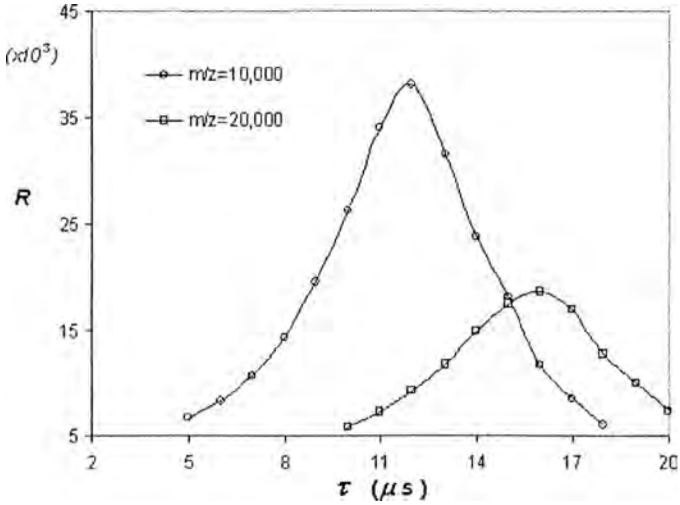

Figure 3.4 Resolution as a function of the optimum time delay for two different m/z ratios under first order focusing. The focusing condition is satisfied by adjusting the applied voltages while the total energy of the system is fixed at 16 keV. There is an optimum m/z dependent time delay where the time spread is minimized. The simulation parameters are *s=4 cm, d=5 cm, D=1 m, u_i=650 ms^{-1}*.

Figure 3.5 shows the effect of total acceleration energy for a single m/z ratio. As the final kinetic energy of the ions is increased the improvement in the time spread compensates for the shorter flight times and the resolving power of the system is maximized. The optimum time delay is reduced as the voltage drop across the two-stage configuration is increased.

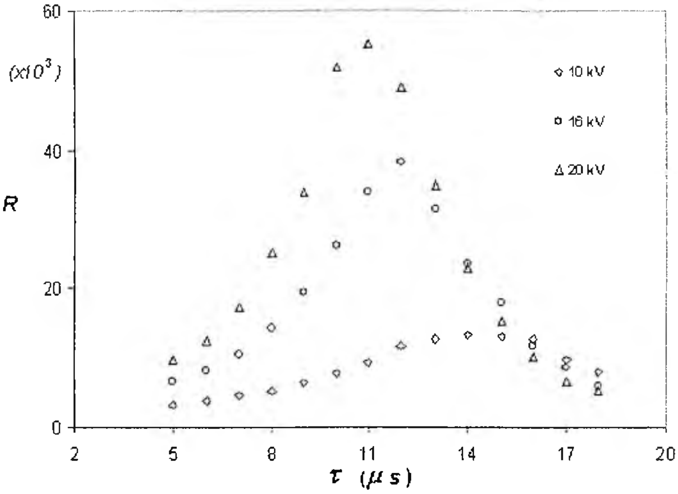

Figure 3.5 Resolution as a function of the time delay for m/z = 10,000. As the final kinetic energy of the ions is increased the resolving power is enhanced. For this single m/z value the optimum time delay is shifted to lower values for the greater voltages applied.

The second-order partial derivatives are:

$$\frac{\partial^2 t_s}{\partial s_i^2} = -\frac{u_c^2 - u_s^2}{\tau^2 a_s u_s^3} \tag{3.1.22}$$

$$\frac{\partial^2 t_d}{\partial s_i^2} = \frac{u_c^2 - u_s^2}{\tau^2 a_d u_s^3} - \frac{u_c^2 - u_d^2}{\tau^2 a_d u_d^3} \tag{3.1.23}$$

$$\frac{\partial^2 t_D}{\partial s_i^2} = \frac{D(3u_c^2 - u_d^2)}{\tau^2 u_d^5} \tag{3.1.24}$$

and the additional requirement for second-order focusing conditions to be satisfied is:

$$D = \frac{s_c u_d^5 (a_d - a_s) + u_s^3 u_d^2 (u_c^2 - u_d^2)}{a_d u_s^3 (3u_c^2 - u_d^2)} \tag{3.1.25}$$

As with the single stage system, second-order focusing can be realized only for a very narrow mass range. Although the time spread for the focused m/z is superior compared to first-order conditions, the focused mass range is not necessarily wider.

3.1.3 *Energy Focusing in Linear TOF MS*

The mathematical formulation of space-velocity correlation focusing is equivalent to space focusing and the application of a *Taylor* series to a function of a single variable (Wiley & McLaren, 1955). In Chapter 2 it was demonstrated that space focusing is in practice potential energy focusing. A similar analysis shows that the theory of delayed extraction can equally be developed in terms of the initial kinetic and potential energies of the ions. Energy focusing in TOF MS unifies the concepts of space and velocity focusing.

In delayed extraction, the focusing condition was originally developed by evaluating the rate of change of the arrival time of the ion with respect to initial position. The original analysis considered the rate of change in the arrival flight times with respect to initial ion velocity (Vestal & Juhasz, 1998). For the single stage system the first partial derivatives are respectively:

$$\frac{\partial t_s}{\partial u_i} = -\frac{\tau a_s - u_i + \sqrt{u_i^2 + 2 s_i a_s}}{a_s \sqrt{u_i^2 + 2 s_i a_s}} \qquad (3.1.26)$$

$$\frac{\partial t_D}{\partial u_i} = \frac{D(\tau a_s - u_i)}{(u_i^2 + 2 s_i a_s)^{3/2}} \qquad (3.1.26)$$

The partial derivative for the first electric field is a negative quantity, $\partial t_s / \partial u_i < 0$. The acceleration time decreases with increasing velocity since the forward displacement during the time delay is greater. The faster moving ions have less distance to travel after the time-delay and will therefore acquire less kinetic energy as they traverse the first electric field. The partial derivative for the field-free region is a positive quantity, $\partial t_D / \partial u_i > 0$. The flight time increases with the initial velocity of the ions, as a result of the lower initial potential energies that the ions are found with at the end of the time delay. Lower potential energies result in lower kinetic energies at the beginning of the field-free ion motion. In general, since $s_i = s - \tau u_i$, then:

$$\frac{\partial t}{\partial s_i} = \frac{\partial t}{\partial(s - \tau u_i)} = -\frac{1}{\tau}\frac{\partial t}{\partial u_i} \tag{3.1.27}$$

$$\frac{\partial^2 t}{\partial s_i^2} = \frac{1}{\tau^2}\frac{\partial^2 t}{\partial u_i^2} \tag{3.1.28}$$

The delayed extraction analysis can be expressed entirely in terms of energy. For the single stage system, the focusing condition can either be evaluated from the time-of-flight equation by correlating initial kinetic and potential energy according to, $T_i = m/2\tau^2[s-(U/q\mathcal{E}_s)]^2$, and taking the derivative with respect to U, or simply by using that $U = q\mathcal{E}_s s_i$:

$$\frac{\partial t}{\partial U} = \frac{\partial t}{\partial(q\mathcal{E}_s s_i)} = \frac{1}{q\mathcal{E}_s}\frac{\partial t}{\partial s_i} \tag{3.1.29}$$

The focusing conditions can then be derived by setting the total partial derivative to zero, $\partial t/\partial U = 0$.

3.2 Ion-Pair Analysis of the Delayed Extraction Technique

Irregularities on the sample surface give rise to a small but finite spatial spread of the ions generated on a planar surface. The ion pair analysis allows for this spread to be incorporated in the focusing properties of the system and identifies a lower limit for the length of the time delay. With reference to Figure 3.6, an ion pair defines the extremes of the ionization volume at a surface. The spatial spread of the ion pair δs_i, is also characterized by the maximum velocity spread, $\delta u = u_2 - u_1$, so that the extreme case is considered in the desorption process. The fastest and the slowest ions define the back and the front extremes of the spatial volume respectively. The time delay must be sufficiently long to allow for the fastest ion to overcome the slowest otherwise correlation between position and velocity cannot be achieved. A minimum time delay, $\tau_{\min} > \delta s_i / \delta u$, is therefore imposed by the spatial and velocity distributions following the ionization event. For a $100\ \mu m$ initial spatial spread and a velocity spread of the order of $1000\ ms^{-1}$, the minimum time delay is $100\ ns$. The spatial spread of the ions at the end of the time delay is then defined by $\delta s = \tau \delta u - \delta s_i$.

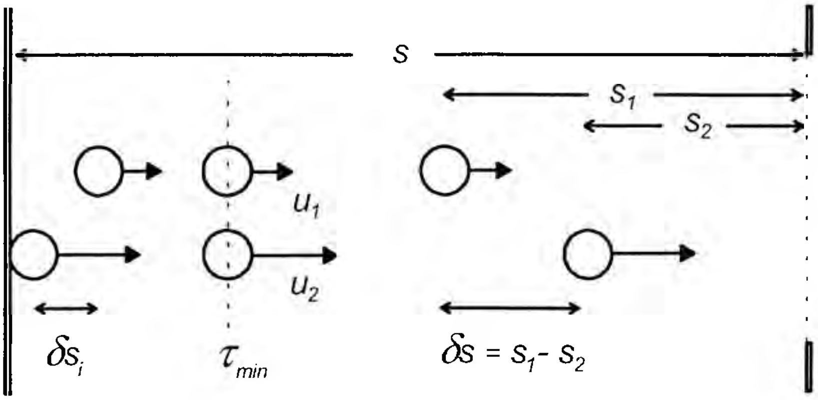

Figure 3.6 The maximum initial spatial and velocity spread at the time of ion formation sets a lower limit to the length of the time delay.

3.2.1 Single Stage System

The trajectories of three isomass-to-charge ion pairs in terms of the distance traveled as a function of time are shown in Figure 3.7. The curve designated A represents two ions with a velocity spread undergoing prompt acceleration. Focusing is impossible since they fall through the same potential difference. B and C indicate the mass-dependent focal point of two isomass-to-charge ion pairs. Focusing can only occur if the ions are provided with a distribution in electric potential energy, in this case correlated with their initial velocities.

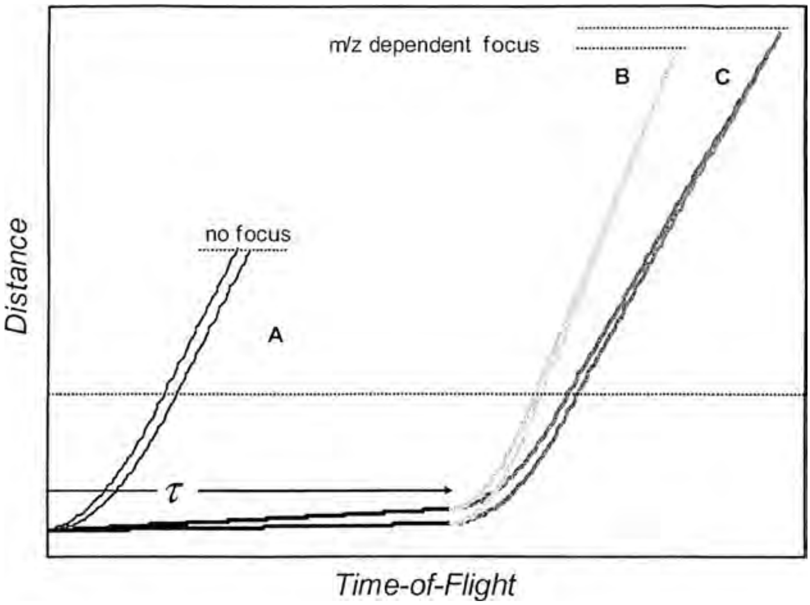

Figure 3.7 Time-distance trajectories of ions pairs in a single-stage system. The first ion pair A undergoes prompt acceleration. Ion pair B is dispersed during the time delay and brought into focus in the field-free region. A third ion pair C with different m/z ratio and the same velocity spread illustrates the mass dependent focusing property (chromatic aberration) of the system.

At the end of the time delay τ the spatial spread of the ions is defined by the two extreme ions and their final velocities at the end of the electric field are respectively:

$$u_{s1} = \sqrt{u_1^2 + 2a_s(s - \tau u_1)} \quad (3.1.30)$$

$$u_{s2} = \sqrt{u_2^2 + 2a_s(s - \tau u_2)} \quad (3.1.31)$$

The acceleration times for the ion pair are respectively:

$$t_{s1} = \frac{\sqrt{u_1^2 + 2a_s(s - \tau u_1)} - u_1}{a_s} \quad (3.1.32)$$

$$t_{s2} = \frac{\sqrt{u_2^2 + 2a_s(s - \tau u_2)} - u_2}{a_s} \quad (3.1.33)$$

where a_s is the constant acceleration experienced by the ions through the electric field. The focal point for the extreme ion pair in a single stage TOF configuration is:

$$D = \frac{u_{s1}u_{s2}}{u_{s1} - u_{s2}}(t_{s1} - t_{s2}) \tag{3.1.34}$$

And eliminating the acceleration times t_{s1} and t_{s2}, the focal point for an isomass-to-charge ion pair is:

$$D = \frac{u_{s1}u_{s2}}{a_s}\left(1 + \frac{\delta u}{u_{s1} - u_{s2}}\right) \tag{3.1.35}$$

Whilst in the case of space focusing there is a significant deviation between the *Taylor* expansion and the ion pair method in terms of their corresponding optimum distances, in delayed extraction this difference is negligible.

3.2.2 The Two Stage System

In a two stage system the ion pair undergoes a second acceleration step after traversing the first electric field. The flight times and ejection velocities for the first electric field are given in Eq. (3.1.30)-(3.1.33). The instantaneous velocities at the end of the second acceleration region are the remaining velocities of the ions throughout the field-free region:

$$u_{d1} = \sqrt{u_1^2 + 2a_s(s - \tau u_1) + 2da_d} \tag{3.1.36}$$

$$u_{d2} = \sqrt{u_2^2 + 2a_s(s - \tau u_2) + 2da_d} \tag{3.1.37}$$

The acceleration flight times through the second electric field of length d are respectively:

$$t_{d1} = \frac{\sqrt{u_1^2 + 2s_1a_s + 2da_d} - \sqrt{u_1^2 + 2s_1a_s}}{a_d} \tag{3.1.38}$$

$$t_{d2}=\frac{\sqrt{u_2^2+2s_2a_s+2da_d}-\sqrt{u_2^2+2s_2a_s}}{a_d} \tag{3.1.39}$$

where $s_1=s-\tau u_1$ and $s_2=s-\tau u_2$. The overall time-of-flight of the ions is determined by the drifting time through the field-free region D:

$$t_{D1}=\frac{D}{\sqrt{u_1^2+2s_1a_s+2da_d}} \tag{3.1.40}$$

$$t_{D2}=\frac{D}{\sqrt{u_2^2+2s_2a_s+2da_d}} \tag{3.1.41}$$

The focal point for the two extreme ions is:

$$D=\frac{u_{d1}u_{d2}}{u_{d1}-u_{d2}}\left(\frac{u_{s1}-u_{s2}+\delta u}{a_s}+\frac{u_{s2}-u_{s1}+u_{d1}-u_{d2}}{a_d}\right) \tag{3.1.42}$$

Eq. (3.1.42) can be applied to any isomass-to-charge ion pair within the finite initial space-velocity correlated distribution. The dimensions of the focal region are then $\delta D=|D_1-D_2|$, where $D_1=\lim\limits_{u_i\to u_1} D$ and $D_2=\lim\limits_{u_i\to u_2} D$ define the beginning and the end of the focal region respectively.

An example of the behaviour of the optimum time delay under first-order focusing conditions was provided in Figure 3.4. Figure 3.8 shows the distribution of ion pair focal points for a fixed two stage TOF geometry and a series of time delays. The starting positions of any ion pair are defined by the two horizontal axes. Their individual focal points (field-free distances) are projected onto the vertical axis providing a three-dimensional representation of the focal region. The range of D values for each time delay is a qualitative measure of the time spread of the ions at a particular distance. The range over which focusing occurs is proportional to the arrival time spread of the ions.

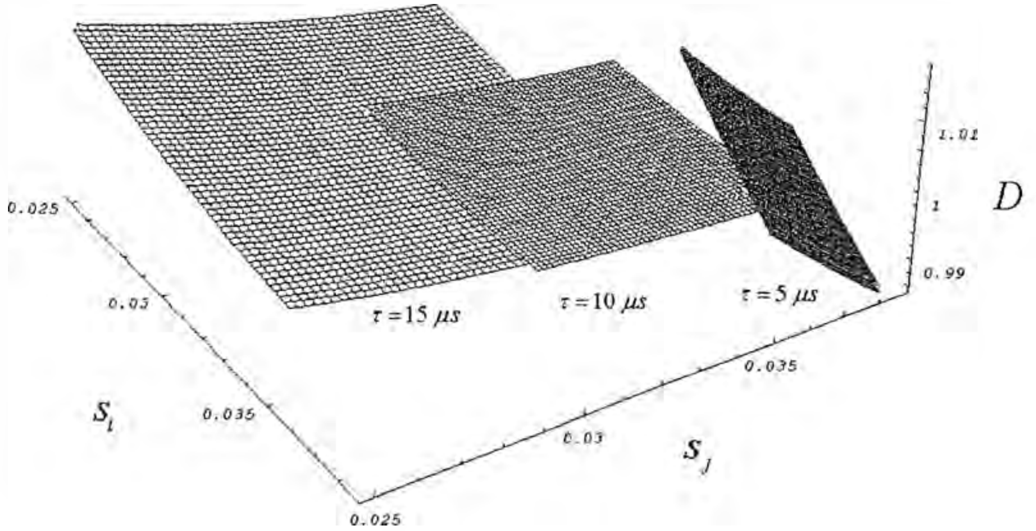

Figure 3.8 Distribution of ion pair focal points under first-order focusing for a series of time delays. Longer time delays increase the spatial spread of the ions and larger surface areas are obtained. The vertical spread of ion pair focusing shows the focal aberration, minimized for $\tau = 10\ \mu s$. For the longer and shorter time delays, the vertical spread of the focused ion pairs is greater and the arrival time distribution to a fixed distance is increased. The simulated parameters are $s=4$ *cm*, $d=2$ *cm*, $D=1$ *m*, $m/z=10{,}000$, $u_1=300\ ms^{-1}$, $u_2=1000\ ms^{-1}$, $V_{tot}=20\ kV$.

MALDI TOF systems satisfying second-order focusing conditions are rather difficult to implement and experimental results have not yet been reported in the literature. The probable reason for not constructing such a geometry is the complexity of the simultaneous equations and the great number of free variables to consider. Second-order focusing systems are considered herein and a method is presented to explore such optimum geometries theoretically.

Once the optimum time delay for first-order systems is computed, as discussed in Figures 3.4 and 3.8, the position of the detector can be displaced towards shorter distances until a point of inflection in the arrival time distribution of the ions is obtained at the mean position/velocity. This is the maximum distance to which the second-order focal point can be projected. An optimum configuration is therefore identified where the minimum time spread is obtained for a relatively longer field-free region and extended flight times. Any alterations in the acceleration geometry shift these properties of the system and the numerical analysis has to be performed from the start.

Further analysis of second-order two stage MALDI TOF instruments is made with reference to Figure 3.9. Following the numerical example presented in Figure 3.8, the distance of the second-order focal point is maximized for $\tau = 10\ \mu s$. As the time delay is reduced, the focal plane is projected to shorter distances and the optimum time spread is minimized. The time spread for $m/z = 10{,}000$ is presented on the left abscissa while the distance of the focal point to the right. Resolution can be further enhanced by increasing the voltage drop across the first field. Second-order conditions are then satisfied by reducing the time delay. For these shorter time delays the focal point is projected to shorter distances providing optimum virtual sources for reflecting geometries.

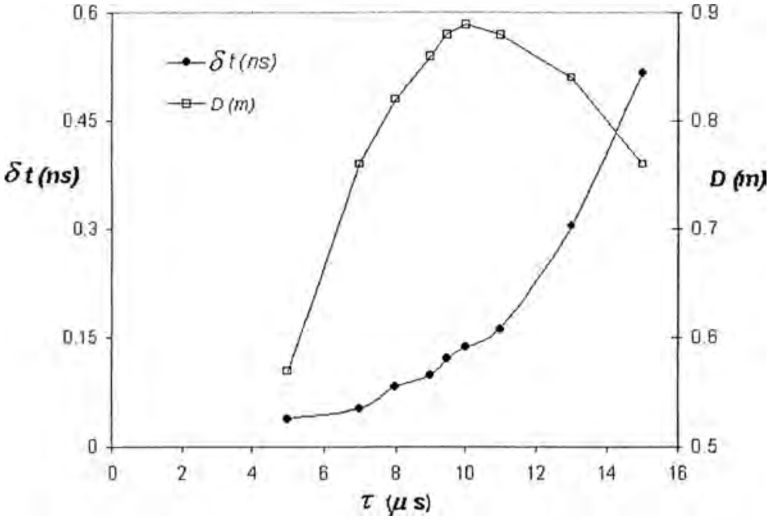

Figure 3.9 The arrival time spread of the ions under second-order focusing for a series of time delays. The length of the field-free region for which the time spread is computed is shown on the right vertical axis. The simulated parameters are *s=4 cm, d=2 cm, m/z=10000,* u_1*=300 ms*$^{-1}$*,* u_2*= 1000 ms*$^{-1}$*,* V_{tot}*=20 kV.*

The pulsed nature of the first electric field sets an upper limit on the maximum voltage that can be applied when three-electrode two stage systems are considered. The advantage of the $s < d$ acceleration configuration is that it allows short time delays to be used with relatively short extraction voltage pulses.

3.3 Remarks

The focusing properties of single and two-stage TOF MS with space-velocity correlated distributions, applicable to laser desorption ionization sources, have been developed. Optimum operating conditions are derived by setting the coefficients of the *Taylor* expansion over the starting position, to zero. The theory presented in this Chapter is a simplified version contrasted to the original theoretical analysis for MALDI instruments (Vestal & Juhasz, 1998). An additional characteristic demonstrated theoretically in this work is that the two stage system decouples the length of the time delay from the total acceleration voltage. The effect of the time delay on the final time spread can therefore be evaluated and an optimum time delay is identified. Although the duration of this delay is in the μs scale, which far exceeds the optimum values determined experimentally and found to be in the ns scale, it is an interesting theoretical argument for enhancing resolution. Optimum time delays are computed by both the *Taylor* truncation method and the ion pair model. The latter defines a lower limit of the order of $\sim 100\,ns$. Finally, a method is presented for studying second-order two stage geometries. The ability to provide quality virtual sources for reflecting systems and wider mass range focusing has been discussed.

Focusing in TOF MS relies on the ability of the system to provide ions with a distribution in initial electric potential energies. Energy focusing for MALDI TOF is developed in *Section 3.1.3*. The fundamental property of the TOF mass analyzer was theoretically demonstrated by Wiley & McLaren for ions with zero initial velocity and was termed space focusing (Wiley & McLaren, 1955). The concept of the truncated *Taylor* series is extended in the delayed extraction experiment, known as velocity focusing (Westal & Juhasz, 1998) and is also expressed in kinetic energy terms for optimizing reflecting geometries (Alikhanov, 1957; Karataev *et al*, 1972). Since space focusing and the space-velocity correlation technique can be put entirely into kinetic and potential energy terms as discussed above, the concept of energy focusing is a rather more accurate description in TOF MS. The analysis is extended to an isotropic distribution of ions in the next Chapter 4 and the missing formula of the original time-lag focusing theory is provided.

Chapter 4

A New TOF Theory

4.1 Space Velocity Correlation in Orthogonal TOF MS

Orthogonal Time-of Flight Mass Spectrometry (oTOF MS) can be considered as the latest major development in TOF instrumentation, and a very successful method for recording TOF spectra from continuous ion sources. The incorporation of the collision cell has greatly facilitated the interface of the oTOF mass spectrometer with atmospheric ion sources. Orthogonal TOF has become the favourite choice as the far end mass analyzer in hybrid instruments.

The formation of a low energy ion beam offers ideal starting conditions for high resolution experiments. Ideally, a slit provides a confined ion beam by reducing both the spatial extent of the ions and their initial velocity distribution along the TOF axis. The natural flight angle has greatly facilitated the incorporation of the reflectron. The undefeated advantage of oTOF instruments today is their ability to focus ions across the entire mass range, provided that monoenergetic beams are introduced into the orthogonal gate.

Since the reinvention of the technique in the late 1980's, the focusing properties in oTOF MS have been a subject of sporadic investigations. The significant reduction in ion energies orthogonal to the beam axis, and the dimensions of the slit prior to the orthogonal gate $(< 2\ mm)$, have established space focusing as the appropriate method for tuning the instrument. The focusing properties in oTOF have not been challenged by any theoretical analysis so far. An attempt is made herein to provide such a theoretical treatment and experimental results are presented in Chapter 6 to support the argument.

4.1.1 Theoretical Background

There are two basic concepts underlying the principles of operation of the oTOF analyzer. The first is the application of the space focusing theory. Space focusing provides an optimum set of voltages, specific to instrumental dimensions (Dawson & Guilhaus, 1989; Bondarenko & MacFarlane, 1997; Cotter, 1997; Guilhaus *et al*, 2000). In general, when the spatial spread of the ions dominates over their velocity distributions, time focusing is approximated with a *Taylor* expansion of the time-of-flight equation with respect to mean starting position. That is, the initial ion velocity is neglected and space focusing is applied. Second-order focusing conditions provide an optimum virtual source in the field-free region for a reflectron (Boesl, 1992). The application of space focusing cannot be justified since ions have thermal velocities, in addition to the energy transferred between the axes as they are directed through the ion optical system into the orthogonal gate. Velocity distributions can considerably limit the resolving power and especially alter the optimum operating conditions of the instrument.

The turn-around time is a mass dependent expression for the maximum contribution of the initial ion velocity to the final time spread of the ions and is given by (Wiley & McLaren, 1955):

$$\delta t = \frac{2mu_i}{q\mathcal{E}_s} \tag{4.1.1}$$

where u_i is the initial ion velocity of a mass m/q accelerating in an electric field $\mathcal{E}_s$. Eq. (4.1.1) is considered by many authors as an upper limit to the maximum resolving power in oTOF (Wollnik, 1993; Chen *et al*, 1999; Muradumov *et al*, 2003). The application of space focusing and the concept of the turn-around time are contradictory. An imperfect space focus (Chen *et al*, 1999) is a rather polite way of expressing the inapplicability of the focusing conditions adopted for orthogonal geometries.

An interesting relationship has been developed between space focusing theory and the turn-around time in terms of designing the orthogonal gate. To start with, the two stage geometry has to satisfy Eq. (4.1.1). The effect of the turn-around time can be reduced by increasing the electric field strength in the first field. There are two ways of doing so. The first is to increase the magnitude of both fields so that their ratio is fixed and space focusing is not violated. However, in this case the turn-around time is reduced at the expense of shorter flight times. The second and widely adopted method is to select the relative lengths s and d so as to maximize $\mathcal{E}_s$, while ions are space focused at a fixed distance. The preferred geometry in oTOF MS is a two stage system with $s << d$. Although this configuration has the additional advantage of reducing field penetration between the two consecutive electric fields, it also reduces the angle of approach to the grid separating the adjacent electric fields.

Scattering and significant loss in resolution is observed when the angle of approach to the grids deviates from the normal (Guilhaus *et al*, 2000). The effect is more pronounced in the early grids where the velocity of the ions is smaller and the ions spend more time accelerating through the non-linear fields (Selby *et al*, 2001). Another problem related to this particular configuration is the restriction imposed on the cross section of the ion beam. Wider slits and longer fields in the s dimension can accommodate wider spatial and velocity spreads and increase throughput.

Figure 4.1 shows a dc ion source and the orthogonal acceleration configuration gating the ions into the TOF mass analyzer. A continuous ion beam is transported through a lens and directed into the relaxed first field of a dual-stage extraction system. The lens corrects for the initial angle of divergence and generates a focal point at the region where ion extraction for mass analysis can take place. The lens minimizes the spatial dimension of the ion beam at the point of extraction. The final time spread at the detector is then defined by ions with opposite velocity vectors and overlapping positions *i.e,* the turn-around time.

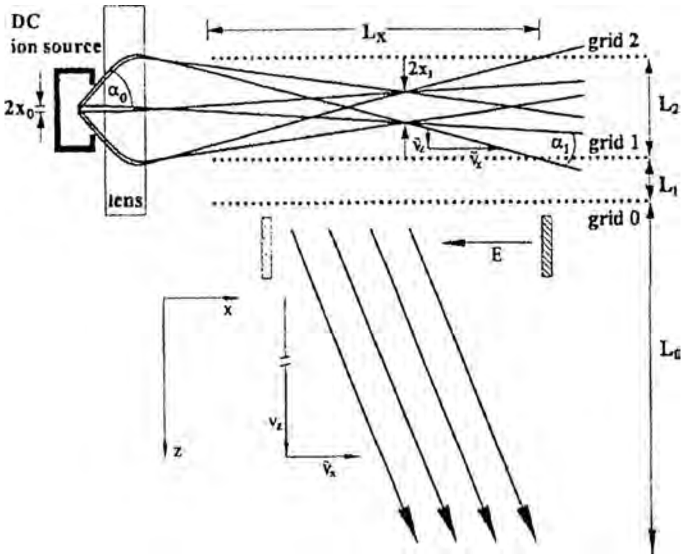

SOURCE: Wollnik, 1993

Figure 4.1 Orthogonal TOF MS operating with a dc ion source. The ion beam is transported through the lens into the orthogonal gate. The focal point of the source is projected at a region where ions are sampled into the TOF analyzer and detected. The spatial spread of the ions within the sampling region is therefore minimized and the final time spread is limited by the turn-around time.

The concepts of space focusing and turn-around time serve as the underlying principles for focusing to occur rather as accurate mathematical tools for optimizing a particular geometry. An exception is the extension of the time-lag concept to MALDI TOF MS. Correlation between initial positions and ion velocities has proved to be a valuable method for designing both linear and reflecting geometries. A similar concise theoretical analysis related to orthogonal TOF instrumentation has not been presented. Optimization considers the turn-around time effect for selecting the dimensions of the orthogonal gate, a rather rough estimation of the voltages according to the space focusing principles, and then a trial and error procedure to optimize the system experimentally.

4.1.2 The Argument

The projection of the source focal point into the effective region of the orthogonal gate introduces turn-around time effects. Ions that are spatially focused to a point into the first region of the orthogonal system have their initial velocity vectors along the TOF axis in opposite directions. The effect cannot be corrected by the pulsed extraction scheme and defines the minimum arrival time distribution at the detector. The angular divergence of the ion beam at the focal point can considerably increase the velocity of the ions in the TOF direction and further limit resolution. Even though the spatial spread can be made wide, the contribution of the initial ion velocity cannot be considered negligible. The focusing technique must address both distributions.

Focusing in TOF MS employing static or uniform time-dependent electric fields is practical when ions are provided with a distribution in their electric potential energies. Turn-around time effects can therefore be removed if ions obtain a spatial separation prior to their acceleration. The time-lag concept has successfully evolved into delayed extraction. Unfortunately in both cases time focusing is mass dependent. In the time-lag method ions start from a point source with equal energies. During the lag, the initial velocity spread transforms into a mass dependent spatial distribution, hence focusing condition. In delayed extraction, ions have a common velocity distribution and have the same spatial spread at the end of the delay. However, their initial kinetic energies are mass dependent and again only one mass can be brought into focus. Only a single m/z ratio can be time-focused at the detector plane.

A different situation arises with the orthogonal geometry. A point source with a mass independent isotropic distribution in initial energies is considered. The initial conditions are equivalent to those in the time-lag focusing experiment at the beginning of the time delay. In this case, the newly formed ions undergo prompt acceleration and are directed through the ion optics into a field-free region. A lens system is usually incorporated to correct for the initial angular divergence of the ions and produces an astigmatic focus at the source exit slit. The cross section of the ion beam at any distance thereafter, is a function of the angular divergence at the source focal point and the total energy of the ions. Considering the properties of the beam in the orthogonal direction, all ions will exhibit a time-dependent lateral spread and acquire a common spatial and kinetic energy spread, provided that enough time is allowed for the slowest ion to fill the orthogonal gate. The concept of a space-velocity correlated distribution is therefore introduced, specific to the orthogonal TOF geometry. A distinction is drawn between the time-lag concept and space-velocity correlation in oTOF MS. In the former case the spatial spread prior to the extraction pulse is mass dependent since the time lag is common for all masses. In the latter case, the arrival time of the ions at the effective region of the orthogonal system is mass dependent and a common spatial spread is obtained. The time dependence of the filling up mode of the orthogonal gate is responsible for the discrimination effects, as discussed in Chapter 1.

An analytical solution is developed based on a linearly correlated distribution in the following section. New insights into the focusing properties in oTOF MS are presented and evaluated by comparing the theoretical argument with experimental results. Linear and non-linear correlated functions are investigated. A SIMION[1] study reveals the ability of the ion optics to generate such correlated distributions at the effective region of the orthogonal gate. The analysis demonstrates the inapplicability of space focusing principles for optimizing orthogonal TOF MS and shows how the turn-around time aberration on the final time spread of the ions can be significantly reduced.

The theoretical argument is supported experimentally by comparing the focusing properties of an electron impact (EI) source and a thermal/surface ionization (TI/SI) source on the same oTOF analyzer. Results are presented in Chapter 6. The

---

[1] Dahl DA. and Delmore J.E., SIMION PC/PS2 v4.0, Idaho National Engineering Laboratory, Idaho Falls, ID 83415

different mechanisms of ion formation and variations between the two ion optical systems provide substantially different starting conditions for the TOF experiment. The difference in the applied voltage required to project the focal points to a fixed detector distance provides information on the initial conditions in the extraction region. The optimum operation of the system is determined by both the initial spatial and velocity spreads of the ions and these can be extrapolated from the experimental results. It is shown that the turn-around time, usually defined by time spread at the detector, can be an underestimation of the actual velocity distribution in the orthogonal direction.

First-order focusing conditions for a linear distribution using the ion pair approach were presented in the ASMS conference in 2004 (McMahon & Papanastasiou, 2004). First and second-order focusing conditions were derived by a composite *Taylor* expansion of the time-of-flight equation and are the main topic of this chapter. Theoretical and experimental findings were summarized in the 2005 ASMS conference (Papanastasiou & McMahon, 2005).

4.2 Linear Correlation

A schematic diagram of the orthogonal TOF geometry is shown in Figure 4.2. Ions formed in the source are directed by an ion optical system through an exit slit and into the orthogonal region. A correlated distribution for the TOF experiment can develop if ions are allowed to disperse according to their velocity vectors in the orthogonal direction. By projecting the source focal point before the orthogonal gate, the lateral dispersion of the ions is velocity dependent and the faster moving ones define the mass independent extreme starting positions prior to acceleration. Ideally, a linear correlation distribution between position and velocities is developed and shown in Figure 4.3.

Two main features are identified for the proposed mode of operation. The projection of the source focal point at the exit slit offers a unique advantage for maximizing ion throughput. The use of a narrow slit to define a low energy parallel beam with reduced spatial and velocity spreads is no longer a strict requirement. In addition, turn-around time effects are expected to be minimized since the focal point is established well before the effective region of the orthogonal geometry. The lateral dispersion provides ions with a spatial separation as they move towards the centre of the orthogonal gate. Ion pairs with opposite velocity vectors and overlapping positions at the source focal point move further apart and practically eliminate turn-around time effects in the oTOF MS. Once the ions are provided with a distribution in their initial electric potential energies, a focal point exists and can be projected at the detector plane by varying the electric fields. The symmetry of the lateral displacement is critical to the operational characteristics of the proposed configuration.

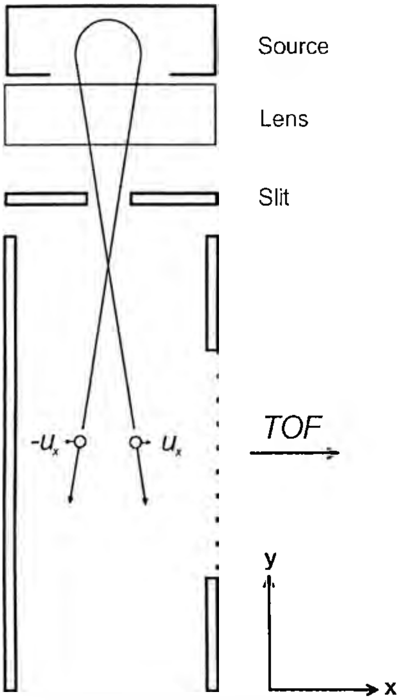

Figure 4.2 Simplified representation of the ion travel from the source through the ion optics and into the orthogonal region.

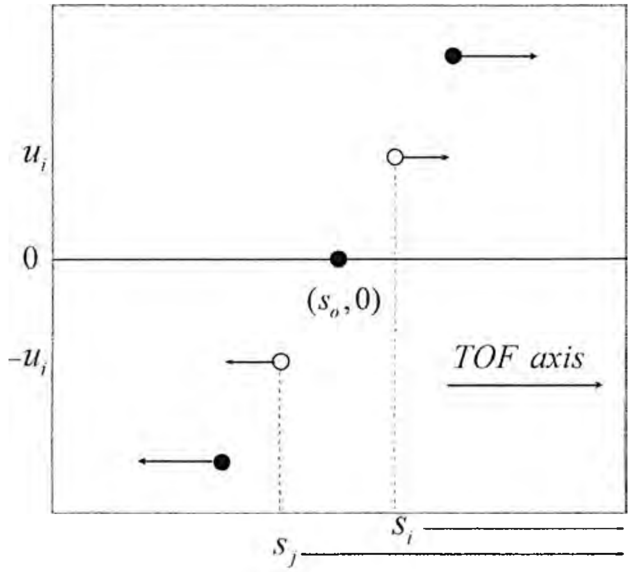

Figure 4.3 Linear space-velocity correlated distribution of the ions in the TOF axis.

The forward and backward correlated distributions are considered separately and the time-of-flight of the whole ion ensemble can be expressed by two ions with the mean position-velocities corresponding to each of the two distributions:

$$t = \begin{cases} t_i, & (s_i,\ u_i \geq 0) \\ t_j, & (s_j,\ u_j \leq 0) \end{cases} \tag{4.2.1}$$

where the i and j subscripts represent the ions in the forward and backward distributions respectively. Eq. (4.2.1) is a continuous function of the initial ion velocity since $\lim_{u_i \to 0} t_i = \lim_{u_i \to 0} t_j = t(s_o,\ 0)$ where $t(s_o,\ 0)$ is the time-of-flight of the *reference* ion with zero initial velocity that is accelerated over a distance s_o within the s field. Ions in the forward distribution undergo an accelerating motion once the extraction pulse is applied. In a two-stage acceleration geometry, the ith ion with the average velocity u_i accelerates over a distance s_i and the overall time-of-flight is:

$$t_i = \frac{u_{si} - u_i}{a_s} + \frac{u_{di} - u_{si}}{a_d} + \frac{D}{u_{di}} \tag{4.2.2}$$

where a_s and a_d are the constant accelerations experienced by the ions in the first and second electric fields of lengths s and d respectively. The position of the detector is defined by the length of the field-free region D. The velocities at the end of each electric field for the ith ion are:

$$u_{si} = \sqrt{u_i^2 + 2s_i a_s} \tag{4.2.3}$$

$$u_{di} = \sqrt{u_i^2 + 2s_i a_s + 2da_d} \tag{4.2.4}$$

The second distribution encompasses the ions with initial velocities in the opposite direction. The jth ion with the average velocity $u_j = -u_i$ decelerates, stops and accelerates back to its starting position. The subsequent motion in the first field is that of an ion with a starting velocity u_i accelerating over a distance s_j, $s_j > s_i$. It is this difference in the acceleration distances of the two ions considered that allows for focusing to occur. The time-of-flight of the jth ion is:

$$t_j = \frac{u_{sj} + u_i}{a_s} + \frac{u_{dj} - u_{sj}}{a_d} + \frac{D}{u_{dj}} \tag{4.2.5}$$

and the velocities at the end of the first and second electric fields are respectively:

$$u_{sj} = \sqrt{u_i^2 + 2s_j a_s} \tag{4.2.6}$$

$$u_{dj} = \sqrt{u_i^2 + 2s_j a_s + 2da_d} \tag{4.2.7}$$

The forward and backward distributions are symmetric relative to the s_o starting position. The symmetry arises from the isotropic distribution in the source and the ideal ion optics considered in this case directing ions into the orthogonal gate. By assuming a point source for the ions at the s_o starting position, correlated distributions develop during a "virtual time delay", which represents the mass dependent arrival time from the source into the effective region of the orthogonal gate. During this time interval, ions are allowed to rearrange their positions according to their initial velocities, as shown in Figure 4.4.

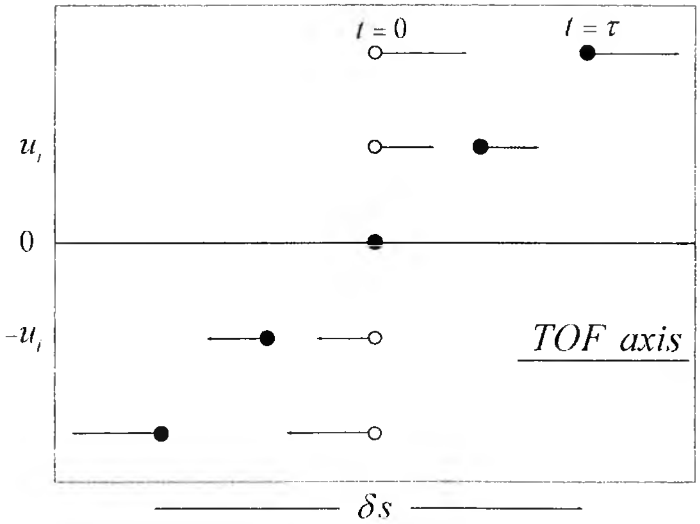

Figure 4.4 Correlated space-velocity distribution in the orthogonal direction. The analysis considers a point source and introduces a "virtual time delay" τ. At the end of the time delay the ions obtain a linear correlation between their position and velocities prior to the application of the extraction pulse. For the orthogonal configuration system this time delay is mass dependent and represents the time required for each mass to travel from the ion source into the orthogonal gate.

The analysis considers the two ions with the average initial velocities, one for the forward and one for backward distributions. The correlated starting conditions for the TOF experiment are respectively:

$$s_i = s_o - u_i \tau \tag{4.2.8}$$

$$s_j = s_o + u_i \tau \tag{4.2.9}$$

where τ is the virtual time delay introduced to facilitate the following computations. The physical meaning of the virtual time delay distinguishes between space-velocity correlation in orthogonal TOF MS and the time-lag technique. If τ is mass independent, ions at the end of the fixed time interval have travelled different distances. The heavier the mass the smaller the velocity during the displacement and a mass dependent spatial spread is generated. This is the case examined by the time-lag focusing technique. However, if τ is mass dependent, ions are allowed to disperse until they all obtain a common spatial and energy spread as a result of an isotropic distribution of ions with equal energy. As we discussed above, the mass dependency of the virtual time delay in orthogonal TOF MS is responsible for the discrimination effects exhibited by this particular mass analyzer.

Eq's (4.2.8) and (4.2.9) allow for the acceleration distances s_i and s_j to be eliminated from the time-of-flight expressions (4.2.2) and (4.2.5) and the latter can then be expanded into a *Taylor* series over the average initial ion velocity u_i. A *backward difference approximation* method[2] is used to describe the time-of-flight of the *reference* ion in terms of the time-of-flight of the ion with the positive initial average velocity in the forward part of the distribution. Neglecting third and higher order terms:

$$t_o = t_i + (0 - u_i)\frac{\partial t_i}{\partial u_i} + \frac{(0 - u_i)^2}{2}\frac{\partial^2 t_i}{\partial u_i^2} \tag{4.2.10}$$

and the time spread is:

$$\delta t_i = t_o - t_i = -u_i \frac{\partial t_i}{\partial u_i} + \frac{u_i^2}{2}\frac{\partial^2 t_i}{\partial u_i^2} \tag{4.2.11}$$

For the backward part of the distribution the *forward difference approximation* gives:

$$t_o = t_j + [0-(-u_i)]\frac{\partial t_j}{\partial u_i} + \frac{[0-(-u_i)]^2}{2}\frac{\partial^2 t_j}{\partial u_i^2} \tag{4.2.12}$$

and the time spread is:

$$\delta t_j = t_o - t_j = u_i \frac{\partial t_j}{\partial u_i} + \frac{u_i^2}{2}\frac{\partial^2 t_j}{\partial u_i^2} \tag{4.2.13}$$

By summing the time spread expressions:

$$\delta t = u_i\left(\frac{\partial t_j}{\partial u_i} - \frac{\partial t_i}{\partial u_i}\right) + \frac{u_i^2}{2}\left(\frac{\partial^2 t_i}{\partial u_i^2} + \frac{\partial^2 t_j}{\partial u_i^2}\right) \tag{4.2.14}$$

where δt is the maximum time spread of the whole ion ensemble, defined as the sum of the two individual space velocity correlated distributions, $\delta t = \delta t_i + \delta t_j$. First and second-order focusing conditions are obtained by setting the successive terms of the composite *Taylor* series to zero. The first-order focusing condition is:

$$\frac{\partial t_j}{\partial u_i} - \frac{\partial t_i}{\partial u_i} = 0 \tag{4.2.15}$$

and the optimum distance where the arrival time distribution of the ions exhibits an extremum is:

$$D = \frac{\dfrac{a_d}{a_s}\left(2 + \dfrac{u_{ci}}{u_{si}} + \dfrac{u_{cj}}{u_{sj}}\right) + \dfrac{u_{ci}}{u_{di}} + \dfrac{u_{cj}}{u_{dj}} - \dfrac{u_{ci}}{u_{si}} - \dfrac{u_{cj}}{u_{sj}}}{\dfrac{a_d u_{ci}}{u_{di}^3} + \dfrac{a_d u_{cj}}{u_{dj}^3}} \tag{4.2.16}$$

where $u_{ci} = \tau a_s - u_i$ and $u_{cj} = \tau a_s + u_i$ are the correlated velocities for the forward and backward distributions respectively. The velocity ratios are defined according to the following dimensionless mass independent relationships:

---

[2] See for example: Numerical Methods for Engineers, Chapra & Canale, Chapter 4, (2002)

$$l_i = \frac{u_{ci}}{u_{si}} = \frac{\frac{h}{2}\sqrt{\frac{\lambda}{s\kappa_s}} - \sqrt{d\kappa_d}}{\sqrt{s_i\lambda + d\kappa_d}} \tag{4.2.17}$$

$$l_j = \frac{u_{cj}}{u_{sj}} = \frac{\frac{h}{2}\sqrt{\frac{\lambda}{s\kappa_s}} + \sqrt{d\kappa_d}}{\sqrt{s_j\lambda + d\kappa_d}} \tag{4.2.18}$$

$$m_i = \frac{u_{ci}}{u_{di}} = \frac{\frac{h}{2}\sqrt{\frac{\lambda}{s\kappa_s}} - \sqrt{d\kappa_d}}{\sqrt{s_i\lambda + d(1+\kappa_d)}} \tag{4.2.19}$$

$$m_j = \frac{u_{cj}}{u_{dj}} = \frac{\frac{h}{2}\sqrt{\frac{\lambda}{s\kappa_s}} + \sqrt{d\kappa_d}}{\sqrt{s_j\lambda + d(1+\kappa_d)}} \tag{4.2.20}$$

and the “effective flight paths” for the two ions that define the units for the optimum distance D:

$$n_i = \frac{a_d u_{ci}}{u_{di}^3} = \frac{\frac{h}{2}\sqrt{\frac{\lambda}{s\kappa_s}} - \sqrt{d\kappa_d}}{2\left[s_i\lambda + d(1+\kappa_d)\right]^{3/2}} \tag{4.2.21}$$

$$n_j = \frac{a_d u_{cj}}{u_{dj}^3} = \frac{\frac{h}{2}\sqrt{\frac{\lambda}{s\kappa_s}} + \sqrt{d\kappa_d}}{2\left[s_j\lambda + d(1+\kappa_d)\right]^{3/2}} \tag{4.2.22}$$

where λ is the ratio of the electric fields, $\lambda = a_s/a_d = \mathcal{E}_s/\mathcal{E}_d$, κ_s and κ_d are the ratios of the average initial ion kinetic energy to the total energies stored in the two fields respectively, $\kappa_s = T_i/U_s$ and $\kappa_d = T_i/U_d$ and $h = s_o - s_i = s_j - s_o$. The first-order focusing constraint is then reduced to:

$$D = \frac{\frac{1}{\lambda}\left(2 + l_i + l_j\right) + m_i + m_j - l_i - l_j}{n_i + n_j} \tag{4.2.23}$$

Eq. (4.2.23) is the mass independent focal distance for the ions in oTOF MS when a linear space-velocity correlated distribution is considered. The distance of the focal point is kinetic energy dependent. An example of the focusing properties of the system is shown in Figure 4.5. The condition for second-order focusing is determined by:

$$\frac{\partial^2 t_i}{\partial u_i^2} + \frac{\partial^2 t_j}{\partial u_i^2} = 0 \tag{4.2.24}$$

and the additional focusing requirement is:

$$D = \frac{\frac{1-\lambda}{\lambda}\left[p l_i\left(1 - l_i^2\right) + l_j\left(1 - l_j^2\right)\right] + p m_i(1 - m_i^2) + m_j(1 - m_j^2)}{p n_i(1 - 3m_i^2) + n_j(1 - 3m_j^2)} \tag{4.2.25}$$

where p is the ratio of the correlated initial ion velocities:

$$p = \frac{u_{cj}}{u_{ci}} = \frac{h + 2s\kappa_s}{h - 2s\kappa_s} \tag{4.2.26}$$

An example of the arrival time distribution of the ions for a second-order configuration is shown in Figure 4.6.

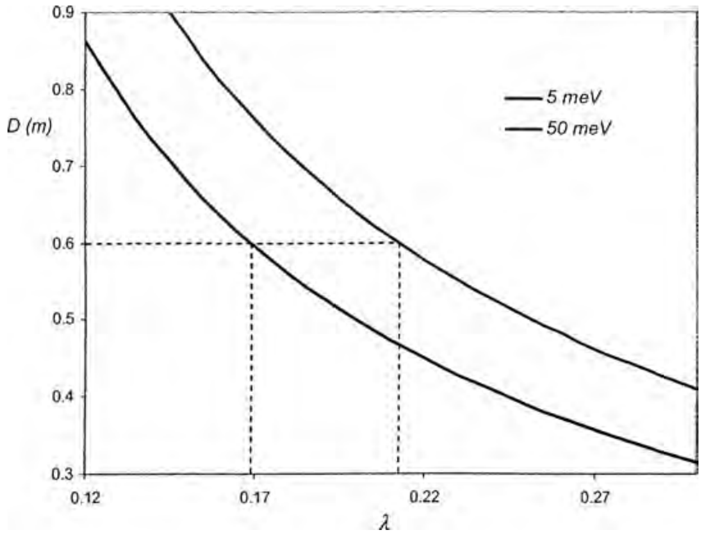

Figure 4.5 First-order focusing conditions in oTOF MS. The distance of the focal point is a function of the electric field ratio λ and can be projected to any distance by altering the values of the latter. Increased initial kinetic energies are compensated by higher λ values. When the average initial ion kinetic energy is increased from *5 meV* to *50 meV*, the correction on the voltage across the first electric field for *5 keV* ions on a *60 cm* long instrument is *~200 V*. The parameters of the one-dimensional numerical simulation *are s=0.38 m, d=0.18 m and δs=2mm.*

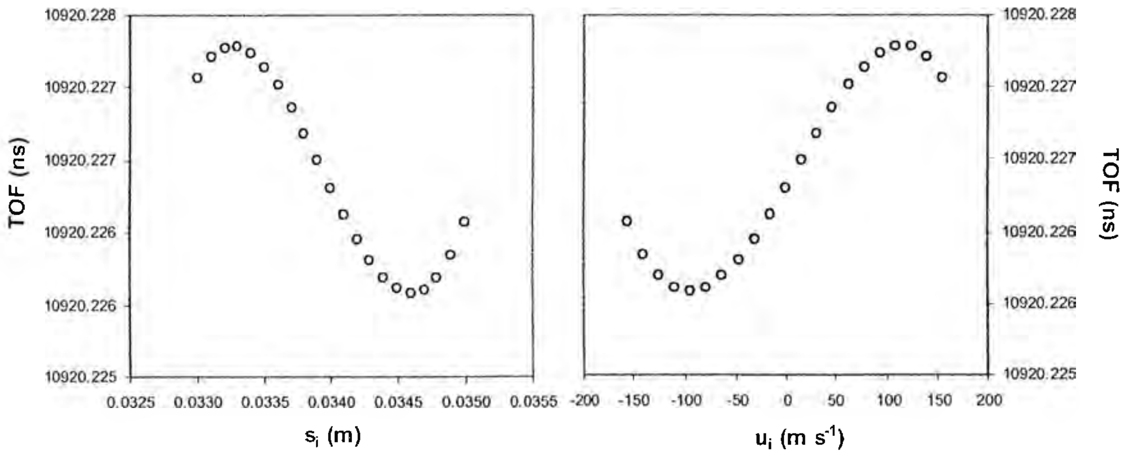

Figure 4.6 Second-order focusing and arrival time distributions as a function of starting positions s_i and initial ion velocities u_i respectively. The simulated parameters are *s=3.8 cm, d=1.8 cm, D=67.5 cm,* V_s*=1244,* V_d*=3452, m/z=150, δs=2 mm and* T_i*=19 meV.*

4.3 Non-Linear Correlation

The linear correlation between position and initial ion velocity in the orthogonal direction is a rather ideal situation and was developed to demonstrate the basic principles of the method. Non-homogeneous electric fields and variations in the position of ion formation in the source distort the linearity. Non-linear phase space distributions of the ions with finite dimensions are a more accurate description of the starting conditions for the TOF experiment. Prompted by SIMION studies, non-linear distributions are investigated and the corresponding arrival time spreads at the detector are examined by one-dimensional numerical analysis. Results are presented in Chapter 6 and compared with experimental data. A brief description of non-linear distributions and their application to oTOF MS is discussed in this section.

Distortion of the linear phase space defines a lower limit for the arrival time spread of the ions. Linear distributions exhibit infinite-order focusing and practically zero arrival time spread at the optimum distance. However, this remains an elusive goal in TOF MS and in practise there is always a finite error associated with the initial conditions of the ions. An important observation with non-linear distributions is that any turn-around time effects occur only for the ions at the centre of the ion beam which is not clearly resolved into its spatial and velocity components in phase space. An example is shown in Figure 4.7. Three non-linear distributions are considered. For a fixed energy spread, a reduction in the cross section of the beam (spatial spread of the ions) brings ions with opposite velocity vectors at the same position before extraction. Interestingly enough, these ions are close to the centre of the beam and their turn-around time effects are much smaller compared with the rest of the ions, since velocity increases with the distance from

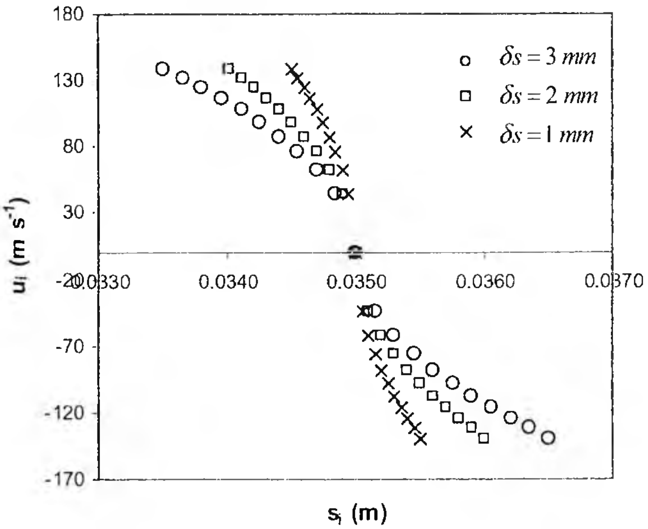

Figure 4.7 Non-linear phase space distributions in the orthogonal direction prior to the application of the electric field pulse. An initial ion kinetic energy of 15 meV is considered for m/z=150.

the centre. As we move to the outer positions, ions with opposite velocity vectors have a spatial separation and the error in their flight times can be corrected.

Figure 4.8 is a numerical time-of-flight analysis for the three distributions presented in Figure 4.7. The arrival time spread of the ions is plotted over the ratio of the electric fields $\xi = V_s / V_d$ of the two-stage orthogonal geometry. An optimum ratio is identified for each distribution for which the focal point is projected to the detector plane. The optimum ratio is mass independent, only if the energy spread is the same for all masses. A reduction in the spatial spread of the ions requires stronger voltage ratios, that is, stronger pulsed fields to project the focal point to the appropriate distance. The final time spread is also reduced. The method suggests that a unique focusing curve exists for a particular set of initial conditions and a non-linear distribution can be extrapolated by fitting theoretical curves to experimental data. Estimation of the initial conditions of the ions prior to acceleration is therefore possible.

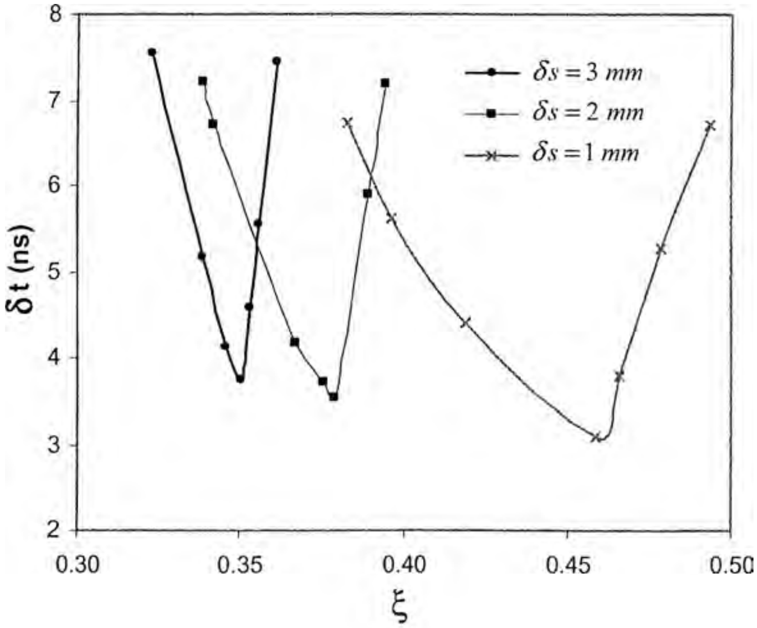

Figure 4.8 Focusing curves for the three distributions shown in Figure 4.7. The parameters for the one-dimensional analysis are *s=3.8 cm, d=1.8 cm, D=67 cm, m/z=150 and* T_i*=15 meV*. The voltage ratio $\xi = V_s / V_d$ is scanned so that the total voltage drop is fixed at 3.5 kV.

An important observation is made with respect to the turn-around time. For an ion of $m/z = 150$ in an electric field of $\mathcal{E}_s = 29,000\ Vm^{-1}$, which corresponds to the optimum operating conditions of the lower curve in Figure 4.8 with $\delta s = 1\ mm$, the time to decelerate and accelerate back to its original position in the field is $14.9\ ns$. The arrival time spread of the whole ensemble is $3.09\ ns$, considerably lower than that calculated by Eq. 4.1.1. The turn-around time is an underestimation of initial kinetic energy spread of the ions since the $3.09\ ns$ gives an estimation of an energy spread of the order of *~1 meV*, far below the *15 meV* considered in the numerical analysis.

Figure 4.9 shows the effect of the initial energy spread on the characteristic focusing curves for the same oTOF system. If the spatial spread of the ions and their drifting energies are constant, higher initial velocities require stronger pulsed fields. The optimum time spread increases with initial ion energy as expected. Ions with $1\ meV$ energy approach the space focusing limit. The latter is the lower voltage that can be applied across the first field to provide any kind of focusing.

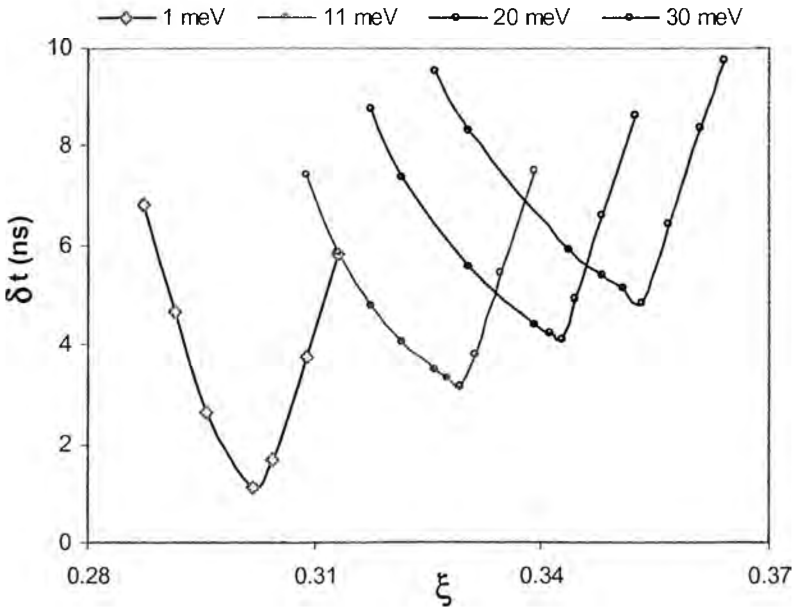

Figure 4.9 Velocity focusing characteristic curves for δs=2 mm and a total energy of 3.5 keV. The simulated parameters are those of Figure 4.8.

4.4 Discussion

A theoretical analysis of linear phase space distributions is developed and first and second-order analytical solutions are provided. The focusing conditions can be considered as the missing solutions from original time-lag technique. The mass dependent focusing properties of the latter method can be explored by identifying the "virtual time delay" τ as a mass independent parameter.

Non-linear phase space distributions are a more appropriate description compared to the infinite-order focusing achieved by the linear case. These studies are prompted by SIMION results. A method is proposed for extrapolating the initial conditions of the ions by fitting theoretical focusing curves to experimental data. Results are presented in Chapter 6 from both EI and TI/SI sources.

The concept of the turn-around time in orthogonal TOF MS is re-evaluated. Turn-around time effects can be reduced by generating distributions where positions and initial ion velocities are correlated. A direct correlation of the arrival time spread of the ions with the initial energy spread in the orthogonal gate by Eq. (4.1.1) is an underestimation and the actual number can be an order of magnitude greater.

The analysis suggests that virtual sources for incorporating a reflectron are strongly dependent on the starting conditions for the TOF experiment. In the ideal case where a linear correlation is considered, the optimum is defined by second-order focusing. Non-linear distributions require a more detailed analysis.

Chapter 5

Experimental

5.1 The Prototype Orthogonal TOF MS

The first orthogonal TOF MS coupled to a thermal/surface ionization (TI/SI) filament source was reported in the 50th ASMS conference in 2002 (McMahon *et al*, 2002). Thermal ionization mass spectrometry is an invaluable tool for isotopic studies and trace analysis by isotope dilution. Instruments must exhibit high isotope ratio precision for most of these applications and therefore ideally incorporate a spatially dispersive spectrometer with multiple detectors. Instruments have been built with quadrupole mass analyzers but they offer lower precision. Time of flight mass analyzers do not appear to be appropriate for these applications, however, the continuous thermal ion beam from a heated filament can be efficiently sampled into a TOF instrument by the pulsed orthogonal acceleration technique. A number of advantages and disadvantages are associated with the combination of thermal ionization and TOF-MS, which are outlined below.

The instrument has been built for diagnostic purposes, allowing investigation of physico-chemical parameters that influence the thermal ionization process. In this context, the spectrometer has the advantage that the complete mass spectrum can be monitored continuously over the lifetime of the filament. The instrument also allows optical access to the filament for pyrometric measurements and laser ionization of neutrals. In orthogonal TOF MS, isotope ratio precision is compromised by the inherent discrimination effects of the orthogonal gate. Since a single detector is used to detect all isotopes, the recovery time of the detection system precludes the measurement of a low abundance isotope immediately following a high abundance isotope, even at very low ion count rates. In addition, the dead time associated with the time-to-digital-converter (TDC) discriminates against high abundance species and accurate measurements can only be performed for the low count rates.

A schematic diagram of the instrument is shown in Figure 5.1. Thermal Ionization filaments (Cathodeon, Cambridge, UK) were resistively heated at currents between 2.0 and 5.0 A using a lab-made filament power supply that could be electrically floated at the source potential. Accelerating potentials in the range 5 to 50 V deliver ions through a 2 mm slit to the orthogonal acceleration region. A Wiley & McLaren two-stage acceleration configuration samples the low energy beam into the vertical flight tube. The first accelerating region was initially 30 mm in length and a uniform field is defined by the back plate and two plane parallel grids (Buckbee-Meers, St. Paul, MN, US). The first grid is at ground potential and the back plate with the second grid are pulsed symmetrically to approximately ± 350 V by a PVM-4210 high voltage pulse generator (DEI, Fort Collins, CO, US) with a rise time of <12 ns. The second accelerating field (15 mm) is defined by a third grid electrically connected with the flight tube, floated at –3.5 kV. The end of the flight tube is defined by the grid at the front of the detector. Ions are post accelerated to –5.0 kV and strike the conversion dynode of an ETP electron multiplier (SGE, Milton Keynes, UK). The output signal of the multiplier was amplified by an ORTEC 9305 d.c. preamplifier (Advanced Measurement Technology, Berkshire, UK) and recorded by an SR430 Multichannel Scaler (Lambda Photometrics Ltd. Harpenden,UK) with a bin size of 5 ns.

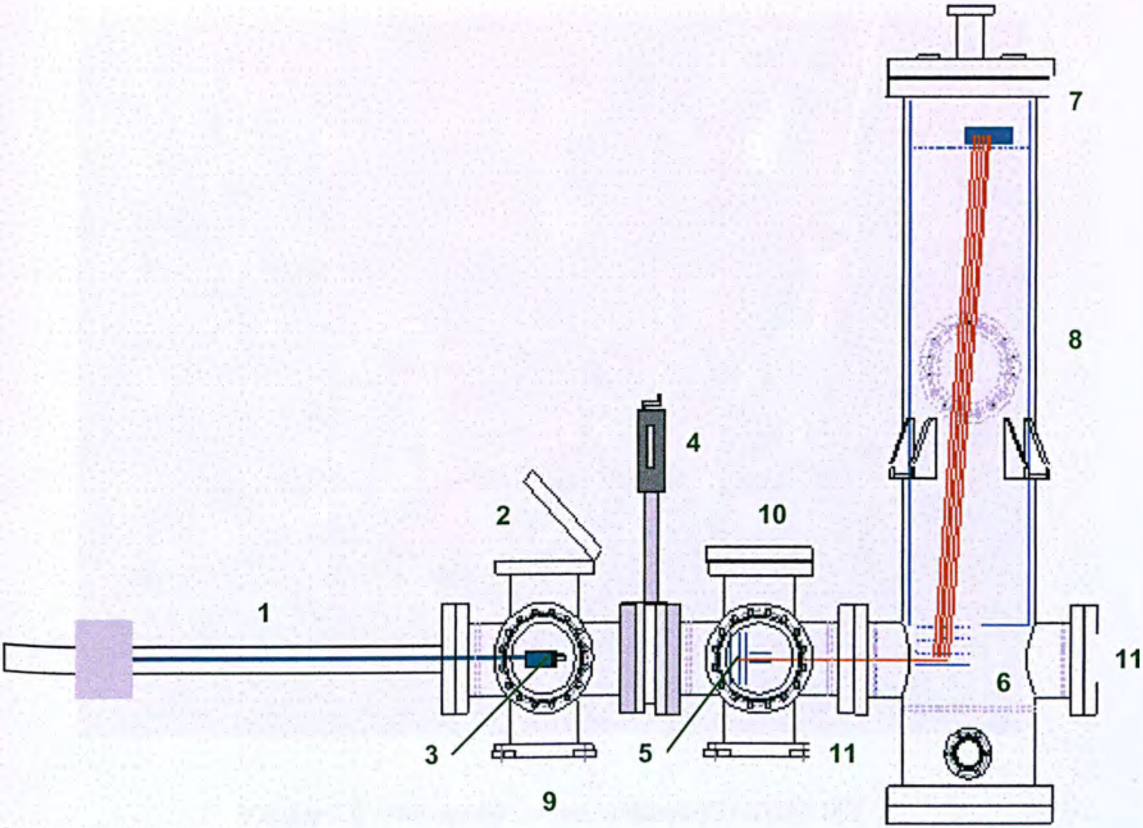

SOURCE: McMahon *et al*, 2002

Figure 5.1 Instrument Schematic. 1 – Magnetic Transfer Arm. 2 – Fast Entry Port. 3 – Filament Holder. 4 – Gate Valve. 5 – Thermal Ion Source. 6 – Orthogonal Acceleration Region. 7 – Electron Multiplier. 8 – Ion Pump. 9 – Turbomolecular Pump. 10, 11, 12 – View-ports.

A photograph of the prototype TI oTOF MS is shown in Figure 5.2. The first six-way cross chamber, the "dirty chamber", is designed for filament pre-heating and outgassing. The manual valve maintains the high vacuum in the source and analyzer when new samples are introduced into the system. The magnetic transfer arm pushes the filament holder into a PTFE block, part of the source assembly, which is used for positioning the filament with respect to the ion optical system. Typical pressures in the source during operation are $< 10^{-6}$ torr, measured by a penning gauge. The 250 Ls^{-1} turbomolecular pump in combination with the ion pump achieve pressures of the order of $\sim 10^{-9}$ torr in the flight tube, measured by an ionization gauge at the lower part of the vertical chamber.

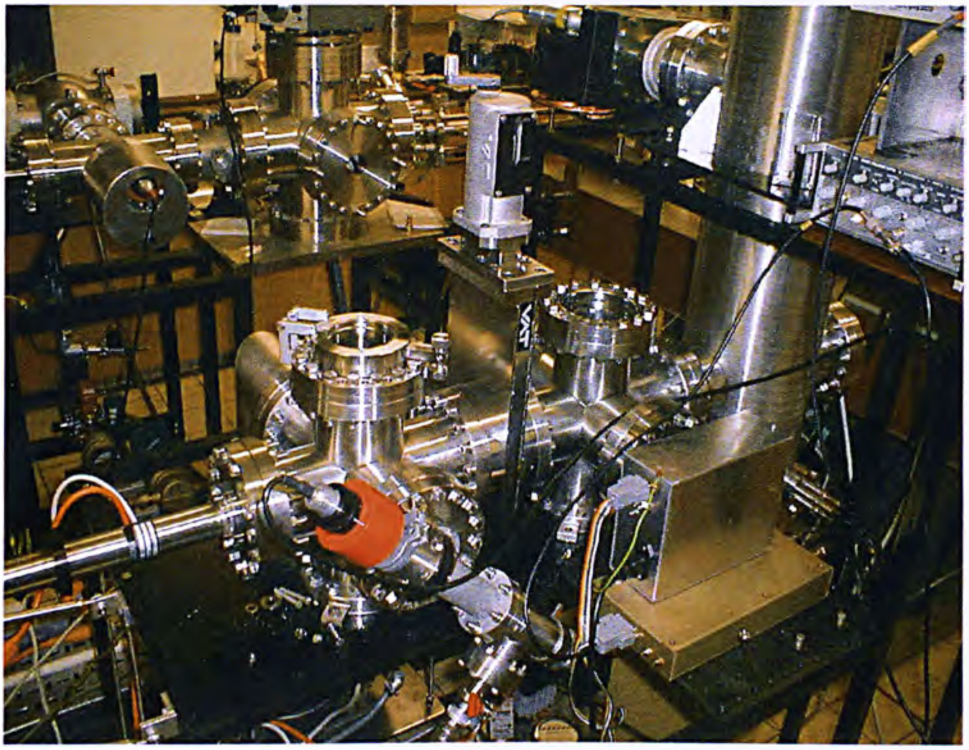

Figure 5.2 Photograph of the prototype TI oTOF MS

A top view into the vertical flight tube is shown in the next Figure 5.3. PTFE washers isolate electrically the inner tube from the main chamber. Voltages up to 10 kV have been applied successfully. The bottom plane of the inner tube lies in parallel with the top gridded plate of the orthogonal gate. In this case the gate is unmasked and the whole area of the grid can be seen. A circular hole is situated next to the orthogonal gate to support the detector for a reflectron geometry. The grid on the left side of the inner tube facilitates pumping by allowing gas molecules to pass through and get trapped in the ion pump. A strong background noise during operation of the system was observed and is attributed to the stray fields between the grid and the pump and the ions drawn into the flight tube and directed towards the detector. The oTOF MS was operated with the ion pump switched off.

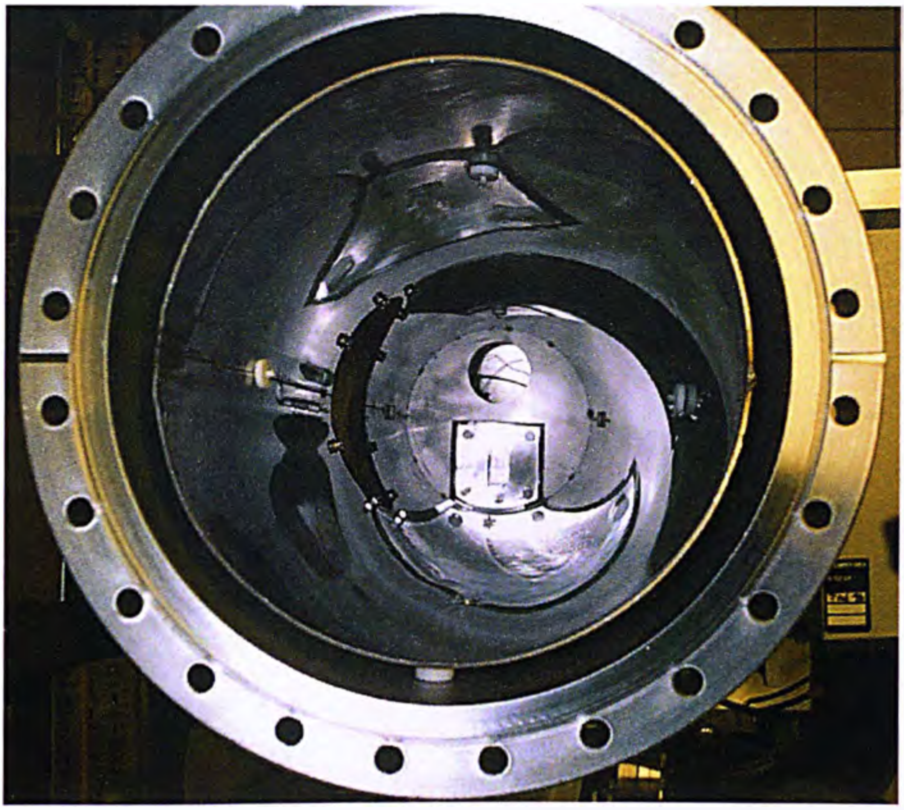

Figure 5.3 Inside view of the vertical flight tube.

5.1.1 Date of Birth 18-01-02

The first spectrum recorded by the prototype TI TOF MS is shown in Figure 5.4. The peaks from left to right correspond to the mono-isotopes sodium and aluminium, ${}^{23}_{11}Na$, ${}^{27}_{13}Al$, the two isotopes of potassium, ${}^{39}_{19}K$ and ${}^{41}_{19}K$, and finally the strontium and barium isotopic clusters shown by single peaks. The noise from the electric pulse on the orthogonal gate is seen on the left side of the spectrum. In this case the duration of the pulse is ~2.45 μs and two spikes are generated, one at the onset and one at the offset of the pulse. The ion signal is generated by passing 3.5 A through the filament. The Sr sample is dried on a Re filament at atmospheric pressure and the *Sr* isotopes are the most abundant species in the spectrum. The remaining peaks are filament impurities and are temperature dependent. They can be removed by progressively increasing the temperature of the filament until the surface is no longer supplied from the bulk material. The heavier the mass the higher the temperature required to deplete the filament of its constituent.

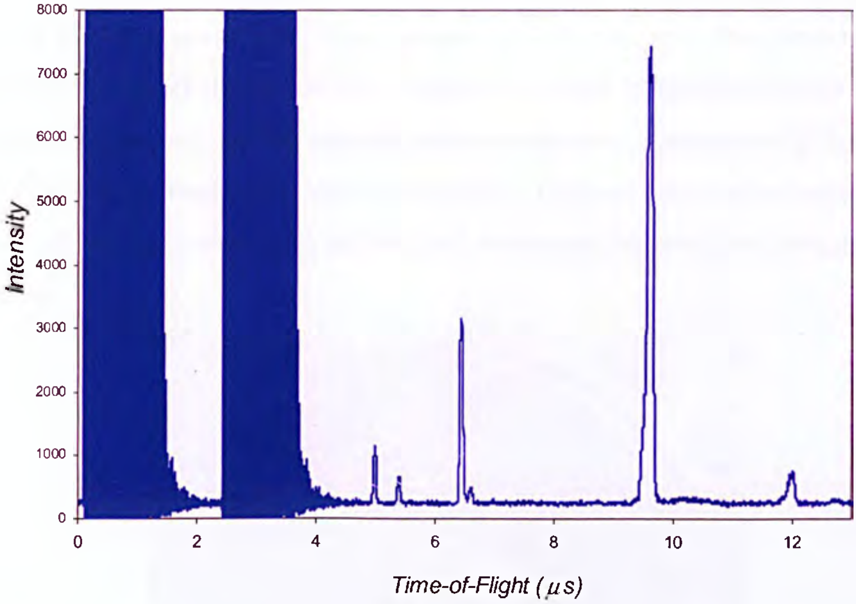

Figure 5.4 The first atomic spectrum of a strontium sample loaded on a rhenium filament with the prototype TI oTOF MS.

Sr resolution in this first spectrum is ~40 with a time spread of ~120 ns at full-width half-maximum (fwhm). The *Sr* cluster peaks at 9.625 µs in a ~70 cm long flight tube. The energy of the ion beam is ~60 eV and the total energy of the ions in the flight tube is 4.2 keV, resulting in a flight angle of 83.22°. The period of the extraction pulse is of the order of ~100 µs (10 kHz), enough to allow the heaviest atomic ion to travel through the analyzer. For the major strontium isotope, $^{88}_{38}Sr$, with 60 eV source energy, the residence time for a 3 cm long grid area is 2.615 µs. The duty cycle for a 10 kHz extraction pulse is then 2.615 %.

Chapters 5 & 6 chronicle the improvements achieved from the very first days of this project and selected experiments are presented and accompanied with simulations of ion trajectories and numerical analysis of the time-of-flight of the ions.

5.1.2 Thermal Ionization Ion Source

A single filament thermal ionization source was initially installed. A side view of the ion source under vacuum is shown in Figure 5.6. A single filament is situated on the left is positioned by the PTFE source block so that the plane of the filament is parallel with the first electrode. The three electrodes are insulated from each other by 1 cm long ceramic spacers and direct the ions through the optical system towards the source exit slit. The surface of the filament is 2x8 mm and the dimensions of the rectangular slits are 2x10 mm. A set of steering plates is situated at the front end of the ion optics to correct for the lateral and/or transverse dispersion of the beam and maximize the ion current in the orthogonal gate. Copper electrodes were installed at the far end of the source axis to collect and measure the positive ion current with an electrometer.

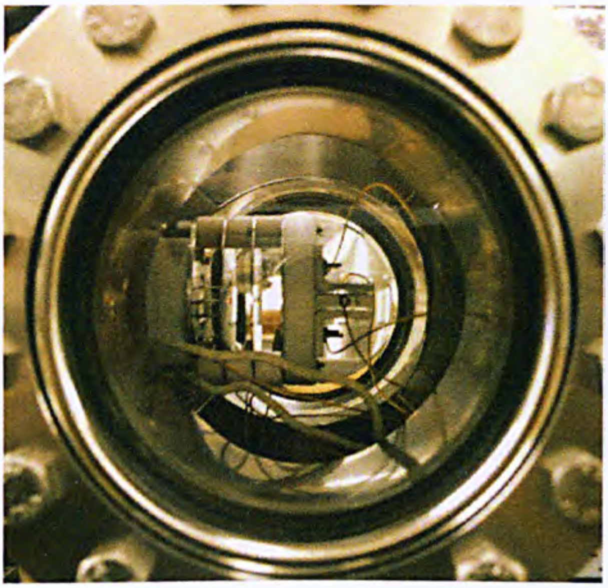

Figure 5.5 Side view of the single filament TI source under vacuum.

“Burn” marks on three elements of the ion optical system are shown in Figure 5.6. From left to right these are the mount plate for the remaining electrodes, the middle element whose surface is facing the filament and finally the source exit slit. Symmetric deposition of the evaporating material can be seen from the diffraction patterns on the surfaces. The side cut on the electrodes allows for laser access onto the filament surface. The transverse and lateral spread of the ion beam can be seen from the patterns on the surface of the last electrode.

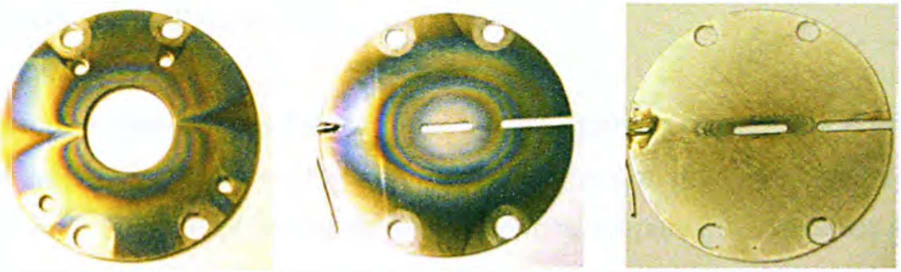

Figure 5.6 Ion optical elements of the single filament TI source.

Single and triple filament configurations are shown in Figure 5.8. Temperature distribution measurements of rhenium filaments using infrared pyrometry have been performed (Papanastasiou, 2001). Figure 5.8 shows the distributions obtained for the different filament currents. The differences between the centre and the edges of the filament can reach 500 °C for the high currents.

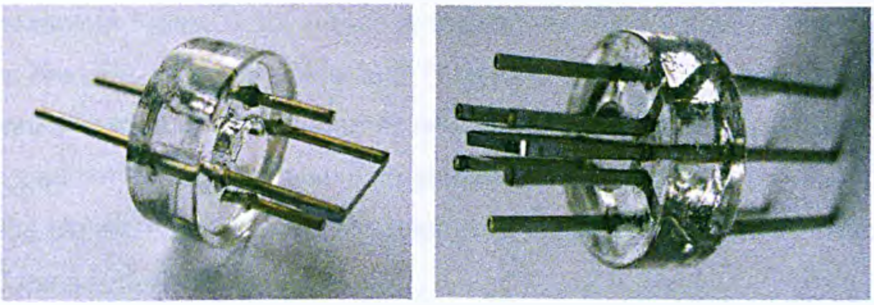

Figure 5.7 Single and triple filament configuration in TI MS

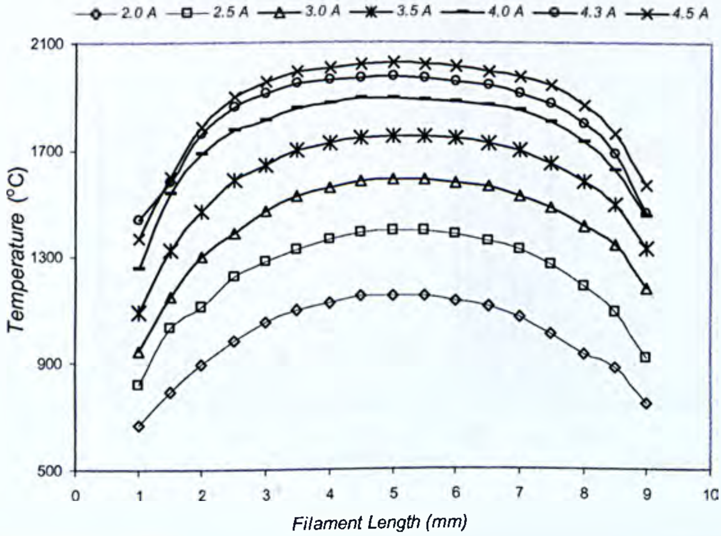

SOURCE: Papanastasiou, 2001

Figure 5.8 Temperature distribution of a rhenium filament using infrared pyrometry.

5.1.3 Time-Evolution Experiments

A few examples demonstrate the ability of the prototype to monitor the entire mass spectrum. Information on the chemistry of the filament and kinetic studies can be performed as a function of temperature and sample preparation. Aqueous samples are deposited and dried on rhenium, tantalum or tungsten surfaces as nitrates. During the drying-out procedure, nitrates reduce to NO, which evaporates in the atmosphere. The oxide species remain on the filament surface. Rhenium is usually the preferred polycrystalline substrate since it combines both a high melting point, 3453 K, and the second highest work function, 4.98 eV, after that of platinum with 5.13 eV.

Figure 5.9 shows the neodymium and neodymium oxide clusters from a Re filament loaded with the nitrate. The time spread is of the order of 15 ns and a resolving power of 400 is achieved. The ability of the oTOF analyzer to monitor the entire mass spectrum is shown in Figure 5.10. All the isotopes and oxide forms of the samples and impurities are simultaneously detected. These include uranium, neodymium and strontium nitrates loaded on the filament, and sodium, aluminium, potassium and barium that constitute the major rhenium impurities. Self ionization of rhenium is also observed at the higher temperatures. The chemistry of the filament can be monitored as function of temperature variations.

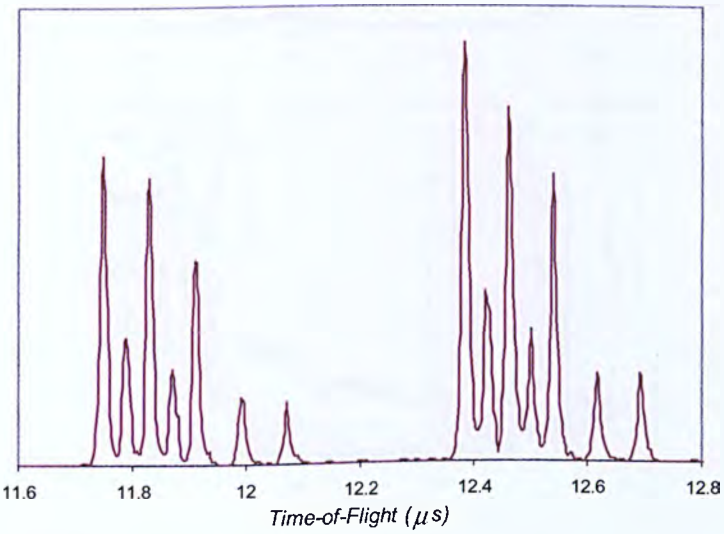

Figure 5.9 The neodymium and neodymium oxide clusters with a resolution of 400.

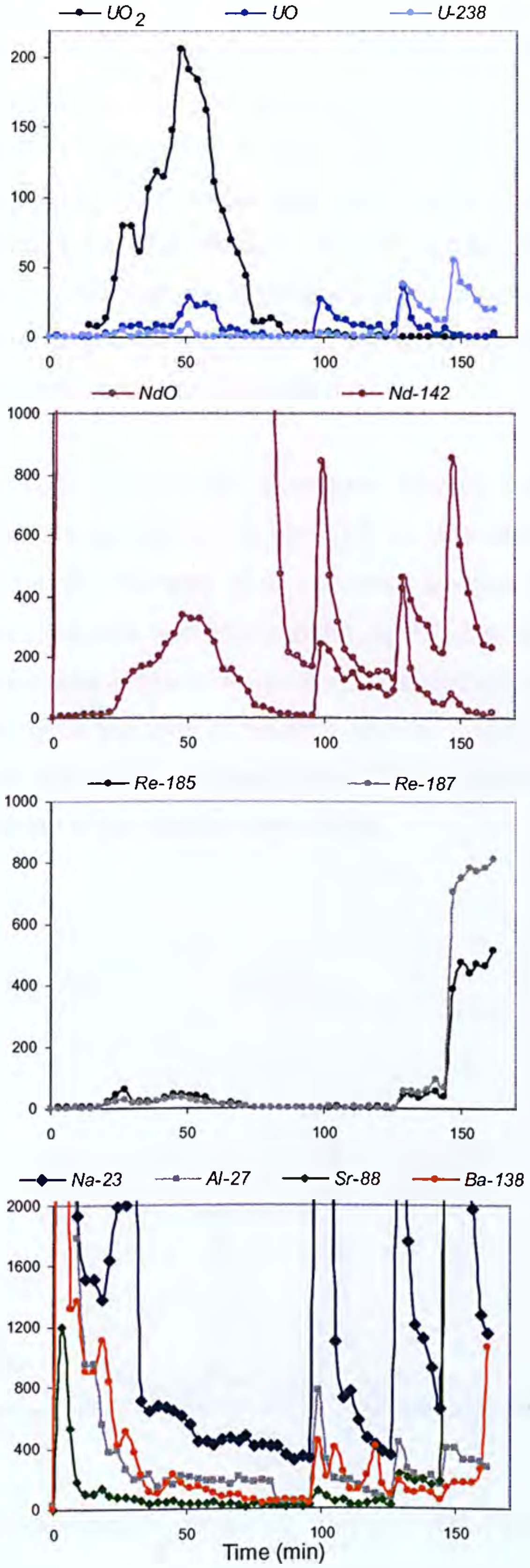

Figure 5.10 Intensity variations for the most abundant species in a single run as a function of time. The system allows for the chemical composition variations on the filament surface to be studied as a function of temperature.

With reference to Figure 5.10, intensity maxima correspond to the higher currents that a *Re* filament is driven to. The uranium and neodymium signal evolutions show the lower availability of oxygen on the surface as the temperature of the filament is raised. The oxides are reduced enhancing the atomic signal. For the higher temperatures self-ionization of the filament becomes significant. At the same time impurities from the bulk of the material reach the surface by diffusion and sublime as ions. Depletion from impurities can be achieved by careful control of the temperature well below the melting point, and provide clean surfaces.

The evolution of uranium dioxide, the monoxide species and atomic ions as a function of temperature is shown in Figure 5.11. In this example, the sample is loaded on a carburized *Re* filament. It is not clear whether the reduction of the dioxide species to the monoxide and finally to the atomic species as the temperature rises is the only process taking place. An alternative explanation would be the faster evaporation of the oxides in the form of neutrals and the greater ionization efficiency of atomic uranium at the higher temperatures. These combined effects can be studied by laser ionization of the neutral evaporates.

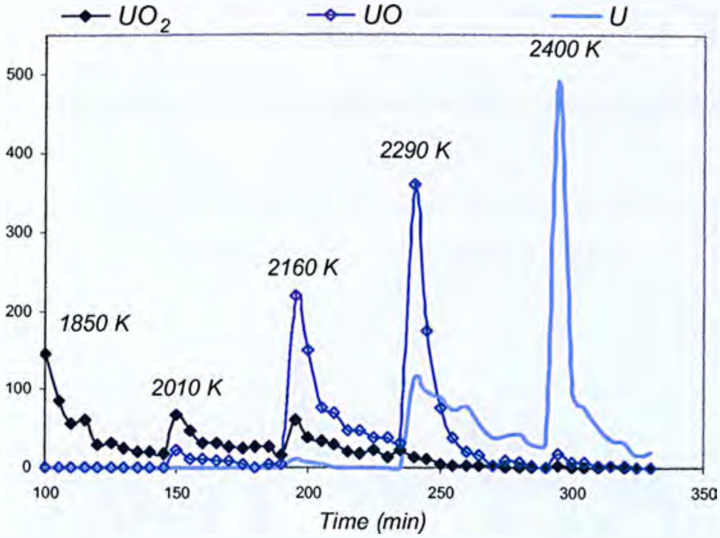

Figure 5.11 Evolution of the uranium species as a function of temperature.

Figure 5.12 shows the variation of K and Rb signals as a function of time. The Rb loaded Re filament runs at 3 A until the K impurity decays exponentially to almost zero levels. Rb ion emission is in a semi-equilibrium state. The temperature of the filament is then raised by increasing the current to 3.3 A. The initial jump in the signal intensity is followed again by an exponential decay. The isotope ratio for the Rb isotopes over time is shown in the next Figure 5.13. The accepted value is ${}^{87}_{37}Rb/{}^{85}_{37}Rb = 0.385617$ (CRC, Handbook of Chemistry & Physics, 67th Edition, 1987). The experimental average isotope ratio over the period of 340 min is ${}^{87}_{37}Rb/{}^{85}_{37}Rb = 0.3850$ with a standard deviation of 0.0174.

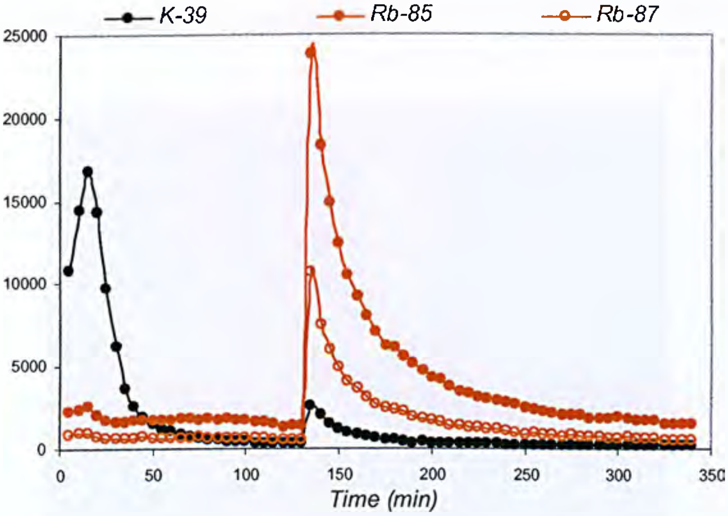

Figure 5.12 Time evolution for potassium and rubidium on a rhenium filament.

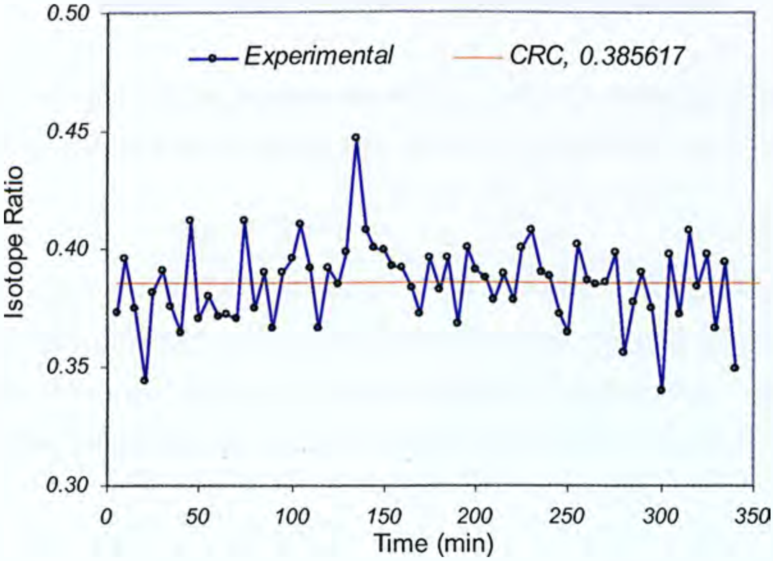

Figure 5.13 Variations in the rubidium isotope ratio measured in the oTOF MS.

5.1.4 The Early Detection System

The first experiments were carried out with a robust ETP electron multiplier model AF850H. The gain of the multiplier is 10^7 when 2 kV are applied across the discrete dynodes and a maximum current of 30 μA can be delivered at the output. The pulse width for single pulse events is 4.5-6.0 ns and the dead time 1 ns. The dynode of the detector has been successfully floated to 10 kV to perform resolution studies. A photograph of the detector housing is shown in Figure 5.14. The fast pre-amplifier was the ORTEC model 9305 with DC coupling. The gain of the pre-amp is $\alpha = 5-10$ with a rise time of <3 ns. The maximum input is +/-1 V and the input impendence is $Z = 50\ \Omega$. The output voltage pulse follows the relationship $V_{out} = Z\ (\alpha\ I_{in})$ and the maximum output for 30 μA input pulse is 15 mV.

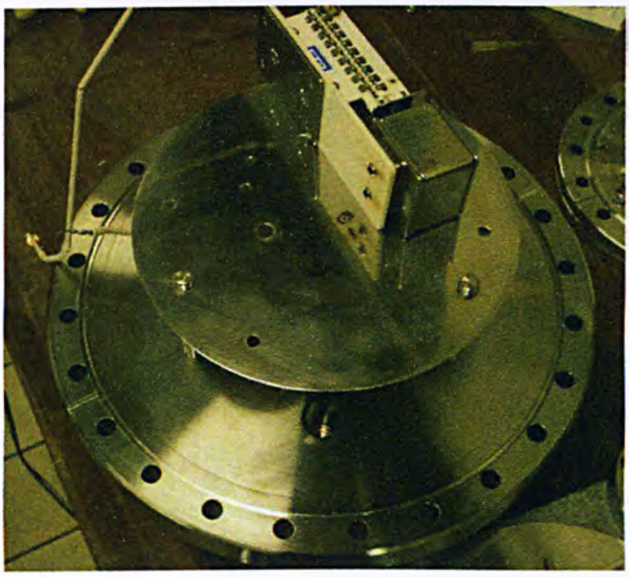

Figure 5.14 Photograph of the detector assembly showing the discharge developed between the detector mount plate and conversion dynode when the flight tube was floated at ~10 kV.

Time-digitization of the signal processed by the 200 MHz Multichannel Scaler model SR430 eliminates problems such as the slow rise times and extended pulse widths of the ETP multiplier and the DC coupled ORTEC pre-amplifier. Time digitization however is jitter sensitive and can set a lower limit to the time spread of the ions.

5.2 Resolution Experiments & Simulations

Initial studies with the ETP multiplier and the 200 MHz multichannel scaler, as a detection system, where performed with the dynode voltage floating at the same potential as the flight tube. The energy of the positively charged atomic ions was maintained >3.5 kV to ensure high electron conversion efficiency on the active film of the dynode. The idea for not post-accelerating the ions is justified by the space focusing conditions, initially adopted for simulating and tuning the oTOF MS, and the theoretical requirement of a definite field-free path length for the ions. Experiments with the prototype showed that field penetration from the discrete dynode arrangement introduced fringing fields and had a significant contribution to the final time spread. Jitter was therefore an important parameter when the system was operated with the ETP multiplier. A series of experimental observations is presented, that led to resolution enhancement and finally to the fruitful comparison between experimental results and the theory of space-velocity correlation in TOF systems.

Numerical analysis was extensively used to reproduce experimental results and study the initial conditions of the ions. The first step in the process was the determination of the field-free path length. Although the dimensions of the orthogonal gate and the spacing of the electrodes are clearly defined by the insulating material, measuring the length of the field-free region is not a straight forward process. A simple one-dimensional time-of-flight analysis was used to compute the arrival times of all the ions detected. The model neglects initial ion velocity and scattering of the ions at the grids. It also does not incorporate the delays introduced by electron transit times through the discrete dynode as well as delays inherent with the triggering circuit. These can be estimated by time differences between theory and experiment, according to the following.

The optimum voltages determined experimentally define the electric fields used in the simulation. The arrival times are then simulated for a series of detector distances. The three curves shown in Figure 5.15 are obtained by subtracting the experimental from the theoretical values, $\delta t = t_{\exp} - t_{sim}$. Arrival flight times are also shown. An estimation for the length of the field-free region can therefore be made, based on the idea of a constant arrival time difference, δt. A constant time difference is justified by the mass independent delay introduced by electron transit times and the electronic circuit. In addition, incorporation of the initial ion velocity reduces the flight times by only a few ns. Since the Tl source provides a nearly monoenergetic ion beam, the corresponding error is m/z independent and small.

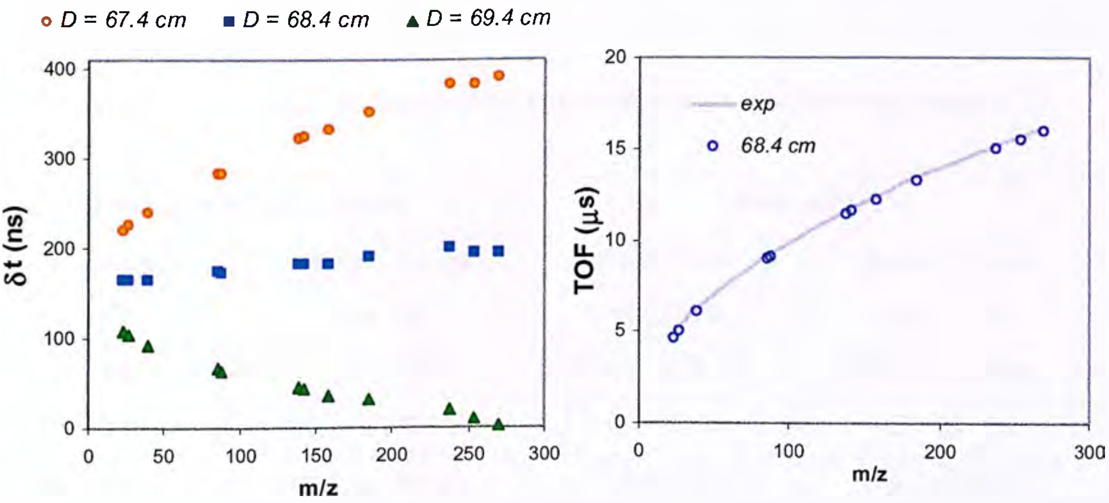

Figure 5.15 Estimation of the length of the field-free region by the difference between experimental and simulated arrival times on the left. Experimental and simulated arrival times are shown on the right.

The following example demonstrates the resolving power achieved with the prototype, and discusses space focusing conditions and their applicability to this initial instrument design. Dimensions and optimum parameters determined experimentally are given in Table 5.1. Results were obtained from a rhenium filament operating at 3.5 A. The corresponding neodymium and uranium spectra are shown in Figures 5.16 and 5.17 respectively. The signal was digitized by the 5 ns bin size SR430 multichannel analyzer. The time spread of the ions, as determined experimentally, was 15 ns and the resolution was limited to ~400. A resolving power of ~400 was observed across the atomic spectrum for all the experiments carried out with this configuration.

Figure 5.18 shows an example of the model used for simulating the prototype. For the same instrumental parameters, space focusing theory predicts a resolution of ~17,000, far exceeding the values observed experimental. Numerical analysis showed that the arrival time spread of the ions was very sensitive to voltage variations, in contrast to the experimental results. In theory, the arrival time spread of an ion ensemble with zero initial velocity distribution exhibits a sharp minimum when scanning the applied voltages. The experimentally determined resolving power of ~400 could be maintained by varying the drifting energy of the ions over ~1000 eV, in direct contrast to theory.

Table 5.1 Comparison of experimental parameters and space focusing theory.

Instrumental Parameters		**Resolution**	
Dimensions (cm)	*Voltage - Energy*	*Experimental*	*Space Focusing*
s = 2.9	$V_s = 725$	m/z = 158	m/z = 158
d = 1.5	$V_d = 3133$	TOF = 12390 ns	TOF = 12235 ns
D* = 68.5	$KE_{TOF} = 3858$ eV	δt = 15 ns	δt = 361 ps
slit = *2 mm*	$KE_{BEAM} = 50$ eV	R = 410	R = 16,900
	$\theta^{**} = 83.55^{o}$		δs^{***} = 3 mm

* The value of D is estimated according to Figure 5.15

** The flight angle θ is determined by Eq. (1.3.9)

*** The space focusing conditions assume a spatial spread of 3 mm and the voltages are those used in the experiment.

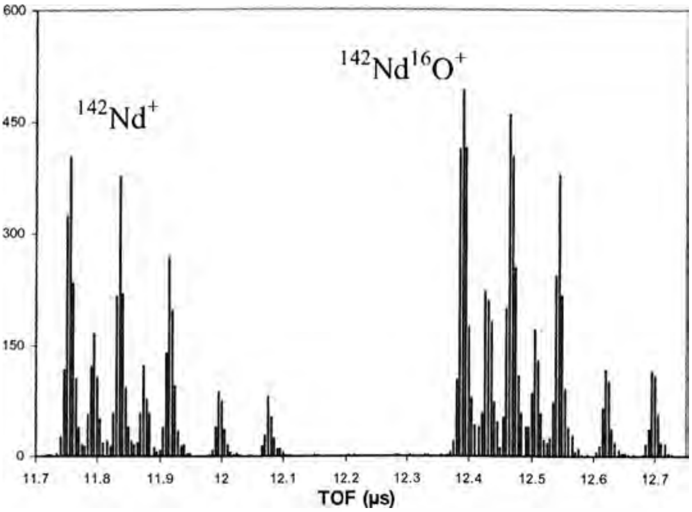

Figure 5.16 Neodymium and oxides with a resolving power of ~400.

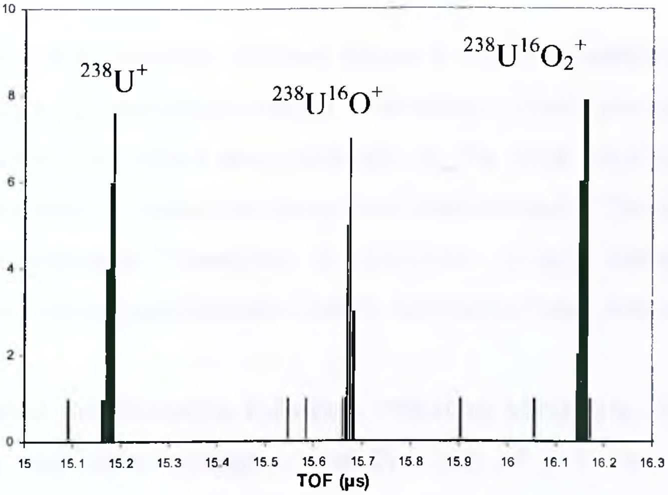

Figure 5.17 Uranium and oxides with a resolving power of ~400.

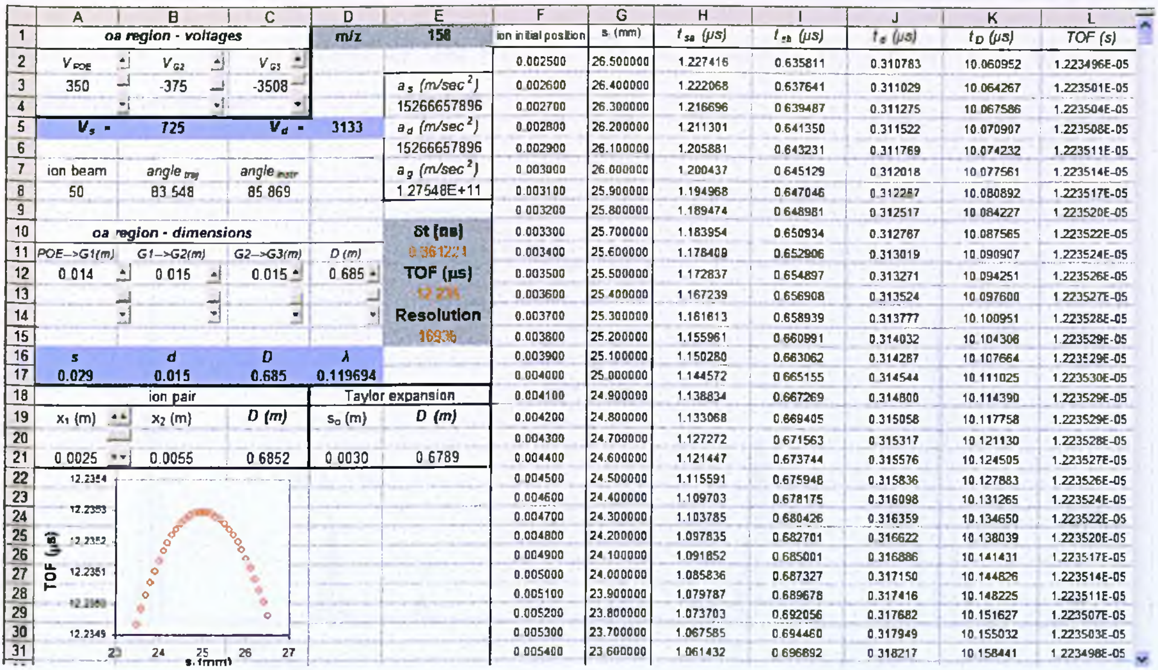

	A	B	C	D	E
1	oa region - voltages			m/z	158
2	V_{POE}	V_{G2}	V_{G3}		
3	350	-375	-3508		a_s (m/sec²)
4					15266657896
5	V_s =	725	V_d =	3133	a_d (m/sec²)
6					15266657896
7	ion beam	$angle_{traj}$	$angle_{instr}$		a_g (m/sec²)
8	50	83.548	85.869		1.27548E+11
9					
10	oa region - dimensions				δt (ns)
11	POE->G1(m)	G1->G2(m)	G2->G3(m)	D (m)	0.361221
12	0.014	0.015	0.015	0.685	TOF (μs)
13					12.235
14					Resolution
15					16936
16	s	d	D	λ	
17	0.029	0.015	0.685	0.119694	
18	ion pair			Taylor expansion	
19	x_1 (m)	x_2 (m)	D (m)	s_o (m)	D (m)
20					
21	0.0025	0.0055	0.6852	0.0030	0.6789

	F	G	H	I	J	K	L
1	ion initial position	s (mm)	t_{sa} (μs)	t_{sb} (μs)	t_e (μs)	t_D (μs)	TOF (s)
2	0.002500	26.500000	1.227416	0.635811	0.310783	10.060952	1.223496E-05
3	0.002600	26.400000	1.222068	0.637641	0.311029	10.064267	1.223501E-05
4	0.002700	26.300000	1.216696	0.639487	0.311275	10.067586	1.223504E-05
5	0.002800	26.200000	1.211301	0.641350	0.311522	10.070907	1.223508E-05
6	0.002900	26.100000	1.205881	0.643231	0.311769	10.074232	1.223511E-05
7	0.003000	26.000000	1.200437	0.645129	0.312018	10.077561	1.223514E-05
8	0.003100	25.900000	1.194968	0.647046	0.312267	10.080892	1.223517E-05
9	0.003200	25.800000	1.189474	0.648981	0.312517	10.084227	1.223520E-05
10	0.003300	25.700000	1.183954	0.650934	0.312767	10.087565	1.223522E-05
11	0.003400	25.600000	1.178409	0.652906	0.313019	10.090907	1.223524E-05
12	0.003500	25.500000	1.172837	0.654897	0.313271	10.094251	1.223526E-05
13	0.003600	25.400000	1.167239	0.656908	0.313524	10.097600	1.223527E-05
14	0.003700	25.300000	1.161613	0.658939	0.313777	10.100951	1.223528E-05
15	0.003800	25.200000	1.155961	0.660991	0.314032	10.104306	1.223529E-05
16	0.003900	25.100000	1.150280	0.663062	0.314287	10.107664	1.223529E-05
17	0.004000	25.000000	1.144572	0.665155	0.314544	10.111025	1.223530E-05
18	0.004100	24.900000	1.138834	0.667269	0.314800	10.114390	1.223529E-05
19	0.004200	24.800000	1.133068	0.669405	0.315058	10.117758	1.223529E-05
20	0.004300	24.700000	1.127272	0.671563	0.315317	10.121130	1.223528E-05
21	0.004400	24.600000	1.121447	0.673744	0.315576	10.124505	1.223527E-05
22	0.004500	24.500000	1.115591	0.675948	0.315836	10.127883	1.223526E-05
23	0.004600	24.400000	1.109703	0.678175	0.316098	10.131265	1.223524E-05
24	0.004700	24.300000	1.103785	0.680426	0.316359	10.134650	1.223522E-05
25	0.004800	24.200000	1.097835	0.682701	0.316622	10.138039	1.223520E-05
26	0.004900	24.100000	1.091852	0.685001	0.316886	10.141431	1.223517E-05
27	0.005000	24.000000	1.085836	0.687327	0.317150	10.144826	1.223514E-05
28	0.005100	23.900000	1.079787	0.689678	0.317416	10.148225	1.223511E-05
29	0.005200	23.800000	1.073703	0.692056	0.317682	10.151627	1.223507E-05
30	0.005300	23.700000	1.067585	0.694460	0.317949	10.155032	1.223503E-05
31	0.005400	23.600000	1.061432	0.696892	0.318217	10.158441	1.223498E-05

Figure 5.18 Numerical analysis of the two stage oTOF MS. The simulated parameters are presented in Table 5.1. A 3 mm initial spatial spread is assumed, and for the experientially applied voltages, a resolution of ~17,000 is predicted for the neodymium oxides. The graph at the lower left part of the figure shows the arrival time distribution of the ions as a function of starting position. The initial velocity in this case is neglected. An extremum is observed for the ion situated at the centre of the distribution, in accordance with space focusing theory and Eq. (2.3.5).

With the experimental parameters defined above it was impossible to infer whether space focusing could be used as a method to provide an optimum set of voltages for operating the system. The effect was attributed to the poor resolving power of the system and the minimal variations in the arrival time spread of the ions over a wide range of applied voltages. Therefore, an optimum voltage value could not be determined and no comparison between theory and experiment was made.

Several instrumental modifications followed, including variations in the orthogonal geometry, higher extraction voltages, and the use of a 1 mm slit before the orthogonal gate, with no substantial improvement on resolution. Attention was then directed towards the detection system and signal processing. A minor resolution enhancement is reported by increasing the extraction voltages to V_s=1400 and V_d=5450. Rubidium and rhenium spectra with a resolution of 700 and 1000 are shown in Figures 5.19 and 5.20 respectively. Resolution is mass dependent since in both cases the time spread of the ions at FWHM is limited by the bin size of the multichannel scaler.

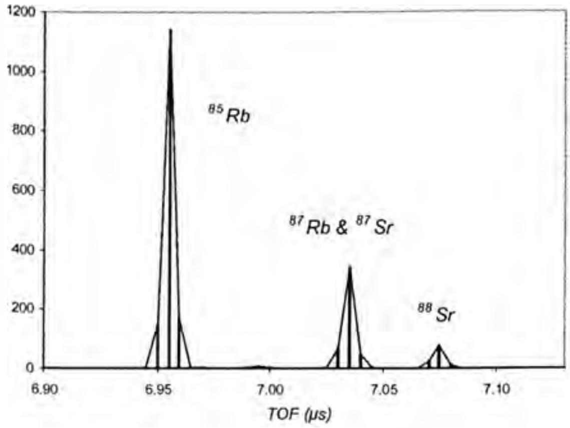

Figure 5.19 Rb & Sr spectrum with 5 ns time spread and a resolution of 700.

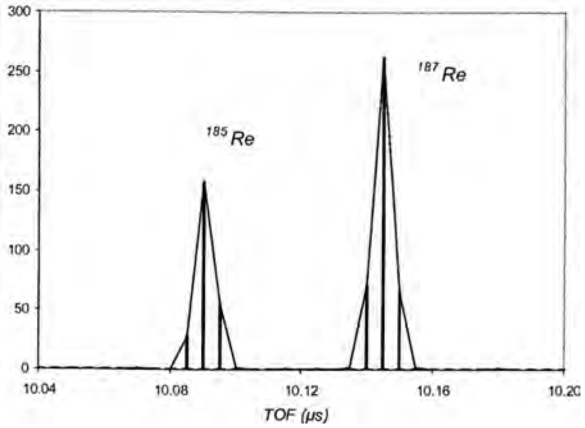

Figure 5.20 Re spectrum with 5 ns time spread and a resolution of 1000.

5.3 Advances with the TI/SI oTOF Analyzer

Three decisive modification steps were made and their influence on resolution is discussed in the following sections. They include a new "open" orthogonal gate, the installation of the ORTEC time-to-digital converter (TDC) and the replacement of the ETP multiplier with a Photek microchannel plate. A significant improvement in terms of the resolving power is reported. The concept of space-velocity correlation and its relevance to orthogonal geometries was tested using this advanced final configuration. The theory of space-velocity correlation was presented in Chapter 4 and the corresponding experimental work is developed in Chapter 6.

5.3.1 The Open Orthogonal Gate

A schematic diagram of the "open" orthogonal design is shown in Figure 5.21. The area of the electrodes is 95x95 mm and the gridded slot is 30x20 mm with the long dimensions along the source axis. The large surface are permitted wide spacing between the electrodes. The first field is defined by the first three elements and is 38 mm long. The second electric field is 18 mm, defined by the position of the final grid. A mask is incorporated at the top of the gate which facilitates high resolution experiments. However, this is at the cost of ion throughput. Two different masks were tested with slot areas 10x10 mm and 20x20 mm respectively. For the unmasked gate, the duty cycle for m/z=150 and a source energy of 20 eV is 6%. The sampling efficiency reduces to 4% and 2% by reducing the effective are to 20 mm and 10 mm respectively.

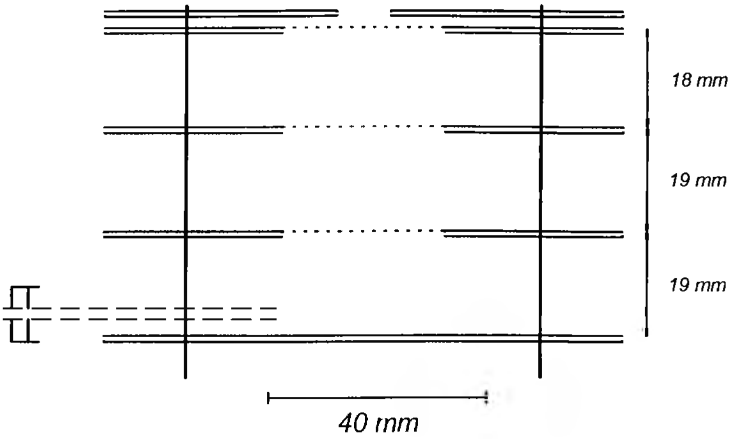

Figure 5.21 Schematic of the "open" orthogonal gate configuration. The first and third electrodes are pulsed symmetrically while the second one is grounded. The length of the second static electric field is defined by electrodes three and four.

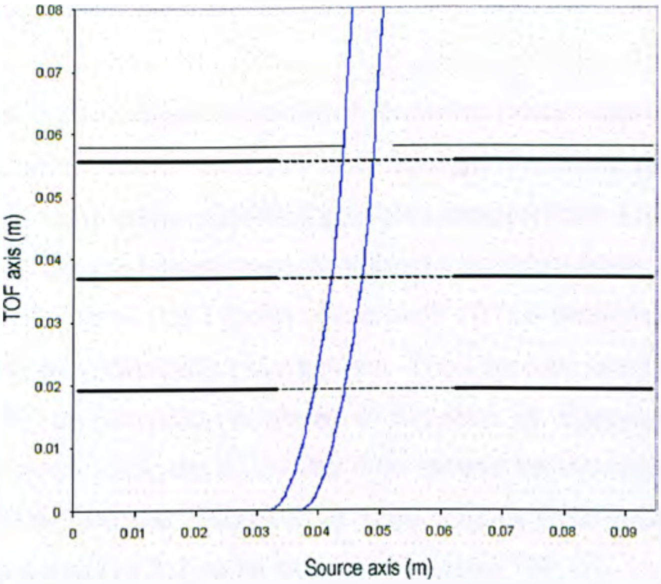

Figure 5.22 Mass independent trajectories for a monoenergetic beam in the "open" orthogonal gate design. Ions experience sharp boundaries between the grids and the voltage drop across the two-stage acceleration configuration is 1400 and 4870 V respectively. The flight angle in the field-free region is 86.8° for a source energy of 20 eV.

The new position for the detector is 67.5 cm, determined by the arrival time difference method as described above. Figure 5.23 shows a rhenium spectrum where the ions are ejected in the field-free region with energies ~8.2 keV. Over 85% of the time spread of the ions falls into one 5 ns bin. The isotope ratio for ^{185}Re/^{187}Re determined experimentally is 0.60213 with an error of 2.2% relative to the accepted value of 0.58906.

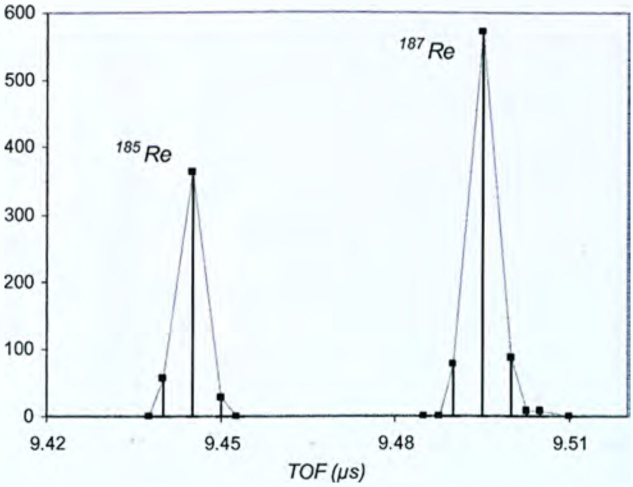

Figure 5.23 Self-ionization of a rhenium filament at ~5.0 A corresponding to a temperature of ~2100 °C. The error in the experimentally determined isotope ratio is 2.2%.

5.3.2 *Time Digitization*

The performance of instrument in terms of resolving power was limited by the bin size of the multichannel scaler model SR430. Spectra like those presented in Figure 5.23 were obtained for a range of drifting energies ranging from 4 to 9 keV and where convincing enough for the laboratory authorities to invest in faster electronics. Soon enough, the ORTEC model 9353 time digitizer with 100 ps resolution and 1 ns pulse-pair resolving time was installed in our system. The rhenium spectrum processed by the TDC with a 400 ps resolution is shown in Figure 5.24. Experimental parameters are equivalent to those in Figure 5.23. The time spread for the two rhenium isotopes is ~3.8 ns at FWHM and the resolution is 1250. Figure 5.25 shows the potassium peaks with a time spread of 3.2 ns for the major isotope ^{39}K.

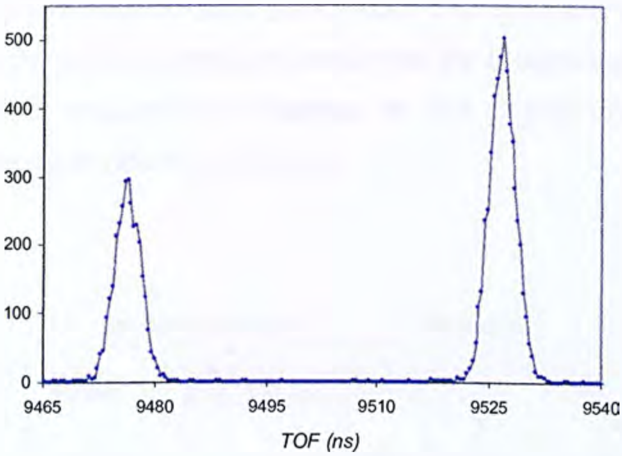

Figure 5.24 Rhenium spectrum recorded with the ORTEC TDC with a 400 ps resolution.

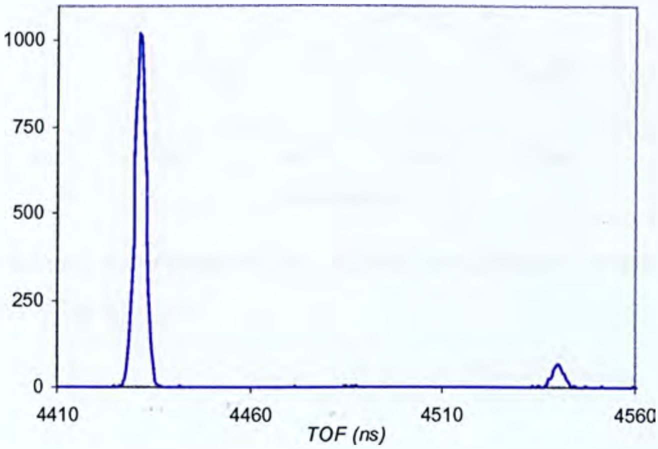

Figure 5.25 ^{39}K and ^{41}K spectrum with a time spread of 3.2 ns a resolution of ~700.

5.3.3 Flight Angle and Detector Rotation

The following experiment demonstrates that fringing fields in the conversion dynode box had a significant contribution to the final resolution of the instrument, which had not permitted studies on the initial phase space distribution of the ions. The experimental curves shown in Figures 5.26 to 5.28 were obtained as follows. The voltages on the orthogonal gate were optimized for maximum resolution. Three final ion energies were examined, these are 8.2, 6.4, 5.0 keV for the three Figures respectively. In all cases the space focusing conditions were violated by a similar amount. Lower electric field ratios λ were required for optimum resolution. The flight angle θ was then scanned by varying the energy of the ions in the source direction. As θ increased, the time spread of the ions was reduced and resolution was maximized. There is a threshold on the minimum voltage that can be applied to the source for directing ions into the orthogonal gate. The minimum voltage defines the maximum flight angle and is usually accompanied by a significant reduction in the count rate. Maximum resolution is observed for the slightly smaller flight angles where a reasonable count rate is maintained.

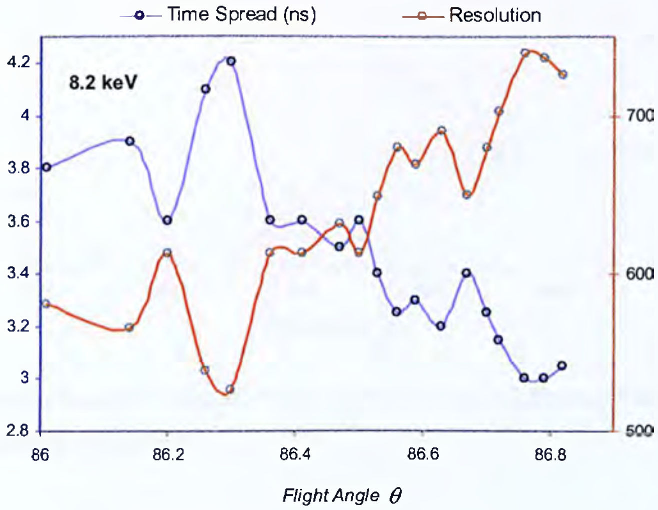

Figure 5.26 Time spread and resolution for m/z=39 as a function of the flight angle θ. The total acceleration energy is 8.2 keV.

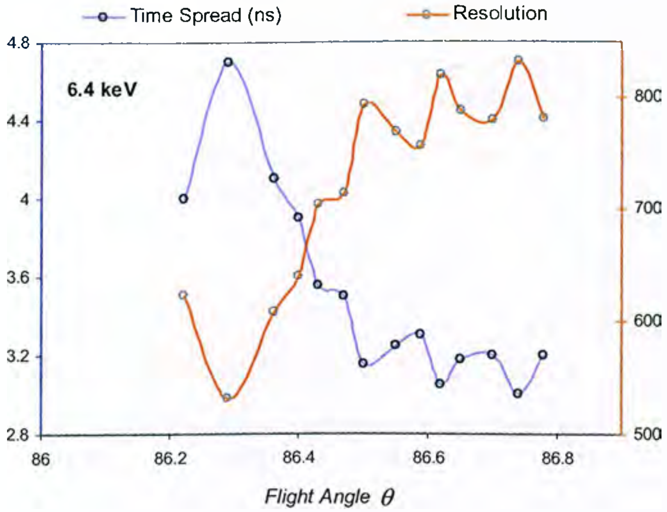

Figure 5.27 Time spread and resolution for m/z=39 as a function of the flight angle θ. The total acceleration energy is 6.4 keV.

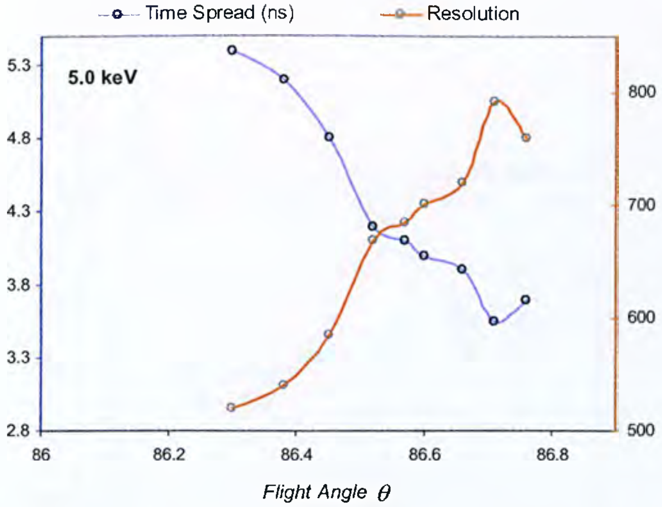

Figure 5.28 Time spread and resolution for m/z=39 as a function of the flight angle θ. The total acceleration energy is 5.0 keV.

The experimental results obtained inidcated that the flight angle was a significant parameter for enhancing the resolving power of the system. The effect was initially attributed to the grids and the stronger deflection experienced by the ions as their angle of approach was reduced. Potassium spectra and the two isotopes ^{39}K and ^{41}K are shown in Figure 5.29 for the three optima, as determined in 5.26-5.28. As the final energy of the ions is increased both time spread and time-of-flight are reduced.

Maximum resolution is observed for the medium energies of 6.4 keV where a compromise between time spread and time-of-flight is made.

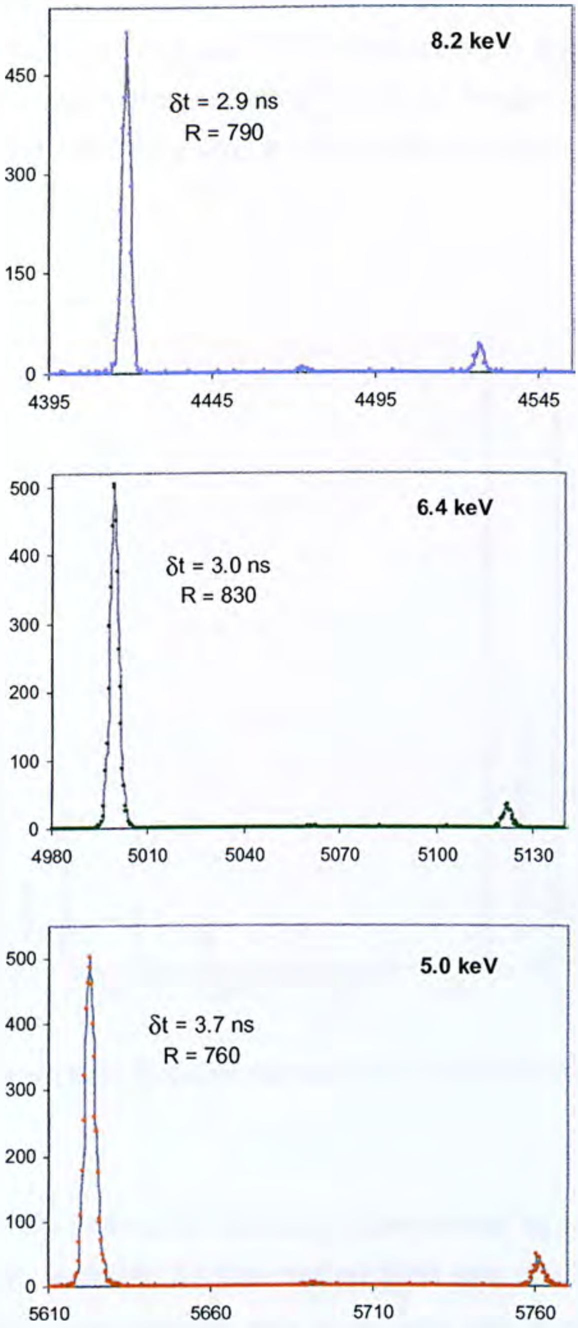

Figure 5.29 Potassium spectra for three different ion energies. Intensities and the flight angle of 86.75° are identical for reasons of comparison. Time spread and resolution are shown for the major isotope ^{39}K in each case.

The time differences between the two masses are 108.8, 122.8 and 139.2 ns for the 8.2, 6.4 and 5.0 keV energies respectively. Both time spread and the time difference between adjacent masses increase as the energy of the ions is reduced and longer flight times are observed. Several experiments were carried out by reducing the energy of the ions in the source axis as low as possible (~20 eV) while the final energies of the ions were maintained at ~6.4 kV. Figure 5.30 shows baseline separation for Nd and NdO ions with a time spread of 4.4 ns and a resolution of ~1100.

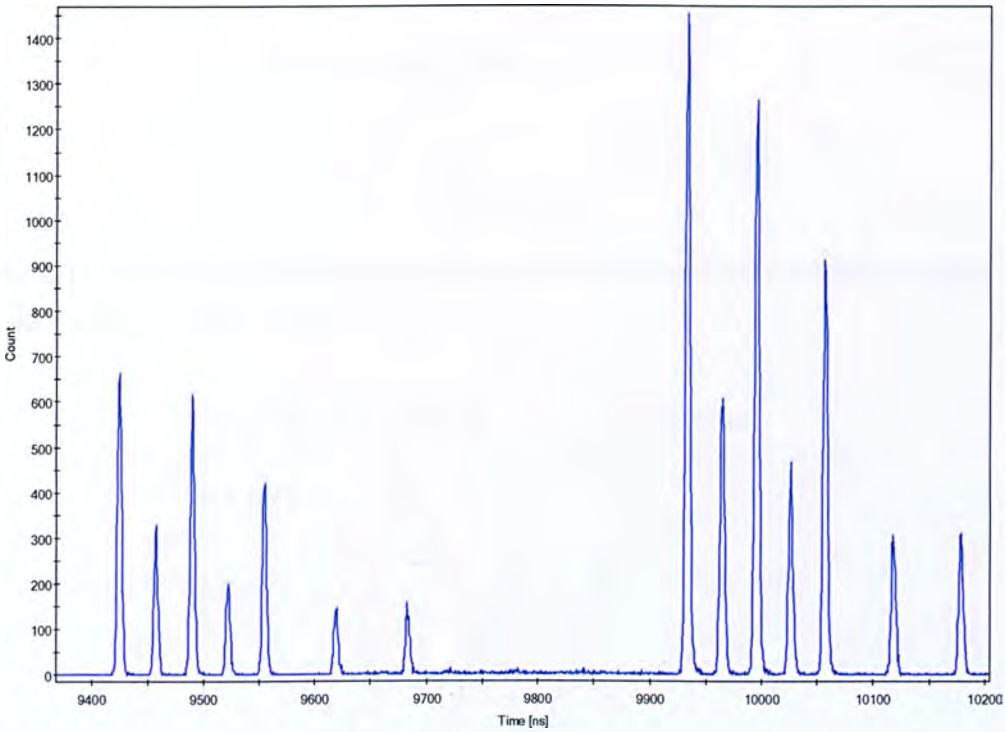

Figure 5.30 Baseline resolution for Nd and NdO ions.

Attempts to increase the flight angle as close to the normal as possible followed. The maximum flight angle achieved by this configuration was ~ 86.85°, allowing for an improvement of 3.15°. One possible way to fly ions with a greater angle was by positioning the orthogonal region further down the source axis. A displacement of 1.5 cm increased the instrumental angle to 87.5°. Significant loss in resolution was observed and was attributed to the lateral spread of the ion beam, since the 2 mm slit had a fixed position. An equivalent improvement in the flight angle was achieved by rotating the detector housing by 180°. Surprisingly, the relationship between the flight angle and the time spread of the ions reversed. The effect is shown in the next two Figures 5.31 and 5.32 for 8.2 keV and 6.4 keV total energies respectively.

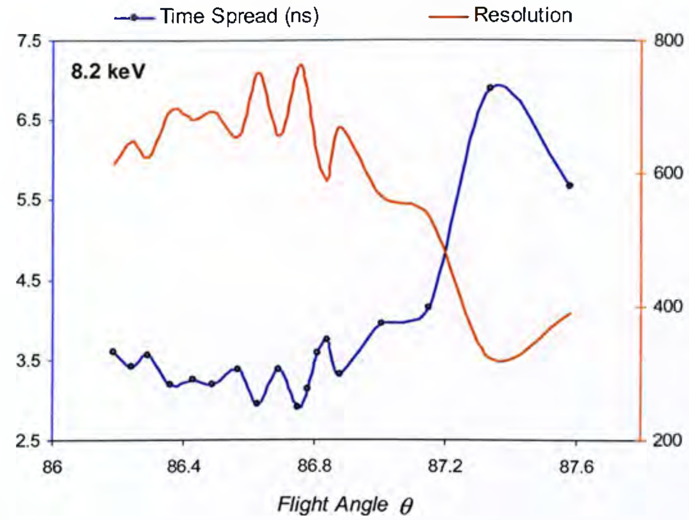

Figure 5.31 Time spread and resolution for m/z=39 as a function of the flight angle θ. The total acceleration energy is 8.2 keV.

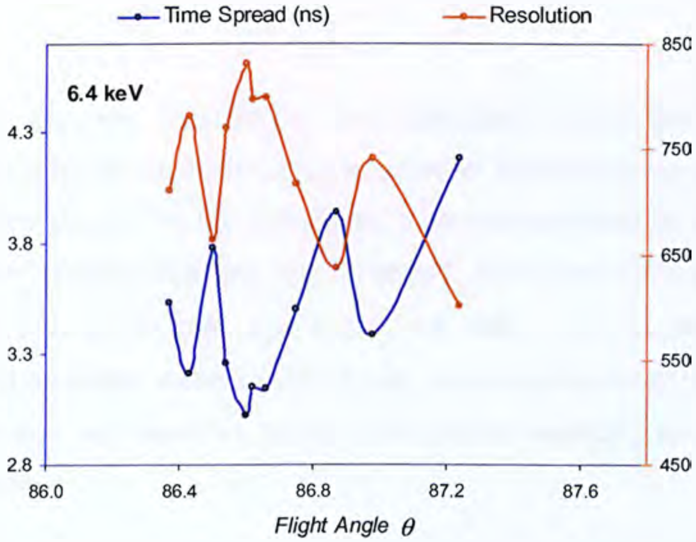

Figure 5.32 Time spread and resolution for m/z=39 as a function of the flight angle θ. The total acceleration energy is 6.4 keV.

It became then apparent that the fringing fields, inherent in the design of the electron multiplier, masked resolution in all the experiments performed so far. By varying the energy of the ions in the source axis, the arriving ion packets scanned the electric field across the conversion dynode. The effect is reflected by the characteristic time spread curves. By rotating the multiplier the reverse effect was seen. In this case, the optimum angle was found to be at a lower value. A Re spectrum is shown in Figure 5.33 obtained with the reversed detector configuration.

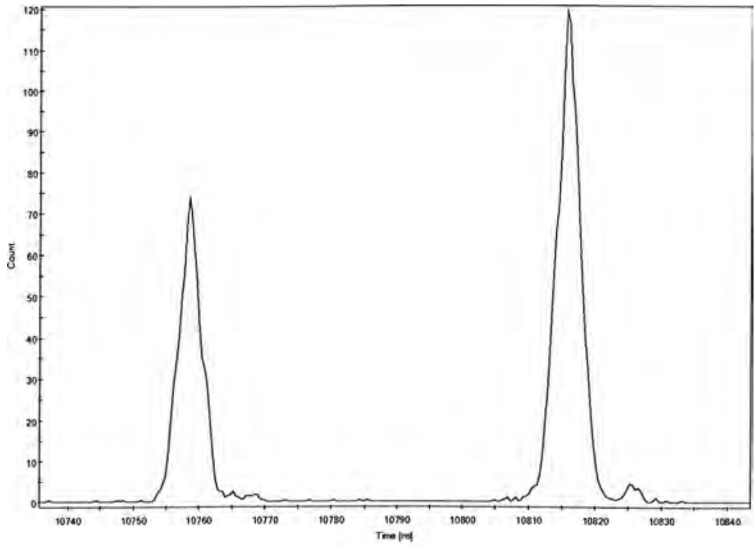

Figure 5.33 Re spectrum with a time spread of the order of ~3.5 ns and a resolution of 1500. The ion energy is 6.4 keV.

Any attempts to improve resolution were unsuccessful since the minimum time spread was defined by the multiplier. That was further justified by two experiments. In the first, the 2 mm slit prior to the orthogonal gate was replaced by a 1 mm slit. No effect on the time spread of the ions was observed. In the second, the four electrode structure of the orthogonal gate was pulsed so that $s < d$, in contrast with the standard mode of operation were $s \approx 2d$. Again, the same minimum time spread was achieved. Resolution was therefore further enhanced by replacing the detector with a microchannel plate.

5.3.4 Microchannel Plate Detector

The microchannel plate is the *chevron* Photek model VPM340 with a 50:1 length over diameter ratio. The device is designed to operate at pressures below 10^{-6} mbar. The gain is x2 per 50 V and the maximum output current is 50 μA. The detector surface area is 40 cm in diameter and a maximum of 3100 V can be applied across the plates. The output signal was amplified with the ac coupled 9306 ORTEC 1 GHz preamplifier. The gain of the 9306 model is 100, x10 that of the 9305 dc coupled model. Typical output rise times are ~350 ps. In combination with the ORTEC 9353 TDC, a fast detection system was available for high resolution studies.

Figure 5.34 shows an analog-to-digital spectrum recorded with the Tektronix TDS3064B 600 MHz oscilloscope. The baseline of the ac coupled fast preamplifier shoots off at the onset and offset of the pulse, thus limiting in some sense the pulse duration and the period for mass analysis when light ions and the corresponding short flight times are considered (<4.5 μs). For example, the flight time for the sodium monoisotope ^{23}Na is of the order of 5 μs, overlapping with the onset pick-up. The flight time for the heaviest mass detected in the prototype, the uranium dioxide $^{238}U^{16}O_2$, is 17 μs restricting the duration of the pulse hence the sampling frequency of the ion beam to ~50 kHz (20 μs pulse period). In Figure 5.35, the pulse duration is 30 μs and the frequency is 20 kHz (50 μs period).

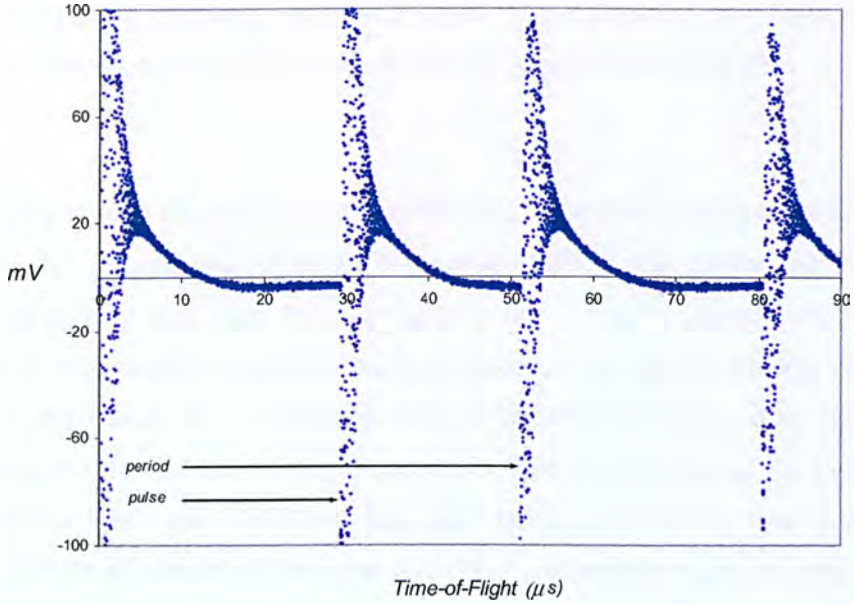

Figure 5.34 Analog-to-digital spectrum of the detection system

A single ion event for ^{39}K is shown in the next Figure 5.35. The peak height is 78 mV and the pulse width is 3 ns (fwhm). The discrimination levels set on the TDC were accordingly adjusted ranging from -8 to -12 mV. Figure 5.35 also shows the random pick-up from the turbo pump with a frequency of 71 MHz (~14 ns). The pick-up could not be removed with chokes or capacitors and was the main source of noise in the system.

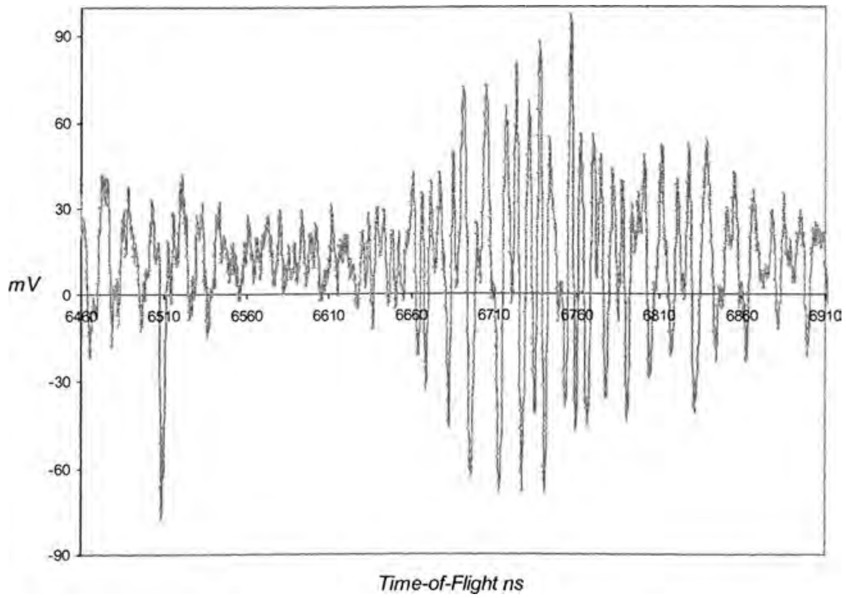

Figure 5.35 Analog-to-digital spectrum of a single ^{39}K ion event and the characteristic pick-up noise from the turbo pump. The transient signal is sampled every 200 ps.

Figure 5.36 is a high resolution mass spectrum of the neodymium oxides. The time spread is ~3.15 ns and resolution slightly exceeds 2000. It is interesting to note that the total energy of the ions for this system is ~3.5 keV. Acceleration to these energies with the original detection system gave a time spread for the neodymium species of the order of 15 ns. The best resolution achieved with the electron multiplier was 1100 with a 4.4 ns time spread for NdO at energies of ~6.4 keV. Figure 5.37 is another NdO spectrum from the same scan, obtained by tuning the source voltages. The time spread of the ions is further reduced to ~2.8 ns and resolution exceeds 2300. These latest results were reported in the ASMS conference in San Antonio (Panastasiou & McMahon, 2005). To the best of the authors knowledge, this is the highest resolution achieved on a 66 cm long oTOF MS operating in the linear mode. Resolving powers of 4000 (FWHM) have been reported for a linear instrument almost three times as long as our orthogonal prototype (~1.5 m) for m/z=1166 with time spreads of the order of 9 ns (Coles & Guilhaus, 1993).

The installation of the MCP detector with the ORTEC 9306 fast preamplifier and the 9353 TDC provided the means for studying the effects of the initial ion conditions on resolution. Experiments carried out with the system at its final stage showed that the source optics, and the spatial and energy characteristics of the ion beam in the effective region of the orthogonal gate, were key parameters for enhancing the resolving power. High resolution mass spectrometry was performed with our prototype and the theory of space-velocity correlation focusing is developed in the following Chapter 6.

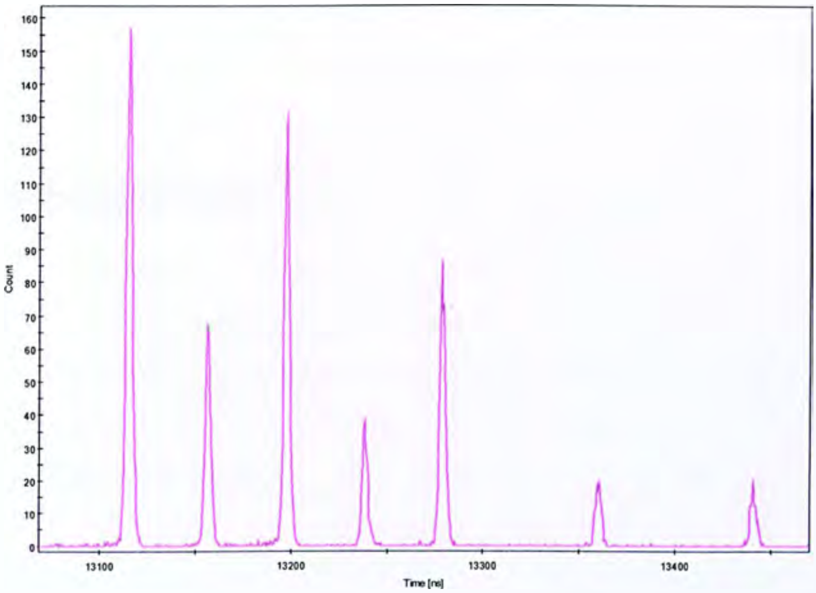

Figure 5.36 NdO spectrum with a time spread of 3.15 ns and a resolution of 2000.

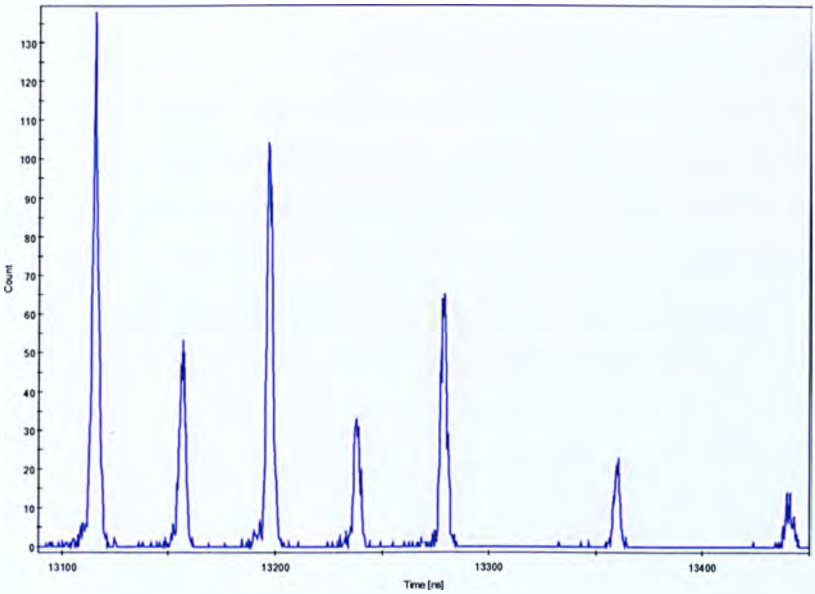

Figure 5.37 NdO spectrum with a time spread of 2.8 ns and a resolution exceeding 2300. Spectra are accumulated over a period of 90 s.

Chapter 6

Theory & Experiment

6.1 Experimental Studies of Correlated Distributions in oTOF MS

In Orthogonal Time-of-Flight Mass Spectrometry (oTOF MS) the mass analysis axis is normal to the direction of propagation of an ion beam. Monoenergetic ion beams with narrow spatial cross sections offer ideal starting conditions for high resolution TOF MS. The inherent flight angle of the ions has greatly facilitated the incorporation of the reflectron device. The orthogonal TOF technique has become the favourite choice for mass analysis in hybrid instrument design.

The widely adopted two-stage acceleration region prevails in orthogonal designs. In oTOF MS a continuous ion beam enters a relaxed electric field at right angles. This first region is operated in the pulsed mode and ions, undergoing a second acceleration step through the second static electric field, are ejected with their final energies into the field free region. Slow monoenergetic beams can be sampled with relatively high efficiencies (<50%) at a frequency of ~10 kHz (1 spectrum per 100 μs). Discrimination against the low m/z values is an inherent limitation of the orthogonal acceleration technique.

The purpose of a two-stage orthogonal acceleration region is two-fold. High electric fields are usually preferred for increasing the total energy of the ions relative to their initial kinetic energy distributions, thus reducing the effect of the latter on the final time spread at the detector plane. The restrictions imposed by the pulsed nature of the first field are eliminated by an additional acceleration step. The consecutive field is a static one and has no practical limitation on the maximum voltage required. Most important is the ability of the two-stage geometry to provide a focal point at variable lengths in the field-free region of the TOF MS. Such focal points, known as virtual sources, are fundamental to the operation of the reflectron. Interestingly enough, there is little or no information available in the literature on the ability of the orthogonal gate to focus ions in the field-free region. Space focusing is generally assumed applicable as the kinetic energy spread of the ions in the direction orthogonal to the beam is reduced and the cross section of the beam is considered as the dominant spread.

Results presented in this Chapter demonstrate that the energy spread of the ions is equally important when the focusing properties of the two-stage orthogonal region are considered. Space focusing is a special case and cannot be widely adopted for identifying optimum operating conditions. The position and the quality of the virtual source in the field-free region is a function of both the initial energy and spatial distributions of ions prior to acceleration.

In this context, the concept of space-velocity correlated ion beams is introduced and its relation with the oTOF analyzer is demonstrated in the remainder of the thesis. The theory of linear correlation was developed in Chapter 4. The analysis is extended to non-linear phase space distributions motivated by SIMION studies. Ion optical systems are investigated and experimental results are presented from the prototype oTOF MS equipped with a thermal/surface ionization (TI/SI) source and an electron impact (EI) ion source. Fundamental differences on the mechanism of ion formation between the two sources define beams with different characteristics. Coupling two ion sources on the same oTOF analyzer provides an excellent opportunity to study and compare the focusing properties of the ions.

Fundamental studies, such as the effect of grids and estimation of the initial ion conditions have been performed on reflecting geometries. The deceleration of ions and any additional grids in the reflectron distort any information on the virtual source in the field-free region. Optimization of the orthogonal gate as a stand-alone TOF element and its ability to project an optimum focus for the ions in the field-free region is the subject of this investigation.

The analysis involves a series of steps that allow for an estimation of the initial spatial and velocity distributions of the ions to be made. Improvements in the resolving power of the mass analyzer can also be achieved. A fruitful comparison between theory and experiment is presented. The characteristics of the ion beam can be inferred from the following steps: (i) Determination of the phase space of the ions in the effective area of the orthogonal gate and the effect of the ion optical system using SIMION. (ii) One-dimensional time-of-flight analysis for the specified starting conditions. Focusing curves are plotted where the time spread of the ions is computed as a function of the parameter ξ, the voltage ratio of the two stage system. (iii) Experimental determination of the focusing curves. The time spread of the ions is observed for a series of ξ values. (iv) Any variations in the starting conditions for the TOF experiment shift the focusing curves and allow for an estimation of the initial phase space distribution of the ions to be made when compared with the corresponding theoretical results. The effect of detector displacements is examined. Deviations between theory and experiment and the associated errors are then discussed in terms of the approximations adopted throughout the analysis.

6.2 Thermal/Surface Ionization Source

A photograph of the triple filament TI/SI source is shown in Figure 6.1. The filament holder, mounted onto the magnetic transfer arm, carries six pin hole extensions to support the triple filament geometry. Electrical contact is made by brass strips on each side of the PTFE source block as the arm pushes the holder into position. A groove at the top of the holder is used for alignment and positioning the filament with respect to the ion optical system. Four lenses are mounted independently on the main supporting disk, which in turn is connected to the inner walls of the six-way cross chamber. A set of four deflectors is used to steer the beam and direct ions from the first lens system into a short field-free flight tube. A closer look on the lens system and the steering plates is shown in Figure 6.2. The tube incorporates 12 electrodes, which remained grounded for all the following experiments. The flight tube extension protects the ions from the high voltage fringing fields in the TOF chamber and shapes the beam with a 1 mm slit at the left far end.

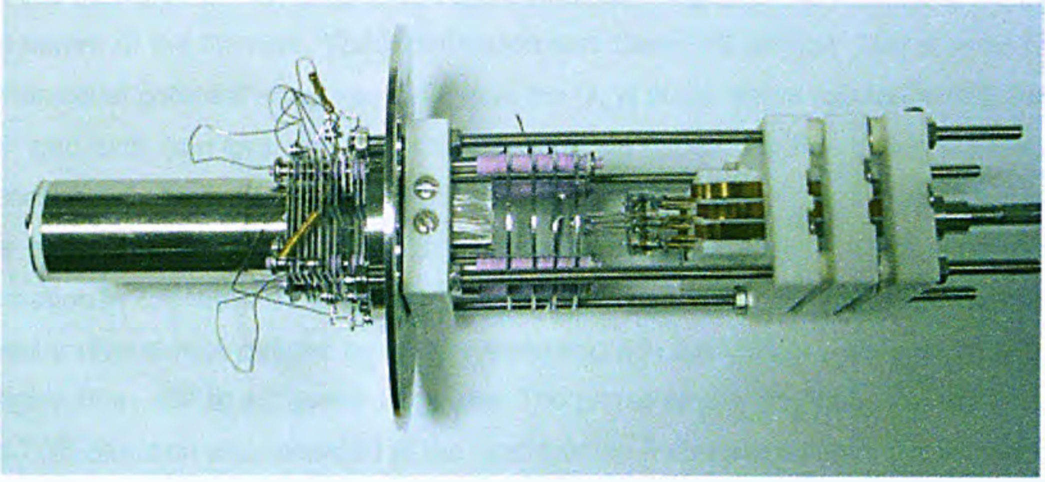

Figure 6.1 Side view of the prototype triple filament thermal/surface ionization source.

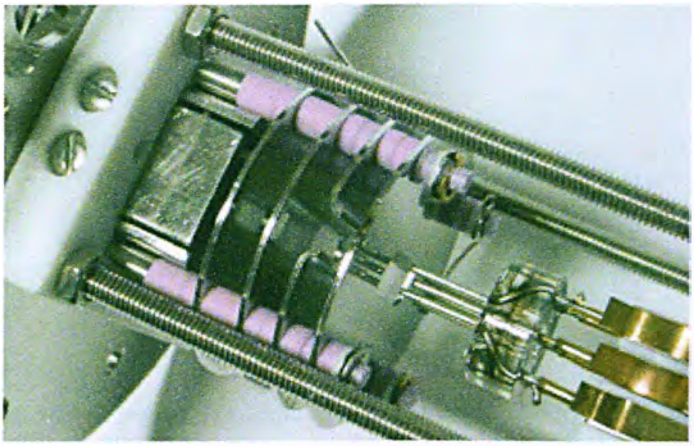

Figure 6.2 A closer look on the triple filament, the lens system and steering optics. The curved element in the lens system was designed for studying chemical interactions between filaments and for the following resolution experiments was replaced by a flat electrode for enhancing transmission.

6.2.1 TI/SI SIMION Study

Space-velocity correlated distributions are conveniently represented by phase space diagrams. SIMION was used to simulate the ion optical configuration and the corresponding initial phase space of the ions at the start of the TOF experiment. The three-dimensional geometry of the TI/SI source is shown in Figure 6.3. The rectangular slits were approximated with planar symmetry (z-axis). The assumption here is that with 10 mm long slits, edge effects are negligible for ions sampled from the centre of the filament. The z-dimension was therefore omitted. The original two-dimensional potential array was defined in the (x, y) plane with a resolution of 0.5 mm per grid unit (mm/gu). Ion trajectories were simulated for the major isotope of Neodymium, ^{142}Nd. The lower temperature threshold of the emitter for which Nd ions are generated is 1800 K (2.9 – 3.0 A). The initial kinetic energy at the point of ion formation is 230 meV, determined by thermal energies at this temperature. The initial angular divergence, defined by the elevation angle in SIMION (x,y-dimension) is 90°, ranging from -45° to 45° in the x-y plane. The phase space distribution of the ions in the TOF direction was recorded at the centre of the field-free region of the orthogonal gate, in this case defined by the end of the potential array.

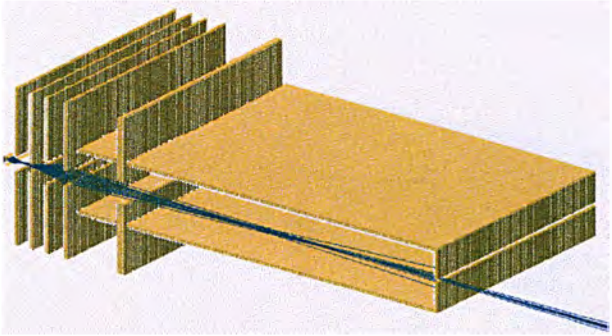

Figure 6.3 Three-dimensional representation of the potential array of the Thermal/Surface Ionization source with planar symmetry. Ion trajectories are shown in the (x, y) dimension.

Two modes have been studied for operating the source and providing correlated phase space distributions in the orthogonal region for the TOF experiment. Mode A and B are examined independently in the following sections. The potential energy surfaces are shown in Figures 6.4 and 6.5 respectively. In both cases, ions experience an accelerating field followed by a decelerating step. The curvature of the electric field provides an astigmatic focus for the ions along the source axis, which can be altered by scanning electrode dimensions and voltages. The aim is to maintain the source focal point at the exit slit and simultaneously optimize the phase space distribution in the orthogonal region. The former enhances transmission while the latter seeks optimum starting conditions for the TOF experiment by minimizing both the spatial and velocity spread of the correlated distribution.

In the particular case of orthogonal TOF systems, low energy beams are a requirement. Efficient beam sampling, minimization of scattering at the grids by increasing the angle of approach, and the necessity to avoid the use of deflectors in the field-free region since it degrades resolution, are all satisfied by slow ions. Ideally, the energy in the source direction can be as small as possible, as long as a collimated ion beam can be extracted from the source. However, slow ions are useful in linear geometries only. In reflectron designs the flight angle is an essential feature and energies of the order of 15-20 eV are more practical. The TI/SI prototype operates in the linear mode and an effort was made to provide the TOF analyzer with the slowest possible ion beam. 10 V on the filament was the minimum value at which ions could be efficiently extracted and directed into the orthogonal gate.

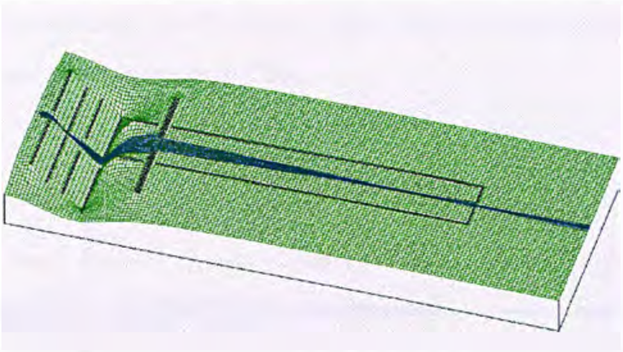

Figure 6.4 Potential energy surface in mode A. Mode A produces a greater kinetic energy spread and a wider spatial spread of the ions in the TOF direction.

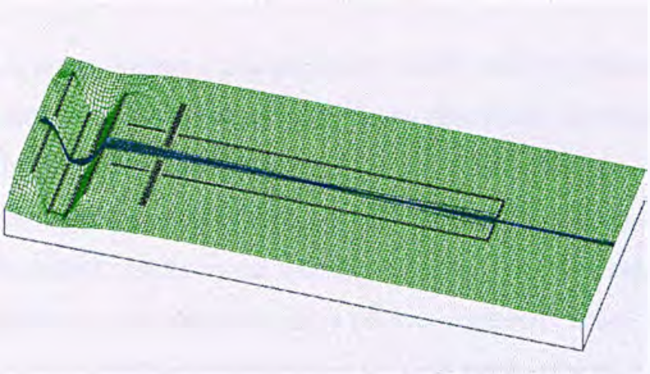

Figure 6.5 Potential energy surface in mode B. Mode B produces a low kinetic energy spread and relatively narrow spatial spread of the ions in the TOF direction. Transmission is reduced.

6.2.2 Source Mode A & Numerical Analysis

The ion optical bench and ion trajectories are shown in Figure 6.6 for mode A. Ions generated on the filament plane are directed through 4 electrodes and 2 pairs of deflectors into a field-free region before the reach the exit slit. The extended field-free region defined by a 10 cm long tube allows for a narrow divergence focal point, which is translated into minimum energy transfer between the axes in the x-y plane. The set of voltages applied on the electrodes from left to right are V_{fil}=10, V_1=10, V_2=-9, V_3=-20, V_4=-40 and V_{def}=-0.4. The phase plane of the ions in the TOF direction (y-axis) is defined by recording velocity u_y and position y at the end of the potential array. The dimensions of the potential array are chosen so that the end of the ion optical bench in the x-direction coincides with the centre of the effective area of the orthogonal configuration. The source focal point is generated before the source exit slit. For the wide initial angular spread on the filament plane, ions are lost on the mount plate and at the exit slit. Transmission exceeds 75%.

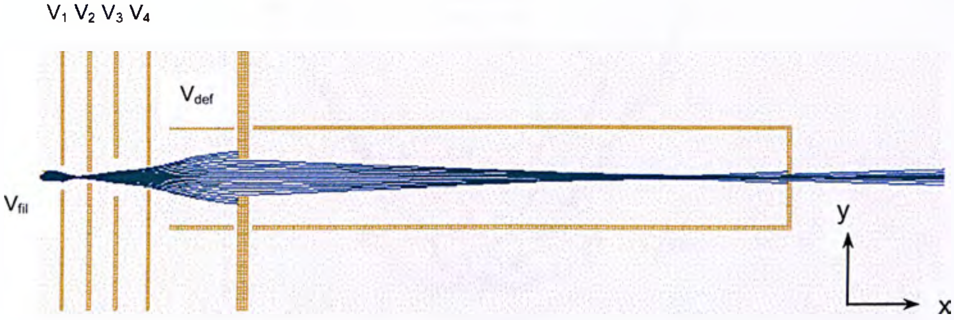

Figure 6.6 Ion optics bench and electrode voltage definitions in mode A.

The effect of the V_4 scan on the y phase plane of the ions is shown in Figure 6.7. By increasing the applied voltage on electrode V_4 the *sigmoidal* distribution incorporating ions with the same starting position having opposite initial velocities, the case examined by the turn-around effect (Wiley & McLaren, 1955), transforms into a linear correlation between initial position and velocity. With the current setup, the ideal case of a linear correlation is counterbalanced by poor ion transmission. Intermediate non-linear distributions are identified, where turn-around time effects are eliminated and ion transmission is acceptable. Figure 6.8 is a transformation of the velocity axis to initial ion kinetic energy. TI/SI sources produce mono-energetic ion beams and Figure 6.7 is a mass independent representation of the initial conditions of the ions prior to acceleration. For V_4=-40, the optimum voltage, the initial spatial spread of the ions is ~2.8 mm and the kinetic energy spread is ~8.5 meV.

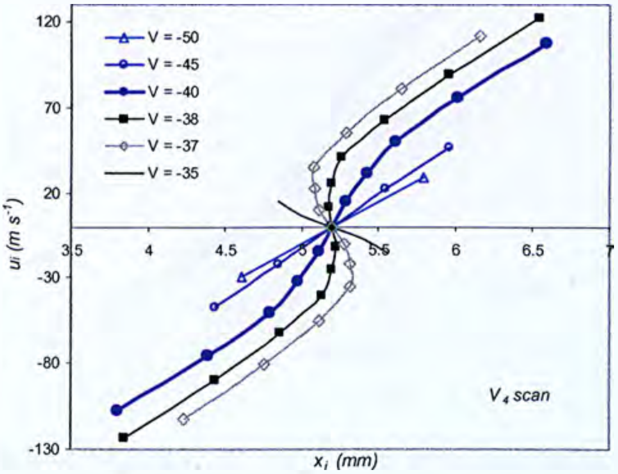

Figure 6.7 Phase plane of the ions in TOF direction (y-axis) for a series of voltages on electrode V_4. The abscissa defines the starting positions relative to the back plate of the orthogonal system. The ordinate defines the starting velocity for m/z=142.

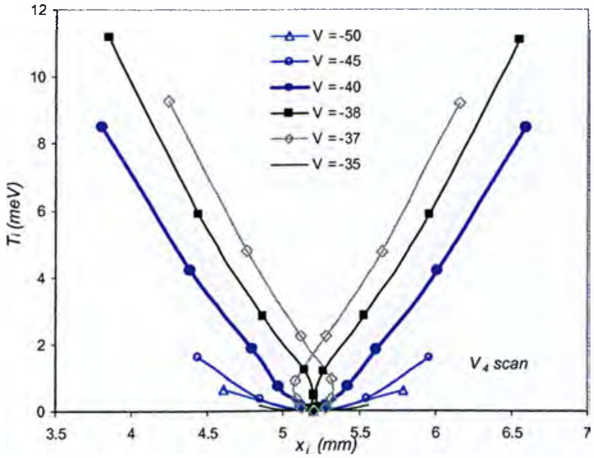

Figure 6.8 Mass-independent initial kinetic energy as a function of starting position for a series of voltage values on V_4.

Variations in the starting phase plane of the ions were studied by scanning the applied voltages on the remaining electrodes of the ion optical system. While V_4 exhibited the greatest effect on the initial conditions, small alterations can further enhance ion transmission and reduce the non-linearity of the phase plane curve. Figure 6.9 shows the effect of the second electrode V_2. Figure 6.10 is a transformation of the mass dependent velocity axis to the mass-independent kinetic energy plot.

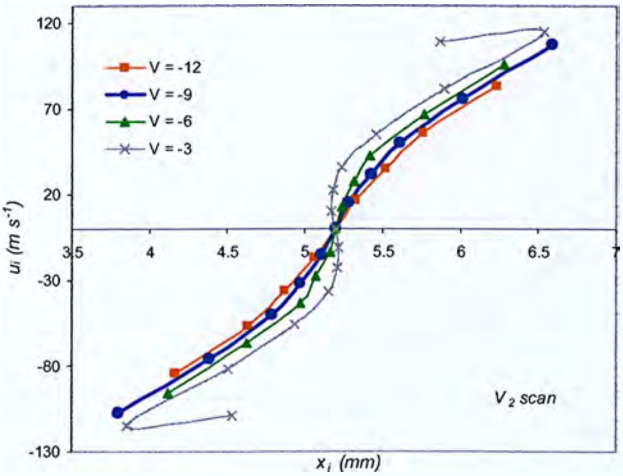

Figure 6.9 Phase plane of the ions in TOF direction (y-axis) for a series of voltage values on V_2. The abscissa defines the starting positions relative to the back plate of the orthogonal system. The ordinate defines the starting velocity for m/z=142.

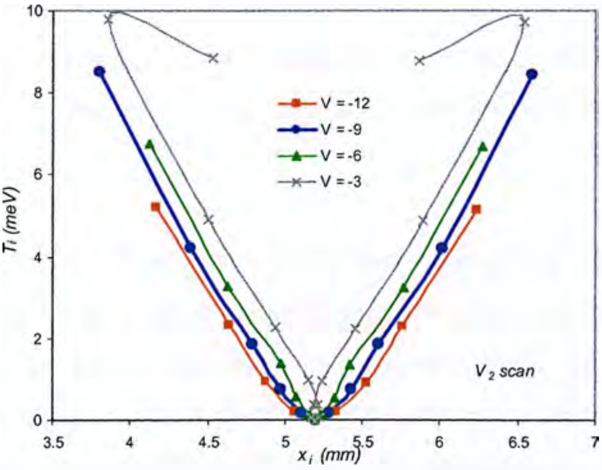

Figure 6.10 Mass-independent initial kinetic energy as a function of starting position for a series of voltages on V_2.

One-dimensional time-of-flight numerical analysis was used to obtain the focusing curves and characterize the time focusing properties of the system. The computational method requires a unique set of initial conditions and cannot incorporate the finite phase space distribution of the ions. Specific functions were used to approximate the phase space distributions of the ions determined by SIMION. An alternative approach was to approximate the mass independent energy plots, as shown in the following example.

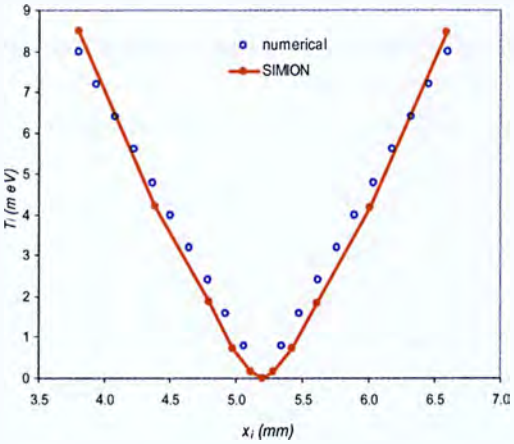

Figure 6.11 Mass-independent energy distribution of the ions.

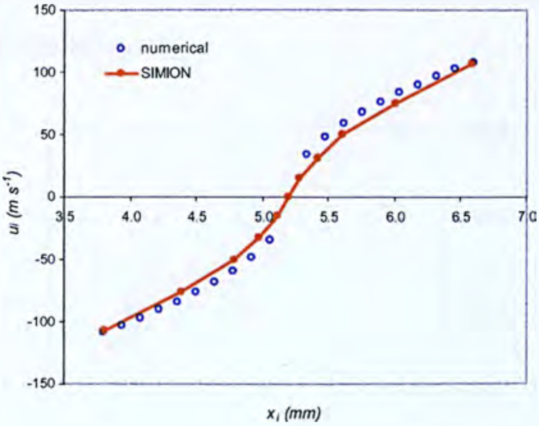

Figure 6.12 Phase plane distribution in the TOF direction for m/z=142.

Figures 6.11 is the mass independent energy plot of the optimum conditions identified in mode A. Two linear segments were used to approximate the energy distribution as a function of initial position. A transformation of these two curves into the mass dependent phase space distribution for m/z=142 is shown in Figure 6.12. In this case, the mass independent spatial spread of the ions is 2.8 mm and the energy spread is ~8 meV.

Numerical analysis of the ion's time-of-flight determined the optimum voltages for which the arrival time distribution exhibits a minimum. The simulated parameters of the mass spectrometer are s=3.8 cm, d=1.8 cm and D=67 cm. The arrival time distributions, plotted as a function of starting positions and initial ion velocities for m/z=142, are shown in Figures 6.13 and 6.14 respectively. The shape of the distributions where the time spread is minimized deviates from the typical ideal cases where a minimum, a maximum or a point of inflection is obtained. The minimum time spread is no longer infinitely small and for the ^{142}Nd isotope is 2.716 ns. The optimum set of voltages is V_s=*896* and V_d=*2652*, defined by the maximum voltage applied to the MCP, -3100 V. It must be noted that the turn-around time for the m/z=142 ion with an initial kinetic energy of 8 meV in the first electric field E_s=23579 V m^{-1} is 13.016 ns. The turn-around time is much greater than the final time spread indicating the ability of the system to focus ions with a spatial separation and highlights the error associated with the concept when space velocity correlated distributions are implemented. The effect of the relative position of the initial spatial spread of the ions on the optimum set of voltages is rather small. An adjustment of less than 2 V is required for a relative shift of 4 mm within the first electric field. In contrast, the optimum set of voltages and the behaviour of the focal point in the field-free region is very sensitive to variations in the initial ion kinetic energy.

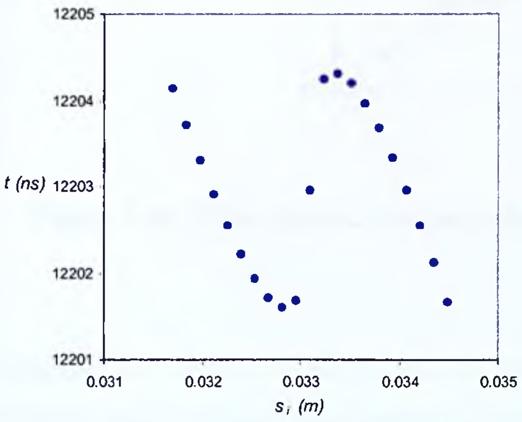

Figure 6.13 Arrival time distribution as a function of acceleration distance.

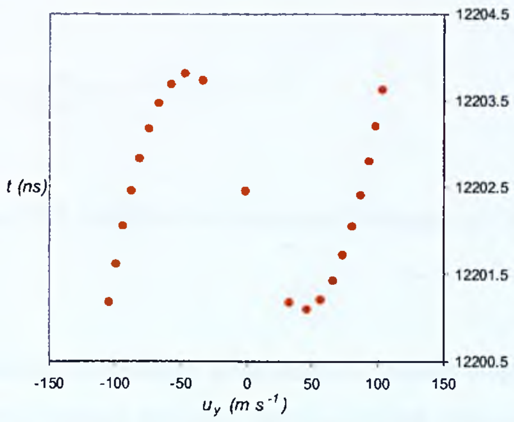

Figure 6.14 Arrival time distribution as a function of initial ion velocity.

6.2.3 *Source Mode B & Numerical Analysis*

The ion optical bench and ion trajectories in mode B are shown in Figure 6.15. The set of voltages applied on the electrodes from left to right, according to the definitions in Figure 6.6, are V_{fil}=11, V_1=11, V_2=-27, V_3=-35, V_4=-0 and V_{def}=1. Figure 6.16 shows the effect of V_3 on the phase plane distribution of the ions. The spatial and kinetic energy spread for V_3=-35 is 2.1 mm and 2 meV respectively.

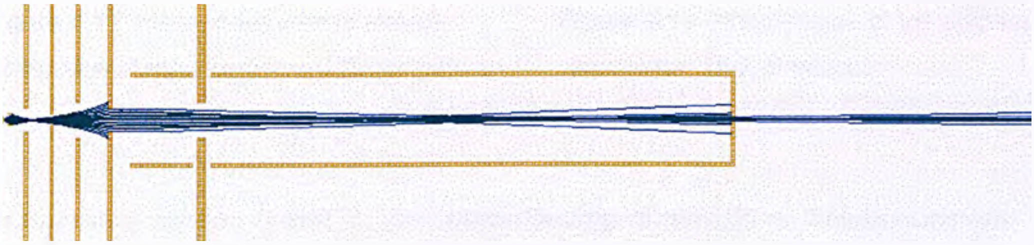

Figure 6.15 Ion optics bench and trajectories in mode B

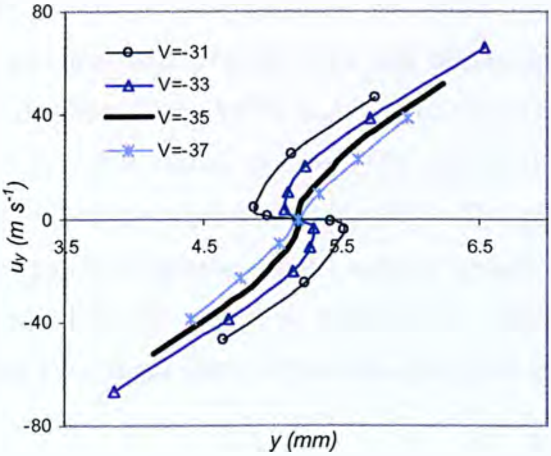

Figure 6.16 Phase plane of the ions in the TOF direction for a series of voltages on V_3.

Figures 6.17 and 6.18 show the non-linear correlated distributions determined by SIMION and the linear approximation of the former adopted for numerical analysis of the TOF system.

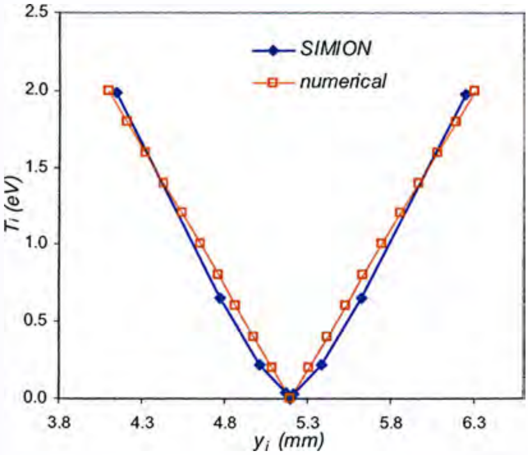

Figure 6.17 Mass-independent energy distribution of the ions in the TOF direction.

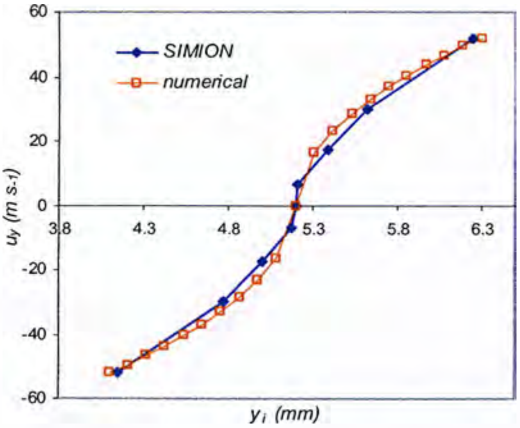

Figure 6.18 Phase plane of the starting ion cloud in the TOF direction.

The operating modes A and B, the corresponding phase plane distributions and the differences in the focusing action of the orthogonal TOF MS are examined in Figure 6.19. The arrival time spread of the ions is plotted as a function of the voltages and an optimum ratio is observed. The voltage profile across the two-stage geometry is scanned according to the relationship $V_s/2+V_d=3100$, defined by the maximum voltage on the front MCP. The starting positions and initial ion velocities are defined by the phase planes as determined by SIMION and presented in Figures 6.12 and 6.18 for modes A and B respectively. Mode B is characterized by a low kinetic energy spread 2 meV and a 2.1 mm spatial spread. The optimum voltage ratio defined numerically is ξ=0.322967 where V_s=862 and V_d=2669. The phase plane of the ions in mode A is characterized by a greater kinetic energy spread of 8 meV and a wider spatial spread of 2.8 mm. The minimum time spread is increased and a greater value in ξ is required to project the focal point at the detector plane where *ξ=0.337858* and *V_s=896, V_d=2652*.

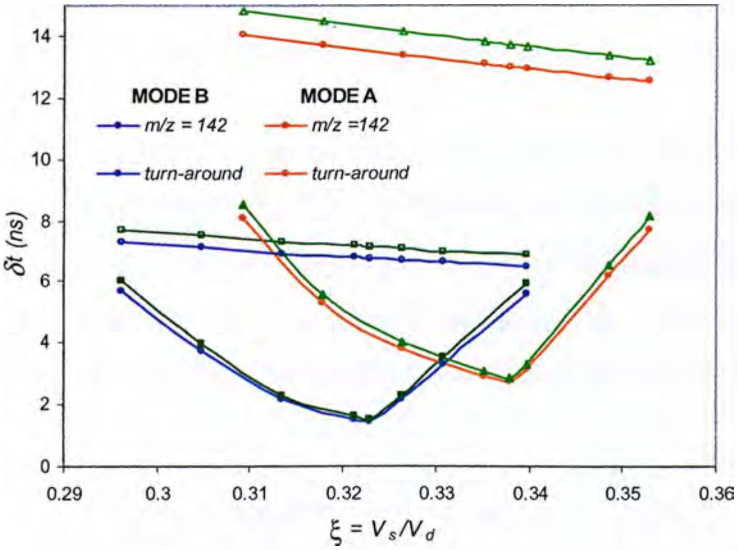

Figure 6.19 Mode A and mode B focusing curves. A mass-dependent minimum time spread and a mass independent voltage ratio is identified in each mode. The turn around time of the ions with 8 and 2 *meV* initial energies respectively is also shown to demonstrate the effect of uncorrelated distributions on the final time spread. Double lines refer to an isotope 2 amu heavier.

The effect of the turn-around time in cases were no correlation between initial position and ion velocity is developed is shown for each mode respectively in Figure 6.18. The turn-around time spread is reduced as we move to greater ξ values but no optimum is observed. The focusing action of correlated distributions and the final time spread cannot be predicted with the turn-around time approximation. Conversely, an underestimation of the initial energy spread of the ions is made when the minimum time spread at the detector is explained in terms of turn-around time effects.

6.2.4 TI/SI Results

In thermal/surface ionization ions are formed at or near the surface of the filament. The voltage drop across the filament generates an electric field transverse to the external field lines. The newly formed ions experience the fringing fields and their trajectories are deflected from the ideal normal direction. The effect can be compensated for by increasing the magnitude of the electric field between the filament and the first electrode. The fringing fields surrounding the emitter are not easy to simulate and can are neglected. The associated error is reduced by increasing the ratio of the external field to the voltage drop across the filament.

Ideally, the ion optical system samples ions from a wide filament area. The phase space distribution finally adopted for the ^{142}Nd isotope is shown in Figure 6.20. The function $u_i = 33(x_i - 2.5)^{1/3}$ used to approximate ions and their starting phase space distribution for the TOF analysis considers ions formed at point source with an angular divergence as well as ions generated across the surface of the filament.

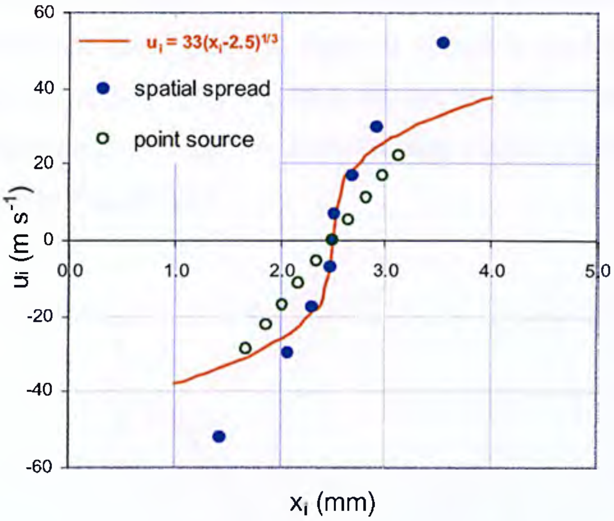

Figure 6.20 Phase space distribution of the ions in the TOF direction for m/z=142.

The experimental curves are obtained as follows. The source is operated according to the conditions determined by SIMION in mode B. It is assumed that a non-linear correlated phase space ion distribution is formed in the orthogonal region, as discussed above. A small variation in the voltages is allowed to enhance the sensitivity of the instrument and increase the count rate. The count rate is important for compensating the noise pick-up from the extraction pulse as well as random spikes that appear in the background originating from the turbo pump. The count rate has to be high enough to improve signal-to-noise ratio but low enough to avoid dead time effects of the TDC, which distort abundance measurements. Controlling the count rate is also very important when the voltage ratio is scanned and the TOF analyzer is out of focus. As the peak intensity is reduced, noise interferes strongly with peak shapes, altering the time spread of the ions and distorting the focusing curves.

The total number of spectra for a pulsing period of 50 µs and a total accumulation time of 30 s is 600,000. For m/z=158 in Figure 5.2.20 the total counts over the 30 s are 6400, that is 93.6 counts per spectrum. The total counts for the same m/z value are spread over 10 ns in a single spectrum (baseline time spread). Spectra are recorded with a resolution of 0.4 ns (bin size). The 93.6 counts per spectrum are therefore spread over 25 bins, which gives approximately 3.75 counts per bin per spectrum.

During the course of an experiment, the voltage ratio is tuned to optimize the resolving power of the TOF analyzer, once a satisfactory signal intensity is achieved. The voltage on the front MCP plate is fixed at -3100 V and defines the floating voltage in the field-free region. The focusing curves are then obtained by scanning the magnitude of the pulsed first electric field. Results from a Re filament loaded with Sr and Nd are shown in Figure 6.21.

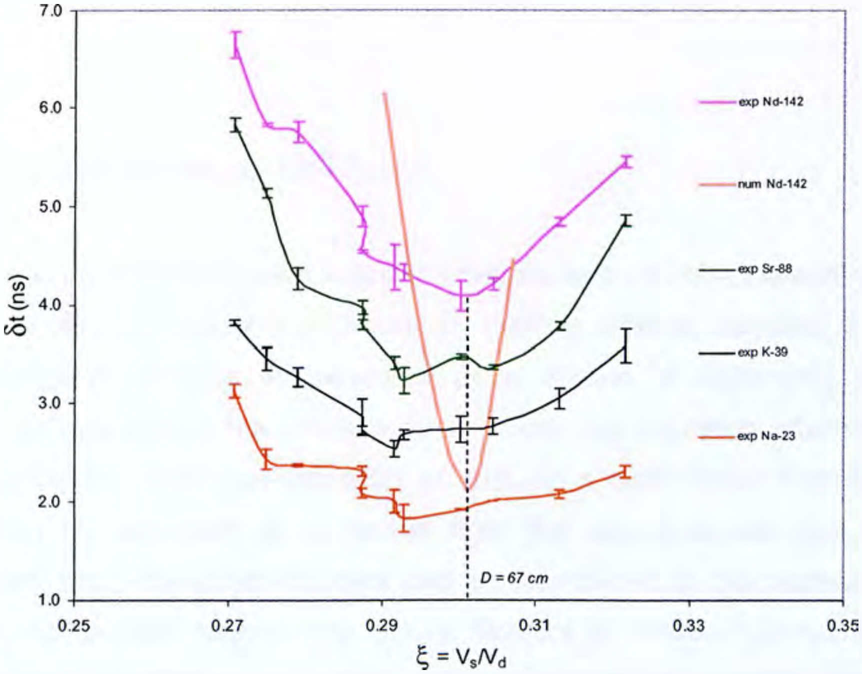

Figure 6.21 Focusing curves Na, K, Sr and Nd isotopes from a single scan.

The time spread of the ions is measured at FWHM of the peak height. Three spectra are obtained at each voltage and the associated error in the measurement is shown by error bars. A small deviation from a mass independent optimum is observed. The isotopes ^{23}Na, ^{39}K and ^{88}Sr exhibit a minimum time spread for a smaller value of ξ.

The shift of the optimum ratio corresponds to a variation of about 10 volts across the first field. The estimation of the initial conditions is made with respect to the ^{142}Nd peak. The experimental minimum time spread is for $\xi \approx 0.305$. The theoretical minimum is for $\xi \approx 0.31$, which is translated into a voltage error of the order of 15 V. The deviation between the optimum ratio determined experimentally and that estimated by non-linear space-velocity correlation theory and Figure 6.20 defines the error in the initial conditions of the ions. For the TI/SI source, the spatial spread is estimated as $3.0 \pm 0.5\ mm$ and the energy spread $2 \pm 1\ meV$. The optimum voltages approach the space focusing limit, which according to the theory define the lower voltage ratio that can be applied in a real experiment. In terms of absolute values, the space focusing limit requires an extraction voltage across the first field of ~800 V and ~2700 V across the second. For the optimum ratio determined experimentally, the magnitude of the symmetric electric pulse varied between ± 400 and ± 410. Since an upper limit of -3100 was imposed by the MCP, the voltage across the first field for the TI/SI source varied from 800 to 820 V.

6.2.5 A Final Attempt with the TI/SI Source

The TI/SI source was redesigned mainly for two reasons. A triple filament geometry can perform very interesting experiments by loading different samples at different filaments kept at variable temperatures as a means of enhancing ionization efficiency. An example is the uranium case, where the ionization efficiency when pure filaments are used is of the order of <1%. In a triple filament configuration, uranium can be vaporized as a neutral from the side filaments kept at lower temperatures while the centre filament can be maintained at the highest possible one. Neutrals directed towards the centre filament at elevated temperature are ionized with higher efficiency according to the Saha-Langmuir equation (see 7.1.1). For single filament analysis, the higher efficiency at elevated temperatures is counterbalanced by the rapid vaporization of the sample. Such experiments could not be performed with the original source as one of the side filaments was off and could not be re-connected. In addition, simulations indicated that transmission could be further enhanced by redesigning electrodes and bringing the source closer to the orthogonal region.

The step was finally taken towards the end of the project and was not proved to be a successful one. Resolution was diminished back to ~1300 and transmission was generally poorer. The reduced performance of the system is attributed to the mechanical design and construction of the source assembly. Deflection plates had to be used to re-direct the defocused beam into the orthogonal gate. Space-velocity correlation was not possible with the new design. However, several experiments were carried out and interesting conclusions can be drawn out in terms of space-velocity correlation and time focusing in oTOF MS, despite the errors introduced by steering the ion beam.

A TOF spectrum recorded with the redesigned source is shown in Figure 6.22. Ionization occurs at ~ 1600 °C, the temperature of the Re surface when ~3 A pass through the filament. At the first stages of the heating-up procedure, NdO peaks are more pronounced relative to the atomic signal. Na and K impurities are always present up to intermediate temperatures and appear in the low m/z side of the spectrum. Their depletion with time indicates the generation of a "clean" surface where only the sample is in contact with the surface of the emitter. Figure 6.23 is a magnification of the NdO isotopic cluster showing the reduced resolving power achieved with the new source.

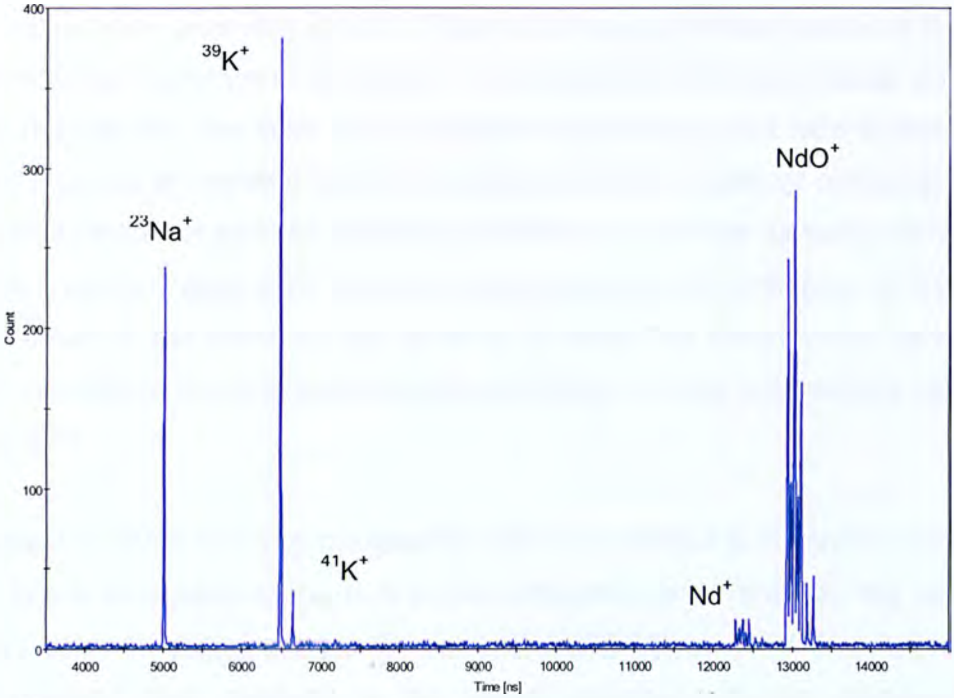

Figure 6.22 TOF spectrum of a Nd sample loaded on a Re filament. Nd and NdO signals are detected along with Re impurities which contain mainly Na and K.

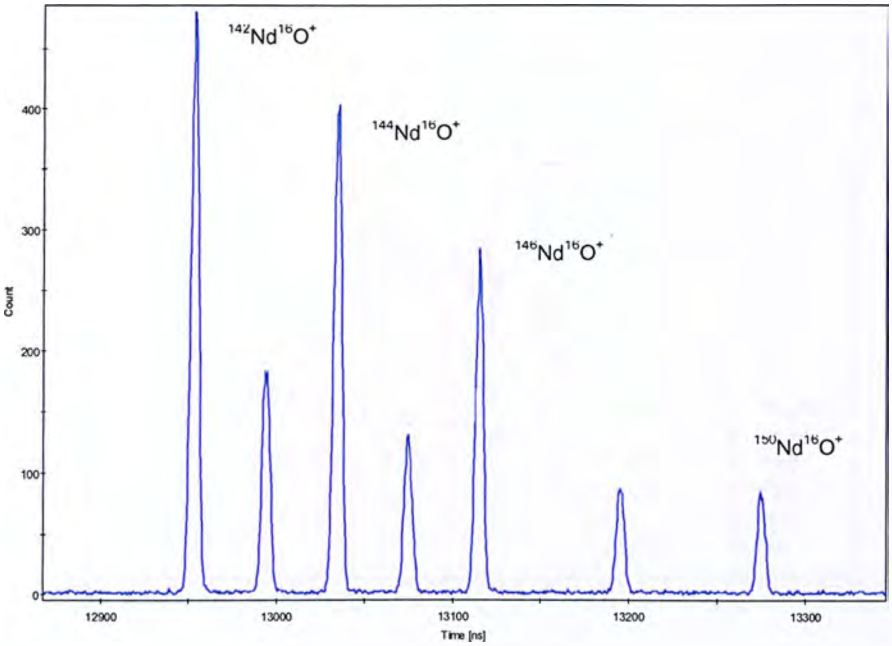

Figure 6.23 Magnification of 5.2.19 showing the NdO spectrum with a time spread of ~4.9 ns and a resolving power of ~1300.

The experimental focusing curves are shown in the following Figures 6.24 and 6.25. The time spread of the ions is plotted as a function of the voltage ratio of the two-stage acceleration geometry, $\xi = V_s/V_d$. Figure 6.24 shows the time spread of the ions at full-width half-maximum of the peaks. The symmetry in the experimental curves is greatly reduced and the error for a common mass independent ratio is increased. When the source is operated out of focus, peak intensity is reduced and peak shape is distorted which can partially explain the variations in the time spread observed for the high ξ values. Figure 6.25 shows the time spread of the ions taken at full-width half-maximum of the peaks for the same set of data. The experimental curves are shifted upwards in the time spread scale and show a mass independent optimum voltage ratio.

The deflection of the beam by the steering optics is expected to distort the correlated phase space distribution of the ions in the orthogonal gate. However, the optimum voltages determined by both the time spread at FWHM and FWTM approach the space focusing limit, similarly to the results obtained with the previous TI/SI installation. The minimum is obtained for, with V_s=814 and V_d=2711, corresponding to a ratio of ξ=0.300258.

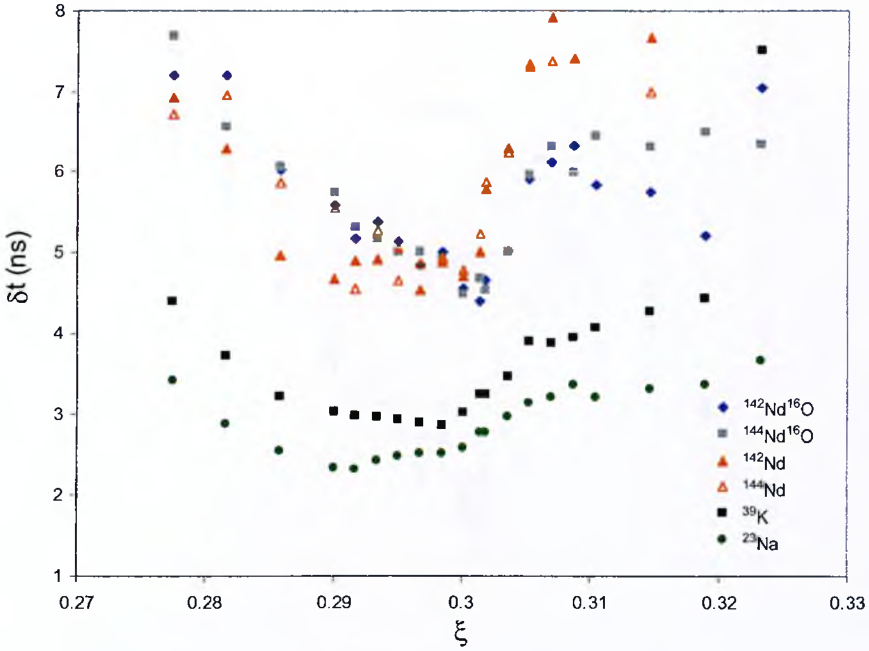

Figure 6.24 Time spread of the ions at full-width half-maximum of the peak intensities plotted against the voltage ratio ξ.

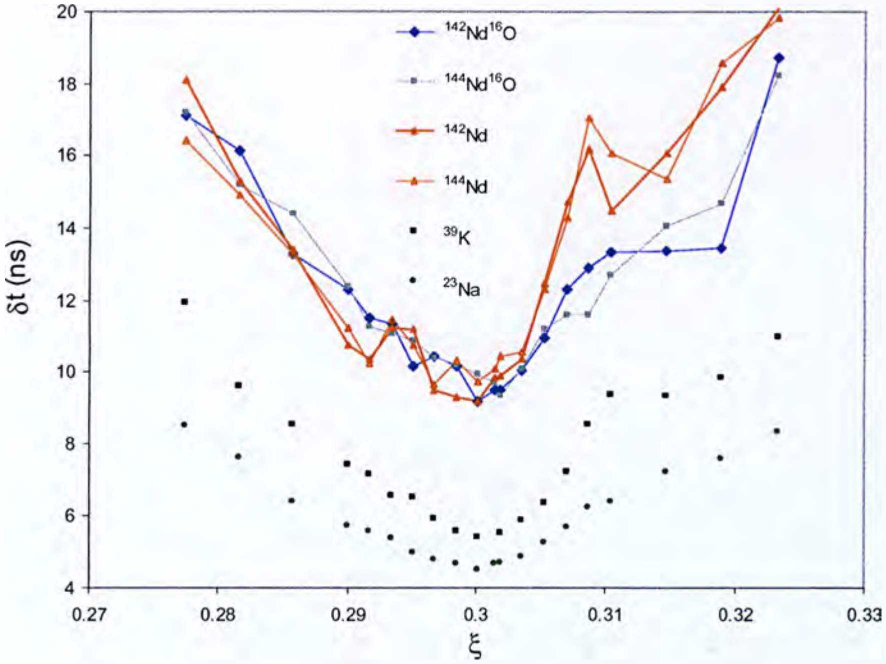

Figure 6.25 Time spread of the ions at full-width tenth-maximum of the peak intensities plotted against the voltage ratio ξ.

Figure 6.26 is a closer look on the NdO focusing curve. Error bars are an indication of the stability of ion production in the source. The stability of the sample is higher compared with that associated with the impurities, as shown in the next Figure 6.27.

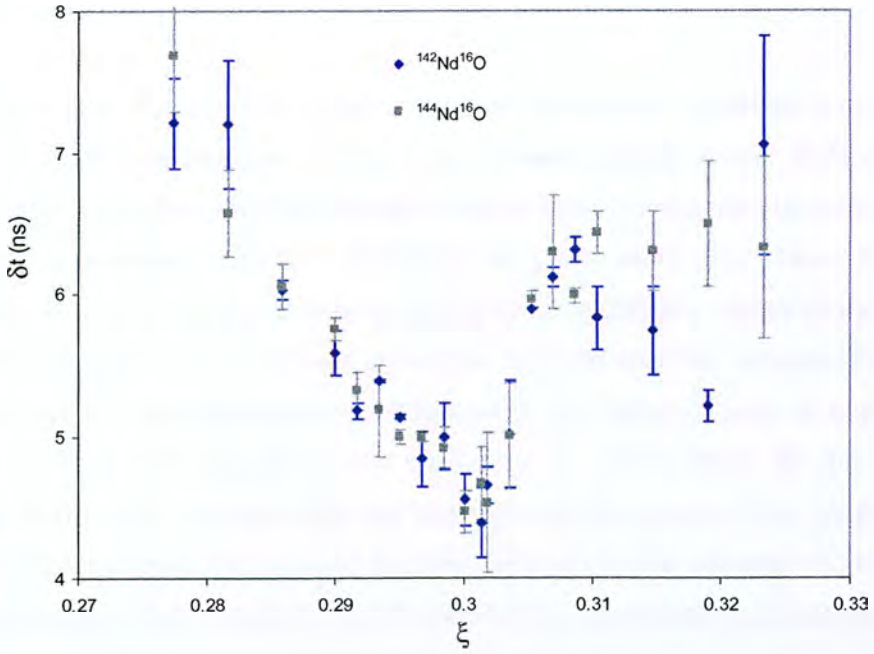

Figure 6.26 NdO focusing curve and the associated error in the measurement which demonstrates the wide variations in the time spread of the ions

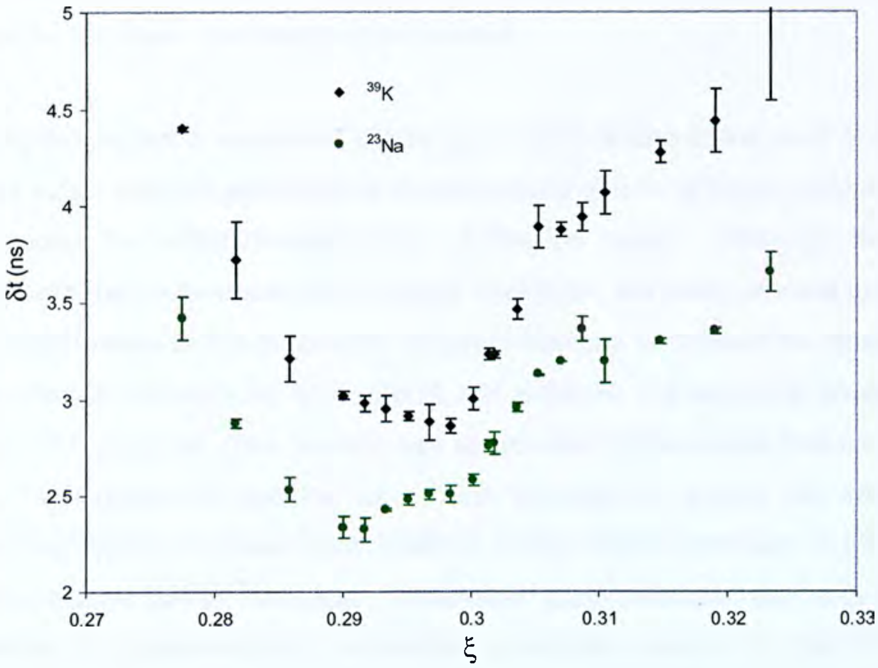

Figure 6.27 Na and K focusing curves and their signal stability which shows minimum variations in the time spread of the ions for successively recorded spectra.

6.2.6 Discussion

Observations are summarized based on the differences between experimental results and numerical analysis of the data. The theoretical arrival time spread is approximately 3 ns lower than the experimental values. Such a discrepancy between theory and experiment can be attributed to parameters that have no direct relationship with the focusing properties of the system. System variables that reduce the resolving power and cannot be corrected by scanning the voltage ratio of the orthogonal system are identified in the following: (a) Detector jitter is expected to increase the final time spread of the ions with no direct effect on the focusing properties of the TOF analyzer and the optimum set of voltages. The magnitude of the additional time spread introduced by jitter depends on the detector model as well as the final energy of the ions with which they hit the conversion dynode/front face of the MCP. (b) Signal processing, impedance mis-matching and analog-to-digital conversion of the input and output signals can also add to the final time spread displayed at the computer output. (c) Mechanical precision, perpendicularity and surface irregularities are important parameters with unpredictable effects on the final resolution. These are difficult to simulate and great care must be taken in a real experiment so that their contribution is minimized.

The assumption is that a non-linear phase space distribution at the start of the TOF experiment exists and that subsequent one-dimensional time-of-flight analysis can be used to predict the initial characteristics of the ion beam. Although the errors associated with the method are by no means negligible, the main concept introduced by these experiments is the production of space-velocity correlated ion beams as a method to counter turn-around time effects and enhance the resolving power of the orthogonal TOF analyzer. The method has succeeded in the sense that for a linear geometry, high resolution spectra have been obtained by tuning the source ion optical system. More accurate determinations of the initial conditions of the ions in the source require further analysis. Theoretical considerations and experimental investigations of space-velocity correlation principles related to the TI/SI are extended to the EI source in the following section.

6.3 Electron Ionization Source

The installation of an electron impact (EI) ion source was the latest modification on the prototype (McMahon & Papanastasiou, 2004*b*). A photograph is shown in Figure 6.28. The EI source is situated on the left hand side of the vertical tube and the ion optical system is facing, through the orthogonal gate, the TI/SI source situated at opposite ends. Both beams can be sampled by the oTOF analyzer by rotating the orthogonal acceleration region. Simultaneous detection was not possible with the current design. The EI source is reviewed in Appendix III.

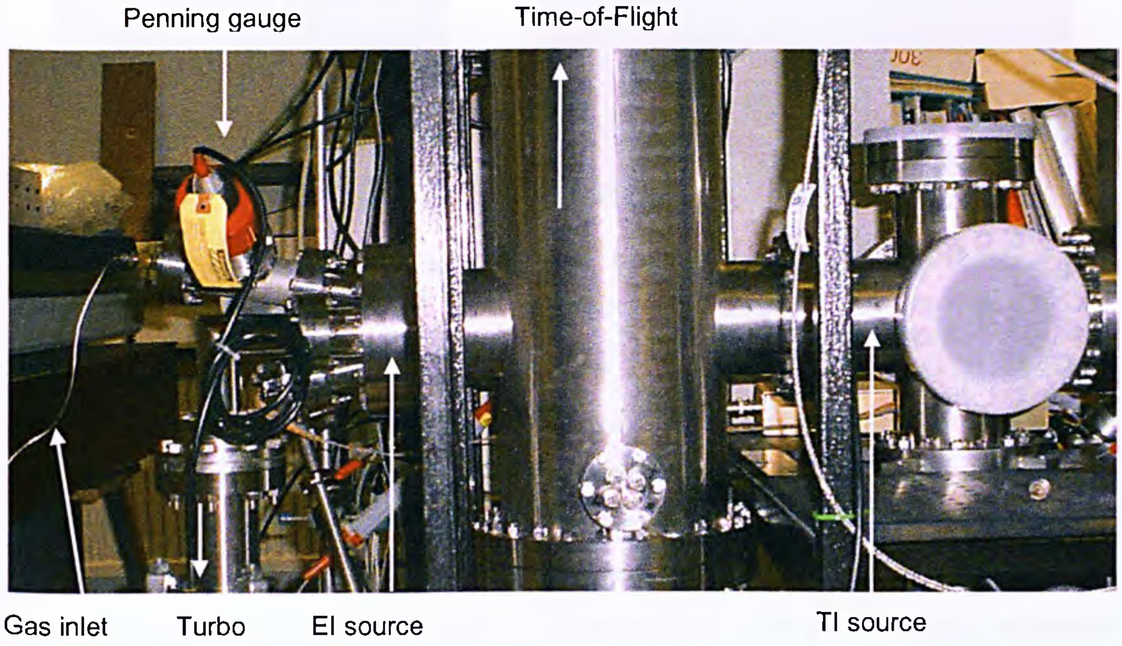

Figure 6.28 Photograph of the EI and TI/SI sources coupled on either side of the vertical flight tube.

The next Figure 6.29 shows the cluster flange incorporating the gas feedthrough, valved roughing line and Penning gauge, a 25 Ls^{-1} turbo-pump and a D9 electrical feedthrough. The original design of the source, shown in Figure 6.30, was mounted on ceramic spacers behind 2 mm disk with a 0.5 mm exit slit. Ions are focused and directed through the slit by two half plates. The source was supplied with analyte via a gas feedthrough flange, carrying a 70 μm i.d stainless steel tube with a PTFE pipe at the far end. Operation of the source at elevated temperatures melted the PTFE piping and the tungsten filament was replaced by a thoriated version. Thoriated tungsten has a much lower work function and can deliver comparable currents to the electron trap at reduced temperatures. Permanent magnets forced electrons into helical paths to increase the probability of collisions in the ionization volume.

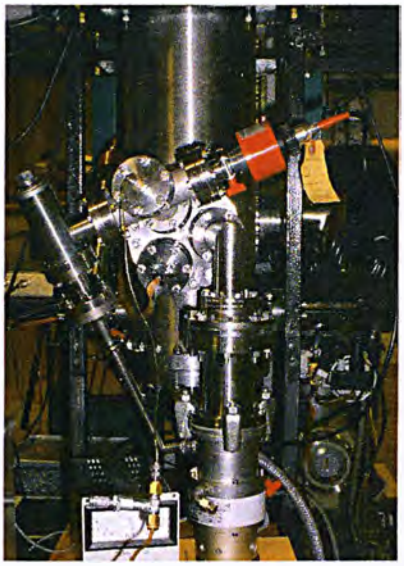

Figure 6.29 The cluster flange supporting the EI experiment.

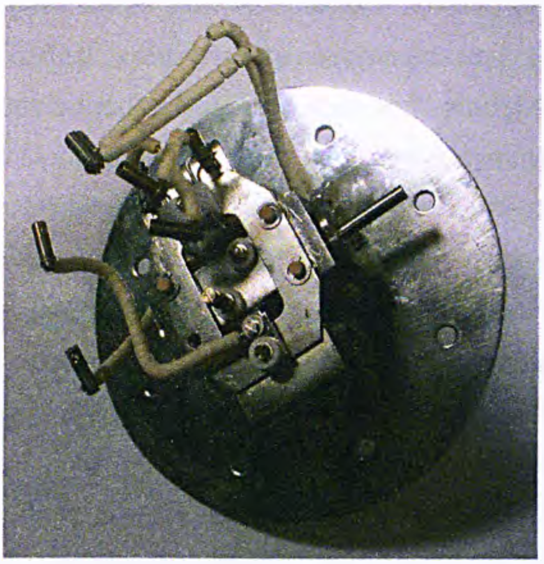

Figure 6.30 Photograph of the EI source mounted on a 2 mm disk.

The body of the final version of the EI source incorporated in the system is shown in the next Figure 6.31. In this final design no auxiliary magnetic field was employed. A slow ~10 eV ion beam was finally produced that could be efficiently sampled by the orthogonal gate. The relative position of the beam in the orthogonal gate is equivalent to that from the TI/SI source. A comparison of the time focusing properties of the TOF analyzer between the sources was then feasible as both beam energies were approximately ~10 eV.

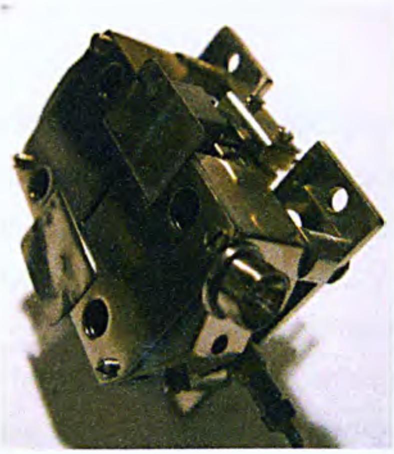

Figure 6.31 The more sophisticated design of the EI source suitable for low energy ion beams, including advanced electron trap for reducing secondary emission.

6.3.1 EI SIMION Study

SIMION studies were carried out to investigate phase space distributions of the ions at the effective region of the orthogonal gate. Initial thermal energies, position of ion formation and the effect of the ion optical system were examined and their contribution to the degree of correlation developed between position and velocity was evaluated. Figure 6.32 is the three-dimensional potential array with planar symmetry (z-axis) designed to approximate the electron impact ion source. Xe ions were used to simulate the formation of the continuous ion beam. A repeller electrode inside the source chamber walls and a weak penetrating field from the lens system facilitate ion extraction. A set of deflectors is installed downstream on the source axis and used to maximize ion throughput. Ions pass through the source exit slit into the relaxed first field of the orthogonal acceleration region. The pulsed electrodes remain grounded until the effective area of the gate is filled by the slowest ions. Ion motion is considered only in the x, y direction and the phase plane of the ions in the TOF direction (y-axis) is recorded at the centre of the orthogonal region.

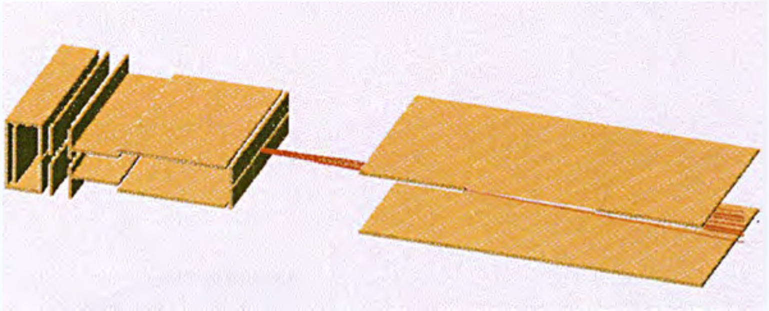

Figure 6.32 Planar symmetric potential array of the electron source, ion optics and the first stage of the orthogonal region.

The source operates in the low voltage regime and generates a ~10 eV ion beam. The weak electric fields are produced by applying voltages to the source box, repeller plate and first electrode of the ion optical system. The remaining components of the ion optics are grounded. A typical set of values is 10.2 V on the source box, 10.7 on the repeller plate and -45 V on the first lens. A two-dimensional representation of the potential array showing ion trajectories and the position where their phase space is determined is shown in Figure 6.33. The potential energy surface of the source and ion optics is shown in Figure 6.34.

Figure 6.33 SIMION ion optics bench for the EI source. Red marks show the position where the phase space of the ions is determined.

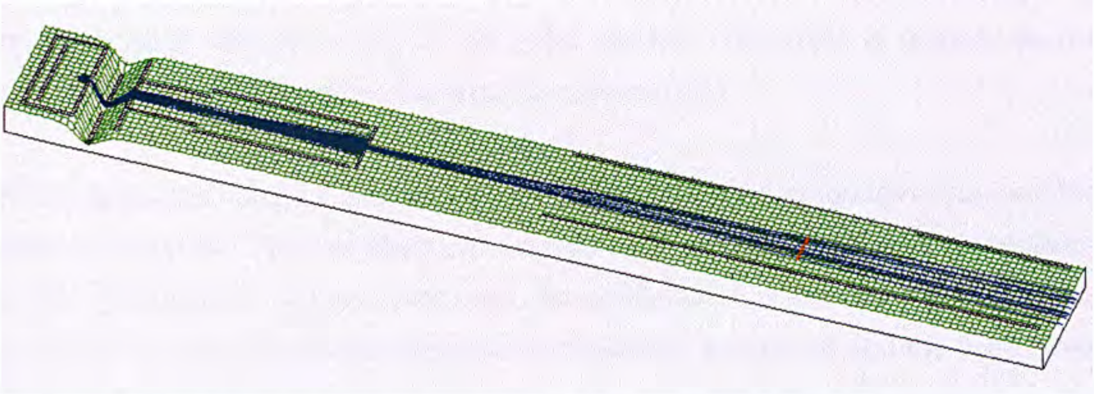

Figure 6.34 SIMION potential energy surface for the EI source.

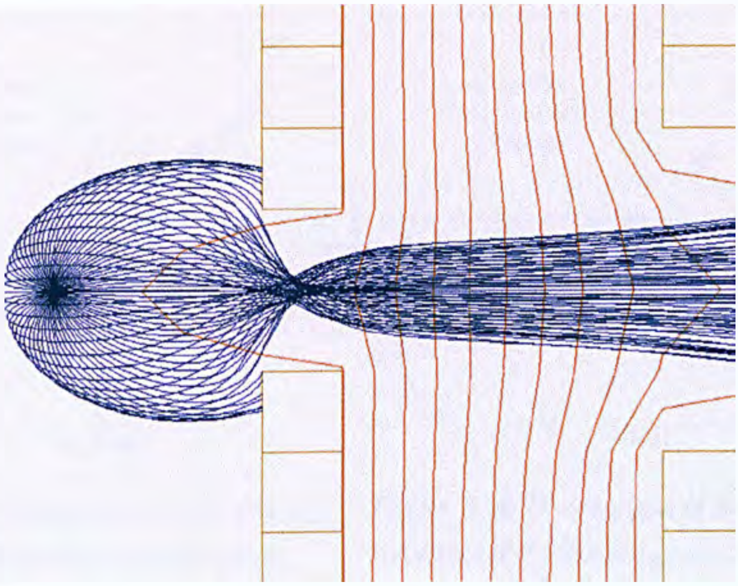

Figure 6.37 Isotropic distribution of ions as they exit the source box. Equipotential lines are also shown in 5 V steps ranging from 10 to -40 V from left to right.

An isotropic distribution for the newly formed ions is adopted to approximate ionization conditions in the box. The point source with an isotropic distribution and the subsequent ion trajectories are shown in Figure 6.37. 72 ions are considered with an angle step of 5° on the direction of the initial velocity vectors. The initial kinetic energy of the ^{129}Xe isotope is 60 meV, defined by the thermal energy of the ions at ~200°C. Figure 6.37 also shows the equipotential lines with a resolution of 5 V ranging from 10 to -40 V from left to right. The weak draw out field defines a focal point for the ions at the source box exit-slit. The angle of acceptance is wide and only ions with initial velocity vectors in the y-axis are lost. The angle is reduced as the point of ion formation is shifted towards the repeller plate.

Phase space distributions are obtained by varying the point of ion formation and the initial ion energies. The two effects are shown in Figures 6.38 and 6.39 respectively for the ^{129}Xe isotope. In the former case, the point source is shifted by an amount of $\pm 0.2\ mm$ to approximate the dimensions of electron source slit and the finite cross section of the electron beam. In the latter case, non-linearity is enhanced as the energy increases. It is interesting to note that the phase space distributions related to the EI source exhibit an inverse behaviour from those in TI/SI.

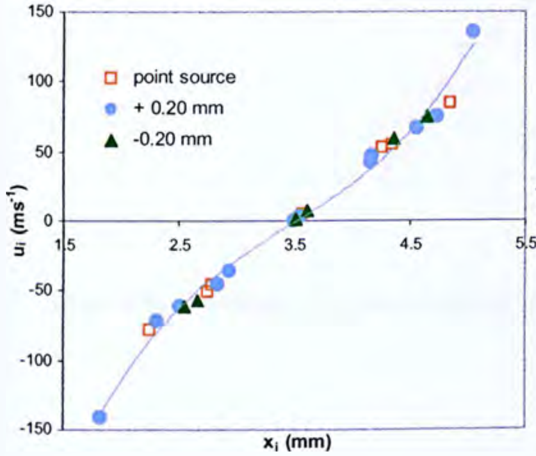

Figure 6.38 Phase plane of the ions and the effect of the point of ion formation.

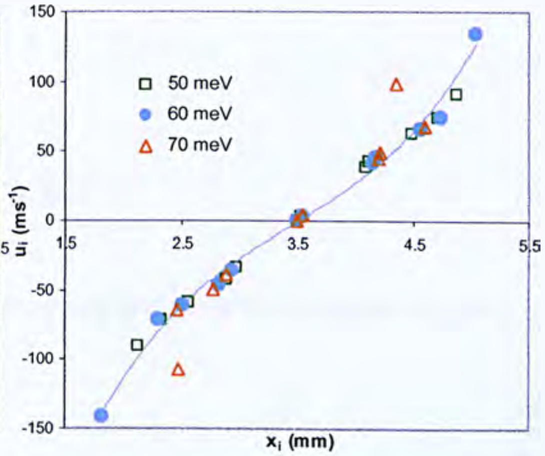

Figure 6.39 Phase plane of the ions and the effect of the initial thermal energy.

Non-linear space-velocity correlation distributions as described by the phase plane diagrams show a strong response to variations in initial conditions and applied voltages. For this simple ion optical system, correlation is lost by relatively small changes in the applied voltages. Such effects have been verified experimentally where resolution and count rate degrades with minimal adjustments in the source.

The effect is attributed to the poorly defined point for ion formation. In contrast, the well defined point for generating ions in TI/SI can justify the observation that the performance of the system is less sensitive to the source ion optics.

Deviations from non-linearity by taking into consideration the effect of the lens system are shown in Figure 6.40. An optimum value of -45 V applied to the first lens is identified, where the extremes of the distribution are reduced while a non-linear correlation between starting position and velocities is maintained. For the lower voltage values, the source focal point is projected to the source exit slit and enhanced transmission is achieved. At the effective region of the orthogonal gate however, ions are found at the same position with opposite velocities. Turn-around time effects are introduced and define the minimum arrival time spread at the detector. For the higher voltages, the dimensions of the distribution in phase space increase.

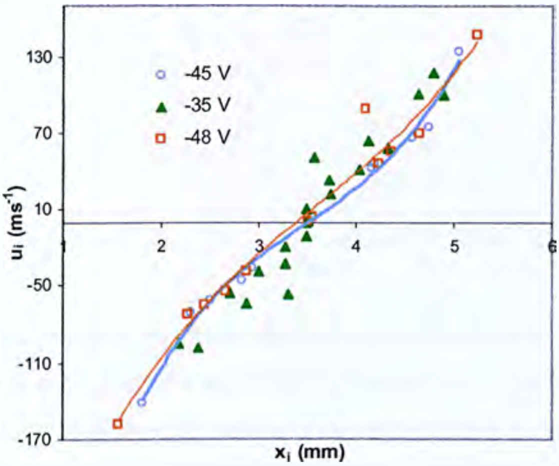

Figure 6.40 Phase plane distributions of the ions and the effect of the lens system.

6.3.2 TOF Analysis

Uncertainties in ionization position and variations in initial kinetic energy result in a finite phase space distribution for the ions. For the electron impact ion source these effects are shown in Figure 6.41. The choice of a particular space-velocity correlation function to describe the starting conditions in the effective region of the orthogonal gate is a rather rough approximation. However, the ability to perform one-dimensional TOF analysis for a uniquely determined set of initial conditions can provide a lot of information about the time focusing properties of the system. In this context, a polynomial function was selected and highlighted in Figure 6.41 that represents the upper bound of the finite phase space. The estimated initial spatial spread is 1.7 mm and the mass independent energy spread is 15 meV. Once the polynomial was identified, one dimensional numerical analysis was used to obtain the focusing curves of the system. The time spread of the ^{129}Xe ions for the optimum voltage ratio ξ is 1.6 ns and the mirrored arrival time distributions with respect to initial position and velocity are shown in Figures 6.42 and 6.43 respectively.

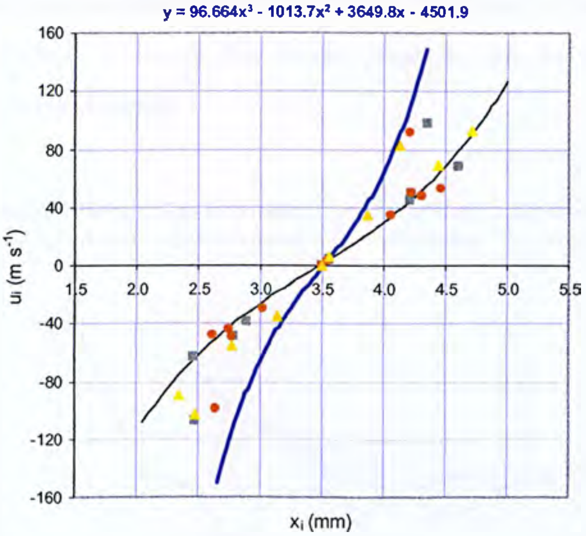

Figure 6.41 Initial phase plane of the ions determined by SIMION for ^{129}Xe. The distribution of points shows the effect of uncertainties in the position of ion formation. A distribution in the nascent velocities is also considered. A third-degree polynomial that defines the upper bound of the finite phase space is adopted for the TOF numerical analysis.

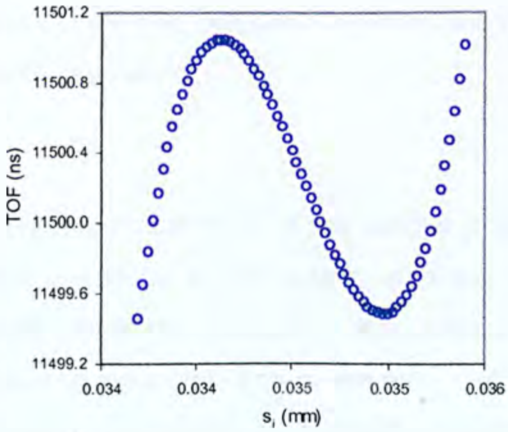

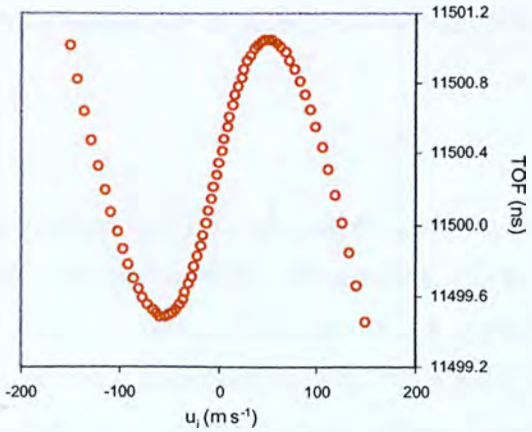

Figure 6.42 Arrival time distribution as a function of acceleration distance within the first electric field for ^{129}Xe.

Figure 6.43 Arrival time distribution as a function initial ion velocity for ^{129}Xe.

6.3.3 EI Results

The voltage gradient across the ionization volume, the operating temperature and variations on the ion optics can all influence the characteristics of the ion beam. The phase space distribution of the ions in the orthogonal gate and therefore the optimum acceleration conditions are a function of the instrumental and physical parameters in the source. An early experiment is presented in Figure 6.44 to demonstrate the effect of a small change in the source voltage on the focusing curves of the system. In either case a theoretical curve can be fitted and an estimation of the initial spatial and energy spreads prior to acceleration can be made. The flaw in the experiment is that there is no direct method to verify the assumption as the initial conditions in the source vary between experiments.

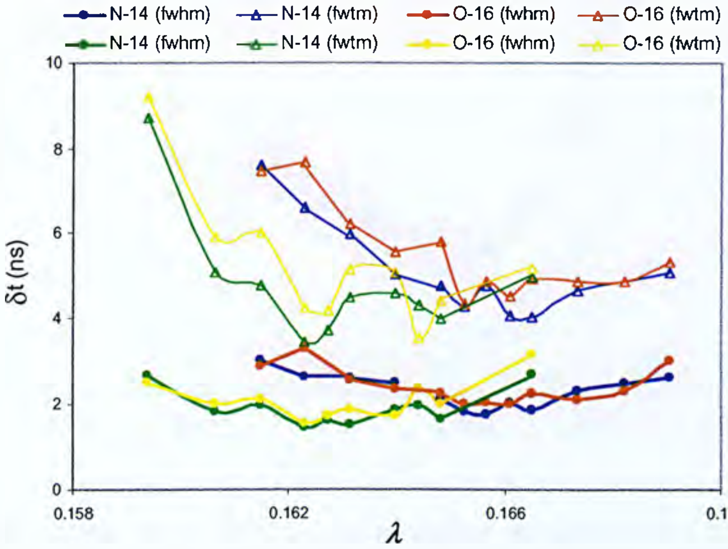

Figure 6.44 Focusing curves for two different operating modes of the EI source. The time spread of the ions, measured at FWHM and FWTM respetively, is plotted as a function of the electric field ratio λ.

A direct demonstration of the validity of the method can be provided by keeping the initial conditions in the source constant and vary instrumental parameters. Such a parameter is the position of the detector since it has no influence on the starting phase space distribution of the ions. In the following experimental set, the source is operated according to SIMION results and the adopted initial phase space distribution is that presented in Figure 6.41.

The first set of experimental data was obtained for a 67 cm long field-free region. The voltage applied to the pulsed first field is scanned and the arrival time spread of the ions falls through a minimum, as shown in Figure 6.45. Data are shown for the two major xenon isotopes, ^{129}Xe and ^{132}Xe. The focusing curve determined by the polynomial in Figure 6.41 is also included. Both experimental and theoretical results exhibit a minimum time spread for $\xi = 0.368$, which corresponds to an extraction pulse of $\pm 466\ V$ with the TOF float fixed at $-3105\ V$. The estimated spatial and energy spread in the TOF direction is therefore 1.7 mm and 15 meV respectively, as discussed above.

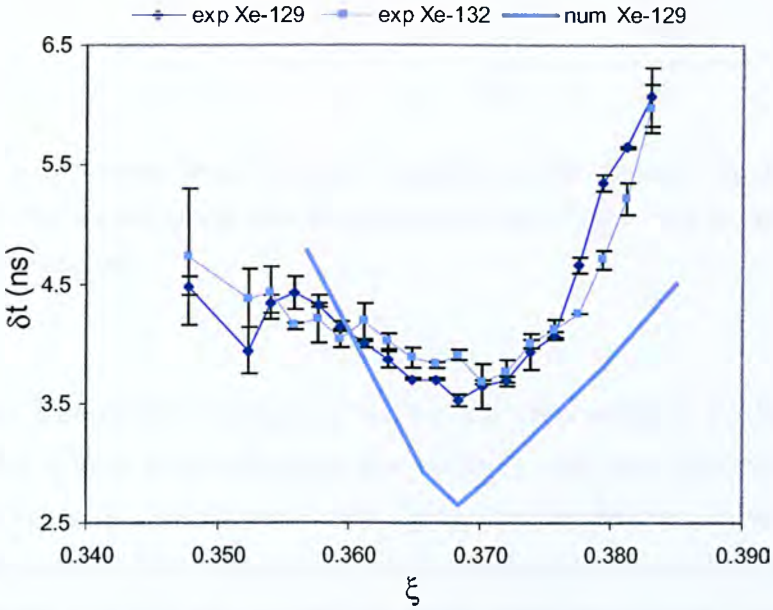

Figure 6.45 Arrival time spread of the ions measured at fwhm for the two major xenon isotopes. The theoretical focusing curve with the minimum deviation from the experimental data is fitted and allows for an estimation of the initial phase space distribution of the ions to be made.

The theoretical argument was further tested by displacing the position of the detector. Figure 6.46 shows experimental data from two detector displacements to shorter distances. As we move to shorter field-free regions the minimum time spread of the ions occurs for the greater voltage ratios. Greater electric pulse amplitudes applied across the first field are required to project the focal point to these shorter distances. The field-free region is floated at the fixed value of -3105 V. The shorter is the field-free region, the narrower the time spread of the ions at the optimum ratio.

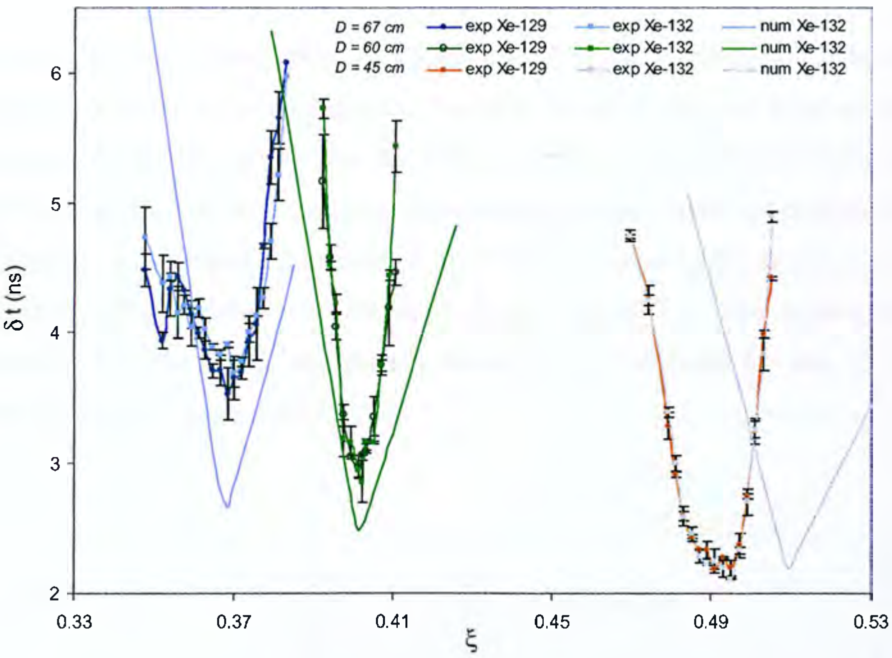

Figure 6.46 Experimental and theoretical focusing curves obtained for three detector positions. The time spread of the ions is reduced and the voltage ratio is increased as we move to shorter distances.

The predicted theoretical focusing curves for the new detector position are also shown. For the 60 cm long instrument the optimum ratio is in agreement with the experimental value. A deviation between theory and experiment is shown for the shortest configuration. The discrepancy can be attributed to variations between the flight angle of the ions and the acceptance angle of the instrument. Data are shown in the following Table 6.1.

Table 6.1 Instrumental parameters and associated errors with respect to the flight angle.

Detector Distance (cm)	*Acceptance Angle**	*Flight Angle***	*Error $\delta\phi$*
67	$86.8^o \pm 1.7^o$	87.02^o	0.22^o
60	$86.4^o \pm 1.9^o$	87.03^o	0.63^o
45	$85.8^o \pm 2.5^o$	87.08^o	1.88^o

* The acceptance angle is an instrumental parameter calculated geometrically from the size of apertures and the detector area.

** The flight angle is determined by the energy of the ions in the source (10 eV) and TOF axes.

The design of the instrument allows only for a vertical displacement of the detector. Since there is a fixed distance between detector and orthogonal gate centres, the acceptance angle is reduced for the shorter field-free regions. At the same time, for the shorter distances the time focusing principles require higher extraction voltages. The flight angle is therefore increased as the energy of the beam is always ~10 eV. These opposing effects introduce an unknown error to the final time spread observed experimentally. Nevertheless, impressive resolution is achieved for the 45 cm long instrument, shown in Figure 6.47.

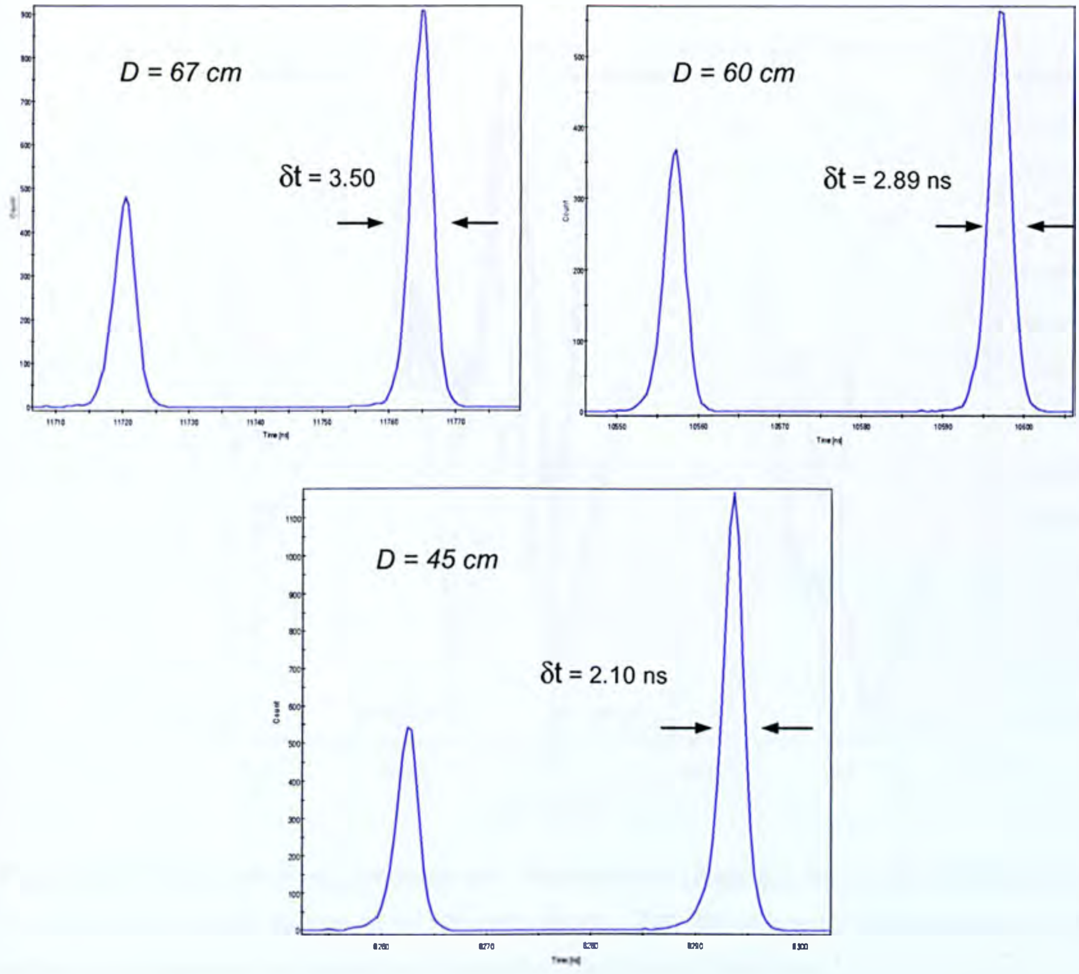

Figure 6.47 ^{131}Xe and ^{132}Xe peaks at the optimum voltage ratios for each of the three detector distances. For the 67 cm long instrument the arrival time for ^{132}Xe is 11765.2 ns with a time spread at FWHM of 3.50 ns. The resolution is ~1700. For the 60 cm long instrument the arrival time of ^{132}Xe is 10597.2 ns with a time spread of 2.89 ns. The resolution is ~1850. For the shortest linear TOF configuration of 45 cm the arrival time of ^{132}Xe is 8293.6 ns with a time spread of 2.10 ns. The resolution is ~2000.

6.4 Discussion

The concept of non-linear space-velocity correlated distributions using SIMION phase space diagrams has been introduced and tested. The prototype oTOF MS, coupled to two different ion sources, demonstrated that variations in the time focusing properties are in direct relation with the initial spatial and velocity distributions of the ions in the orthogonal gate. Low energy correlated ion beams produced by TI/SI and EI sources are studied in terms of focusing curves, as shown in Figure 6.48.

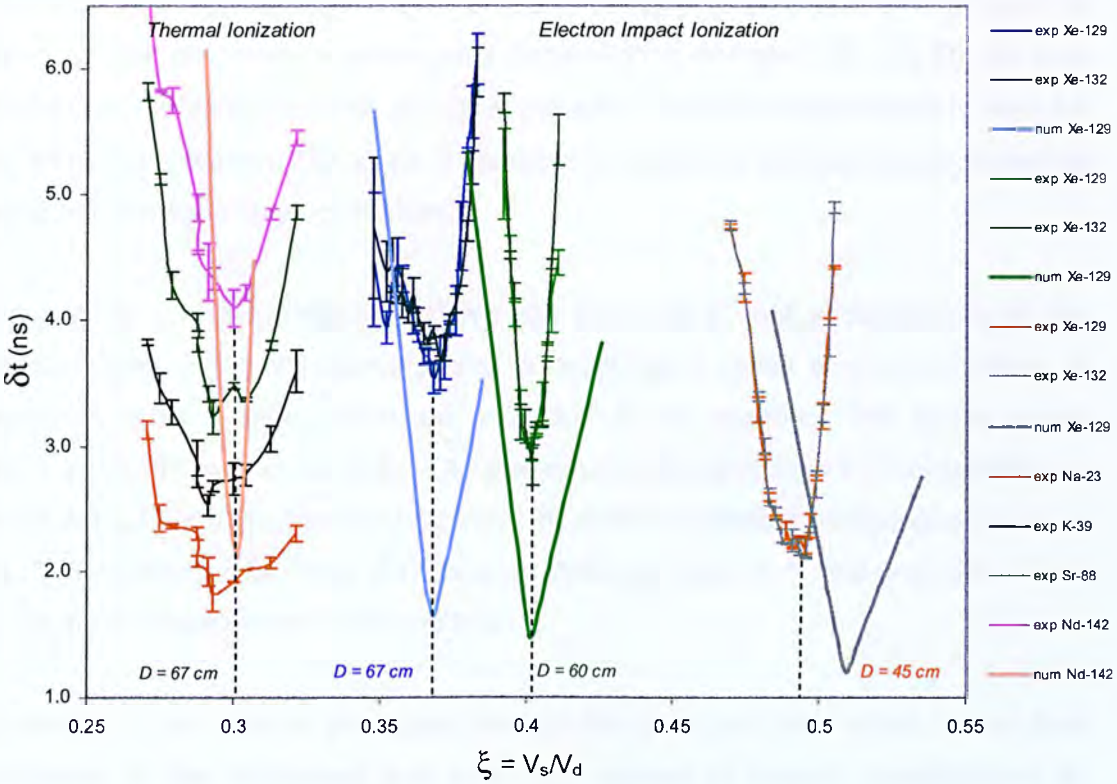

Figure 6.48 Total plot of experimental and theoretical focusing curves for the TI/SI source at 67 cm and for the EI source at 67, 60 and 45 cm. The difference in the magnitude of the optimum voltage ratio is a measure of the initial conditions of the ions.

A direct comparison can be made between the TI/SI oTOF MS and the EI oTOF MS for the 67 cm long field-free region. The former exhibits an optimum time spread for the lower voltage ratios approaching the space focusing limit. A spatial spread of $3.0 \pm 0.5\ mm$ and the energy spread of $2 \pm 1\ meV$ were extrapolated by numerical analysis and curve fitting methods. The latter requires a higher extraction pulse, represented by the higher voltage ratio, to time focus ions. The estimated spatial and energy spread in the TOF direction is $1.5 \pm 0.5\ mm$ and $14 \pm 1\ meV$ respectively. The difference in the pulsed extraction voltage between the TI/SI and EI sources is $\sim 120\ V$ when the total energy of the ions is $\sim 3.5\ keV$. Space focusing is not applicable and can only be used to define the minimum possible voltage ratio required to project ions to any distance.

The method is further tested by displacing the detector distance while the operational characteristics of the EI source are maintained constant. As we move to shorter distances the time spread of the ions is reduced and the optimum voltage ratio is increased. Stronger extraction pulses are necessary to project the focal point to these shorter distances. A satisfactory correlation is observed for the 60 cm long instrument. A shift of the order of $\sim 20\ V$ between theory and experiment is seen for the 45 cm long system. The effect is attributed to variations between the instrumental angle and the flight angle of the ions.

Curve fitting and extrapolation of the initial and spatial energy distributions in the effective area of the orthogonal region is based on a series of approximations. A series of errors is then introduced and have to be identified. The phase space distributions of the ions are finite. The analysis adopts non-linear 1:1 relationships to represent such distributions and facilitate the one-dimensional numerical analysis of the TOF system. The three-dimensional characteristics of a real experiment are therefore not incorporated in the method.

Scattering of the ions as they pass through the grids and their effect on the final resolution of the instrument has been the subject of several investigations in orthogonal TOF MS literature. Their contribution to the time focusing properties of the system has not been considered herein. The TOF numerical analysis assumes sharp discontinuities between the consecutive electric fields and neglects the time spread introduced by the fringing fields. Two comments are made with respect to the grids. As ions pass through the higher order fields, energy is transferred between the axes. Depending on the position relative to adjacent wires, some ions will be decelerated while others accelerated. The overall effect might as well be a symmetric broadening of the peak and it is questionable whether the optimum voltages on the orthogonal gate can correct for it. In addition, the selection of a two stage system where the first electric field is longer than the second, $s>d$, maximizes the angle of approach to the intermediate grids. The effect is however balanced by the lower voltage ratios which allow for greater penetration through the grids. The overall effect is unknown.

Although the errors associated with the method are by no means negligible, the main concept introduced by these experiments is the generation of space-velocity correlated ion beams as a method to counter turn-around time effects and enhance the resolving power of the orthogonal TOF analyzer. The method has succeeded in the sense that for a linear geometry, high resolution spectra have been obtained by tuning the source ion optical system.

Since the reinvention of the oTOF MS, space focusing principles are considered to be relevant to this mass analyzer and are applied in order to describe the focusing properties of the system. Instrument design and optimum operating conditions are identified according to the principles of the turn-around time and the space focusing requirements. Historically, these concepts have been implemented with two-stage acceleration configurations. Designs where the first electric field is always kept shorter than the second, $s<d$, have dominated. This restriction is challenged by the open geometry reported in this work.

The experimental results demonstrate that the space focusing principles describe a rather static situation and in the best case can define a lower limit on the magnitude of the first electric field. Furthermore, it is shown that the final arrival time spread is not directly related to the turn-around time, which is an underestimation of the initial ion energy. A comparison between experiment and theory shows that time spreads of the order of 1.5 ns can be achieved when the initial energy is 15 meV and the total energy of the system is 3.5 keV. A degree of correlation between initial position and ion velocity is therefore suggested to explain the results.

The concept of non-linear space-velocity correlated distributions is developed with particular emphasis to the time focusing properties of the oTOF analyzer. It is demonstrated that improvements in the time spread of the ions can be achieved by advanced operation of the ion optical system. The quality of virtual sources for reflectrons is directly related to the ion source of the mass spectrometer.

Chapter 7

Further Studies & Conclusions

7.1 Surface Analysis in TI/SI

Interactions between the analyte and the surface of a hot polycrystalline substrate are related to fundamental studies in experimental and theoretical physics. Electron emission and kinetic energy distribution measurements, the determination of the work function of a surface, thermionic emission and the formation of positive and negative ions on the surface, transformation of electrical power into light and ionization of organic molecules, are only a few of the concepts developed and studied. A vast amount of information is available in the literature and it is remarkable that after ~80 years the processes of thermal/surface ionization and the mechanism of ion formation is still not clearly understood. In this chapter the theory of thermal/surface ionization is traced back to its origins and a series of experiments is proposed to provide a deeper understanding of filament surface chemistry, emission kinetics and temperature effects. Kinetic energy distribution of emitted electrons and work function measurements are also presented for Re filaments, since the relationship between current and temperature is known (Papanastasiou, 2001).

7.1.1 Thermal/Surface Ionization

The theory of thermal ionization, more accurately defined as surface ionization, involves the interactions of a vapour enclosed in a hot metallic cavity followed by the subsequent emission of ions into the gas phase. Experimental studies on the emission of singly charged positive or negative ions from heated salts and electrolytes date back to the beginning of the 20th century (Richardson, 1921). The nature of the emitted charged atomic or molecular species has established the presence of impurities which usually exhibit enhanced emission efficiencies over those of the materials in which they are incorporated. The emission of impurities from solids is determined by the physicochemical processes taking place in an adsorbed layer, in this case sustained by diffusion from the bulk of the solid. The complex behaviour and the innumerable results produced from such investigations did not allow a theoretical basis to be established at these early stages of experimentation. It was only until these experiments were simplified and the idea of “equilibrium” was introduced that a firm theoretical treatment was developed. The “equilibrium processes” of ion emission that have been identified can be divided into three different mechanisms. These are desorption of foreign particles diffusing from the bulk of the emitter to the surface (emission of impurities), the evaporation of ions of the emitter itself (sublimation) and the desorption of foreign particles temporarily adsorbed from the gaseous phase on the surface (Zandberg & Ionov, 1969).

The efficiency of the process under which positive or negative ions are emitted from a hot polycrystalline surface is described by the degree of ionization usually referred to as the "Saha-Langmuir" equation. The degree of ionization α is equal to the ratio of the number of ions to the number of neutrals leaving the surface at the same time, $\alpha = v_p / v_a$. The origin of the "Saha-Langmuir" equation has been buried under the vast amount of literature concerning such experiments and the "Langmuir-Kingdon" equation (Langmuir & Kingdon, 1925) has been extensively mis-referenced instead. It is even more remarkable that the equation does not appear in the work by Langmuir and Kingdon.

Following our extensive literature investigations, the degree of ionization α and the assumptions of the theoretical treatment were located in one of the later works of Irving Langmuir (Langmuir, 1932). The original relationship between the number of positive ions v_p, to the number of neutral atoms v_a of a vapour in equilibrium with a hot polycrystalline surface in the absence of external electric fields is:

$$\ln(2v_p) = \ln(v_a) + (q/kT)(V_w - V_i - V) \tag{7.1.1}$$

The equation can be rearranged into the more familiar form:

$$\alpha = \frac{v_p}{v_a} = \frac{1}{2} e^{\frac{q}{kT}(V_w - V_i - V)} \tag{7.1.2}$$

where V_w is the electron affinity (work function) of the pure metal, V_i is the ionization potential of the gas phase species and V the contact potential difference between a clean surface and a surface with the adsorbed species under investigation. The latter parameter accounts for any alterations on the work function of the clean surface due to the adsorbed species. q, k and T are the elemental charge, $1.602177x10^{-19}$ C, Boltzmann's constant, $8.617387x10^{-5}$ eV K^{-1}, and the temperature of the emitter respectively. The parameter $1/2$ is a statistical weight factor for the particular case of tungsten, the basic refractory metal with which all the first experiments were carried out.

Eq. (7.1.1) is a combination of two fundamental relationships. *Fowler's* condition utilizes the third law of thermodynamics and specifies a state of equilibrium between electrons, atoms and positive ions in a metallic enclosure containing a vapour (Fowler, 1929). *Richardson's* equation determines the emission of electrons from a clean hot filament and was subsequently updated according to *Fermi-Dirac* statistics by *Dushman* in 1923 and by Fowler in 1929 who introduced the electron spin in the computational process (Richardson, 1901; Richardson, 1903; Dushman, 1923, Fowler, 1929). The latter is known as the *Richardson-Dushman* equation. These are, respectively:

$$K_v = \frac{v_p v_e}{v_a} = \frac{2\pi m_e (kT)^2}{h^3} e^{-qV_i/kT} \tag{7.1.3}$$

$$v_e = \frac{2\pi m_e (kT)^2}{h^3} e^{-q(V_w - V)/(kT)} \tag{7.1.4}$$

where v_e and m_e are the number of gas phase electrons and the electron's rest mass, 9.109389*x*10^{-31} Kg, respectively and h is Planck's constant, 4.135670*x*10^{-15} eV s^{-1}. Eq. (7.1.4) quantifies the emission of electrons from a partially covered metallic surface therefore accounts for the change in the work function of the material due to the presence of the adsorbed species. Substituting Eq. (7.1.4) into (7.1.3) one obtains the degree of ionization by determining the number of ions to the number of neutrals emitted from the hot surface to the vacuum continuum in the absence of external electric fields.

Eq. (7.1.3) can be traced back to the fundamental theoretical studies performed on plasmas by *Saha* (Saha & Srivastava, 1958). *Richardson's* formula (7.1.4) has its origins in the *Drude* classical electron theory of metals in the 19th century, which assumed a *Maxwellian* distribution for the kinetic energy distribution of the free electron cloud in the metal. Thermal ionization is one of the oldest experiments in modern physics. Interactions between conduction electrons and adsorbed species on polycrystalline surfaces, the emission of positive or negative ions from what Langmuir named the "genode", the physicochemical processes involved, the effect of temperature variations and externally applied electric fields on the chemical shifts and especially the reflection of low energy free electrons at the potential barrier on the surface are few of the numerous phenomena that have never been completely understood. A comprehensive study of the fundamental processes of chemisorbed species on metal surfaces along with a thermodynamic, a kinetic and a statistical derivation for the degree of ionization can be found in an excellent review by Zandberg and Ionov (Zandberg & Ionov, 1969). A reformulation of thermionic theory for vacuum diodes was recently presented (Marshall, 2002).

The validity of the “Saha-Langmuir” equation to single filament mass spectrometry is subjected to a series of approximations. The most fundamental one is that of the “equilibrium” achieved between neutrals directed onto the hot metallic surface and the ions and neutrals leaving the surface. Such an approximation ensures a time independent constant ion current which is never observed in a real experiment. Here, one should distinguish the “equilibrium” between the incoming and the outgoing particle flux from the “thermal equilibrium achieved between the adsorbed species and the hot polycrystalline surface. In ion emission at thermal equilibrium the dissociation time of the emitter-particle system is large compared to the time required for the electron states of the emitter and the particle to redistribute. In adiabatic processes, the time required for the establishment of the electron states is much less than the time required for the particle to leave the surface.

In a single filament analysis, the positive ion current decreases with time because the sample is gradually depleted from the surface. Constant ion emission currents, a requirement for precise isotopic analysis, can however be achieved over a long period of time suggesting a possible regeneration of the surface material from the bulk of the metal. Diffusion of the sample deposited on the surface into the bulk must then occur at the first stages of the heating up procedure. Preliminary results and the limitations encountered in the study of the “solvation” of ions and their migration in the bulk of the filament using Scanning Electron Microscopy (SEM) and X-ray Photoelectron Spectroscopy (XPS) are presented in the following Sections 7.1.2 and 7.1.3.

7.1.2 Scanning Electron Microscopy

In Scanning Electron Microscopy (SEM) a high energy beam of electrons is used to form a magnified image. An electron beam is sharply focused by a magnetic lens onto the surface of a specimen. The beam of primary electrons scans the surface and those reflected together with the secondaries are collected and used to modulate a separate electron beam in a TV monitor. A perspective image is therefore formed as the electron beam scans the screen at the same frequency. High energy electrons are associated with considerably shorter wavelengths than those used in optical microscopy. Electrons accelerated to 10^5 eV have a *de Broglie* wavelength of 0.004 nm enabling a resolution of 0.2 to 0.5 nm to be achieved. This is true however for transmission electron microscopes. SEM can be used with thicker samples and exhibits a resolution of 10-20 nm.

The instrument employed for the analysis of the filaments was the JEOL 5600LV SEM. This conventional design operates at pressures of the order of $\sim 10^{-6}$ mbar. The accelerating voltage is 0.5 to 30 kV, with a resolution in ideal conditions of 3.5nm. The addition of the x-ray spectrometer (energy dispersive analysis system) allows quantitative elemental analysis for elements with an atomic number greater than 5.

An SEM image of a Re filament loaded with 50 μg of Sr in HCl is shown in Figure 7.1. The sample is dried out on the surface of the filament in atmospheric conditions. The filament is overloaded and most of the sample dries out on the sides. The image shows one half of the filament length, from the leg support to the centre. The total length is 8-9 mm. A line scan with the energy dispersive spectrometer (EDS) is shown in the next Figure 7.2.

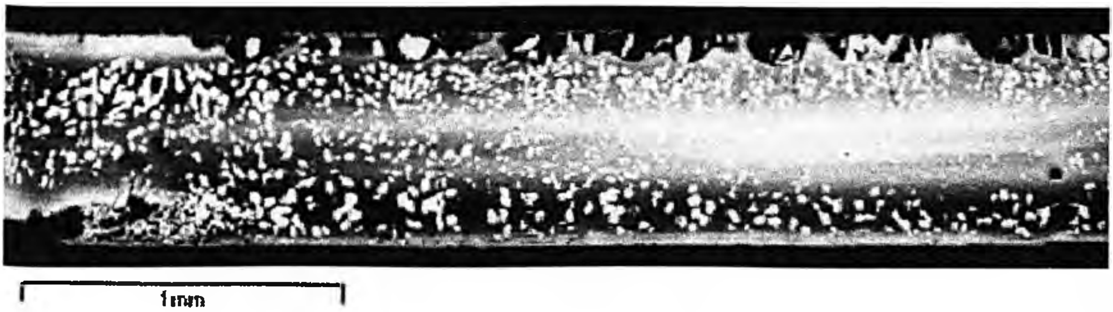

Figure 7.1 SEM image of an unconditioned Re filament loaded with Sr in HCl.

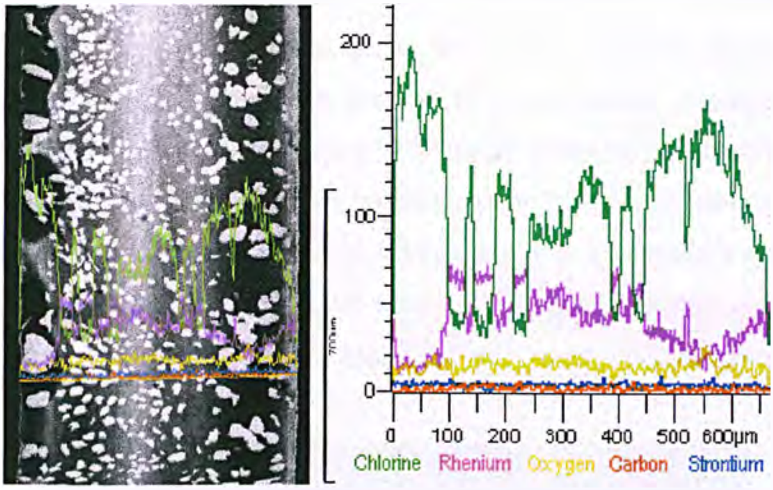

Figure 7.2 Energy dispersive spectrum across the filament width.

Chlorine dominates the spectrum and covers most of the filament area. The Re surface is exposed were Cl intensity drops. The Sr analyte intensity is much lower. Carbon is detected and probably related to hydrocarbon contamination of the sample and the filament. Oxygen is always present at appreciable amounts. The filament is installed in the mass spectrometer, heated, and back into the SEM. Figure 7.3 shows the distribution of the species on the surface following a 20 min heating process at 1.5 A, which corresponds to a temperature of ~750°C. It must be noted that this is the temperature at the centre of the filament where the Re intensity is the highest. Cl easily decomposes at these temperatures and evaporates, most probably in the form of negative ions. For the lower temperatures towards the side of the filament, Cl is still present. Oxygen, carbon and strontium exhibit uniform distributions across the surface.

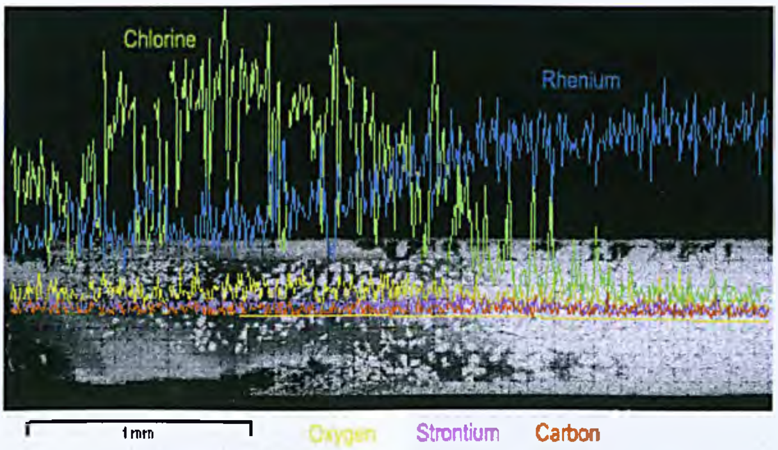

Figure 7.4 Distribution of species across half the filament length after a baking process of 20 minutes at ~750°C.

Figure 7.4 shows the ED spectrum after baking the filament for 20 minutes at 2.0 A, which corresponds to a temperature of ~1140°C. No chlorine and strontium are detected. Oxygen and carbon are still present at similar levels. A subsequent mass spectrometric analysis with the prototype TI/SI oTOF showed a very strong signal for strontium at filament currents of 2.7 A corresponding to a temperature of ~1450°C. The filament was reinstalled in the SEM instrument and ED spectra were obtained. No strontium was detected, showing the poor sensitivity of the instrument relative to the MS technique. SEM sees the cold static surface while TI/SI MS the hot dynamic behaviour of the filament.

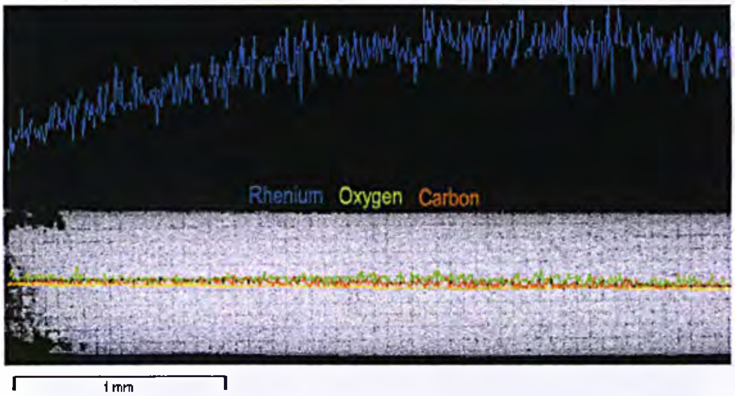

Figure 7.4 Distribution of species across half the filament length after a baking process of 20 minutes at ~1140°C.

Experiments performed with SEM and EDS were incapable of detecting samples and following signal variations as the filament was baked at the higher temperatures. It was impossible therefore to ascertain whether the sample diffuses into the filament or remained on the surface. The following Figures 7.5 and 7.6 show topographic images of the filament before and at the end of the heating cycle respectively, as described above. 20 minutes at 2.0 A are enough to smooth out surface irregularities.

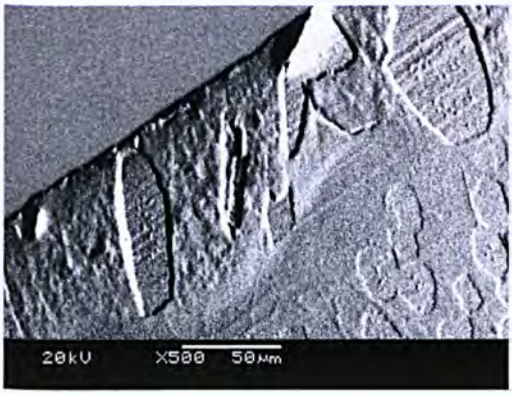

Figure 7.5 Topographic image of an unconditioned Re filament.

Figure 7.6 Topographic image of a Re filament baked at ~1140 °C.

Despite the fact that SEM is not very sensitive when compared to mass spectrometric analysis, it can provide information on the state of the surface as a function of temperature and localize the sample. An interesting example is shown in Figure 7.7 where a carburized Re filament is loaded with uranium and baked at low temperatures. Carburized Re filaments form grains and the uranium load can be detected only at the grain boundaries. Energy-dispersive spectra of the grain and grain boundaries are shown in Figures 7.8 and 7.9 respectively.

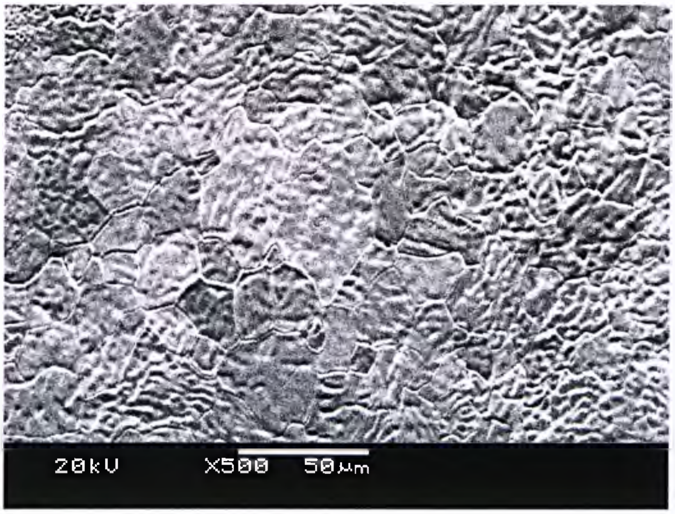

Figure 7.7 Carburized rhenium filament and the formation of large grains.

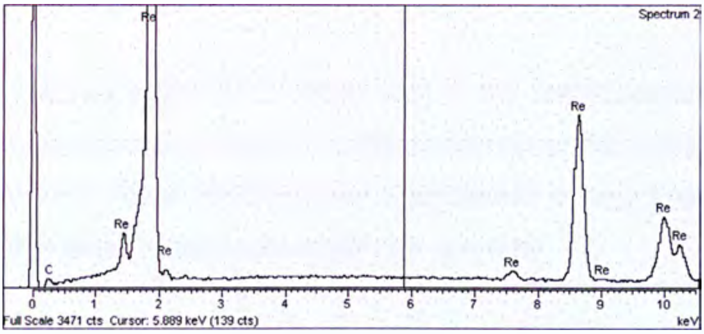

Figure 7.8 Energy dispersive spectrum of the grains in C-Re filament.

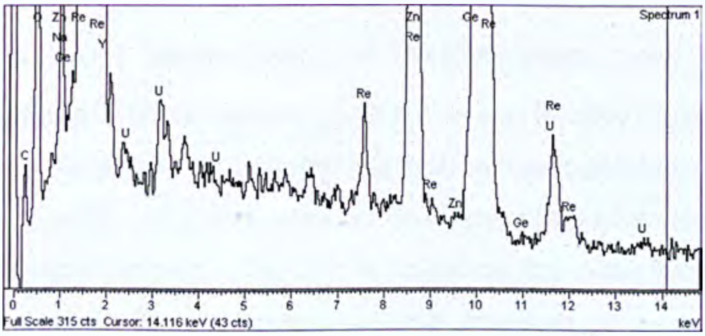

Figure 7.8 Energy dispersive spectrum of the grain boundaries in C-Re filament.

7.1.3 X-ray Photoelectron Spectroscopy

X-ray Photoelectron Spectroscopy (XPS) was developed in the mid 1960s by K. Siegbahn and his research group in Uppsala University in Sweden. Siegbahn was awarded the Nobel Prize for Physics in 1981 for his work in XPS. The phenomenon is based on the photoelectric effect outlined by Einstein in 1905 where the concept of the photon was introduced to describe the ejection of electrons from a surface when photons impinge upon it. In XPS, Al or Mg surface targets are irradiated by high energy electrons resulting in the emission of soft x-rays of energy 1486.6 eV and 1253.6 eV respectively for the two elements. The XPS technique is highly surface specific due to the short range of the photoelectrons that are excited from the solid. The energy of the photoelectrons leaving the sample is determined using a concentric hemispherical analyzer (CHA) and this gives a spectrum with a series of photoelectron peaks. The kinetic energy of the photoelectrons is inversely proportional to the binding energy of the peaks which are characteristic of the species present. The shape of each peak and the binding energy can be slightly altered by the chemical state of the emitting atom. Hence XPS can provide chemical bonding information. XPS is not sensitive to hydrogen or helium, but can detect all other elements. Such experiments are always performed under ultra-high vacuum conditions.

The principle of analysis in the XPS experiment is the measurement of the kinetic energy of the photoelectrons emitted from the specimen under x-ray bombardment. The latter is performed with a hemispherical electrostatic energy analyzer. To a first approximation, the energy of the photoelectron is given by:

$$E_e = h\nu - E_b - e\phi \qquad (7.1.5)$$

where E_e is the kinetic energy of the ejected photoelectron, $h\nu$ is the energy of the incident x-rays, E_b is the binding energy of the photoelectron and $e\phi$ is the work function of the analyzer. Since the energy of the x-rays is fairly high, core electrons as well as valence electrons can be released from atoms constituting the specimen surface. After the ejection of a core electron, the inner shell of an ionized atom has two possible relaxation pathways. The first is known as the x-ray fluorescence effect where an outer electron fills the vacancy and a quantum of x-ray is released to remove the excess energy. The second relaxation path is the radiationless Auger effect. In this case the excess energy is removed by an Auger electron hence Auger electron spectroscopy can also be performed at the same time.

X-ray photoelectron spectroscopy is a valuable analytical tool for sensitive surface chemical composition investigations. The surface of the filaments employed in isotopic MS provides a unique environment for such studies. The x-ray photoelectron spectroscopic experiment is usually performed at room temperatures. Chemical shifts as a function of temperature can reveal the physicochemical processes during both the pre-heating process as well as for the high temperatures that the filaments are usually driven to for the subsequent isotopic analysis.

The fundamental difference between a mass spectrometric analysis and the x-ray photoelectron spectroscopic approach is that the former can detect either positive or negative gas phase ions while the latter examines the chemical composition of the atoms or molecules present at the surface, prior to the desorption/ionization process. The use of an argon ion beam for sputtering may also allow depth profiling therefore reveal whether the sample diffuses into the bulk of the material provided there are no serious sub-surface mixing effects. XPS studies at the high temperatures (> 1500 K) used with thermal ionization filaments during isotopic abundance measurements have not been reported.

Preliminary experiments on pure Re filaments have been performed with the Kratos XSAM800 instrument. Figure 7.9 shows the wide photoelectron spectrum of a pure Re filament bombarded by Mg x-rays. Figure 7.10 shows the wide spectrum of a Re filament loaded with 96 ng of Uranium.

Future experiments should examine uranium loads on pure and carburized rhenium filaments. Once the detection limits are identified, the analysis must be performed at the minimum sample loads. The system should then be modified to accommodate resistively heated filaments. Saturation of the detector from electrons emitted at high temperatures are easy to avoid since their initial energy is far below the 15 eV limit required to enter the CHA.

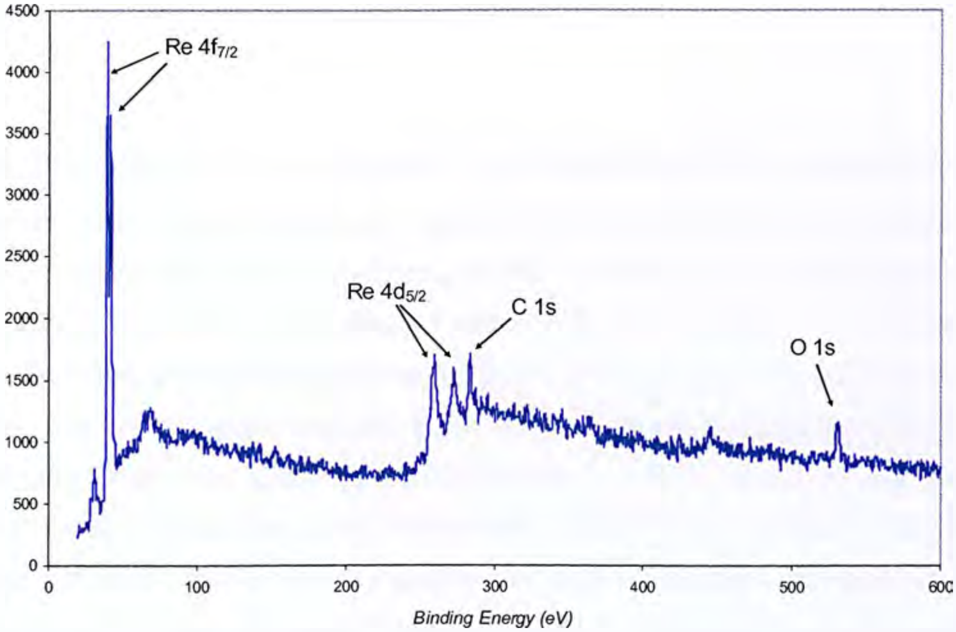

Figure 7.9 Wide photoelectron spectrum scan of a pure rhenium filament. Carbon and oxygen are the two major surface impurities.

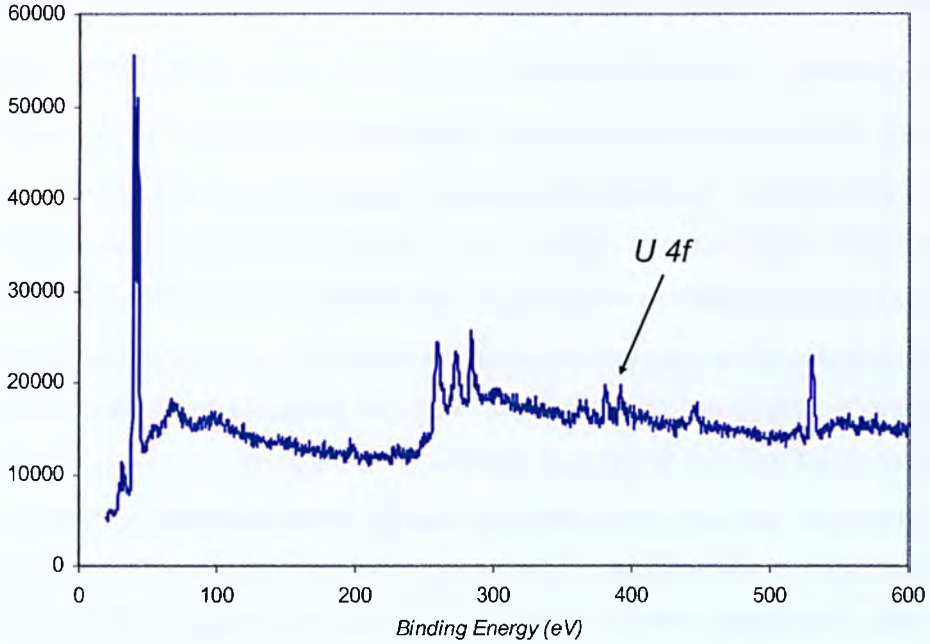

Figure 7.10 Wide photoelectron spectrum scan of a rhenium filament loaded with 96 ng of uranium. The U 4f peaks are marked.

7.2 Electron Emission & Work Function

Thermionic emission is an expression for the thermoelectric current density j emerging from a metal surface in terms of the temperature of the metal. The *Richardson-Dushman (R-D)* equation (Dushman, 1923) has its origins back in the *19th* century and the *Drude* classical electron theory of metals. The latter is an extension of the kinetic theory of gases to the free electrons contained in the metallic volume. The first emission formula, which proved to be the sound foundation of all subsequent work, was obtained by Richardson in 1901 based on the classical electron theory (Richardson, 1901; Richardson, 1903), which assumed a *Maxwellian* velocity distribution of the internal electron gas. The *R-D* electron emission formula is an expression of the *saturation*[1] current density j_o $(amp\ cm^{-2})$ of the electrons emitted by the uniform surface of a metal at high temperatures:

$$j_o = A(1-\bar{r})T^2 e^{-e\phi/kT} \qquad (7.2.1)$$

where T (K) is the surface temperature of the emitting area and k is the Boltzmann constant $(0.8617\text{x}10^{-4}\ eV\ K^{-1})$. A is considered as a universal constant $(120\,A\ cm^{-2}\ K^{-2})$ however its magnitude is a function of the state of the surface (patchiness) and the crystallographic direction. The value of A differs from metal to metal and is considered to be a temperature dependent parameter. The coefficient $(1-\bar{r})$ introduces the wave properties of the electrons and their average reflection at the surface boundary. The parameter $\bar{r}$ represents the ratio of the reflected electrons to the total number of electrons reaching the surface of the emitter. Consequently, the quantity $(1-\bar{r})$ expresses the transmitted fraction of the free electron gas. The effect of electron reflection at the surface boundary was assumed negligible and the term has been usually ignored. However, recent developments in thermionic theory (Marshall, 2002) suggest that electron reflection is more significant than usually assumed. The discrepancies between experiment and conventional formulations for predicting net currents are mainly attributed to this approximation in addition with the

---

[1] *Saturation current*: The approach based on thermodynamics and statistical mechanics assumes a dynamic equilibrium of electrons between the solid and the gas phase. At *saturation* conditions there is a net current flowing only from the metal towards the vacuum and into the gas phase. No electrons return back to the metal. It is also assumed that transition from equilibrium to saturation does not change the rate of emission (Herring & Nichols, 1949).

unknown state of the surface. A measure of the latter is reflected in the quantity $e\phi\ (eV)$ known as the *apparent* work function of the metal.

The term work function arises from the application of quantum statistics to the conduction electrons of a metal and the description of their kinetic energy distribution. *Fermi-Dirac* statistics and the free electron model are used to describe the available energy levels within the conduction band of a metal and the distribution of the free electrons among all possible energy states.

The work function is related to the kinetic energy required to remove an electron from the metal to the vacuum. This amount of energy is a function of temperature and therefore of the energy distribution of the electrons in the electron gas. Surface conditions modify the properties of the surface and for that reason alter the work function. The orientation of the surface relative to the crystal lattice of the metal and the presence of external electric fields are also considered.

A quantitative theory of the emission process must incorporate the condition of the internal electrons, since these electrons comprise the thermionic current (Reimann, 1934). The derivation of the *R-D* equation is based on thermodynamics and statistical mechanics. The emission formula incorporates the conduction electrons that have sufficient *kinetic* energy to overcome the potential barrier at the surface of the metal and enter the vacuum. Quantum statistics and the work function of a metal determine the conditions of the internal electrons therefore the work function is an essential parameter of the thermionic process.

Several assumptions have been made for the derivation of the *R-D* electron emission formula. The surface of the conductor is uniform thus any contributions of the patchy polycrystalline substrate to work function variations are ignored. Saturation current (electrons flow only from the metal towards the vacuum) can be produced by very weak external electric fields the strength of which can be set equal to zero. Significant departures from the above basic assumptions are (a) the dependence of the work function on temperature variations (apart from variations between the different crystal faces), (b) the effect of the external electric field on electron emission (c) the space charge surrounding the emitter and (d) the presence of adsorbed species on the surface.

The work function is a fundamental electronic property of a metallic surface which is becoming increasingly useful in many scientific research areas. It is well accepted that the classical approach and *ab initio* methods, although useful in understanding physical phenomena, show a great divergence relative to experimental observations. The term work function has been redefined and expressed in terms of the Fermi energy and the density of free electrons (Halas & Durakiewicz, 1998; Durakiewicz *et al*, 2001*a*). This new approach developed as an alternative to the *ab initio* methods claims an excellent agreement with experiment.

7.2.1 Definition of the work function

The work function of a metal, $e\phi$, is the kinetic energy required to extract an electron from the highest occupied level in a conduction band to the vacuum level with zero kinetic energy. Thus the work function is a temperature dependent parameter since the occupation of the available energy states in the upper-conduction band of a metal depends on the temperature of the crystal as shown by the *Fermi-Dirac* statistics. The amount of energy required to remove an electron from the metal reduces with temperature since the higher the temperature of the metal the higher the energy levels that electrons occupy.

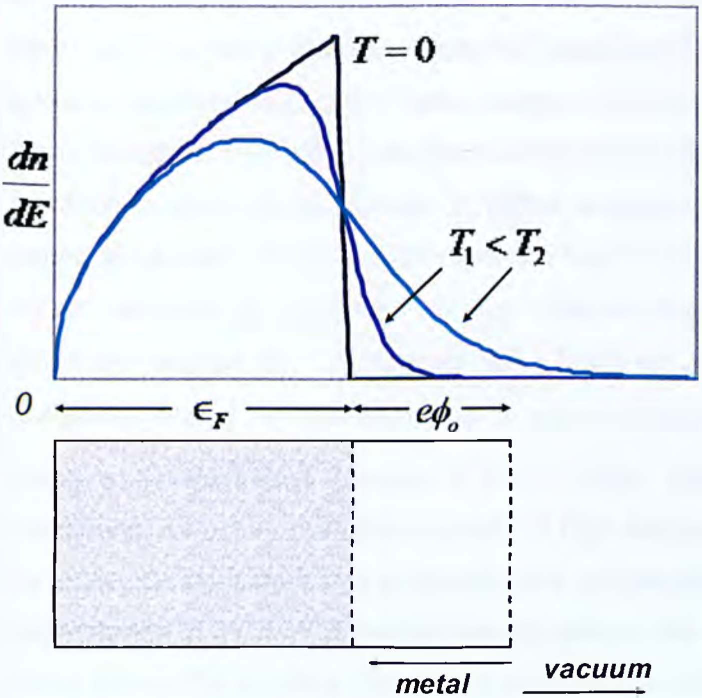

Figure 7.11 *Fermi-Dirac* statistics for the free electrons in the conduction band of a metal and the definition of the work function at absolute zero.

The term work function is usually defined for a metal in its ground state, $e\phi_o$. The ground state of a metal is at absolute zero and all electrons occupy the lowest possible energy levels compatible with the *Pauli* exclusion principle. At absolute zero the *Fermi* energy is the uppermost occupied level. The work function $e\phi_o$ at absolute zero is the amount of energy required to extract an electron from the *Fermi* level to the vacuum level with zero kinetic energy (Bleaney & Bleaney, 1976). A schematic representation of the distribution of electrons at absolute zero, the *Fermi* energy level $\in_F$ and the work function $e\phi_o$ is shown in Figure 7.11.

The vacuum level is considered to be at a finite distance from the surface of the emitter where there is no interaction between the electron and the surface of the metal. This distance can be as far as $1000\ \mathring{A}$. The interactions that alter this distance depend on the state of the surface, the presence of adsorbed species and therefore the temperature of the emitter. The presence of an external electric field will also modify the potential barrier experienced by an electron moving normal to the surface.

In addition, the ability of an electron to overcome the potential barrier at the surface, which as previously discussed can be extended hundreds of *Angstroms* from the surface, will depend on the kinetic energy of the free electrons. According to *Fermi-Dirac* statistics, only those electrons at the upper most occupied energy levels of the conduction band can be excited in higher energy states since these higher energy states are empty. For the electrons at the lower energy levels there will be no empty states available for excitation. At room temperature the uppermost electrons are thermally excited by an amount $kT \sim 0.025\ eV$, a very small energy change compared with $\in_F$. Therefore, $e\phi$ is considered practically constant over a wide range of temperatures (Alonso & Finn, 1968). However, in thermionic emission conditions, refractory materials operate at high temperatures and the work function is no longer be considered as a temperature independent parameter. The temperature dependence of the work function partially reflects the temperature dependence of the Fermi level. The existing theoretical calculations yield results inconsistent with the experimental data.

7.2.2 *Temperature-dependence of the work function*

The work function of any polycrystalline material is a temperature dependent parameter. For most emitters the variation in the *apparent* work function can be approximated in terms of a first power temperature contribution (Dushman, 1923; Nottingham, 1936):

$$e\phi = e\phi_o + \alpha_\phi T \tag{7.2.2}$$

where $e\phi_o$ (eV) is the work function at absolute zero, the temperature-independent term of the *apparent* work function. The parameter α_ϕ is the temperature coefficient of the *apparent* work function, a temperature-dependent term. The values of the temperature coefficient range from 10^{-4} to $10^{-5}\ eV\ K^{-1}$. The temperature dependence of $e\phi$ is governed by physical properties such as the *principal thermal expansion effect* and the *internal electrostatic effect of atomic vibrations* (Herring & Nichols, 1949). Both quantities $e\phi_o$ and α_ϕ are necessary in determining the *apparent* work function of an emitter and are most often used in describing the thermionic properties of polycrystalline materials.

Thermal work function shifts for polycrystalline metal surfaces have been a subject of intense investigations and recent experimental data indicate that the term α_ϕ, usually expressed as $\alpha_\phi = d(e\phi)/dT$, cannot be treated as constant over a broad temperature range (Durakiewicz, 2001*b*).

7.2.3 *The Schottky Effect*

The reduction of the work function due to the presence of an external electric field was investigated by *Schottky*. The potential energy of an electron leaving the surface of the emitter is expressed as:

$$U_e = U_\varepsilon + U_f \tag{7.2.3}$$

U_ε is the electric potential energy of the electron due to the presence of the external electric field. The field does positive work on the electron thus its potential energy decreases with distance, $U_\varepsilon(x) = -q\mathcal{E}x$. The electric potential energy of the electron due to the surface charge is represented by the *image force* (see Appendix X) and its corresponding image potential which is expressed as $U_f(x) = -\frac{1}{4\pi\varepsilon_o}\frac{q^2}{4x}$. The image potential U_f represents the work done to the electron by the surface charge. The surface charge is expressed in terms of unique image particle with opposite charge. This interaction is always attractive (irrespective of the sign of the true charge leaving the surface) and the potential energy is negative. The potential energy decreases with distance and becomes effectively zero at an infinite distance from the surface where the interaction of the electron with its image particle is infinitely small. The *total* potential energy of the electron is the imposition of the electric potential due to the external field on the image electric potential:

$$U_e(x) = -q\mathcal{E}x - \frac{1}{16\pi\varepsilon_o}\frac{q^2}{x} \qquad (7.2.4)$$

The electric potential as a function of distance from the surface is shown in Figure 7.12. In the absence of an external electric field the only force acting on the emitted electron is the image force and the corresponding image potential energy represented by the parabolic curve. Imposition of the external field modifies the potential energy of the emitted particle.

The distance where the rate of change of the potential energy becomes zero defines the end of the electron retarding field. At this distance the pulling force due to the presence of the external electric field becomes greater than the attractive image force. The potential energy at this distance represents the potential barrier that an electron has to overcome to enter the vacuum. The rate of change of the potential energy of the electron as a function of distance is:

$$\frac{dU}{dx} = \frac{q^2}{16\pi\varepsilon_o}\frac{1}{x^2} - q\mathcal{E} \qquad (7.2.5)$$

The maximum of the potential barrier is obtained for $dU/dx = 0$ and the distance, for an electron moving normal to the surface, is:

$$x_o = \frac{1}{4}\sqrt{\frac{q}{\pi\varepsilon_o}}\frac{1}{\sqrt{\mathcal{E}}} \tag{7.2.6}$$

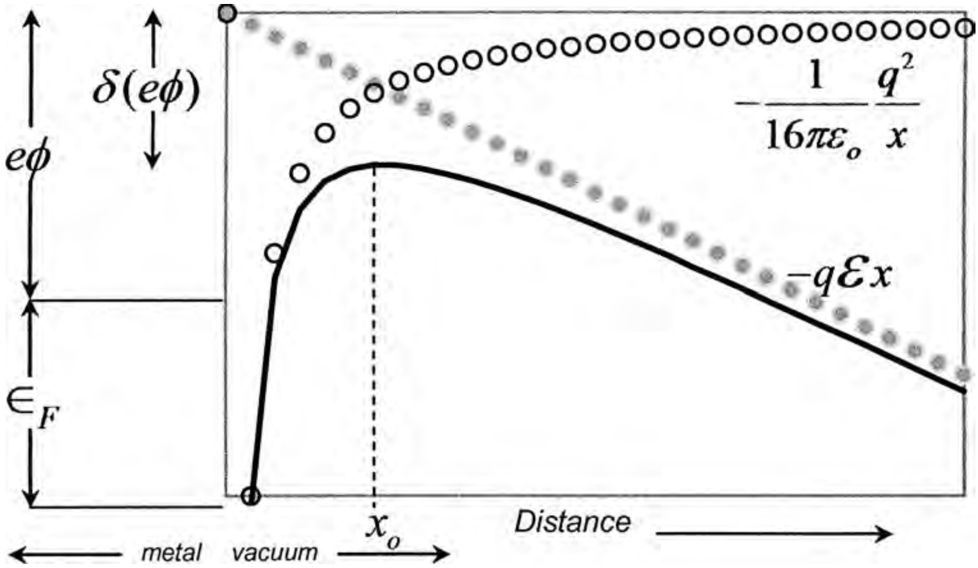

Figure 7.12 The electric potential energy of an electron moving normal to the surface of the emitter.

The potential energy of the electron at this distance is:

$$U_o = -\frac{1}{2}\sqrt{\frac{q^3}{\pi\varepsilon_o}}\sqrt{\mathcal{E}} \tag{7.2.7}$$

The negative sign of the potential energy is qualitative and expresses the positive work done by the field on the electron. Therefore, this amount of energy corresponds to a reduction of the work function (a reduction of the kinetic energy required) by an amount of $\delta(e\phi) = -U_o$:

$$\delta(e\phi) = \frac{1}{2}\sqrt{\frac{q^3}{\pi\varepsilon_o}}\sqrt{\mathcal{E}} \tag{7.2.8}$$

Substituting the value of the permittivity of free space $\varepsilon_o = 8.854x10^{-12}\ C^2 J^{-1} m^{-1}$ and the elementary charge $q = 1.602x10^{-19}\ C$, the reduction in the work function is expressed as a function of the electric field $\mathcal{E}$:

$$\delta(e\phi) = 3.795x10^{-4}\sqrt{\mathcal{E}} \tag{7.2.9}$$

where $\delta(e\phi)$ is expressed in eV and the electric field in $V\ cm^{-1}$. The change in the work function in terms of the external electric field is shown in Figure 7.13, known as the *Schottky* effect. For an anode-cathode spacing of $1\ cm$ and a potential difference of $1\ kV$, the reduction in the work function is about $0.012\ eV$. Although the effect is not great it should never be overlooked. Small changes in the applied voltage are always accompanied by variations in the electron emission.

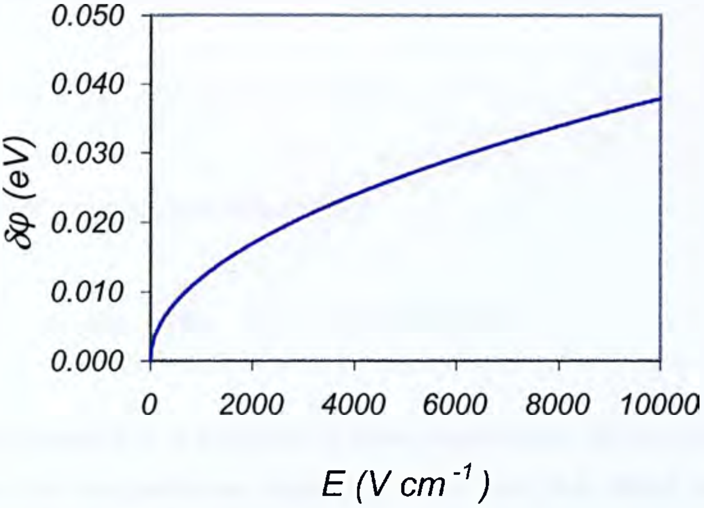

Figure 7.13 The reduction in the work function due to the presence of an external electric field.

There are several mechanisms in electron emission processes the explanation of which is attributed to experimental and theoretical investigations performed by Schottky. The *shot effect* refers to the stream of the electrons emitted by the metallic surface. In accordance with the experimental observations, the emission of each electron is assumed to be a perfectly random effect, independent in time of the emission of any other. At certain instants the number of electrons entering the vacuum must be above and at certain instants below an average value. Therefore, emission currents cannot be considered as a continuous stream of electrons. A quantitative theory for the description of the emitted current fluctuations has been proposed (Schottky, 1926). Another observation derived from the *Schottky plot* is the effect of the patchy surface on the electron current giving rise to the so-called low- and high-field work functions. According to experimental investigations, there is break point in Schottky curves indicating regions with different work functions (Juenker, 1957).

7.2.4 The Extended Electron Emission Formula

The *saturated* current density is expressed by the *R-D* Eq. (7.2.1). Introducing the effect of the temperature expressed through Eq. (7.2.2) and the reduction in the work function $\delta(e\phi)$ expressed by a decrease in the potential energy of the electron through Eq. (7.2.9), the thermionic current density of an emitter is:

$$j = A(1-\tilde{r})T^2 e^{-[(e\phi_o+\alpha T)-\delta(e\phi)]/kT} \tag{7.2.10}$$

and the final form of the equation becomes:

$$j = A(1-\tilde{r})T^2 e^{-a/k} e^{-e\phi_o/kT} e^{\sqrt{q^3\mathcal{E}}/(2kT\sqrt{\pi\varepsilon_o})} \tag{7.2.11}$$

where the current density is a function of three exponential terms, the temperature independent and the temperature dependent term and the effect of the external electric field. Eq. (7.2.11) is considered to be an extended form of the *R-D* emission formula (Kaminsky, 1965). Substituting for the *saturated* current density j_o and Eq. (7.2.1) into the extended *R-D* equation:

$$j = j_o e^{\sqrt{q^3\mathcal{E}}/(2kT\sqrt{\pi\varepsilon_o})} \tag{7.2.20}$$

The last expression is known as the *Schottky* formula and serves as the basis of the *Schottky* plots:

$$\ln j = \ln j_o + \frac{1}{2kT}\sqrt{\frac{q^3}{\pi\varepsilon_o}}\sqrt{\mathcal{E}} \qquad (7.2.21)$$

Eq. (7.2.21) is used for the experimental determination of the *apparent* work function. It relates the actual current density of an emitter, a parameter which is determined experimentally, with the *saturated* current density. The latter parameter is an extrapolation to zero electric fields and cannot be determined experimentally.

7.3 Experimental determination of the work function

Experimental determination of the *apparent* work function for single crystals, patchy metallic surfaces and non-metallic emitters can be considered as one of the *historical* experiments in physical science. The theoretical framework of thermionics and their related phenomena have been developed for over 100 years. Theoretical and experimental investigations of the term work function comprise a significant portion of the scientific literature. The numerous methods developed have been reviewed (Riviere, 1969) and include the thermionic emission method, the photoelectric effect, field emission, contact potential differences (Langmuir & Kingdon, 1929), calorimetric approaches (Kraftmakher, 1997) and the thermal ionization experiment (Hertel, 1967). The most widely adopted method prior to the invention of the laser was the electron emission method.

Rhenium work function measurements are performed with the thermionic emission method (Riviere, 1969). The first step in the experimental procedure is the investigation of electron current variations as a function of the applied voltage. For various temperatures of the emitter, the negative current is plotted as a function of the voltage difference between the anode and the cathode. The response curves produced are characteristic of the diode configuration and essential in the determination of the work function.

Three regions can be identified in current-voltage characteristic curves. In the first, an electron retarding field is generated across the diode and electrons are collected by the anode. Since the anode is held at a negative potential with respect to the cathode, the collected current determines the finite velocity with which electrons are emitted from the cathode. Retarding fields have been used for the determination of the *Maxwellian* velocity distribution of the emitted electrons (Nottingham, 1936; Hutson, 1955; Turvey, 1990). Results from rhenium filaments are presented in Section 7.3.3. Weak accelerating fields are accompanied by a sharp increase in the emitted current, the slope of which suggests that a negative space charge developed around the cathode suppresses the emission. Therefore, in the absence of strong electric fields not all the emitted electrons are collected by the anode due to the electrical repulsions exerted on the electrons by the negative space charge surrounding the emitter. In the thermionic emission experiment, space charge effects are neglected as it is assumed that *saturated* currents can be produced by very weak electric fields. The extrapolation to weak electric fields is a key feature of the method and is explained in detail in the following Section 7.3.1. Stronger electric fields are employed to remove space charge and collect all the electrons emitted from the cathode. The collected current is the *saturation* current. The region where *saturation* occurs is the *Schottky* region and any increase in the collected current is explained in terms of a reduction of the *apparent* work function due to the presence of the external electric field. Electric fields of the order of $10^7\ Vcm^{-1}$ are capable of liberating electrons without addition of energy to the cathode. The area of study is referred to as field emission (Horovitz & Johnson, 1959).

7.3.1 Schottky & Richardson Plots

Determination of the *apparent* work function requires the identification of the *Schottky* region, specific to the anode-cathode electrode arrangement. A typical diode arrangement for thermionic emission studies and work function experiments consists of a resistively heated emitter (cathode) and current collector (anode) and is shown in Figure 7.14 and. In this case the cathode is a thin long wire and a set of 3 cylinders are threaded over the cathode. Current is collected only in the middle cylinder while the other two are maintained at the same potential to reduce electric field imperfections. Ideally, electrons must be collected from a very narrow region across the filament where the temperature is constant. The advantage of a long filament is that the temperature distribution is smoothed out and electrons are collected from a region where temperature does not vary significantly. However, the voltage drop across the filament increases with the length of the wire and can be a significant source of error, especially when weak electric fields are used to force electrons towards the anode.

A threshold of the voltage is determined above which all the emitted electrons are collected on the anode. The thermionic current is then called the saturated current. It must be emphasized that the higher the applied voltage, the greater the collected current, which never truly saturates. A *Schottky* plot is then performed over a wide range of electric fields, sufficiently strong to remove space charge and direct all electrons onto the anode. In a *Schottky* plot, the natural logarithm of the current density is plotted as a function of the square root of the electric field for a series of fixed emitter temperatures, $\ln j$ vs $\sqrt{\mathcal{E}}$. Such a theoretical plot is shown in Figure 7.15. Each curve is extrapolated to zero electric field strength to define the values of the saturation current density j_o that correspond to specific temperatures of the emitting surface. Extrapolation is a mathematical trick introduced to justify the assumption of saturation conditions and equilibrium theory.

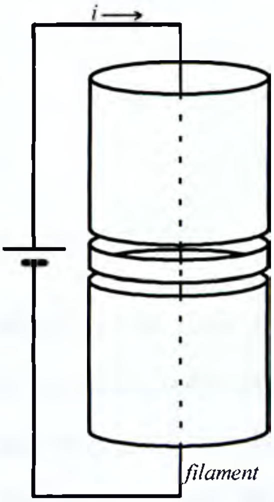

Figure 7.14 Diode configuration for work function experiments.

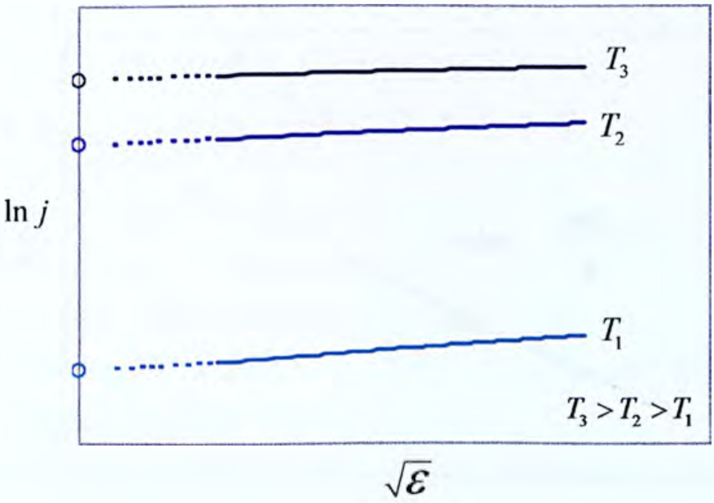

Figure 7.15 The *Schottky* plot. Current density is plotted as a function of the external electric field for the different temperatures of the emitting surface. The *saturation* current density is extrapolated to zero electric field for each temperature.

For zero electric field and neglecting the reflection coefficient, Eq. (7.2.20) reduces to:

$$j_o = Ae^{-a/k}T^2e^{-e\phi_o/kT} \tag{7.2.22}$$

The equation can be rearranged as:

$$\ln\frac{j_o}{T^2} = -\frac{e\phi_o}{k}\frac{1}{T} + \ln Ae^{-a/k} \tag{7.2.23}$$

A plot of $\ln\frac{j_o}{T^2}$ vs $\frac{1}{T}$ is called the *Richardson* plot, as shown in Figure 7.16. The experimental data should yield a straight line with a slope of $-e\phi_o/k$, thus the temperature independent parameter of the *apparent* work function is determined. The quantity $Ae^{-a/k}$ is the intersection with the abscissa from which the temperature coefficient a can be computed. The *apparent* work function is then evaluated by Eq. (7.2.2) since both $e\phi_o$ and a are known. The terms $e\phi_o/k$ and $A_R = Ae^{-a/k}$ are usually referred to as the *Richardson* work function and the *Richardson* emission constant respectively and are used to describe the characteristics of an emitter.

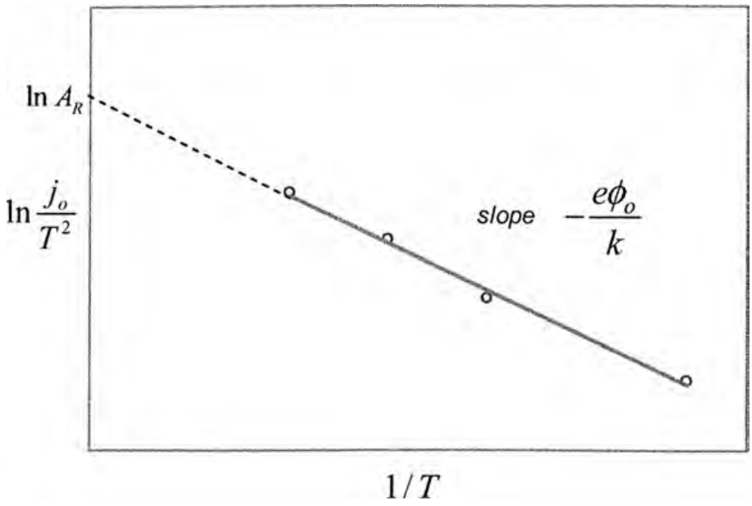

Figure 7.16 The *Richardson* plot for the saturation current density as a function of temperature.

7.3.2 The Rhenium Work Function

The diode configuration installed in a small vacuum chamber is shown in Figure 7.17. An oil diffusion pump was used and experiments were performed at pressures of the order of 5x10^{-6} torr. The Re filament was connected to a homemade constant current supply and was floated according to the requirements of the experiment. A cylindrical tube, surrounding the filament, was kept at ground potential and connected to a Keithley electrometer. Electrons emitted from the cathode were collected by the cylinder and measured. A vacuum window allowed for optical access to the filament and temperature measurements using infrared pyrometry could also be performed (Papanastasiou, 2001).

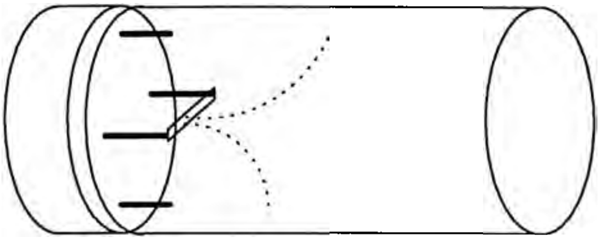

Figure 7.17 Diode configuration for work function measurements of Re filaments

The *Schottky* regions, characteristic of the diode configuration used and the TI/SI filaments employed in this experiment, were determined by plotting the emitted current as a function of the potential difference applied between the anode and the cathode. In this case the filament was negatively biased by the filament power supply, while current was collected and measured on the cylinder, connected on an electrometer. Current-voltage characteristic curves are shown in Figure 7.18 for a series of temperatures. The temperature range extended from ~1400 K to 2200 K. Experimental results showed that a single voltage threshold could not be assigned for all the response curves. Saturation levels and the corresponding voltage threshold in order to remove space charge depended on temperature. The higher the temperature the stronger the electric field required to saturate electron emission. Little or no saturation was observed for the very low temperature range. Variations on the voltage threshold and the indirect relationship between temperature and voltage have been discussed (Jones, 1936). A second observation is the slope of the saturation level, which reduces with temperature. A threshold of $>100\ V$ was finally chosen to define the *Schottky* region and perform the *Schottky* plot. Figure 7.19

shows the *Schottky* plot for a wide range of temperatures and relatively weak electric. The saturation current density is extrapolated to zero electric fields and is plotted as a function of temperature. The *Richardson* plot for rhenium is shown in Figure 7.20. Current densities are expressed in $A\ cm^{-2}$, the electric field in $V\ cm^{-1}$ and temperature in K.

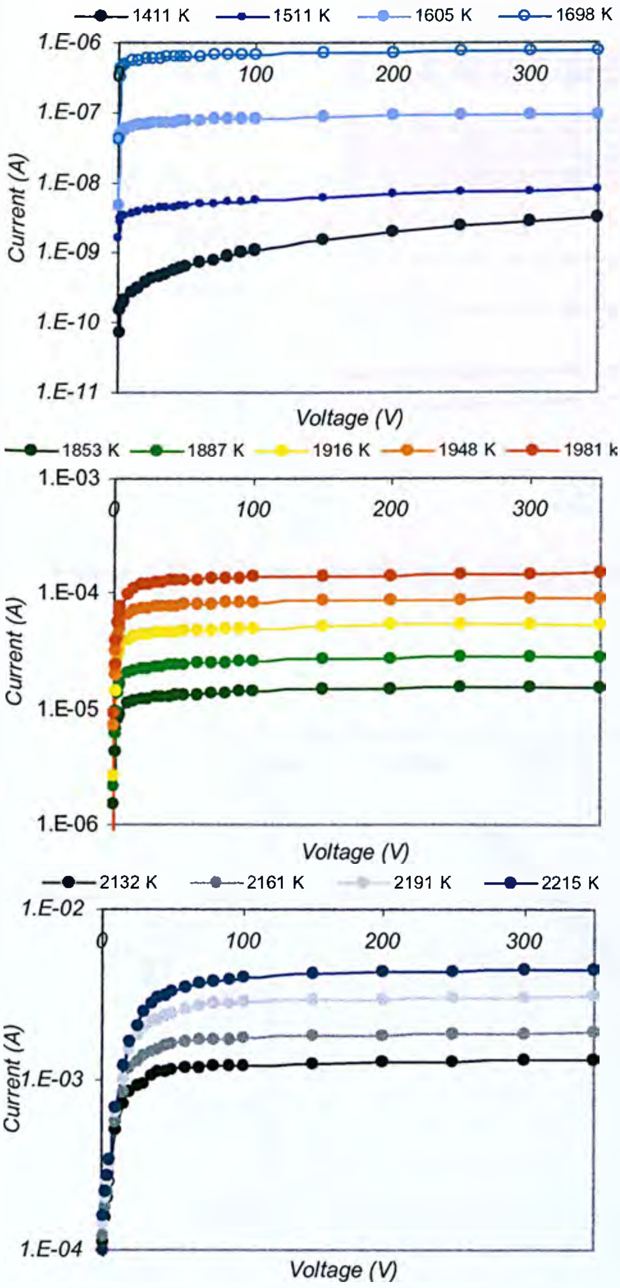

Figure 7.18 Anode-cathode response curves for low. Intermediate and high temperatures.

The temperature independent and dependent terms are computed by the *Richardson* plot and the *apparent* work function is shown in Figure 7.21. A value of $\sim 5.5\ eV$ is obtained for the temperature independent term $e\phi_o$. This value is $0.5\ eV$ greater than the accepted value for rhenium, $4.98\ eV$[2].

Several aspects of the derivation method and associated errors are identified. The value of the work function value is very sensitive to variations in temperature of the emitter. For an $\pm 50\ K$ error in the temperature measurement, the deviation in the work function is $\pm 0.32\ eV$. For an overestimation of the temperature, the slope of the *Richardson* slope reduces and the experimentally determined temperature independent term of the work function diverges from the accepted value of $4.98\ eV$. Several approximations have been made throughout the experimental

---

[2] CRC Handbook of Chemistry and Physics, 67th Edition, 1986-1987

and theoretical analysis respectively and are briefly outlined. Ideally, work function measurements are conducted for single crystal faces. In this case electrons are emitted from a surface area of $16\ mm^2$, the area of the filament. It is also probable that the back of the filament has an equal contribution to the measured current.

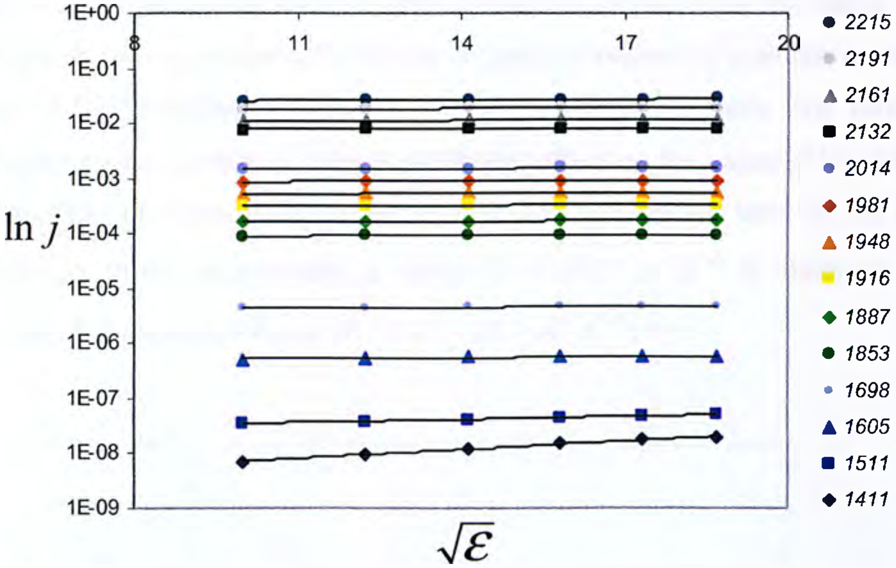

Figure 7.19 *Schottky* plot of a pure rhenium filament for a wide range of temperatures.

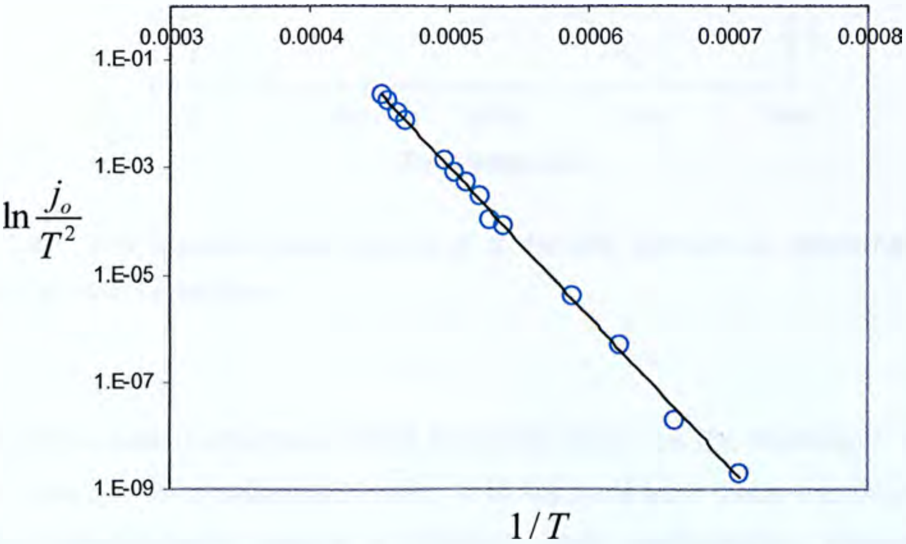

Figure 7.20 *Richardson* plot of a pure rhenium filament

Furthermore, electron emission across the filament is not constant and depends on the temperature distribution. Variations as high as $500\ K$ have been measured within a distance of $4\ mm$ (Papanastasiou, 2001). Therefore, an average value for electron emission over the whole surface area cannot be justified. The ordinate in the *Schottky* plot requires the conversion of volts to electric field units. For the diode configuration shown in Figure 7.17 this cannot be done since the fields are non-homogeneous and a unique value for the distance travelled by a single electron does not exist. In the calculations the value of $1\ cm$ was used. Finally, any variations on the *Schottky* region threshold have a significant effect on the value of the intercept in the *Richardson* plot and thus on the temperature dependent term of the apparent work function. In this experiment, a value of $-0.0017\ eV\ K^{-1}$ is obtained, which is greater than the expected value of $\sim 10^{-4} - 10^{-5}\ eV\ K^{-1}$.

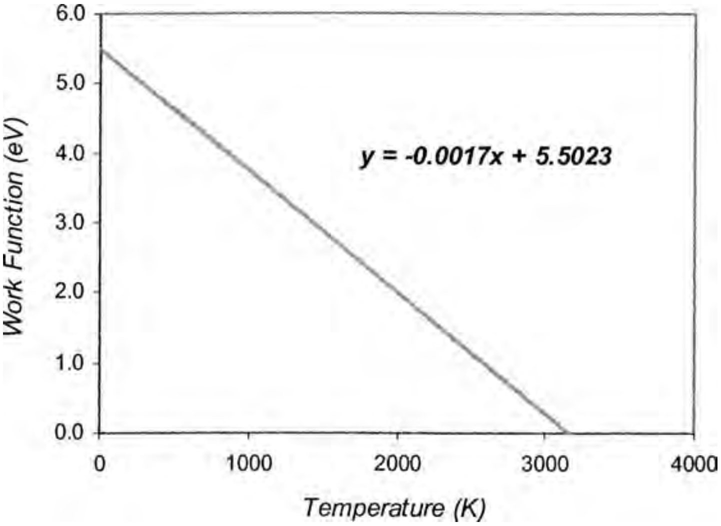

Figure 7.21 The *apparent* work function of a rhenium filament as determined by the thermionic emission experiment.

Work function measurements on TI/SI filaments based on the thermionic emission method have not been presented before. It is apparent from these experiments that accurate measurements require a different diode configuration. However, the principles of the experimental procedure and a detailed background of the theoretical aspects underlying the measurement have been presented.

7.3.3 Electron Energy Distribution

The anode-cathode response curves for the diode geometry employed in this work were shown in Figure 7.18. Electron accelerating fields were used to identify the *Schottky* threshold and extrapolate the electron current density to zero external fields. When the filament is floated positively with respect to the cylindrical tube, electrons experience a retarding field. Only electrons with energies higher than the potential energy of the field can reach the cylinder and are measured by the electrometer. Figure 7.22 shows the negative voltage part of the anode-voltage response curves.

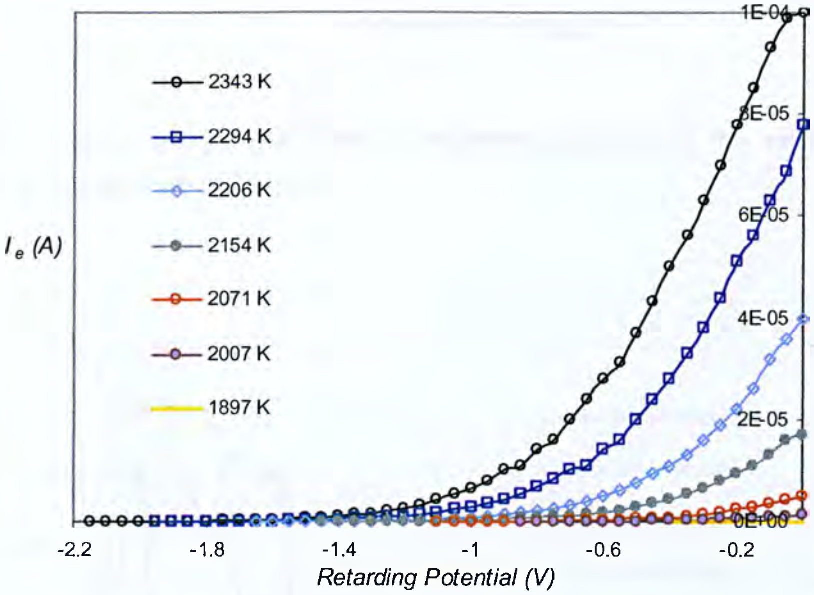

Figure 7.22 Anode-voltage characteristic curves for electron retarding fields.

The voltage is scanned in steps of $0.05\ V$. By subtracting adjacent values for the electron current, the energy distribution can obtained for each temperature separately. Electron intensity is shown as a function of kinetic energy in Figure 7.23 for the electrons emitted at the highest temperature of $2343\ K$. Again, a uniform electric field is assumed to convert the retarding potential to electron kinetic energy. The *Maxwellian* character of the electron distribution can be clearly seen by an approximate polynomial function and interestingly enough, the values for the kinetic energy are in close proximity with those in the literature. The energy distributions for a series of filament currents and the corresponding filament temperatures are shown in Figure 7.24.

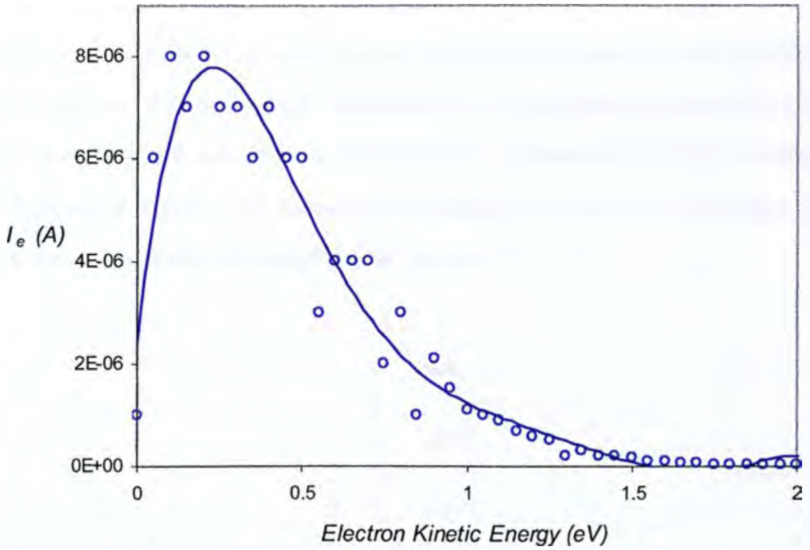

Figure 7.23 Kinetic energy distribution of electrons, defined by the retarding voltage technique, at a temperature of 2343 K.

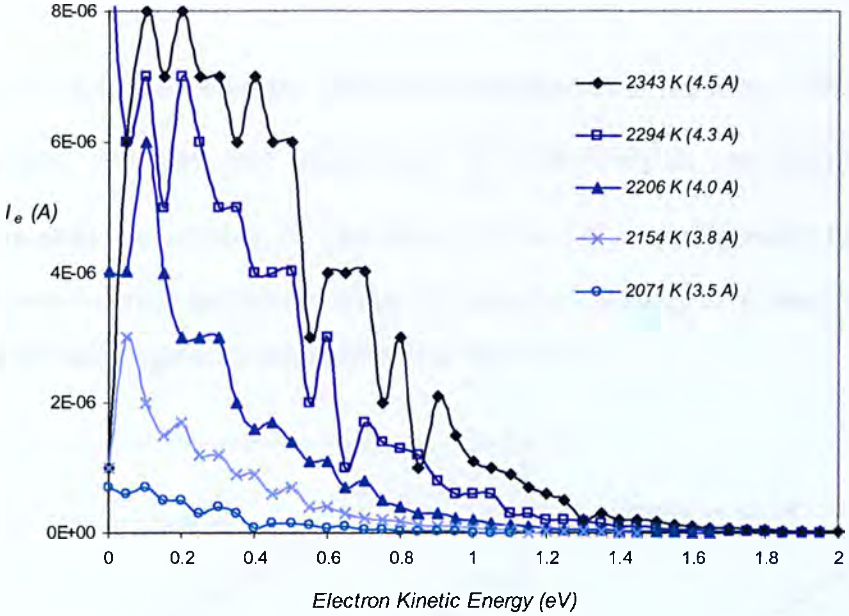

Figure 7.24 Kinetic energy distribution of electrons, defined by the retarding voltage technique, at a temperature of 2343 K.

7.4 Filament Emission Kinetics

In a relaxation process, the composition of a system returns to equilibrium, following a perturbation in one of the system variables. An interesting behaviour was observed in the signal intensity of positive ions formed by thermal/surface ionization and is reported. Figures 7.25 and 7.26 show the relaxation process of the two Rb isotopes following a filament current increase from 3.0 A to 3.3 A.

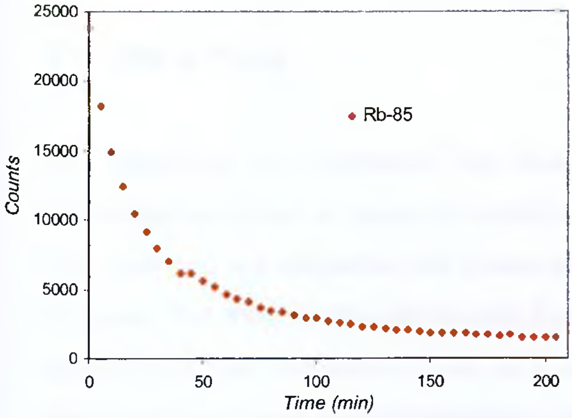

Figure 7.25 Signal decay of the ^{85}Rb isotope.

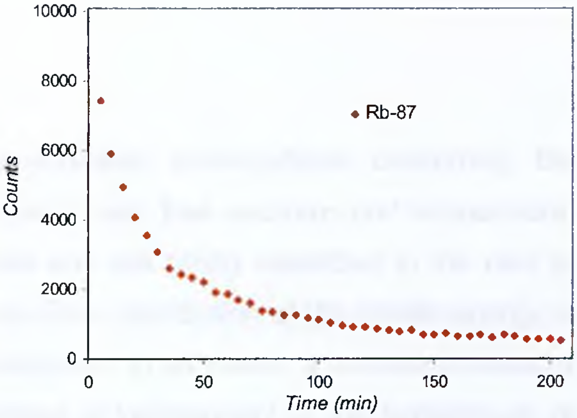

Figure 7.26 Signal decay of the ^{87}Rb isotope.

For a second-order reaction, the differential equation is of the form $-dN/dt = kN^2$. By separating variables and integrating, $\int_{N_o}^{N} N^2 dx = -k\int_0^t dt$, we obtain a linear equation relating the variable N with time, $1/N = 1/N_o + kt$. Figures 7.27 and 7.28 show the second-order behaviour of the Rb signal by plotting $1/N$ over time t. The slope of the linear segments determines the value of k.

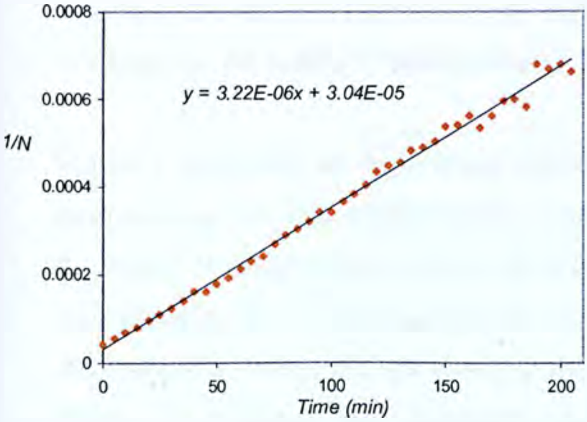

Figure 7.27 Second-order behaviour of the ^{85}Rb isotope.

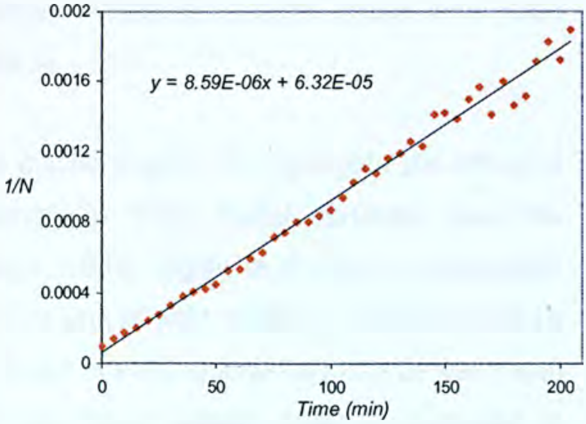

Figure 7.28 Second-order behaviour of the ^{87}Rb isotope.

Similar behaviour has been observed in our work with impurities such as K. Further studies should consider relaxation processes and the determination of the variable k at different temperatures. Activation energies for desorption/ionization and their relationship with the work function of the surface and/or enthalpies of adsorption can then be predicted using the *Arrhenius* method. Non-*Arrhenius* behaviour might provide insights into quantum mechanical effects on adsorbate-substrate interactions.

7.5 The X-Point

Our attention was attracted by three unrelated investigations concerning the behaviour of metals in terms of radiation properties, free electrons and temperature. The first two are experimental observation and are briefly described in the next to Figures. The third is the well known *Fermi-Dirac* distribution of the kinetic energy of electrons in the conduction band of a conductor. In all cases, a wavelength/energy was identified were radiation/electron energy is independent of the temperature of the solid.

Figure 7.29 shows the spectral emissivity of Re as a function of wavelength for a series of temperatures (Marple, 1956). Emissivity is defined as the ratio of the total radiant emittance of a body (W m^{-2}) to that of a blackbody. Direct methods for measuring surface spectral emissivities are performed on resistively heated hollow metal tubes. A small hole on the side of the tube is made giving blackbody radiation. Radiation is measured inside the hole and on the surface of the metal. X-points have been observed for many metals and despite the substantial amount of related literature, the effect is far from being explained. Emissivity and the x-point have been reviewed by the author (Papanastasiou, 2001).

Figure 7.30 shows an experiment carried out by Fowler to investigate the effect of temperature on the photoelectric sensitivity of clean metal surfaces near the threshold of photoelectron emission (Fowler, 1931). Again, a particular wavelength was observed for which the photocurrent per unit of light intensity was temperature independent. Fowler did not question the effect. A striking similarity can be seen with Figure 7.11 where the probability that the Fermi energy level is occupied is temperature independent.

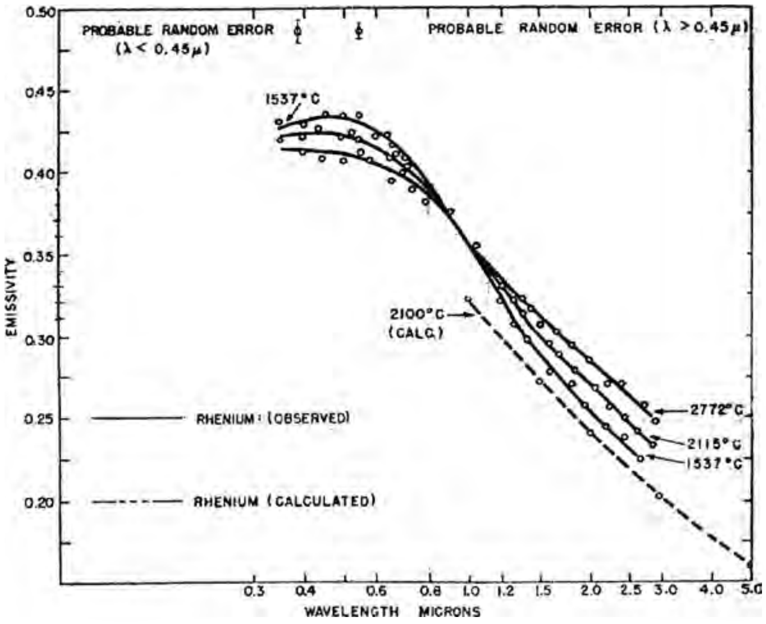

SOURCE: Marple, 1956

Figure 7.29 Spectral emissivity distribution for rhenium isotherms. The x-point is observed at 0.95 mm for an emissivity value of 0.36.

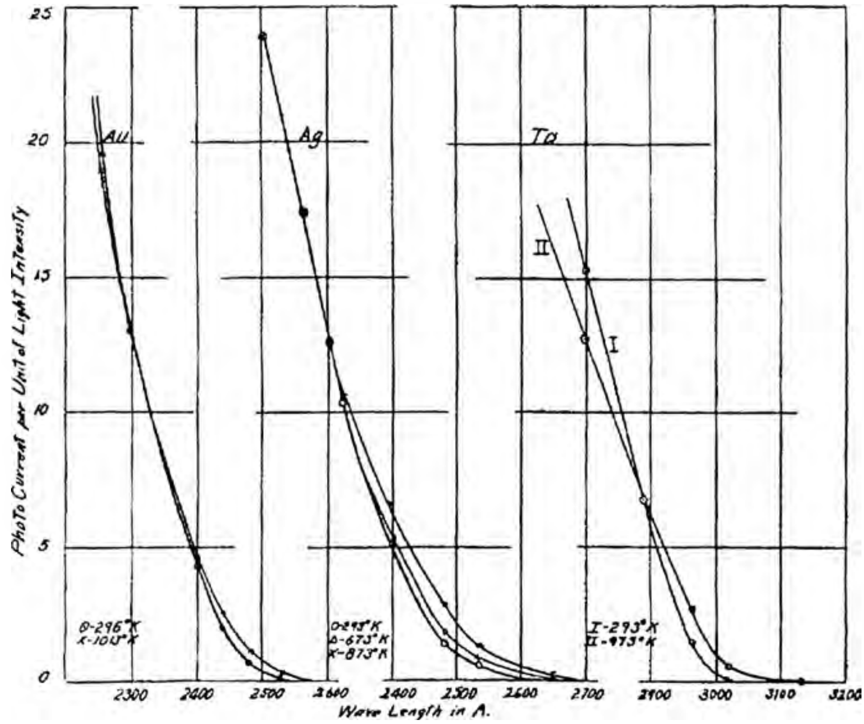

SOURCE: Fowler, 1931

Figure 7.30 Photocurrent per unit of light intensity as a function of wavelength for silver, gold and tantalum.

7.5 Conclusions

By taking into account the correlation between the positions and velocities of ions forming a continuous beam, a new theory for enhancing resolution in orthogonal TOF MS is developed. Analytical solutions to the time focusing properties of ions are presented based on a composite *Taylor* expansion of the time-of-flight equation. First and second-order space-velocity correlation focusing conditions are derived for uniform electric fields in two-stage TOF systems. Ideal focusing is established by considering linear phase space distributions at the start of the TOF experiment. The concept of correlated ion beams is extended to cases where the ions obtain non-linear distributions in phase space. For the latter, numerical analysis is performed to measure the finite time spread associated with such non-linear phase space distributions. The new TOF theory, which provides the missing focusing formula from the original Wiley & McLaren paper and the concept of time-lag focusing (Wiley & McLaren, 1955), is developed in Chapter 4.

A prototype oTOF MS operating in the linear mode has been constructed in our laboratory. The orthogonal gate samples ions from a thermal/surface ionization source and an electron impact source situated on either side of the mass spectrometer. The difference in the mechanism of ion production and optics employed to direct ions into the gate are reflected on the time focusing properties of the system. Variations in the optimum set of voltages required to focus ions from each source respectively are interpreted using SIMION modelling and attributed to the different non-linear phase space distributions formed at the start of the TOF experiment. In Chapter 6, experimental focusing curves are used to extrapolate the initial conditions of the ions prior to the extraction pulse of the two-stage oTOF MS by curve fitting methods.

The "open" orthogonal two-stage configuration is for the first time explored and the associated advantages such as high ion throughput and minimization of scattering at the grids are reported. A low energy electron impact source with no auxiliary magnetic field and a simple ion optical system has been proved very efficient for high resolution experiments. Resolving powers exceeding 2000 are reported for a 45 cm long oTOF MS. A fast detection system incorporating a MCP detector and a TDC to record TOF spectra was essential for resolution experiments.

The theory of space focusing is revised. The idea of ion pairs is introduced and focusing conditions are derived, demonstrating that time focusing in TOF MS is not an instantaneous property of the system. Finite focal regions with variable dimensions in time and space are computed and preferred two-stage acceleration geometries are identified. In Chapter 2, the concept of energy-time focusing is proposed, justified by reformulating space focusing into potential and kinetic energy terms. Ion pairs and velocity focusing merge in Chapter 3. A full account of the delayed extraction technique is provided and second-order systems are for the first time investigated.

A comprehensive literature survey of TOF MS is presented in Chapter 1. The role of TOF MS in high mass analysis and laser desorption techniques is discussed. Emphasis is given on TOF instrumentation, linear configurations and finally the latest development in the field, the orthogonal mass analyzer.

Appendix I

I.i Differentials

Consider the continuous and differentiable function $z = f(x_1, x_2 ... x_n)$. The total differential or the principal part of f is:

$$df = \frac{\partial f}{\partial x_1} dx_1 + \frac{\partial f}{\partial x_2} dx_2 + ... + \frac{\partial f}{\partial x_n} dx_n \qquad \text{(I.i)}$$

regardless of whether the variables $x_1,\ x_2 ... x_n$ are independent or dependent on other variables. The quantities $dx_1,\ dx_2 ... dx_n$ are the differentials of the function f and need not be small. The error in f in terms of an error in the variables $x_1,\ x_2 ... x_n$ is:

$$\delta f = \frac{\partial f}{\partial x_1} \delta x_1 + \frac{\partial f}{\partial x_2} \delta x_2 + ... + \frac{\partial f}{\partial x_n} \delta x_n \qquad \text{(I.ii)}$$

where in general $\delta f \neq df$. If $\delta x_i = dx_i$ then df is a good approximation of δf.

I.ii Taylor Expansion for Bivariate Functions

For bivariate functions $f(x, y)$, where $x,\ y$ are independent variables, the *Taylor* series is:

$$f(x+dx,\ y+dy) = f(x,\ y) + \left[\frac{\partial}{\partial x} dx + \frac{\partial}{\partial y} dy\right] f(x,\ y) + \frac{1}{2!}\left[\frac{\partial}{\partial x} dx + \frac{\partial}{\partial y} dy\right]^2 f(x,\ y) +$$

$$... + \frac{1}{n!}\left[\frac{\partial}{\partial x} dx + \frac{\partial}{\partial y} dy\right]^n f(x,\ y) \qquad \text{(I.ii)}$$

Neglecting third and higher order terms, the error in the function can then be approximated as:

$$\delta f = \left[\frac{\partial f}{\partial x} \delta x + \frac{\partial f}{\partial y} \delta y\right] + \frac{1}{2!}\left[\frac{\partial^2 f}{\partial x^2} (\delta x)^2 + 2\frac{\partial^2 f}{\partial x \partial y} \delta x \delta y + \frac{\partial^2 f}{\partial y^2} (\delta y)^2\right] \qquad \text{(I.iv)}$$

The last expression is always an upper bound for δf whether or not the errors are *independent* and *random*. The first-order truncation error $\delta f = \frac{\partial f}{\partial x}\delta x + \frac{\partial f}{\partial y}\delta y$ is often probably an overstatement of δf since there may be partial cancellation of the errors in x and y. When the errors are correlated a better value for the uncertainty is:

$$\delta f = \sqrt{\left(\frac{\partial f}{\partial x}\delta x\right)^2 + \left(\frac{\partial f}{\partial y}\delta y\right)^2 + 2\delta x \delta y \frac{\partial f}{\partial x}\frac{\partial f}{\partial y}} \qquad \text{(I.v)}$$

and if the variables are *independent* and *random* a better value for the first-order uncertainty is:

$$\delta f = \sqrt{\delta f_{\delta x}^2 + \delta f_{\delta y}^2} \qquad \text{(I.vi)}$$

where $\delta f_{\delta x} = \frac{\partial f}{\partial x}\delta x$ and $\delta f_{\delta y} = \frac{\partial f}{\partial y}\delta y$.

I.iii A Statistical Approach in TOF MS

Truncation errors can be expressed in statistical terms. The variance for bivariate functions is:

$$\sigma_f^2 = \left(\frac{\partial f}{\partial x}\right)^2 \sigma_x^2 + \left(\frac{\partial f}{\partial y}\right)^2 \sigma_y^2 + 2\frac{\partial^2 f}{\partial x \partial y}\sigma_{xy} \qquad \text{(I.vii)}$$

where σ_x^2 is the variance defined through the standard deviation σ_x:

$$\sigma_x = \frac{1}{n}\sum_{i=1}^{n}(x_i - \bar{x})^2 \qquad \text{(I.viii)}$$

and the covariance σ_{xy} relates the two variables x and y:

$$\sigma_{xy} = \frac{1}{n}\sum_{i=1}^{n}(x_i - \bar{x})(y_i - \bar{y}) \qquad \text{(I.ix)}$$

If $\sigma_{xy} \neq 0$ then x, y are correlated. The variance of the bivariate function σ_f^2 gives the standard deviation σ_f whether or not x, y are normally distributed and whether or not x, y are independent. An equivalent expression for the variance in arrival time can be derived as follows.

In TOF MS the arrival time of an ion is considered as a function of its initial position and initial velocity, $t(s_i, u_i)$. The average initial position and average initial velocity s_o and u_o respectively define the reference ion and its arrival time $t(s_o, u_o)$. The variance in the arrival times for n ions is:

$$\sigma_t^2 = \frac{1}{n}\sum_{i=1}^{n}\left[t(s_i,u_i) - t(s_o,u_o)\right]^2 = \frac{1}{n}\sum_{i=1}^{n}\left[\delta t(s_i,u_i)\right]^2 \tag{I.x}$$

Similarly, the variances in initial position and initial ion velocity are respectively:

$$\sigma_{s_i}^2 = \frac{1}{n}\sum_{i=1}^{n}(s_i - s_o)^2 = \frac{1}{n}\sum_{i=1}^{n}(\delta s_i)^2 \tag{I.xi}$$

$$\sigma_{u_i}^2 = \frac{1}{n}\sum_{i=1}^{n}(u_i - u_o)^2 = \frac{1}{n}\sum_{i=1}^{n}(\delta u_i)^2 \tag{I.xii}$$

The covariance between initial position and velocity is:

$$\sigma_{s_i u_i} = \frac{1}{n}\sum_{i=1}^{n}\delta s_i \delta u_i \tag{I.xiii}$$

The error in arrival time for each ion relative to the reference ion is:

$$\delta t(s_i,u_i) = \left[t(s_i,u_i) - t(s_o,u_o)\right] \tag{I.xiv}$$

Using the fundamental approximation of calculus for truncation errors, for the n arrival times:

$$\delta t(s_1,u_1) = \frac{\partial t}{\partial s_o}\delta s_1 + \frac{\partial t}{\partial u_o}\delta u_1 \tag{I.xv}$$

$$\vdots \qquad \vdots \qquad \vdots$$

$$\delta t(s_n,u_n)=\frac{\partial t}{\partial s_o}\delta s_n+\frac{\partial t}{\partial u_o}\delta u_n \tag{I.xvi}$$

Raising the equations in the power of two:

$$\left[\delta t(s_1,u_1)\right]^2=\left(\frac{\partial t}{\partial s_o}\delta s_1\right)^2+\left(\frac{\partial t}{\partial u_o}\delta u_1\right)^2+2\frac{\partial^2 t}{\partial s_o\partial u_o}\delta s_1\delta u_1 \tag{I.xvii}$$

$$\vdots \qquad\qquad \vdots \qquad\qquad \vdots$$

$$\left[\delta t(s_n,u_n)\right]^2=\left(\frac{\partial t}{\partial s_o}\delta s_n\right)^2+\left(\frac{\partial t}{\partial u_o}\delta u_n\right)^2+2\frac{\partial^2 t}{\partial s_o\partial u_o}\delta s_n\delta u_n \tag{I.xviii}$$

Adding and multiplying both sides by $1/n$ the left term is:

$$\frac{1}{n}\left[\delta t(s_1,u_1)^2+\ldots+\delta t(s_n,u_n)^2\right]=\frac{1}{n}\sum_{i=1}^{n}\delta t(s_i,u_i)^2=\sigma_t^2 \tag{I.xix}$$

and the right term:

$$\frac{1}{n}\left[\left(\frac{\partial t}{\partial s_o}\delta s_1\right)^2+\ldots+\left(\frac{\partial t}{\partial s_o}\delta s_n\right)^2\right]+\frac{1}{n}\left[\left(\frac{\partial t}{\partial u_o}\delta u_1\right)^2+\ldots+\left(\frac{\partial t}{\partial u_o}\delta u_n\right)^2\right]$$
$$+\frac{1}{n}\left[2\frac{\partial^2 t}{\partial s_o\partial u_o}\delta s_1\delta u_1+\ldots+2\frac{\partial^2 t}{\partial s_o\partial u_o}\delta s_n\delta u_n\right] \tag{I.xx}$$

working inside the square brackets:

$$\left(\frac{\partial t}{\partial s_o}\right)^2\frac{1}{n}\sum_{i=1}^{n}(\delta s_i)^2+\left(\frac{\partial t}{\partial u_o}\right)^2\frac{1}{n}\sum_{i=1}^{n}(\delta u_i)^2+2\frac{\partial^2 t}{\partial s_o\partial u_o}\frac{1}{n}\sum_{i=1}^{n}\delta s_1\delta u_1 \tag{I.xxi}$$

Using the variances for initial ion position and velocity the last expression simplifies to:

$$\left(\frac{\partial t}{\partial s_o}\right)^2\sigma_{s_i}^2+\left(\frac{\partial t}{\partial u_o}\right)^2\sigma_{u_i}^2+2\frac{\partial^2 t}{\partial s_o\partial u_o}\sigma_{s_iu_i} \tag{I.xxii}$$

Equating left and right term:

$$\sigma_t^2 = \left(\frac{\partial t}{\partial s_o} \right)^2 \sigma_{s_i}^2 + \left(\frac{\partial t}{\partial u_o} \right)^2 \sigma_{u_i}^2 + 2 \frac{\partial^2 t}{\partial s_o \partial u_o} \sigma_{s_i u_i} \tag{I.xxiii}$$

or

$$\sigma_t = \sqrt{\left(\frac{\partial t}{\partial s_o} \right)^2 \sigma_{s_i}^2 + \left(\frac{\partial t}{\partial u_o} \right)^2 \sigma_{u_i}^2 + 2 \frac{\partial^2 t}{\partial s_o \partial u_o} \sigma_{s_i u_i}} \tag{I.xxiv}$$

which is the standard deviation of the arrival times in terms of the variances in initial positions, velocities and their covariance. In the case for which initial position and velocity are not correlated:

$$\sigma_t = \sqrt{\left(\frac{\partial t}{\partial s_o} \right)^2 \sigma_{s_i}^2 + \left(\frac{\partial t}{\partial u_o} \right)^2 \sigma_{u_i}^2} \tag{I.xxv}$$

Appendix II

II.i Equations of Motion

Newton's second law is a second-order differential equation of the form $m\ddot{x} = F(x, \dot{x}, t)$ where $\ddot{x} = d^2x/dt^2 = a$ is the acceleration experienced by the body and F is the force, a function of position, velocity and time. For a constant force, the first integration of $d^2x/dt^2 = a$ yields:

$$\int \frac{d^2x}{dt^2}\, dt = \int a\, dt + C_1 \quad \Rightarrow \quad \frac{dx}{dt} = at + C_1 \tag{II.i}$$

or $u = at + C_1$ where C_1 is evaluated by the initial conditions x_o, u_o, t_o namely, $C_1 = u_o - at_o$. The velocity of the body is expressed as a function of time according to:

$$u = u_o + a(t - t_o) \tag{II.ii}$$

The successive indefinite integral of $u = at + C_1$ is:

$$\int u\, dt = \int at\, dt + \int C_1\, dt + C_2 \quad \Rightarrow \quad x = \frac{1}{2}at^2 + C_1 t + C_2 \tag{II.iii}$$

The second constant C_2 is evaluated by the initial conditions, $C_2 = x_o - at_o^2/2 - C_1 t_o$ and the position of the body is expressed as a function of time:

$$x = x_o + u_o(t - t_o) + \frac{1}{2}a(t - t_o)^2 \tag{II.iv}$$

By setting $t_o = 0$ the position of the particle can be written in the form of a quadratic equation in terms of the time variable, $at^2/2 + u_o t - (x - x_o) = 0$. The time interval of the motion can then be computed:

$$t = \frac{\sqrt{u_o^2 + 2(x - x_o)a} - u_o}{a} \tag{II.v}$$

II.ii Work Energy Theorem

The work done by the conservative field on the particle is $W = \int_{x_1}^{x_2} F(x)dx$. For a constant force F independent of position x, the work is proportional to the displacement $\delta x = x_2 - x_1$ and $W = Fdx$. Newton's second law states that $F = m\ddot{x} = m\frac{d^2x}{dt^2}$. Incorporating the equation of motion the integral is expressed by (II.6):

$$W_{1\to 2} = \int_{x_1}^{x_2} m\frac{d^2x}{dt^2}\,dx = \int_{x_1}^{x_2} m\frac{d}{dt}\left[\frac{dx}{dt}\right]dx = \int_{x_1}^{x_2} m\frac{du}{dt}\,dx = \int_{x_1}^{x_2} m\frac{du}{dx}\frac{dx}{dt}\,dx = \left[\frac{1}{2}mu^2\right]_{u_1}^{u_2} = \Delta T$$

A force field is conservative, if and only if, it can be expressed as the gradient of a time independent scalar field. In one dimension, if $F(x)$ is conservative a scalar field exists $U(x)$ such that $F(x) = -dU(x)/dx$ therefore:

$$-\Delta U = -(U_2 - U_1) = \int_{x_1}^{x_2} F(x)dx = W_{1\to 2} \qquad \text{(II.vii)}$$

Along any particular motion the gain in kinetic energy is equal to the loss in potential energy, $\Delta T = -\Delta U \;\Rightarrow\; T_2 - T_1 = U_1 - U_2$, or, $E = T_1 + U_1 = const$. This equation is a "first integral" of the equation of motion in conservative systems.

II.iii The Time Integral

Time intervals of the equation of motion are determined by indefinite integration. The equation of motion where the force is independent of time, Newton's second law, is written as:

$$mu\frac{du}{dx} = F(x) \;\Rightarrow\; mudu = F(x)dx \qquad \text{(II.viii)}$$

The indefinite integration gives:

$$\int mudu \;=\; \int F(x)dx + C_1 \qquad \text{(II.ix)}$$

where C_1 is the first constant of integration. The indefinite integral of the force $F(x)$ with respect to the displacement dx is $\sigma_1 = \int F(x)dx$ therefore:

$$\frac{1}{2}mu^2 = \sigma_1(x) + C_1 \tag{II.x}$$

The first constant of the indefinite integration is determined by the initial conditions of the equation of motion, x_o, u_o, t_o and $C_1 = mu_o^2/2 - \sigma_1(x_o)$ and:

$$\frac{1}{2}mu^2 = \sigma_1(x) + \frac{1}{2}mu_o^2 - \sigma_1(x_o) \tag{II.xi}$$

Solving for the ions velocity:

$$u = \pm\sqrt{\frac{2}{m}\left[\sigma_1(x) - \sigma_1(x_o)\right] + u_o^2} \tag{II.xii}$$

or

$$\frac{dx}{dt} = \pm\sqrt{\frac{2}{m}\left[\sigma_1(x) - \sigma_1(x_o)\right] + u_o^2} \tag{II.xiii}$$

The time interval is then expressed by splitting the independent variables dx, dt and taking the indefinite integral in both sides:

$$t = \int \frac{dx}{\pm\sqrt{\frac{2}{m}\left[\sigma_1(x) - \sigma_1(x_o)\right] + u_o^2}} + C_2 = \sigma(x) + C_2 \tag{II.xiv}$$

where $\sigma(x)$ is the evaluated integral. The constant C_2 is determined from the initial conditions, $C_2 = t_o - \sigma(x_o)$ and the time interval is finally expressed as:

$$t - t_o = \sigma(x) - \sigma(x_o) \tag{II.xv}$$

The function $\sigma_1(x)$ represents the potential energy of the motion, a function of position only:

$$\sigma_1(x) = \int F(x)dx = -\int \frac{U(x)}{dx}dx = -U(x) \qquad \text{(II.xvi)}$$

Determination of the time interval requires the solution of the integral $\sigma(x)$.

II.iv Solution of the time-integral in uniform electric Fields

The force integrals are identified as the potential energy are, $\sigma_1(x) = -U(x)$ and $\sigma_1(x_o) = -U(x_o)$. Setting $t_o = 0$, $\sigma(x_o) = 0$ and neglecting the initial velocity u_o, the time interval $t = \sigma(x)$ is:

$$t = \int \frac{dx}{\pm\sqrt{\frac{2q}{m}[-V(x)+V(x_o)]}} \qquad \text{(II.xvii)}$$

If $U(x) = qV(x)$. The potential of a uniform electric field $\mathcal{E} = -\frac{dV}{dx} = const$ is $V(x) = V(x_o) - \mathcal{E}(x - x_o)$:

$$t = \int \frac{dx}{\pm\sqrt{\frac{2q\mathcal{E}}{m}(x - x_o)}} \qquad \text{(II.xviii)}$$

and the integral is transformed as:

$$t = \sqrt{\frac{m}{2q\mathcal{E}}} \int \frac{d(x-x_o)}{\pm\sqrt{(x-x_o)}} = \pm\frac{\sqrt{m}}{\sqrt{2q\mathcal{E}}} \int \frac{d}{dx}\left(2\sqrt{x-x_o}\right) d(x-x_o) = \pm\frac{\sqrt{m}}{\sqrt{2q\mathcal{E}}} \left(2\sqrt{x-x_o}\right)$$

The time interval in terms of the loss in the electric potential energy $U = q(x-x_o)\mathcal{E}_s$ is:

$$t = \frac{\sqrt{2m}}{q\mathcal{E}}\sqrt{U} \qquad \text{(II.ixx)}$$

Appendix III

III.i Electron Impact Ion Source

The electron impact source, was first introduced into mass spectrometry by Dempster (Dempster, 1921) and became the classical source for ionization in MS. The first EI sources were immersed into the field of a solenoid magnet used for mass analysis (Bleakney, 1929; Bleakney, 1930). The original designs were further developed over the years (Tate & Smith, 1934; Nier, 1937; Nier, 1938; Nier, 1940). The classical model for EI sources, known as the "orthdodox" model was presented in 1947 (Nier *et al*, 1947). Several possible configurations have been proposed and fundamental variations from the orthodox pattern have been reported (Finkelstein, 1940; Coggeshall &Jordan, 1943; Heil, 1943; Barnard, 1949) in attempts to increase the sensitivity and the accuracy of the source.

III.ii Ion Source Characteristics

Electron impact ionization is performed with gaseous species at a wide range of temperatures (100 °C – 250°C) for the generation of both positive and negative charged particles. A stream of sample material is allowed to flow from a chamber of relatively high pressure, through an ion optical system, into a mass analyzer.

A schematic of the ion source is shown in Figure III.i. Electrons from a filament, confined by a magnetic field parallel to their optical axis, pass through a collimation slit into a collision chamber and hit a collecting cage situated at opposite ends. The energy of the electrons is approximately defined by the voltage difference between the filament and the source chamber walls. In the gas-containing collision chamber, a repeller electrode defines a transverse to the electron beam axis electric field, which aids the extraction of ions through the front slit. The ion extraction is further assisted by field penetration from the ion optical system of the source. Additional slits are interposed to focus the ions and reduce chromatic aberrations.

The three-dimensional potential distribution in the chamber is defined by the voltage difference between the repeller electrode and the source walls and is altered by field penetration of the ion optical system, the filament and the collecting cage. The situation is further complicated by the passing electron beam and the resulting negative and positive space charge. At the lowest electron currents and operating pressures, the ion energies are mainly defined by the source chamber electrode potentials (Hagstrum, 1951). For the more intense electron beams, the electron space charge controls the potential configuration by creating a negative potential across the beam and only energetic ions can escape (Pierce, 1954). Above a certain gas pressure the positive ion space charge may distort the ion energy distribution by its own configuration (Hasted, 1964).

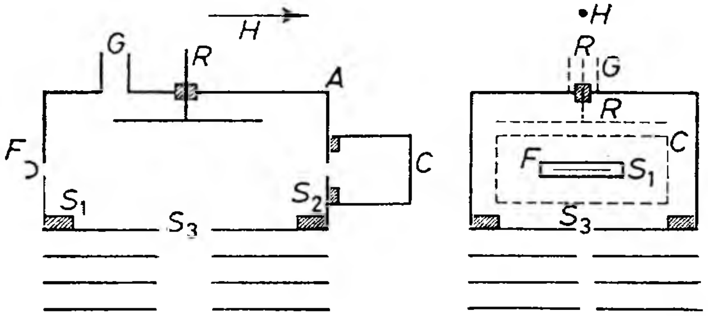

Source: Hasted, 1964

Figure III.i Orthogonal views of the Nier mass spectrometer source. Electrons from a filament F confined by a magnetic field H pass through collimation slits S1 and S2 , thence into a collecting cage C. Potential differences can be held between the source chamber A, the repeller R, C and S3.

The ion source can be operated over a range of pressures. At the high pressure range, $10^{-2} – 10^{-3}$ mm Hg (1 mm Hg =1 torr), the source operates as a low voltage arc. At the lower pressure range, 10^{-4}-10^{-6} mm Hg, it can be regarded as a confined beam electron impact device (Hasted, 1964).

The intensity of the extracted ion beam increases with gas pressure, until a maximum is reached. Beyond this pressure threshold the ion beam attenuates due to the attenuation of the electron beam before it reaches the collision region from which ions are sampled by the ion optical system.

III.iii Sensitivity

The number of atoms or molecules ionized in the source depends on the cross section σ_i, the current density of the electron beam I_e, the number of atoms or molecules per unit volume n_a and the effective volume of ionization V. If all the ions produced in the ionization volume reach the detector, the positive ion current emitted from the source is:

$$I_i = I_e V n_a \sigma_i \qquad \text{(III.i)}$$

The theoretical background and experimental methods for the determination of ionization cross sections and optimum impact energies can be found in a few excellent textbooks (Hasted, 1964; Valyi, 1977).

The current density of the electron beam and the positive ion current at the detector are determined experimentally. I_e is measured at the trap, outside the ionization chamber. Not all electrons from the interaction region are collected and measured. This is also true for I_i since not all the ion current produced inside the ionization chamber is transmitted to the detector. The application of Eq. (III.i) to determine relative ion abundances and ionization cross sections is not a straight forward process and transmission coefficients must be known, which are specific to both the dimensions/characteristics of the source and the mass analyzer (Kurepa *et al*, 1998).

III.iv Electron Trajectories

In the conventional source design, the resistively heated filament is held at a negative potential relative to the ionization chamber and the energy of the emitted electrons is of the order of 70 eV. The electron trap/collecting cage is usually floated at a positive potential relative to the chamber in order to enhance the collection of the electrons and prevent the escape of the secondary ones. Variations in the collecting current are compensated by a feedback amplifier system which controls the electron emission by automatically adjusting the power of the filament. Typical collection currents are found between 10 and 200 μA. The filament material is usually a ribbon of tungsten or rhenium. Lower work function materials require less power to sustain high electron emission rates and the source can be operated at the lower temperatures.

Electrons are forced into cycloidal-helical trajectories by the presence of an auxiliary weak magnetic field. Their helical motion increases the total path within the chamber and therefore the probability of successful collisions. The electron motion can be analyzed by considering the velocity resolved into two components, one along and one transverse to the magnetic field. A force normal to the defined geometrical direction of motion results from the transverse velocity. Purely helical trajectories result from parallel electric and magnetic fields. The helical path of an electron in a magnetic field is shown in Figure 7.28. The radius of the circular orbit is proportional to the transverse velocity, $r = m_e u_\perp / qB$ but the time of revolution is the same for all electrons, $T = 2\pi m_e / qB$. The distance travelled along the field in one revolution, or the pitch of the helix, is approximately identical for all electrons, and proportional to the velocity component along the field. Only for certain values of the electron acceleration voltage the distance between the entrance and exit slits of the source chamber will be equal to an integral multiple of the pitch of the helical motion. In this case the electron beam will converge on the exit slit. A well defined image of the entry slit is then projected to the exit slit. For all other kinetic energy values, the electron beam section in the plane of the exit slit will be larger than the entry slit (Barnard, 1953). The cycloidal motion is attributed to the transverse electric field imposed by the repeller plate. Under the influence of these fields the electron beam has a drift orthogonal to both fields. The behaviour of the electron beam in crossed electric and magnetic fields has been investigated by many authors (Vauthier, 1955; Taylor *et al*, 1974) and a method for producing monoenergetic ions has been reported (Stamatovic & Schulz, 1968). There are two consequences of the drift. The first is that its position in front of the exit slit is not defined by the geometric dimensions of the entrance aperture. The second is that the electron beam can miss the exit slit partially or even totally (Kurepa *et al*, 1998).

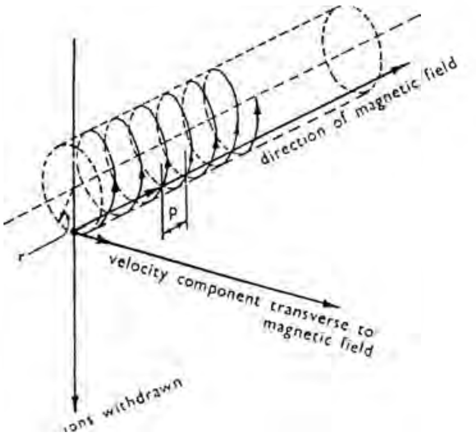

Source: Barnard, 1953

Figure III.ii Helical electron trajectories in the Nier source.

III.v Ion Energy Distribution

The finite kinetic energy spread of the ions as they exit the source gives rise to chromatic aberrations at the detector. The ion beam cannot be considered as monoenergetic and the image at the detector plane is characterized by both a spatial and energy spread. The final energy spread of ions that enter the mass analyzer can be of the order of *0.1 - 5.0* eV (Kiser, 1965). A list of parameters that contribute to the kinetic energy spread of the ions is given below.

The potential distribution inside the chamber walls is mainly defined by the repeller plate and field penetration from the ion optical system. Ions are therefore formed across a potential gradient and acquire a distribution in their initial electric potential energies. The effect can be reduced if concentrated electron beams with very small cross-sectional areas are used.

Chromatic aberration can arise from energy changes due to collisions between similar ions in the gas phase (binary collisions). The gas pressure in the ionization chamber must not be increased beyond an optimum level if such effects are to be avoided. Poor vacuum conditions can also lead to energy changes due to collisions between dissimilar ions and neutrals.

The average thermal energy of a molecule is $3kT/2$ or $T/$ *7730* eV, where T is the absolute temperature. For a source operating at *250* °C, the average thermal energy is *67* meV. It must be noted that this is only the average energy spread and a fraction of the species will be found with higher energies.

Ions formed from molecular dissociation products always have associated with them varying amounts of dissociation energy. Kinetic energies of the order of 10 eV for ions formed in dissociative collisions have been reported (Hanson, 1937) which can take them far from the exit slit (Hagstrum & Tate, 1941).

The distribution of initial ion energies is also modified by the distribution in the kinetic energy of the emitted electrons. The latter is defined by the voltage drop across the wire/ribbon and the fringing fields between the filament and the source chamber. Contact potential differences and thermal energy contributions must also be considered in assessing precisely the energy of the ionizing electrons.

For the ion sources operating at the higher voltage regime, usually coupled to magnetic deflexion instruments, short-term variations in the apply voltage can further increase the kinetic energy distribution of the ions. Contact potentials existing between the different sections of the source assembly, the build-up of surface charges and the gas phase space charge can also modify the energy of the ions emerging from the source.

III.vi Source Modifications

In the *Nier*-type electron impact source (Nier, 1940; Nier, 1947), the electron beam in a central section of the source is directed parallel to the long axis of the first ion slit and ion extraction is perpendicular to the electron path. Variations of this model have been presented but most of them conform to the general pattern with respect to the electron and ion beam directions. Alternatively, the electron beam can be directed onto an atomic beam rather than through a chamber containing the gas or vapour to be ionized. The collisions may take place between the beams oriented in either normal or parallel directions with respect to each other (Valyi, 1977). In the Finkelstein source the electron beam was introduced collinear to the final beam of ions (Finkelstein, 1940). The co-propagation of the charged particles was assisted by a magnetic field and had a dramatic increase in the flux of ions from the source. Simulations comparing conventionals design over the Finkelstein source have been reported (Colby, 1997).

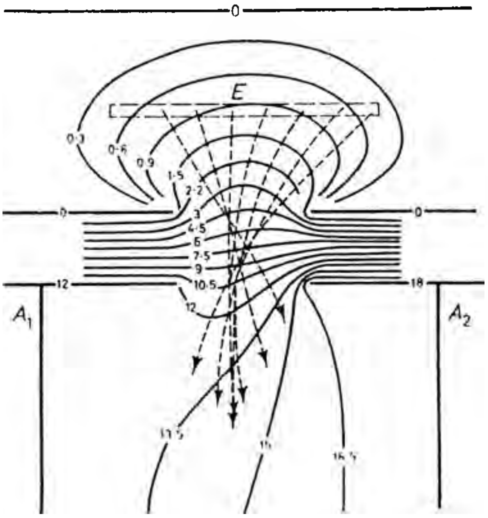

Source: Hagstrum, 1951

Figure III.iii Equipotentials and approximate ion trajectories in a Nier source without a repeller. Electrodes A_1 and A_2 are maintained at different potentials, for compensation of the ion path curvature in a magnetic field.Helical electron trajectories in the Nier source.

Considerable effort has been made to develop techniques to produce monochromatic electron beams. A straightforward approach is the construction of electron spectrometers using magnetic (Nottingham, 1939) or electrostatic deflection (Clarke,

1954) of electrons as a way of selecting a beam of narrow energy. Trochoidal electron monochromators employing both electrostatic and magnetic fields and their distinct mode of operation have also been presented (Stamatovic & Schulz, 1968; Grill *et al*, 2001). A second technique is based on the use of a special electron gun containing at least two supplementary electrodes (Fox *et al*, 1951; Fox *et al*, 1955). The principle of operation is based on the "retarding potential difference" method where the energy of the electrons allowed to enter the ionization chamber is controlled by the electron optical system. Electron impact sources have also been operated with no auxiliary magnetic field (Coggeshall & Jordan, 1943) in order to avoid their influence on the ion extraction efficiency. In the absence of a magnetic field, the electron beam is deflected by the weak positive ion extraction field. The potential gradient increases the cross section of the electron beam. Such effects can only be reduced if electrons with a narrow energy distribution and a narrow initial spatial profile are allowed to enter the ionization chamber. An ion optical arrangement introducing a split extraction electrode to compensate for the effect of the magnetic field on the ion trajectory (Hagstrum, 1951) is shown in Figure 7.29. Special source arrangements have been proposed in order to enhance the sensitivity over the conventional design. Tenfold enhancement in total ion current has been reported using trochoidal electron beams employing weak magnetic fields (Barnard, 1953), as shown in Figure 7.30. Enhancement on the efficiency of the EI source has also been reported using multicathodes (Clausnitzer, 1963) or the Pierce-cathode geometry (Pierce, 1940; Pierce, 1954).

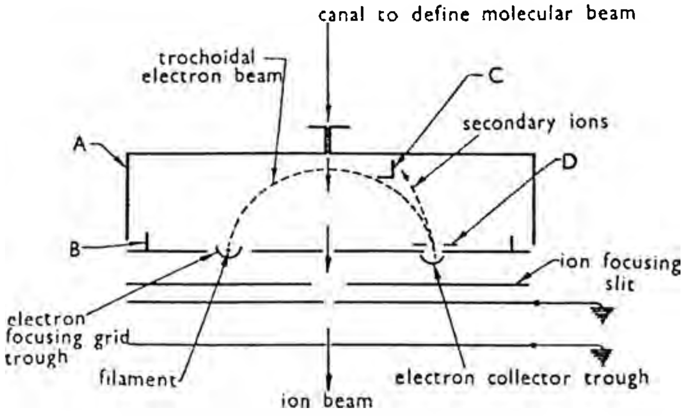

New type of source using trochoidal electron beam and greatly reduced magnetic field in source region.

A, ionization chamber screen connected to anode of electron gun.
B, screen to shield insulating material on terminal assembly.
C, primary ion alinement electrode and secondary ion trap.
D, slot connected to grid trough for location of electron beam trajectory.

Source: Barnard, 1953

Figure III.iv The Barnard-type electron impact ion source.

The equilibrium temperature in the centre of the ionization chamber is likely to rise to at least 100 -150 °C, due to heat from the filament alone. Operation of the source at high temperature is desirable since it allows for its elements to outgas over time. A thoroughly outgassed element may act as a getter for the gas introduced in the source for analysis (Barnard, 1953). So long as appreciable volumes of gas remain adsorbed or absorbed in any source material, electron bombardment of the material may lead to background ion beams of appreciable magnitude. The effect is reduced by collimating the electron beam and minimizing the surface area subjected to bombardment. In addition, surface deposits may modify the source potential and distort the ion beam path. The result is a reduction in sensitivity and can only be removed by dismantling and cleaning.

The stability of the extracted ion beam depends, amongst other things, upon a constant density and distribution of electrons in the ionizing region. Uncontrolled secondary electron emission following bombardment of internal surfaces by the primary electron beam is bound to lead to erratic behaviour. Even with perfectly aligned geometries, bombardment of the entry defining slit cannot be avoided and an appreciable amount of secondaries is likely to be present.

The position of ion formation is critical to the overall performance of the source. Ions are formed into regions from which direct extraction does not take place. The ionization probability is of the order of $\sim 10^{-4}$. With a sample pressure inside the ionization chamber of 10^{-5} torr and a current of 100 μA of 70 eV energy electrons, the ion current output can be of the order of 10^{-9} A (Errock, 1964). The ionization probability differs between substances and the optimum electron energies lie within 50 and 100 V.

The efficiency with which ions are extracted from the source has been a subject of long discussions involving trajectory simulations in crossed electric and magnetic fields, anisotropic angular distributions of the initial ion velocities, excessive initial kinetic energies of fragment ions, etc. These effects apart from being mass dependent are strongly influenced by the source dimensions/characteristics and the applied voltages. A detailed analysis can be found in an excellent review paper (Kurepa *et al*, 1998).

Any accelerating electrode system can discriminate between ions of different m/z values, that is, the ion optical system systematically favours the extraction of a narrow m/z range relative to others m/z values. The ability of the EI source to deliver true/accurate abundance ratio measurements has been the subject of long discussions (Barnard, 1953).

III.viii Applications

Electron impact experiments have long been used for the determination of *ionization* and *appearance potentials*. The *ionization potential* (IP) is the minimum energy required to remove an electron from an atom/molecule in the gas phase. The minimum energy to dissociate molecular ions into fragments is defined as the *appearance potential* (AP) of the fragment ion. IPs and APs are closely related to the chemical nature of the molecule, to the structure and thermodynamic characteristics such as heats of formation of molecules, radicals and ions. Electron impact ionization provides information on the higher excited electronic states of ions and their vibrational levels and frequencies (Collin, 1965). The determination of ionization cross sections has been an active area of research since the data are of importance to various fields of science such as plasma physics, astrophysics, etc.

Beyond the ionization threshold, ion abundance varies with the energy of the bombarding electrons. A typical “ionization efficiency curve” is shown in Figure III.v and is characteristic of the type of the process involved. The problem of determining the IP is a problem of interpreting the efficiency curve. Conventional methods are performed with inhomogeneous electron beams. Electron emission is usually obtained by heating W, Re, Ta and Mo filaments at high temperatures. The emission obeys *Richardson's* law and the electrons exhibit a temperature dependent relatively wide kinetic energy spread *Maxwellian* in character (1.0-2.0 eV). Most of the curvature near the ionization onset is attributed to this effect. Considerable efforts have been made to produce monochromatic electron beams by using magnetic or electrostatic selection of a part of the beam, as mentioned above. A second experimental requirement is the necessity of a suitable calibration of the electron energy scale. The accelerating voltages are not representative since contact and surface potentials are always present. The voltage drop across the filament and the presence of non-homogeneous electric fields due to field penetration in the source chamber further complicate the situation. The simplest way to eliminate these difficulties is to use calibrating gases with accurately known IPs. Rare gases (Ar, Kr, or Xe) have been used as reference standards and are admitted to the mass spectrometer simultaneously with the sample. The measurement is performed at such a pressure that the ion being studied and the reference ion give about the same current intensity. Such delicate experiments are difficult to perform and have been discussed at length in many general textbooks (Barnard, 1953; Robertson, 1955; Field and Franklin, 1957; McLafferty, 1963; Collin, 1965).

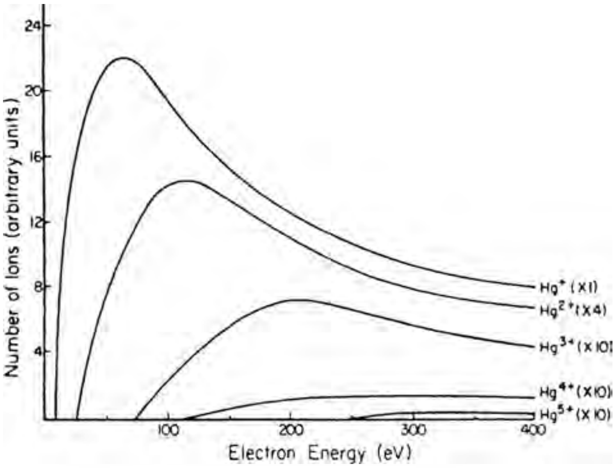

Source: Cooks *et al*, 1973

Figure III.v Ionization efficiency curves for mercury. The probabilities of producing mercury ions carrying various numbers of positive charges is a function of the energy of the bombarding electrons.

Other applications involve the use of Knudsen cells which when coupled with electron impact sources provide thermochemical information of the samples under investigation. The dynamic capabilities of the mass spectrometric technique play a special part in chemical kinetic research and allow the identification of unstable species produced in the transitory steps of a reaction mechanism. Electron impact sources have a wide range of applications (Barnard, 1953; Reed, 1965).

References

Aicher KP, Muller M, Wilhem U, Grotemeyer J, *Eur Mass Spectrom*, *1*,331,(1995)

Alikhanov SG, *Sov Phys JETP, 4*,452,(1957)

Alonso M., Finn E., *University Physics, Vol 3, Quantum and Statistical Physics*, Addison-Wesley, (1968)

Alvarez LW, Cornog R, *Phys Rev*, *56*,379,(1939)

Alvarez LW, Cornog R, *Phys Rev*, *56*,613,(1939)

Antoine R, Arnaud L, Rahim AE, Rayane D, Broyer M, Dugourd P, *Int J Mass Spectrom*, *239*,1,(2004)

Aston FW, *Phil Mag*, *38*,707,(1919)

Aston FW, *Phil Mag*, *39*,449,(1920)

Aston FW, *Phil Mag*, *45*,707,(1923)

Bakker JMB, *The Spiratron*, Ph.D Thesis, University of Warwick, (1969)

Bakker JMB, *Int J Mass Spectrom Ion Phys*, *6*,291,(1971)

Bakker JMB, *Adv Mass Spectrom*, *278*,5,(1971)

Bakker JMB, *J Phys E*, *6*,785,(1973)

Bakker JMB, Freer DA, Todd JFJ, *Dyn Mass Spectrom*, *6*,91,(1981)

Baldeschwieler JD, *Science*, *159*,263,(1968)

Barber NF, *Proc Leeds Phil Lit Soc, Soc Sect*, *2*,427,(1933)

Barber M, Bordori RS, Sedgwick RD, Tyler AN, *J Chem Soc Chem Commun*, p325,(1981*a*)

Barber M, Bordori RS, Sedgwick RD, Tyler AN, *Biomed Mass Spectrom*, *8*,493,(1981*b*)

Barnard GP, *Nature (Lond.)*, *164*,283,(1949)

Barnard GP, *Modern Mass Spectrometry*, The Institute of Physics, London, (1953)

Beavis RC, Chait BT, *Chem Phys Lett*, *181*,479,(1991)

Becker CH, Gillen KT, *Anal Chem*, *56*,1671,(1984)

Beckey HD, Schuelte D, *Z Instrumen*, *68*,302,(1960) Beckey HD, *Principles of Field Ionization and Field Desorption Mass Spectrometry*, Pergamon Press, Oxford, (1977)

Belu A, Graham D, Castner D, *Biomaterials*, *24*,3635,(2003)

Bemont E, Bostel A, Bouet M, Da Costa G, Chambreland S, Deconihout B, Homo K, *Ultramicroscopy*, *95*,231,(2003)

Benninghoven A, Jaspers D, Sichtermann W, *Appl Phys*, *11*,35,(1976)

Benninghoven A, Sichtermann W, *Anal Chem*, *50*,1180,(1978)

Benninghoven A, In Benninghoven A, (Ed), *Ion Formation from Organic Solids*, Springer, Berlin, (1983)

Berger C, *Int J Mass Spectrom Ion Processes*, *46*,63,(1983)

Bergmann T, Martin TP, Schaber H, *Rev Sci Instr*, *60*,347,(1989*a*)

Bergmann T, Martin TP, Schaber H, *Rev Sci Instr*, *60*,792,(1989*b*)

Bergmann T, Martin TP, Schaber H, *Rev Sci Instr*, *61*,2592,(1990)

Berkout VD, Cotter RJ, Segers DP, *J Am Soc Mass Spectrom*, *12*,641,(2001)

Beuhler RJ, Flanigan E, Greene E, Friedman LJ, *J Am Chem Soc*, *96*,3990,(1974)

Beussman DJ, Vlasak PR, McLane RD, Seeterlin MA, Enke CG, *Anal Chem*, *67*,3952,(1995)

Beynon JH, *Mass Spectrometry and its Applications to Organic Chemistry*, Elsevier, (1960)

Blauth EW, *Dynamic Mass Spectrometers*, Elsevier, (1966)

Bleakney W, *Phys Rev*, *34*,157,(1929)

Bleakney W, *Phys Rev*, *35*,139,(1930)

Bleaney BI, Bleaney B, *Electricity and Magnetism*, 3rd Edition, Oxford University Press, (1976)

Boesl U, Weinkauf R, Schlag EW, *Int J Mass Spectrom Ion Processes*, *112*,121,(1992).

Bondarenko PV, MacFarlane RD, *Int J Mass Spectrom Ion Processes*, *160*,241,(1997)

Boyle JG, Whitehouse CM, *Anal Chem*, *64*,2084,(1992)

Brinckerhoff WB, Cornish TJ, McEntire RW, Cheng AF, Benson RC, *Acta Astronautica*, *52*,397,(2003)

Brock A, Rodriquez N, Zare RN, *Anal Chem*, *70*,3735,(1998) Brown RS, Lennon JJ, *Anal Chem*, *67*,1998,(1995)

Brunee C, Radio Frequency Mass Spectrometers and their Application, p37 *In* Reed R. I. (Ed), *Mass Spectrometry – A NATO Advanced Study Institute on Theory, Design and Applications*, Glascow, (1964)

Brunee C, *Int J Mass Spetrom Ion Processes, 76*,125,(1987)

Cameron AE, Eggers DF, *Rev Sci Instr, 19*,605,(1948)

Caprioli RM, Farmer TB, Gile J, *Anal Chem*, *69*,4751,(1997)

Carrico JP, *J Phys E: Sci Instr*, *10*,31,(1977)

Chait BT, Standing KG, *Int J Mass Spectrom Ion Phys, 40*,185,(1981)

Chait BT, Field FH, *Int J Mass Spectrom Ion Processes*, *41*,17,(1981)

Chandezon F, Huber B, Ristori C, *Rev Sci Instr*, *65*,3344,(1994)

Chaurand P, Lutzenkirchen F, Spengler BJ, *J Am Soc Mass Spectrom*, *10*,91,(1999)

Chaurand P, Schwartz SA, Caprioli RM, *Current Opinion in Chemical Biology*, *6*,676,(2002)

Chen YH, Gonin M, Fuhrer K, Dodonov A, Su CS, Wollnik H, *Int J Mass Spectrom*, *185/186/187*,221,(1999)

Chernushevich IV, Ens W, Standing KG, *Anal Chem*, *71*,452A,(1999)

Chernushevich IV, Loboda AV, Thomson BA, *J Mass Spectrom*, *36*,849,(2001)

Chien MSM, Lubman DM, *Rev Sci Instr*, *63*,4277,(1992)

Chien MSM, Michael SM, Lubman DM, *Anal Chem*, *65*,1916,(1993)

Clarke EM, *Can J Phys*, *32*,764,(1954)

Classen J, *Z Phys*, *9*,762,(1908)

Clausnitzer G, *Nucl Instr Meth*, *23*,309,(1963)

Coggeshall ND, Jordan EB, *Rev Sci Instr*, *14*,125,(1943)

Cole RB, (Ed), *Electrospray Ionization Mass Spectrometry*, Wiley, New York, (1997)

Coles JN, Guilhaus M, *J Am Soc Mass Spectrom*, *5*,772,(1994)

Colby SM, King TB, Reilly JP, *Rapid Commun Mass Spectrom*, 8,865,(1994)

Colby SM, Reilly JP, *Anal Chem*, *68*,1419,(1996)

Colby S, Application of SIMION 6.0 to a study of the Finkelstein Ion Source: Part 1 & Part 2, Scientific Instrument Services, Inc, Application Notes 69 & 70, (1997)
Link: http://www.sisweb.com/apnote.htm#simion

Collin JE, The Determination of Ionization and Appearance Potentials & Photon and Electron Impact Processes, in Reed R.I. (Ed), *Mass Spectrometry, A NATO Advanced Study*, Academic Press, (1965)

Collings BA, Campbell JM, Mao D, Douglas DJ, *Rapid Commun Mass Spectrom, 15*,1777,(2001)

Conover CWS, Twu YJ, Yang YA, Bloomfield LA, *Rev Sci Instr, 60*,1065,(1989)

Conzemius RJ, Capellen JM, *Int J Mass Spectrom Ion Phys*, *34*,197,(1980)

Cooks RG, Beynon JH, Caprioli RM, Lester GR, *Metastable Ions*, Elsevier, (1973)

Cordero MM, Cornish TJ, Cotter RJ, Lys IA, *Rapid Commun Mass Spectrom, 9*,1356, (1995)

Cordero MM, Cornish TJ, Cotter RJ, *J Am Soc Mass Spectrom*, *7*,590,(1996)

Cornish TJ, Cotter RJ, *Rapid Commun Mass Spectrom*, *7*,1037,(1993)

Cornish TJ, Cotter RJ, *Rapid Commun Mass Spectrom, 8*,781,(1994)

Cornish TJ, Cotter RJ, *Anal Chem*, *69*,4615,(1997)

Cosslett VE, *Introduction to Electron Optics*, Clarendon Press, Oxford, (1950)

Cotter RJ, Fenselau C, *Biomed Mass Spectrom,* 6, 287,(1979)

Cotter RJ, *Anal Chem*, *56*,2594,(1984)

Cotter RJ, Honovich JP, Olthoff JK, In Benninghoven A, Colton RJ, Simons DS, Werner HW, (Eds), *Secondary Ion Mass Spectrometry, SIMS V*, Springer, Berlin, p182, (1986)

Cotter RJ, *Anal Chem*, *64*,1027A,(1992)

Cotter RJ, *TOF MS - Instrumentation and Applications in Biological Research*, ACS, Washington, DC, (1997)

Courant ED, Livingston MS, Snyder HS, *Phys Rev, 88*,1190,(1952)

Damoth DC, Recent Advances in Time-of-Flight Mass Spectrometry, Reprinted from *Adv. Anal Chem Instr*, 4, (Ed) Reilly C. N., John Wiley & Sons, (1964*a*)

Damoth DC, Advances in Time-of-Flight Mass Spectrometry, p61 In Reed RI (Ed), *Mass Spectrometry – A NATO Advanced Study Institute on Theory, Design and Applications*, Glascow, (1964*b*)

Dawson PH, *Quadrupole Mass Spectrometry and its Applications*, Elsevier, Amsterdam, (1976)

Dawson JHJ, Guilhaus M, *Rapid Commun Mass Spectrom*, *3*,155,(1989)

Della Negra S, LeBeyec Y, *Anal Chem*, *57*,2035,(1985) Della Negra S, LeBeyec Y, In Benninghoven A, (Ed), Ion Formation from Organic Solids, IFOS III, Springer, Berlin, p42. (1986)

Dempster AJ, *Phys Rev*, *11*,316,(1918)

Dempster AJ, *Phys Rev*, *18*,415,(1921)

Ding L, Sudakov M, Kumashiro S, *Int J Mass Spectrom, 221*,117,(2002)

Dodonov AF, Chernushevich IV, Dodonova TF, Raznikov VV, Tal'roze VL, USSR Patent, No.1681340A1, (1987)

Dodonov AF, Chernushevich IV, Laiko VV, *Proc. 12th Int Mass Spectrom Conf*, 26-30 August, Amsterdam, Netherlands, p153, (1991)

Dodonov AF, Chernushevich IV, Laiko VV, Electrospray Ionization on a Reflecting Time-of-Flight Mass Spectrometer, In Cotter RJ, (Ed), Time of Flight Mass Spectrometry, Am Chem Soc Symp Ser 549, Washington, DC, p108-123, (1994)

Dole M, Mach LL, Hines RL, Mobley RC, Ferguson RC, Alice MB, *J Chem Phys*, *49*,2240,(1968).

Dole M, Cox HL, Gieniec Jr, Gieniec J, *Advances in Chemistry Series*, *125*, 73,(1971)

Doroshenko VM, Cotter RJ, *J Am Soc Mass Spectrom*, *10*,992,(1999)

Doroshenko VM, *Eur J Mass Spectrom*, *6*,491,(2000)

Douglas DJ, French JB, *J Am Soc Mass Spectrom*, *3*,398,(1992)

Duckworth HE, *Mass Spectroscopy*, Cambridge University Press, London, (1960)

Durakiewicz T, Halas S, Arko A, Joyce JJ, Moore DP, *Phys Rev B*, *64*,045101, (2001*a*)

Durakiewicz T, Arko AJ, Joyce JJ, Moore DP, Halas S, *Surf Science*, *478*,72,(2001*b*)

Dushman S, *Phys Rev*, *21*,623,(1923)

Dushman S, *Phys Rev*, *21*,623,(1932)

Dutt PK, *Nucl Instr Meth*, *10*,37,(1961)

Ebert AA, *Anal Chem*, *33*,1865,(1961)

Eland JHD, *Meas Sci Technol*, *4*,1522,(1993)

Erickson ED, Yefchak GE, Enke CG, Holland JF, *Int J Mass Spectrom Ion Processes* *97*,87,(1990)

Erroc GA, Mass Spectrometry Design – Magnetic Deflexion Instruments, In Reed RI (Ed), *Mass Spectrometry, A NATO Advanced Study*, Academic Press, (1965) Even U, Dick B, *Rev Sci Instr*, *71*,4415,(2000*a*)

Even U, Dick B, *Rev Sci Instr*, 71,4421,(2000*b*)

Ezoe H, Hayashi T, *Sci Pap IPCR, 53*(1497),1,(1959)

Fabris D, Vestling MM, Cordero MM, Doroshenko VM, Cotter RJ, Fenselau C, *Rapid Commun Mass Spectrom*, *9*,1051,(1995)

Fasset JD, Moore LJ, Travis JC, DeVoe JR, *Science*, *230*,262,(1985)

Feynman RP, Leighton RB, Sands M, *The Feynman lectures on physics, Mainly electromagnetism and matter*, Chapter 6, Addison-Wesley, Reading, Massachusetts, (1964)

Field FH, Franklin JL, *Electron Impact Phenomena and the Properties of Gaseous Ions*, Academic Press, New York, (1957)

Finkelstein TA, *Rev Sci Instr*, *11*,94,(1940)

Flory CA, Taber RC, Yefchak GE, *Int J Mass Spectrom Ion Processes*, *152*,169,(1996)

Flory CA, Taber RC, Yefchak GE, *Int J Mass Spectrom Ion Processes*, *152*,177,(1996)

Forbes MW, Sharifi M, Croley T, Lausevic Z, March RE, *J Mass Spectrom*, 34,1219,(1999)

Fowler RH, Statistical Mechanics – The theory of the properties of matter in equilibrium, Cambridge University Press, Chapter XI, (1929)

Fowler RH, *Phys Rev*, *33*,45,(1931)

Fowler TK, Good WM, *Nucl Instr Meth*, *7*,245,(1960)

Fox RE, Hickam WM, Kjeldaas T, Groove DJ, *Phys Rev*, *84*,859,(1951)

Fox RE, Hickam WM, Kjeldaas T, Groove DJ, *Rev Sci Instr*, *12*,1101,(1955)

Gard E, Mayer JE, Morrical BD, Dienes T, Fergenson DP, Prather KA, *Anal Chem*, *69*,4083,(1997)

Gardner BD, Holland JF, *J Am Soc Mass Spectrom*, *10*,1067,(1999)

Gardner BD, Cotter RJ, *51st ASMS Conf*, Montreal, Canada, (2003)

Ghosh TK, Pal S, Sinha T, Chattopadhyay S, Golda KS, Bhattacharva P, *Nucl Instr Meth Phys Res*, A*540*,285,(2005)

Giannakopulos AE, Thomas B, Colburn AW, Reynolds DJ, Raptakis EN, Makarov A, Derrick PJ, *Rev Sci Instr*, *73*,2115,(2002)

Gieniec J, Mack LL, Nakamae K, Gupta C, Kumar V, Dole M, *Biomed Mass Spectrom*, *11*,259,(1984) Giessmann U, Rollgen FW, *Org Mass Spectrom, 11*,1094,(1976)

Gillig KL, Ruotolo B, Stone EG, Russel DH, Fuhrer K, Gonin M, Schiltz AJ, *Anal Chem*, *72*,3965,(2000)

Glashchenko VP, Semkin ND, *Sov Phys Tech Phys, 32*,665,(1987)

Glenn WE, *Phys Rev, 85*,763(A),(1952)

Glish GL, Goeringer DE, *Anal Chem*, *56*,2291,(1984)

Glish GL, McLuckey SA, McKown HS, *Anal Instrum*, *16*,191,(1987)

Gohlke RS, *Anal Chem*, *31*,535,(1959)

Goldstein E, *Berlin Akd Monatsber,* 279,(1876); US Patent 2,758,214

Goldstein E., *Berlin Akd Monatsber,* (II),691,(1886); Wied Ann *64*,38,(1898)

Goudsmit SA, *Phys Rev*, 74,622(L),(1948); US Patent 2,698,904

Grill V, Drexel H, Sailer W, Lezius M, Mark TD, *Int J Mass Spectrom*, *205*,209,(2001)

Grix R, Kutscher R, Li G, Gruner U, Wollnik H, *Rapid Commun Mass Spectrom*, *2*,83,(1988)

Grove WR, *Phil Trans Roy Soc, 142*(I),87,(1852)

Guevremont R, Siu KWM, Wang J, Ding L, *Anal Chem*, *69*,3959,(1997)

Guilhaus M, *J Am Soc Mass Spectrom*, *5*,588,(1994)

Guilhaus M, *J Mass Spectrom*, *30*,1519,(1995)

Guilhaus M, Mlynski V, Selby D, *Rapid Commun Mass Spectrom*, *11*,951,(1997)

Guilhaus M, Selby D, Mlynski V, *Mass Spectrom Rev*, *19*,65,(2000*a*)

Guilhaus M, *Spectrochimica Acta Part B*, *55*,1511,(2000*b*)

Hagstrum HD, Tate JT, *Phys Rev*, *59*,354,(1941)

Hagstrum HD, *Rev Mod Phys*, *23*,185,(1951).

Halas S, Durakiewicz T, *J Phys: Cond Matter*, *10*,10815,(1998)

Hansen G, Munson B, *Anal Chem*, *50*,1130,(1978)

Hanson EE, *Phys Rev*, *51*,86,(1937)

Harvey A, Monteiro F, Reed I, *Int J Mass Spectrom Ion Phys*, *4*,365,(1970)

Harvey DJ, Bateman RH, Bordoli RS, Tyldesley R, *Rapid Commun Mass Spectrom*, *14*,2135,(2000) Hashimoto Y, Waki I, Yoshinari K, Shishika T, Terui Y, *Rapid Commun Mass Spectrom*, *19*,221,(2005).

Hasted JB, *Physics of Atomic Collisions*, Butterworth & Co. Ltd, London, (1964)

Hays EE, Richards PI, Goudsmit SA, *Phys Rev*, *84*,824,(1951)

Hays EE, *Phys Rev*, *96*,1454(A),(1954)

He L, Liu YH, Zhu Y, Lubman DM, *Rapid Commun Mass Spectrom*, *11*,1440,(1997)

He L, Lubman DM, *Rapid Commun Mass Spectrom*, *11*,1467,(1997)

Heil H, *Z Phys*, *120*,212,(1943)

Henderson SC, Valentine SJ, Counterman DE, Clemmer DE, *Anal Chem*, *71*,291,(1999)

Henneberg W, *Ann Physik*, *19*,335,(1934)

Herring C, Nichols MH, *Rev Mod Phys*, *21*,185,(1949)

Hertel GR, *J Chem Phys*, *47*,133,(1967)

Herzog R, *Z Phys*, *89*,447,(1934)

Hillenkamp F, Kaufmann R, Nitsche R, Unsold E, *Nature*, *256*,119,(1975)

Hillenkamp F, Kaufmann R, Nitsche R, Unsold E, *Appl Phys*, *8*,341,(1975)

Hillenkmamp F, Karas M, *Int J Mass Spectrom*, *200*,71,(2000)

Hipple JA, Bleakney W, *Phys Rev*, *49*,884,(1936)

Hipple JA, Bleakney W, *Phys Rev*, *53*,521,(1938)

Hipple JA, Sommer H, Thomas HA, *Phys Rev*, *76*,1877,(1949)

Hipple JA, Sommer H, *Phys Rev*, *85*,712 (A),(1952)

Hiraya A, Senba Y, Yoshida H, Tanaka K, *J Electron Spectrosc Related Phenom*, *101*,1025,(1999)

Hoaglund CS, Valentine SJ, Clemmer DE, *Anal Chem*, *69*,4156,(1997)

Hoaglund CS, Valentine SJ, Reilly JP, Clemmer DE, *Anal Chem*, *70*,2236,(1998)

Hoaglund CS, Li J, Clemmer DE, *Anal Chem*, *72*,2737,(2000)

Horovitz K, Johnson V, *Methods of Experimental Physics*, Vol 4, Part 4, Chapter 1, Academic Press, (1959)

Hsu BH, Xie YX, Bush KL, Cooks RG, *Int J Mass Spectrom Ion Processes*, *51*,225,(1983) Huber M, Spengler B, Kaufman R, *Proc of the 42nd ASMS Conf Mass Spectrom*, Chicago, Illinois, p1044,(1994)

Hughes A, Rojansky V, *Phys Rev*, *34*,284,(1929)

Hughes A, McMillan JH, *Phys Rev*, *34*,291,(1929)

Hunt DF, Shabanowitz J, Botz FK, Brent DA, *Anal Chem, 49*,1160,(1977)

Hutson AR, *Phys Rev*, *98*,889,(1955)

Ibuki T, Okada K, Saito K, Gejo T, Saito N, Suzuki IH, *Nucl Instr Meth Phys Res*, A *467*,1505,(2001)

Ihara A, *et al*, *Astroparticle Pysics,* 17,263,(2003)

Inghram MG, Hayden RJ, *A Handbook on Mass Spectroscopy*, Nuclear Science Series, Report No. 14, National Academy of Sciences, Washington DC, (1954)

Ionov NI, Mamyrin BA, *J Tech Phys (USSR), 23*,2101,(1953)

Ishihara M, Toyoda M, Matsuo T, *Int J Mass Spectrom*, *197*,179,(2000)

Jardine DR, Morgan J, Alderdice DS, Derrick PJ, *Org Mass Spectrom*, *27*,1077,(1992)

Johnson EG, Nier AO, *Phys Rev*, *91*,10,(1953)

Johnson GP, Hedin AB, Hakansson PL, Sundqvist BUR, Save BG, Nielsen PF, Roepstorff P, Johansson KE, Kamensky I, Lindberg MS, *Anal Chem*, *58*,1084,(1986)

Jones TJ, *Thermionic Emission*, Methuen's Monographs on Physical Subjects, London, (1936)

Joy JWK, Time-of-Flight Mass Spectrometry; In Price D, Williams JE, (Eds), Heyden & Son Ltd, London, England, p247-260, (1969)

Juenker DW, *J Appl Phys*, *28*,1398,(1957)

Kaminsky M, *Atomic and Ionic Impact Phenomena on Metal Surfaces*, Chapter 1, Springer-Verlag, (1965)

Karas M, Hillenkamp F, *Anal Chem*, *60*,2299,(1988)

Karataev VI, Mamyrin BA, Shmikk DV, *Sov Phys-Tech Phys, 16*,1177,(1972)

Katzenstein HS, Friedland SS, *Rev Sci Instr, 26*,324,(1955)

Kaufman R, Spengler BJ, Lutzenkirchen F, *Rapid Commun Mass Spectrom*, *7*,902,(1993)

Keller R, *Helv Phys Acta*, *22*,386,(1949)

Kimmel JR, Engelke F, Zare RN, *Rev Sci Instr*, 72,4354,(2001) Kinsel GR, Johnston MV, 37th ASMS *Conf Mass Spectrom*, (1989)

Kinsel GR, Mowry CD, McKeown PJ, Johnston MV, *Int J Mass Spectrom Ion Processes*, 104,35,(1991)

Kiser RW, *Introduction to Mass Spectrometry and it's Applications*, Prentice Hall, (1965)

Kissel J, In Todd JFJ, (Ed), Proc 10th *Int Mass Spectrom Conf*, Swansea, 1985, Wiley, London, p175, (1986)

Knorr FJ, Chatfield MA, Chatfield DA, *Anal Chem*, *58*,690,(1986)

Knorr FJ, Chatfield DA, Proc 33rd ASMS *Conf Mass Spectrom,* San Diego, p719,(1993)

Knox BE, Vastola FJ, *Chem Eng News*, *44*,48,(1966)

Kraftmakher Y, *Am J Phys*, *66*,225,(1998)

Krutchinsky AN, Chernushevich IV, Spicer V, Ens W, Standing KG, *J Am Soc Mass Spectrom*, *9*,569,(1998*a*)

Krutchinsky AN, Loboda AV, Spicer V, Dworschak R, Ens W, Standing KG, *Rapid Commun Mass Spectrom*, *12*,508,(1998*b*)

Kurepa M, Josifov G, Madzunkov S, Cadez I, *Hemijska Industrija*, *52*,530,(1998)

Kutscher R, Grix R, Li G, Wollnik H, *Int J Mass Spectrom Ion Processes, 103*,117,(1991)

Laiko VV, Dodonov AF, *Rapid Commun Mass Spectrom*, *8*,720,(1994)

Langmuir I, Kingdon KH, *Proc Roy Soc Lond*, *107*,61,(1925)

Langmuir I, Kingdon KH, *Phys Rev*, *34*,129,(1929)

Langmuir I, *J Am Chem Soc*, *54*,2798,(1932)

Lawrence ED, Livingston MS, *Phys Rev*, *40*,19,(1932)

Lenon JJ, Brown RS, 42nd ASMS *Conf Mass Spectrom*, Chicago, IL, (1994)

Lewin M, Guilhaus M, Wildgoose J, Hoyes J, Bateman B, *Rapid Commun Mass Spectrom*, *16*,609,(2002)

Llewellyn PM, US Patent 3,390,265

Lockyer NP, Vickerman JC, *Appl Surf Sci*, *231*,377,(2004)

MacFarlane RD, Skowronski RP, Torgesson DF, *Biochem Biophys Res Commun*, *60*,616,(1974)

MacFarlane RD, Torgesson DF, *Int J Mass Spectrom Ion Phys*, *21*,81,(1976) MacFarlane RD, *Anal Chem*, *55*,1247A,(1983*a*)

MacFarlane RD, In Benninghoven A (Ed), Ion Formation from Organic Solids, Springer, Berlin, p32, (1983*b*)

Makarov A, Raptakis EN, Derrick PJ, *Int J Mass Spectrom Ion Processes*, *146/147*,165,(1995)

Makarov A, *Anal Chem*, *72*,1156,(2000)

Mamyrin BA, Karataev VA, Shmikk D, Zagulin VA, *Sov Phys JETP*, *37(1)*,45,(1973)

Mamyrin BA, Shmikk DV, *Sov Phys JETP*, *49*,762,(1979)

Mamyrin BA, *Int J Mass Spectrom*, *206*,251,(2001)

Marable NL, Sanzone G, *Int J Mass Spectrom Ion Phys*, *13*,185,(1974)

Marple DTF, *J Opt Soc Am*, *46*,490,(1956)

Marshall AG, Schweikhard L, *Int J Mass Spectrom Ion Processes*, *118/119*,37,(1992)

Marshall AG, Hendrickson CL, Jackson GS, *Mass Spectrom Rev*, *17*,1,(1998)

Marshall AG, *Int J Mass Spectrom Ion Processes*, 200,331,(2000)

Marshall AC, *Surf Sci*, *517*,186,(2002)

March RE, Hughes RJ, Todd JFJ, Quadrupole Storage Mass Spectrometry, Wiley-Interscience, New York, (1989)

March RE, Todd JFJ (Eds), Practical Aspects of Ion Trap Mass Spectrometry, Vols 1, 2 and 3, CRC Press, Boca Raton, FL, (1995)

March R.E., Todd J.F.J., Quadrupole Ion Trap Mass Spectrometry, John Wiley & Sons, (2005)

Mattauch JA, Herzog R, *Z Phys*, *89*,786,(1934)

McFadden WH, Teranishi R, Black DR, Day JC, *J Food Sci*, *28*,316,(1963)

McLachlan NW, Theory and Application of the Mathieu Functions, Clarendon Press, Oxford, (1947)

McLafferty FW, *Mass Spectrometry of Organic Molecules*, Academic Press, New York, (1963)

McMahon AW, Papanastasiou D, Rego CA, 50th ASMS *Conf*, Orlando, FL, (2002)

McMahon AW, Papanastasiou D, 51nd ASMS *Conf*, Montreal, Canada, (2003)

McMahon AW, Papanastasiou D, 52nd ASMS *Conf*, Nashville, TN, (2004) McMahon AW, Papanastasiou D, Electron Impact TOF MS for the Analysis of Permanent Gases, Project performed on behalf of the AWE, Aldermaston, Interim Report, May, (2004*b*)

Medzihradszky KF, Campbell JM, Baldwin MA, Falick AM, Juhasz P, Vestal M, Burlingame AL, *Anal Chem*, *72*,552,(2000)

Melzner F, Reflexionmassenspektrometer, *unpublished*, (1962), In Blauth EW, *Dynamic Mass Spectrometers*, ref [173], p115, Elsevier, Amsterdam, (1966)

Meuzelaar HLC, Posthumus MA, Kistemaker PG, Kistemaker J, *Anal Chem*, *45*,1546,(1973)

Michaud AL, Frank AJ, Ding C, Zhao X, Douglas DJ, *J Am Soc Mass Spectrom*, *16*,835,(2005)

Mildner M, *et al*, 49th *ASMS Conf*, (2001)

Millikan RA, *Phys Rev*, *26*,198,(1908); Millikan RA, *Phil Mag*, *19*,209,(1910)

Mirgorodskaya OA, Shevchenko AA, Chernushevich IG, Dodonov AF, Miroshnikov AI, *Anal Chem*, *66*,99,(1994)

Moorman CJ, Parmater JQ, US Patent 3,576,992

Morris HR, Paxton T, Dell A, Langhorne J, Berg M, Bordoli RS, Hoyes J, Bateman RH, *Rapid Commun Mass Spectrom*, *10*,889,(1996)

Muga ML, *Anal Instrum*, *16*,31,(1987)

Muller EW, Panitz JA, McLane SB, *Rev Sci Instr*, *39*,83,(1968)

Muradumov MZ, Davis S, Hasin YI, Krasnov NV, Makarov A, Verentchikov AN, *Int Conf Mass Spectrom*, Edinburgh, Scotland, (2003)

Myers DP, Li G, Yang P, Hieftje GM, *J Am Soc Mass Spectrom*, *5*,1008,(1994)

Myers DP, Li G, Mahoney PP, Hieftje GM, *J Am Soc Mass Spectrom*, *6*,400,(1995*a*)

Myers DP, Li G, Mahoney PP, Hieftje GM, *J Am Soc Mass Spectrom*, *6*,411,(1995*b*)

Niehuis E, Heller T, Feld H, Benninghoven A, In Benninghoven A (Ed), Ion Formation from Organic Solids, IFOS III, Springer, Berlin, p198, (1986)

Niehuis E, Heller T, Feld H, Benninghoven A, *J Vac Sci Technol*, *A5*,1243,(1987)

Nier AO, *Phys Rev*, *50*,1041,(1936)

Nier AO, *Phys Rev*, *52*,933,(1937)

Nier AO, *Phys Rev*, *53*,282,(1938)

Nier AO, *Rev Sci Instr*, *11*,212,(1940*a*)

Nier AO, *Phys Rev*, *57*,546,(1940*b*)

Nier AO, Ney EP, Inghram MG, *Rev Sci Instr, 18*,191,(1947)

Nottingham WB, *Phys Rev, 49*,78,(1936)

Nottingham WB, *Phys Rev, 55*,2003,(1939)

Oakey NS, MacFarlane RD, *Nucl Instrum Meth, 49*,220,(1967)

Oelsner A, Krasyuk A, Fecher GH, Schneider CM, Schonhense G, *J Electron Spectrosc Relat Phenom, 137*,757,(2004)

O'Halloran GJ, Fluegge RA, Betts JF, Everett WJ, Report No. ASD-TDR-62-644 Part I & II: Determination of Chemical Species Prevalent in a Plasma Jet. Technical Report prepared by the Bendix Corporation Research Laboratories Division, Materials Laboratory Research and Technology Division Air Force Systems Command, (1964)

Ohashi M, Yamada S, Kudo H, Nakayama N, *Biomed Mass Spectrom, 5*,578,(1978)

Oksman P, *Int J Mass Spectrom Ion Processes, 141*,67,(1995)

Oktem B, Tolocka MP, Johnston MV, *Anal Chem, 76*,253,(2004)

Opsal RB, Owens KG, Reilly JP, *Anal Chem, 57*,1884,(1985)

Oyly-Watkins D, Hillman C, Winsor DE, Ardrey RE, In *Dynamic Mass Spectrometry*, Price D, Williams JE, (Eds), Heyden & Son, Ltd, London, England, Vol 1, p163,(1970)

Palmer PT, Limero TF, *J Am Soc Mass Spectrom, 12*,656,(2001)

Papanastasiou D, *Analysis of Focusing Conditions and Filament Temperatures in Thermal Ionization oTOF MS*, MSc Thesis, MMU, Manchester, (2001)

Papanastasiou D., McMahon A.W., 53rd ASMS Conf, San Antonio, TX, (2005)

Paul W, Steinwedel H, *Z Naturforsch, A8*,448,(1953)

Paul W, Steinwedel H, German Patent, 944,900; US Patent 2,939,952

Pierce JR, *J Appl Phys, 11*,548,(1940)

Pierce JR, *Theory and Design of Electron Beams*, Van Nostrand & Co., New York, (1954)

Pinkston JD, Rabb M, Watson JT, Allison J, *Rev Sci Instr, 57*,583,(1986)

Piseri P, Iannotta S, Milani P, *Int J Mass Spectrom Ion Processes, 153*,23,(1996)

Piyadasa CKG, Hakansson P, Ariyaratne TR, *Rapid Commun Mass Spectrom, 13*,620,(1999)

Poschenrieder WP, *Int J Mass Spectrom Ion Phys, 6*,413,(1971) Poschenrieder WP, *Int J Mass Spectrom Ion Phys*, *9*,35,(1972*a*)

Poschenrieder WP, *Int J Mass Spectrom Ion Phys*, *9*,357,(1972*b*)

Price D, Williams JE, (Eds), *Dynamic Mass Spectrometry*, Heyden & Son Ltd, London, England, Vol 1, (1970)

Price D, (Ed), *Dynamic Mass Spectrometry*, Heyden & Son Ltd, London, England, Vol 2, (1971)

Price D, Todd JFJ, (Eds), *Dynamic Mass Spectrometry*, Heyden & Son Ltd, London, England, Vol 6, (1981)

Prieto MC, Kovtoun VV, Cotter RJ, *J Mass Spectrom*, *37*,1158,(2002)

Reed RI, *Mass Spectrometry, A NATO Advanced Study*, Academic Press, (1965)

Reimann AL, *Thermionic Emission*, Ch 1, Chapman & Hall, London, (1934)

Richardson OW, *Proc Camb Phil Soc*, *11*,286,(1901)

Richardson OW, *Phil Trans Roy Soc*, *201*,497,(1903)

Richardson OW, *The Emission of Electricity from Hot Bodies*, Longmans Green & Co., 2nd edition, Chapter VIII, (1921)

Riviere JC, Ch 4, In Green M, *Solid State Surface Science*, Vol 1,(1969)

Robertson JB, *Mass Spectrometry*, Methuen, London, (1955)

Robinson CF, Hall LG, *Rev Sci Instr*, *27*,504,(1957)

Rockwood AL, *Proc 34th ASMS Conf*, Cincinnati, OH, p173, (1986)

Rollgen FW, Giessmann U, Heinen HJ, *Int J Mass Spectrom Ion Phys*, *24*,235,(1977)

Saha MN, Srivastava BN, A Treatise on Heat, 4th Edition, Indian Press, (1958)

Schey K, Cooks RG, Grix R, Wollnik H, *Int J Mass Spectrom Ion Processes*, *77*,49,(1987)

Schey K, Cooks RG, Kraft A, Grix R, Wollnik H, *Int J Mass Spectrom Ion Processes*, *94*,11,(1989)

Schottky W, *Phys Rev*, *28*,74,(1926)

Screbalus CA, Li J, Marshall WS, Clemmer DE, *Anal Chem*, *71*,3918,(1999)

Seccombe DP, Reddish TJ, *Rev Sci Instr*, *72*,1330,(2001)

Selby DS, Mlynski V, Guilhaus M, *Rapid Commun Mass Spectrom*, *14*,616,(2000)

Selby DS, Mlynski V, Guilhaus M, *Int J Mass Spectrom*, *206*,201,(2001) Selby DS, Mlynski V, Guilhaus M, *Int J Mass Spectrom*, *215*,31,(2002)

Shevchenko A, Chernushevich I, Ens W, Standing KG, Thompson B, Wilm M, Mann M, *Rapid Commun Mass Spectrom*, *11*,1015,(1997)

Sin CH, Lee ED, Lee ML, *Anal Chem*, *63*,2897,(1991)

Smith LG, *Rev Sci Instr*, 22,166,(1951*a*)

Smith LG, *Rev Sci Instr*, 22,115,(1951*b*); US Patent 2,709,750

Smith LG, *Phys Rev*, *81*,295(A),(1951*c*)

Smith LG, Damm CC, *Rev Sci Instr*, *27*,638,(1956)

Smith DH, *Thermal Ionization Mass Spectrometry*, Ch 1, In *Inorganic Mass Spectrometry*, Practical Spectroscopy, A Series, 1st Edition, Marcel Dekker, New York-Basel, (2000)

Sommer H, Thomas HA, Hipple JA, *Phys Rev*, *82*,697,(1951)

Spengler BJ, *J Mass Spectrom*, *32*,1019,(1997)

Srivastava SK, Iga I, Rao MVVS, *Meas Sci Technol*, *6*,1379,(1995)

Stamatovic A, Schulz GJ, *Rev Sci Instr*, *39*,1752,(1968)

Standing KG, Beavis R, Ens W, Tang X, Westmore JB, In *The Analysis of Peptides and Proteins by Mass Spectrometry*, NcNeal CJ, (Ed), Wiley, Chichester, England, p267-278, (1988)

Standing KG, *Int J Mass Spectrom*, *200*,597,(2000)

Stein R, *Int J Mass Spectrom Ion Processes*, *14*,205,(1974)

Stein R, *Int J Mass Spectrom Ion Processes*, *132*,29,(1994)

Stephens WE, Hughes AL, *Phys Rev*, *45*,123,(1934)

Stephens WE, *Phys Rev*, *45*,513,(1934)

Stephens WE, *Phys Rev*, *69*,691,(1946); *Bull Am Phys Soc*, *21*,22,(1946); US Patent 2,612,607.

Stone EG, Ruotolo B, Gillig KJ, Russel DH, Fuhrer K, Gonin M, Shultz AJ, *Anal Chem*, *73*,2233,(2001)

Studier MH, *Rev Sci Instrum*, *34*,1367,(1963)

Suckau D, Resemann A, Schuerenberg M, Hunfagel P, Holle A, *Anal Bioanal Chem*, *367*,952,(2003)

Suess DT, Prather KA, *Chem Rev*, *99*,3007,(1999)

Surman DJ, Vickerman JC, *J Chem Soc Chem Commun*, p324-325, (1981) Suzuki T, *et al*, *Nucl Phys*, A*754*,375c,(2005)

Tabet JC, Cotter RJ, *Anal Chem*, *56*,1662,(1984)

Takekoshi H, Tsuruoka K, Shimizu S, *Bull Inst Chem Res Kyoto Univ*, *27*,52,(1951)

Talrose VL, Karachevtsev GV, *Adv Mass Spectrom*, *211*,3,(1966)

Tanaka K, Waki H, Ido Y, Akita S, Yoshida Y, Yoshida T, *Rapid Commun Mass Spectrom, 2*,151,(1988)

Tang X, Beavis R, Ens W, Lafortune F, Schueler B, Standing KG, *Int J Mass Spectrom Ion Processes*, *85*,43,(1998)

Tate JT, Smith PT, *Phys Rev*, *46*,773,(1934)

Taylor PO, Dolder KT, Kouppila WE, Dunn G, *Rev Sci Instr*, *45*,538,(1974)

Thomson JJ, *Phil Mag, 5*,293,(1897)

Thomson JJ, *Phil Mag, 21*,225,(1911)

Toyoda M, Okumura D, Ishihara M, Katakuse I, *J Mass Spectrom*, *38*,1135,(2003)

Toyoda M, Okumura D, Ishihara M, Katakuse I, *Adv Mass Spectrom*, *16*,335,(2004)

Trapp O, Kimmel JR, Yoon OK, Zuleta IA, Fernandez FM, Zare RN, *Angew Chem Int Ed, 43*,6541,(2004)

Turvey K, *Eur J Phys*, *11*,51,(1990)

Unsoeld E, Hillenkamp F, Nitsche R, *Analysis*, *4*,115,(1976)

Valentine SJ, Counterman A, Clemmer DE, *J Am Soc Mass Spectrom*, *10*,1188,(1999)

Valyi L, *Atom and Ion Sources*, John Wiley & Sons, London-Budapest, (1977)

van Wuijckhuijse AL, Stowers MA, Kleefsman WA, van Baar BLM, Kientz CE, Marijnissen JCM, *Aerosol Science*, 36,677,(2005)

Vauthier R, *Comptes Rendus*, *236*,1033,(1955)

Verentchikov AA, Ens W, Standing KG, *Anal Chem*, *66*,126,(1994)

Vestal M, Juhasz J, *J Am Soc Mass Spectrom, 9*,892,(1998)

Vlasak PR, Beussman DJ, Ji Q, Enke CG, *J Am Soc Mass Spectrom*, *7*,1002,(1996)

Walter K, Boesl U, Schlag EW, *Int J Mass Spectrom Ion Processes, 71*,309,(1986)

Wien W, *Ann Physik*, *65*,440,(1898)

Whittal RM, Liang L, *Anal Chem*, *76*,1950,(1995) Wiley WC, McLaren IH, *Rev Sci Instr*, *26*,1150,(1955)

Wiley WC, Science, *24*,817,(1956)

Wilkins CL, Weil DA, Yang CLC, Ijames CF, *Anal Chem*, *57*,520,(1985)

Williams MW, Beekman DW, Swan JB, Arakawa ET, *Anal Chem*, *56*,1348,(1984)

Wilson RR, *The Isotron*, AECD-3373, 19,(1952)

Wobschall D, *Rev Sci Instr*, *36*,466,(1965)

Wolff MM, Stephens WE, *Rev Sci Instr*, *24*,616,(1953)

Wollnik H, *Optics of Charged Particles*, Academic: Orlando, (1987*a*)

Wollnik H *et al*, *Nucl Instr Meth A*, *258*,331,(1987*b*)

Wollnik H, *Mass Spectrom Rev*, *12*,89,(1993)

Wood SH, Prather KA, *Trends Anal Chem*, *17*,346,(1998)

Wright LG, Cooks RG, Woods KV, *Biomed Mass Spectrom*, *12*,159,(1985)

Xu HJ, Wada M, Tanaka J, Kawakami H, Katayama I, Ohtani S, *Nucl Instrum Meth Phys Res A*, *333*,274,(1993)

Yamashita M, Fenn JB, *J Chem Phys*, *88*,4451,(1984)

Yefchak GE, Enke CG, Holland JF, *Int J Mass Spectrom Ion Processes*, *87*,313,(1989)

Yoshida Y, US Patent 4,625,112

Young CE, Edelson D, Falconer WE, *J Chem Phys*, *53*,4295,(1970)

Xu HJ, Wada M, Tanaka J, Kawakami H, Katayama I, Ohtani S, *Nucl Instrum Meth A*, *333*,274,(1993)

Zabielski MF, Diem HT, Kendall BR, *Int J Mass Spectrom Ion Phys*, *5*,349,(1970)

Zakett D, Schoen AE, Cooks RG, Hemberger PH, *J Am Chem Soc*, *103*,1295,(1981)

Zandberg EY, Ionov NI, Surface Ionization, Moscow, (1969); Translated from Russian, Reproduced by the National Technical Information Service, Published for the US Department of Commerce, National Bureau of Standards, Israel program for Scientific Translations, (1971)

Zare RN, Fernandez FM, Kimel JR, *Angew Chem Int Ed*, *42*,30,(2003)